Advancing Atomistic Modeling of Defects in Plastic Deformation of Metallic Crystalline Materials

by

Chaoming Yang

A dissertation submitted in partial fulfillment
of the requirements for the degree of
Doctor of Philosophy
(Materials Science and Engineering)
in The University of Michigan
2020

Doctoral Committee:

Assistant Professor Liang Qi, Chair
Professor John Allison
Assistant Professor Yue Fan
Professor Amit Misra

Chaoming Yang

chaomy@umich.edu

ORCID iD: 0000-0002-2899-6001

To my parents

ACKNOWLEDGEMENTS

I want to express the most profound gratefulness to my advisor Prof. Liang Qi for his continuous support and guidance from the first day we met. He supervised me on research with his exceptional patience, curiosity, and immense knowledge, and he inspired me in everyday life with his sincerity, self-discipline, responsibility, humbleness, and forgiveness. I feel fortunate and honored as a Ph.D. student of Prof. Qi, to work with him, to learn from him.

I want to thank my dissertation committee members Prof. John Allison, Prof. Amit Misra, and Prof. Yue Fan, for their insightful comments and encouragement. I want to express my sincere thanks to Dr. Sylvie Aubry for her support and guidance on my internship research at Lawrence Livermore National Laboratory. I want to thank Dr. Timofey Frolov for instructing me on atomistic simulations of grain boundaries. I want to appreciate Dr. Zhihua Huang and Dr. Lianfeng Zou, for their excellent experimental work in collaboration with me. I want to thank Dr. Yongjie Hu for sharing his experience of materials simulations and presentation techniques with me. I am grateful to Mingfei Zhang for his valuable discussion and help on my research work. I am thankful to Aditya Sundar for setting up the workstation in our laboratory. I want to appreciate Mohsen Taheri Andani for sharing his experimental data of grain boundaries. I am thankful to Junjie Yang for his assistance in my research work in 2019 summer.

Last, I want to express my heartfelt gratitude to my parents for their unselfish love, thoughtful guidance, and unlimited support.

TABLE OF CONTENTS

DEDICATION ii

ACKNOWLEDGEMENTS iii

LIST OF FIGURES vii

LIST OF TABLES xvii

LIST OF ABBREVIATIONS xix

ABSTRACT xxii

CHAPTER

I. Introduction 1

- 1.1 Experimental and theoretical background 1
- 1.2 Outline 4

II. Fundamental Concepts and Modeling Methodologies 7

- 2.1 Materials modeling techniques 7
  - 2.1.1 Density functional theory (DFT) 7
  - 2.1.2 Molecular dynamics (MD) 10
- 2.2 Concepts in materials mechanics 12
  - 2.2.1 Lattice instability 12
  - 2.2.2 Ideal strength 13
  - 2.2.3 Dislocation 15
  - 2.2.4 Grain boundary (GB) 17

III. Lattice Instability and Intrinsic Ductility of W and W Alloys 20

- 3.1 Introduction 20
- 3.2 Computational methods 22
  - 3.2.1 Ideal tensile strength and phonon instability 22

3.2.2 Details of DFT calculations 24
3.2.3 Stacking fault and surface energies 25
3.2.4 Linear elastic fracture mechanics (LEFM) 26
3.3 Results and discussion 30
3.3.1 Benchmarks of ideal strength and phonon calculations . 30
3.3.2 Ideal strength and shear instability 31
3.3.3 Ideal strength and phonon instability (PI) 40
3.3.4 LEFM analyses 49
3.4 Conclusion 53

IV. Accurate Interatomic Potential of Nb for Studies on Deformation Defects 54

4.1 Introduction 54
4.2 Computational methods 56
4.2.1 Modified embedded-atom method 56
4.2.2 Force matching method 57
4.2.3 Fitting procedures 58
4.3 Results and discussion 63
4.3.1 Structural and elastic properties 64
4.3.2 Phonon, volume-pressure and thermal expansion 65
4.3.3 Point defects 69
4.3.4 Surfaces, twin boundaries and generalized staking faults 72
4.3.5 Ideal strengths 77
4.3.6 Screw dislocation cores 82
4.3.7 Simulations of crack evolution under tensile loading . . 89
4.4 Conclusion 95

V. Complex Grain Boundary Structures from Evolutionary Algorithm . . 97

5.1 Introduction 97
5.2 Computational methods 100
5.2.1 Basics of evolutionary algorithm (EA) 100
5.2.2 Atomistic simulations of GBs 101
5.2.3 Flowchart of the EA based GB structure search implementation 102
5.2.4 Crossover and mutation 105
5.2.5 Control of atomic density 108
5.2.6 Selection and structure fingerprints 111
5.2.7 Details of GB setups and simulations 113
5.3 Results and discussion 114
5.3.1 The [001] STGBs in FCC Cu 114
5.3.2 The [110] STGBs in BCC W 119
5.3.3 The $[1\bar{2}10]$ STGBs in HCP Mg 123
5.3.4 Predictions of metastable GB structures 127

5.3.5 Simulations of Tensile Loading on $[1\bar{2}10]$ STGBs in HCP Mg . . . 128
5.4 Conclusion . . . 134

VI. Simulations of Dislocation-precipitate Interactions in Mg-Nd Alloys . . 135

6.1 Introduction . . . 135
6.2 Computational methods . . . 140
6.2.1 DFT calculations for stacking fault energy . . . 140
6.2.2 Dislocation line tension in HCP lattice . . . 141
6.2.3 MD simulations of dislocation-precipitate interactions . 141
6.3 Results and discussion . . . 145
6.3.1 Theoretical estimation of critical resolved shear stress (CRSS) for slip transmission across a β_1 precipitate . . . 145
6.3.2 Verification of empirical potentials in MD simulations . 150
6.3.3 β_1 precipitate-dislocation interaction . . . 153
6.4 Conclusion . . . 160

VII. Summary and Future Work . . . 161

7.1 Summary . . . 161
7.2 Suggested future work . . . 164

BIBLIOGRAPHY . . . 167

LIST OF FIGURES

Figure

2.1 Schematic representation of the self-consistent cycle for solving of DFT based Kohn–Sham equations. 9

2.2 Schematic representation of the iteration cycle molecular dynamics (MD) based on the Verlet algorithm 11

2.3 (a): Sketch of two types of supercells of BCC crystals in the ideal strength calculations. The Cartesian coordinate system is defined along $\langle 100 \rangle_{\mathrm{BCC}}$. $\mathbf{a}_{\mathbf{1},\mathbf{2},\mathbf{3}}$ indicates the base vector of a 2-atom BCC supercell applied for tetragonal tensile path, and $\mathbf{b}_{\mathbf{1},\mathbf{2},\mathbf{3}}$ indicates base vector of a 4-atom BCC supercell applied for orthorhombic tensile path. (b) Illustration of supercell geometry changes due to elastic shear instability (ESI) under $[100]_{\mathrm{BCC}}$ tensile strain. The sketch includes the BCC lattice before/after shear instability viewed from [001] direction. 14

2.4 A schematic illustration of atomic arrangement for an edge (left) and screw (right) dislocation in simple cubic crystal. Green arrows form the Burgers circuit for edge and screw. The Burgers vector is perpendicular and parallel to the dislocation line direction in edge and screw, respectively. 15

2.5 electron backscatter diffraction (EBSD) grain map for extruded Mg-Al alloy. Random colour indicates different GBs. The image is from Mohsen Andani. 18

2.6 Sketch to show variables to define a grain boundary. Xa, Ya, Za and Xb, Yb, Zb are the axes of the coordinates to represent crystallographic directions in grains A and B, respectively. The rotation axis and the rotation (misorientation) angle θ represent the translation between two grains. **n** determines the orientation of the grain boundary plane. 19

3.1 (a) Paths (green lines) along high-symmetry points in the first Brillouin zone (FBZ) of BCC primitive cell for phonon calculations. (b) Changes of FBZ and the symmetric paths under $[100]_{\mathrm{BCC}}$ tension along TP. The reciprocal coordinate system (x^*-y^*-z^*) is defined based on the Cartesian coordinate system defined in Figure 2.3 (a). 23

3.2 Schematic diagram of the semi-infinite crack orientation and the dislocation slip system at the crack front for LEFM analyses. (a) $[11\bar{1}](2\bar{1}1)$ dislocation with $(\theta, \phi) = (54.73^\circ, 0.00^\circ)$; (b) $[111](01\bar{1})$ dislocation with $(\theta, \phi) = (90.00^\circ, 35.27^\circ)$, where θ and ϕ are defined in Equation 3.5. . . . 29

3.3 The phonon dispersion relations of pure W along high-symmetry points of FBZ of the primitive unit cell calculated by the DFPT method using QE, which are consistent with results from the FDM method using VASP (these results are not shown here). 31

3.4 The correlation of lattice constant (a), C_{44} (b) with the concentration of Re in $W_{1-x}Re_x$, respectively, calculated in VCA scheme. 32

3.5 The correlation of C' (a) and bulk modulus (b) with the concentration of Re in $W_{1-x}Re_x$, respectively, calculated in VCA scheme. 33

3.6 The ideal tensile strength behaviors of the perfect W and W-Ta alloy systems under [100] tensile strain. (a): The stress-strain curves along both tetragonal path (TP) and orthorhombic path (OP) of W, $W_{15}Ta_1$ supercell and WTa in B2 supercell from VASP calculations; (b): The corresponding variations of the lattice constants of the tetragonal supercells under [100] tensile strain along the OP from VASP calculations, where $\mathbf{b}_2$ and $\mathbf{b}_3$ are defined in Figure 2.3. 34

3.7 The ideal tensile strength behaviors of the perfect W and W-Ta alloy systems under [100] tensile strain. (a): The stress-strain curves along both TP and OP of W, $W_{15}Ta_1$ supercell and WTa in B2 supercell from QE calculations; (b): The corresponding variations of the lattice constants of the tetragonal supercells under [100] tensile strain along the OP from QE calculations, where $\mathbf{b}_2$ and $\mathbf{b}_3$ are defined in Figure 2.3. 35

3.8 The ideal tensile strength behaviors of the perfect W and W-Re alloys under [100] tensile strain. (a) The stress-strain curves along both TP and OP of W, $W_{15}Re_1$ supercell and WRe in B2 supercell from VASP calculations; (b) The corresponding variations of the lattice constants of the tetragonal supercells under [100] tensile strain along OP from VASP calculations, where $\mathbf{b}_2$ and $\mathbf{b}_3$ are defined in Figure 2.3. 37

3.9 The ideal tensile strength behaviors of the perfect W and W-Re alloys under [100] tensile strain. (a) The stress-strain curves along both TP and OP of W, $W_{15}Re_1$ supercell and WRe in B2 supercell from QE calculations; (b) The corresponding variations of the lattice constants of the tetragonal supercells under [100] tensile strain along OP from QE calculations, where $\mathbf{b}_2$ and $\mathbf{b}_3$ are defined in Figure 2.3. 38

3.10 The ideal tensile behavior of $W_{1-x}Re_x$ in the VCA scheme under [100] tensile strain. (a): Stress-strain curves along both TP and OP. (b): The corresponding variations of the lattice constants of the tetragonal supercells under [100] tensile strain along OP. Here $\mathbf{b}_2$ and $\mathbf{b}_3$ are defined in Figure 2.3. 39

3.11 Phonon frequencies of pure W under different ε_{11} along TP during the [100] ideal tensile deformation. Only the branches with the lowest frequencies of the phonon dispersion relations are plotted. (a) Phonon dispersion curves calculated by FDM methods using VASP. (b) Phonon dispersion curves calculated by DFPT method using QE. 41

3.12 (a) The ideal tensile behavior of $W_{0.5}Ta_{0.5}$ in the VCA scheme under [100] tensile strain. (b) Phonon frequencies of VCA $W_{0.5}Ta_{0.5}$ under different ε_{11} along TP during the [100] ideal tensile deformation calculated by DFPT method using QE. Only the branches with the lowest frequencies of the phonon dispersion relations are plotted. 43

3.13 A sketch of the unstable $T_{[001]}[0\ \xi\ 0]$ phonon mode in VCA $W_{0.5}Ta_{0.5}$ alloy:(a) The polarization vector $\mathbf{p}$ and the wave vector $\mathbf{k}$ of the unstable phonon mode. (b) Projection of the crystal structure on $(100)_{BCC}$ plane to illustrate the phonon instability is equivalent to the ESI in Figure 2.3 (b). 44

3.14 Phonon frequencies of VCA $W_{1-x}Re_x$ under different ε_{11} along TP during the [100] ideal tensile deformation calculated by DFPT method using QE. (a): $W_{0.9}Re_{0.1}$. (b): $W_{0.75}Re_{0.25}$. (c): $W_{0.5}Re_{0.5}$. 46

3.15 The most negative phonon frequencies along different branches of phonon dispersion curves for different VCA $W_{1-x}Re_x$ alloys at ε_{11} = 12% during the [100] ideal tensile deformation. 47

3.16 A schematic illustration of the dynamic instability of $T_{[2\bar{1}1]}[2\xi\xi\bar{\xi}]$ phonon mode in VCA $W_{0.75}Re_{0.25}$ alloy. (a): The polarization vector **p** and the wave vector **k** of unstable phonon mode shown in the 3D lattice (left) and on the projection of atoms on (011) plane (right). (b): Sketch of the hard sphere "*roll over*" model [141]. The polarization vector **p** is the instantaneous tangent direction along the transition path of the dislocation nucleation event, and it has a small angle with Burgers vector b. Here the green/blue circles stand for atoms at the corner/center of BCC unit cells. . 48

3.17 Cleavage and dislocation emission competition for different W alloys in the VCA scheme predicted by anisotropic LEFM analyses based on crack tip geometry in Figure 3.2. The number of valence electrons per atom is 6.0 for pure W, and it decreases/increases linearly in variance of Ta/Re concentration. (a): The variations of critical stress intensity factor K_{Ic} for Griffith cleavage and K_{Ie} for dislocation emissions of 1/2 $\langle 111 \rangle \{\bar{2}11\}$ and 1/2 $\langle 111 \rangle \{\bar{1}10\}$ slip. (b): The variation of the ductility parameter K_{Ie}/K_{Ic} for both slip systems. 51

4.1 The cubic splines function of ϕ(r) in the MEAM Nb potential. 61

4.2 The cubic splines function of ρ(r) in the MEAM Nb potential. 61

4.3 The cubic spline function of f(r). in the MEAM Nb potential. 61

4.4 The cubic spline function of U(n) in the MEAM Nb potential. 62

4.5 The cubic spline function of g[cos(θ)] in the MEAM Nb potential. 63

4.6 Schematic illustration of sampled phonon paths in the primitive cell of BCC reciprocal lattice. 66

4.7 Nb phonon band structures obtained by the MEAM potential (MEAM), DFT (PAW-PBE) and experiments [195] 67

4.8 Nb 0K pressure-to-volume curve calculated by the MEAM potential and DFT. 68

4.9 Nb thermal expansion curve from 0K to 2500 K by the MEAM potential calculations. 68

4.10 Schematic illustration of six interstitial configurations in BCC lattice. . . 71

4.11 Schematic illustration of deformation twinning pathway. A single red arrow indicates one $\langle 111 \rangle$ Burgers vector magnitude. Atoms are visualized by the software OVITO [227] with color assigned by common neighbor analysis. Blue corresponds to BCC crystal and white corresponds to defects. 75

4.12 Generalized stacking fault energies obtained by the Nb MEAM potential and DFT calculations along $[111](\bar{1}10)$ and $[111](\bar{2}11)$ slip. 76

4.13 The curves of energy and tensile stress in response to ideal tensile strain along [100] direction, calculated by DFT using a PAW-PBE pseudopotential. 78

4.14 The curves of energy and tensile stress in response to ideal tensile strain along [100] direction, calculated by molecular statics (MS) with the Nb MEAM potential. 79

4.15 Energy and shear stress of ideal shear by MS with the Nb MEAM potential. 80

4.16 Energy and shear stress of ideal shear calculated by DFT with PAW-PBE pseudopotential. 81

4.17 Equilibrium screw dislocation core structure given by the MEAM potential calculation. Arrows indicate the differential-displacement of atoms along the [111] Burgers vector direction [247]. 83

4.18 Dislocation core energy calculated by the MEAM potential. 85

4.19 Schematic representation of the unit cell and periodicity vectors within the quadrupolar arrangement [142, 111]. Atomic belong to three different $\langle 111 \rangle$ planes in BCC crystal are represented by three different colors. The dislocation dipole is visualized by its differential displacement map. . . . 86

4.20 Screw dislocation trajectory of moving from one easy core to an adjacent easy core. E: easy core, H: hard core, S: split core, M: the middle point between two easy cores. The red dots are the dislocation core positions extracted from the cost-function method based on Equation 4.17 [244]. . . 87

4.21 The energy path of the infinite straight screw dipole moving between adjacent easy core positions in (110) plane by the NEB calculations based on the MEAM potential. 88

4.22 Energy and tensile stress in response to ideal tensile strain along [100] direction from MS calculations using the Mo MEAM potential [179]. . . 90

4.23 The stress-strain curve of [001] tensile on the BCC crystal bulk with a microcrack from MD simulations using Nb and Mo MEAM potential, respectively. 91

4.24 The atomistic structure evolution of a microcrack under [001] tensile in MD simulations using the Mo MEAM potential [179]. 92

4.25 The atomistic structure evolution of a microcrack under [001] tensile in MD simulations using our Nb MEAM potential. 94

5.1 The sketch of the basic EA workflow for the search of GB structures. . . . 100

5.2 The supercell model of GB representation in our atomistic simulations. . . 101

5.3 Flow chart for finding GB structures by using an evolutionary algorithm with effective mutation methods. 102

5.4 The sketch of crossover based on swapping cuboids or slabs of atoms. . . 105

5.5 The sketch of crossover based on swapping cuboids or slabs of atoms from the crystal nuclei pool generated externally based on 230 space groups. 106

5.6 The sketch of crossover based on swapping cuboids or slabs of atoms using the crystal nuclei pool generated internally, which means those nuclei are chosen from local structures of GBs in previous generations of EA. . . 107

5.7 The sketch of insertion and deletion of a single atom into/from the GB region. 110

5.8 A diagram of extraction and calculation of structure fingerprints for each GB structure 112

5.9 Two projected views of the ground-state STGB structures of the $\Sigma17(410)[001]$ and $\Sigma53(720)[001]$ GBs at the misorientation angle of 28.07° and 31.89°, respectively, obtained in the grand canonical ensembles at 0 K. The left images show the view along the z-axis (the tilt axis) and the right images show the view along the x-axis. The grain boundary plane is on the x-z plane. All the following GB images are plotted according to the same orientation setup. 114

5.10 The projected views along z-(left images) and x-(right images)axis of the STGB structures of the $\Sigma5(310)[001]$ with the misorientation angle of 36.87° at the ground state (top images) or a near-ground state (bottom images) obtained in the grand canonical ensembles at 0 K. 115

5.11 The projected views along z-(left images) and x-(right images) of the STGB structures of the $\Sigma 29(520)[001]$ with the misorientation angle of 43.60° at the ground states obtained in the grand canonical ensembles at 0 K. Two ground-state structures (top vs. bottom images) are obtained. . . 116

5.12 The projected views along z-(left images) and x-(right images)axis of the STGB structures of the $\Sigma 5(210)[001]$ with the misorientation angle of 53.37° at the ground state (top images) or a near-ground state (bottom images) obtained in the grand canonical ensembles at 0 K. 117

5.13 The projected views along z-(left images) and x-(right images)axis of the STGB structures of the $\Sigma 13(320)[001]$, $\Sigma 25(430)[001]$ and $\Sigma 61(650)[001]$ with the misorientation angle of 67.38°, 73.74° and 79.61°, respectively, at the ground states obtained in the grand canonical ensembles at 0 K. . . 118

5.14 The projected views along z-(left images) and x-(right images)axis of the ground-state STGB structures of the $\Sigma 3(112)[1\bar{1}0]$ at $\phi = 70.53^\circ$ (top images) and $\Sigma 3(332)[1\bar{1}0]$ at $\phi = 129.52^\circ$ (bottom images) obtained in the grand canonical ensembles at 0 K. 120

5.15 The projected views along z-(left images) and x-(right images)axis of ground-state STGB structures of the $\Sigma 33(118)[1\bar{1}0]$ at $\phi = 20.05^\circ$, $\Sigma 43(335)[1\bar{1}0]$ at $\phi = 80.63^\circ$, $\Sigma 3(111)[1\bar{1}0]$at $\phi = 109.47^\circ$, and $\Sigma 27(552)[1\bar{1}0]$ at $\phi = 148.41^\circ$ obtained in the grand canonical ensembles at 0 K. 122

5.16 Two projected views along z-(left images) and x-(right images)axis of the ground-state STGB structures of the $(10\bar{1}3)[1\bar{2}10]$ at $\phi = 63.99^\circ$, the $(10\bar{1}2)[1\bar{2}10]$ at $\phi = 86.28^\circ$, the $(10\bar{1}1)[1\bar{2}10]$ at $\phi = 123.83^\circ$ and the $(20\bar{2}1)[1\bar{2}10]$ at $\phi = 150.12^\circ$ obtained the grand canonical ensembles at 0 K. All the four GBs have coherent twin boundary structures, and the blue dashed line indicates the twin boundary plane. 124

5.17 Two projected views along z-(left images) and x-(right images)axis of the ground-state STGB structures of the $(10\bar{1}\,12)[1\bar{2}10]$ at $\phi = 17.75^\circ$ and the $(10\bar{1}8)[1\bar{2}10]$ at $\phi = 26.37^\circ$ obtained the grand canonical ensembles at 0 K. Each purple sign indicates a single edge-type grain boundary dislocation, and the blue dashed line highlights the middle plane of each GB. 125

5.18 Two projected views along z-(left images) and x-(right images)axis of the ground-state STGB structures of the $(50\bar{5}6)[1\bar{2}10]$ and $(50\bar{5}4)[1\bar{2}10]$ at the misorientation angle of 114.74° and 133.77° obtained the grand canonical ensembles at 0 K. The blue dashed line indicates the GB plane that is characterized by the common neighborhood analysis [103]. 126

5.19 A spectrum of stable/metastable GB energies at $\Sigma27(552)[1\bar{1}0]$ at ϕ = 148.41° in BCC W 128

5.20 The tensile stress strain curve for MD tensile normal to the planes of the GB $(10\bar{1}8)[1\bar{2}10]$ at the misorientation angle ϕ = 26.37° and $(50\bar{5}6)[1\bar{2}10]$ at the misorientation angle ϕ =114.74° based on Mg EAM potential [146]. 129

5.21 Atomistic structure evolution near the GB $(10\bar{1}8)[1\bar{2}10]$ at the misorientation angle of 26.37° during increasing tensile strain normal to the GB plane at 300 K based on Mg EAM potential [146]. 130

5.22 Atomistic structure evolution near the GB $(50\bar{5}6)[1\bar{2}10]$ at the misorientation angle of 114.74° during increasing tensile strain normal to the GB plane at 300 K based on Mg EAM potential [146]. 131

5.23 The critical tensile stress to activate plastic deformation in relation to the GB energy for $[1\bar{2}10]$ STGBs with different misorientation angles using both the EAM [146] and MEAM potential [48]. The value of the misorientation angle for each GB is labeled in the figure. 133

6.1 Dark field image a) and bright field image b-d) show microstructure and precipitate configuration for 30 minutes a), 6 hours b), 9 hours c) and 100 hours d) aging of Mg-Nd alloy. Fine β''' precipitates dominate the 30-min sample, and β_1 precipitates are profuse in other conditions. The view is close to [0001] direction, and the triad represent $\{1\bar{2}10\}$ direction. All aging is at 250 °C. 136

6.2 Undeformed samples show straight precipitates with an intact interface with the matrix in a) and b). Images c) and d) are taken from samples compressed 5% showing that the precipitate is cut by basal dislocations leaving an offset at the sheared interface. Image c) is an annular bright field (ABF) image and the thin dark lines (marked with arrows) are dislocations impinging on the precipitate. The inset in c) is a high magnification image of interface offsets. All images are viewed from $[1\bar{2}10]$ direction. 137

6.3 Engineering stress-strain curve of heat treated Mg-2.4wt.%Nd alloy in six aging conditions at 250 °C 138

6.4 Sequence of dislocation interactions with β_1 precipitates from *in situ* experiments, viewed along $[1\bar{2}1\bar{3}]$. The bright field transmission electron microscopy (TEM) images in a), b), c) and d) show the progression of the interaction at different times. Images show a cross-slipped dislocation pinned at the departure side of the precipitate, The pinning point of dislocations 1 and 2 are marked with blue and green dots. The dislocations of interest are marked by dashed blue line in the enlarged inset at top right of each image. 139

6.5 MD simulation setups for interactions between a single basal $\langle a \rangle$ screw dislocation and a β_1 precipitate. The blue dashed vectors indicates the lattice orientation of each β_1 precipitate; an orange cuboid indicates the β_1 precipitate in 3D view of the supercell in the bottom subfigure. 142

6.6 MD simulation setups for interactions between a single basal $\langle a \rangle$ edge dislocation and a β_1 precipitate. The blue dashed vectors indicates the lattice orientation of each β_1 precipitate; an orange cuboid indicates the β_1 precipitate in 3D view of the supercell in the bottom subfigure. 143

6.7 Illustration of the APB generated by $1/4[1\bar{1}1]$ Burgers vector in the lattice of a β_1 precipitate. Purple and yellow atoms stand for Mg and Nd, respectively. b) Sketch of energy increment when $\langle a \rangle$ basal dislocations consecutively cut the lattice of a β_1 precipitate 146

6.8 Images show how dislocations overcome the blocking precipitates. From a) to c), the number of piled-up dislocations is tracked with white arrowheads. The yellow triangle in b), c) and d) show that the leading dislocation escapes from the confined region. 149

6.9 (a) A 2D periodic unit cell of $(\bar{1}10)_{\beta 1}$ plane defined by the dashed rectangle, where yellow atoms are Nd or Y. (b) the color contour of the GSF energy landscape on $(\bar{1}10)_{\beta 1}$ plane of $D0_3$ Mg_3Y, calculated from MEAM potential [7]. 151

6.10 The corresponding GSF energy curve for the displacement along $[111]_{\beta 1}$ on $(\bar{1}10)_{\beta 1}$ plane. Numbers in red color are GSF energy values calculated from DFT for Mg3Nd [27], and values in black color are calculated from MEAM potential for Mg_3Y [31]. 152

6.11 Snapshots of the process of the single basal edge ⟨a⟩ dislocation shearing the β_1 precipitate. a) The dislocation starts to meet the precipitate. b) The dislocation bows out and forms the interface dislocation on the precipitate-matrix interface. c) The dislocation almost cut through the precipitate. Each snapshot includes a top view in the top subfigure and a side view in the bottom subfigure. 154

6.12 Snapshots of a single basal edge ⟨a⟩ dislocation shearing the β_1 precipitate for the second time. a) The dislocation forms a screw component on the precipitate-matrix interfaces perpendicular to $[10\bar{1}0]$ due to the dislocation bow-out and interface glide. b) A part of screw component cross slips on the prismatic plane. c) The cross slipped dislocation segment glides on another basal plane. d) The dislocation cross slips back to the original basal plane. 155

6.13 Schematic of the Friedel-Escaig (FE) cross-slip mechanism. A cross-slipped basal dislocation dissociates into two partial dislocations. The shadow areas represent stacking faults on the basal plane (blue) and green lines represent the perfect screw dislocation segment that cross slips on the prismatic plane (green) before dissociation to partials on an adjacent basal plane (orange). 157

6.14 Snapshots of the basal screw ⟨a⟩ dislocation interacting with the β_1 precipitate for the second time due to the periodic condition of the supercell. a) The screw dislocation contacts with the precipitate. b) The dislocation starts to cross-slip on the prismatic plane toward ⟨c⟩ direction. c-d) The cross-slip process continues and spans over 7 nm along ⟨c⟩ direction, and the cross-slip portion and bow-out portion of the screw dislocation are pinning each other. 159

LIST OF TABLES

Table

3.1 Coordinates of the high-symmetry k-points in FBZ of BCC and BCT (body-centered tetragonal) primitive cells shown in Figure 3.1. The reciprocal coordinate is defined as the unit length equal to $2\pi/|\mathbf{a}_{\mathbf{i=1},2,\mathbf{3}}|$. Here $\mathbf{a_i}$ as labeled in Figure 2.3 can have different lengths due to the ideal tensile deformation. 24

3.2 Lattice constant a (Å), bulk modulus B (GPa), shear modulus $C'(= 1/2(C_{11}-C_{12}))$ (GPa), the ideal tensile strength σ_{11}^{IT} (GPa), and the critical tensile strain ε_{11}^{IT} (%) for pure W from our calculations and previous studies. . . . 30

3.3 Parameters in LEFM analyses: lattice constant a [Å], elastic constants [GPa], and unstable stacking fault energy γ_{usf} and surface energy γ_s [J/m^2]. The deviations between the values of pure W from our DFT calculations and those from previous results [151] should result from the usage of different pseudopotentials. 50

4.1 The cohesive energy E_{cos}, lattice parameters, elastic constants, bulk modulus $B = 1/3(C_{11} + 2C_{12})$, shear modulus $C' = 1/2(C_{11} - C_{12})$ calculated by Nb MEAM potential and DFT calculations in this work, previous DFT calculations [63] and experiment values [33]. The experimental lattice parameter and elastic constants were measured at 4.2 K. The MEAM values for the energies and lattice parameters of meta-stable phases for BCC metals are compared to DFT results. The energies are denoted by their relative value to the cohesive energy. Units: Lattice [Å], Elastic constants [GPa], Energies [meV/atom] 64

4.2 Sampled high-symmetry k-points in the primitive cell of BCC reciprocal lattice. 66

4.3 Single vacancy formation energy E^{f}_{vac}, migration energy E^{m}_{vac} and diffusion activation energy Q_{vac} in Nb [in eV] by the MEAM and DFT (PAW-PBE) calculations in this work (first three rows in the table). Results from previous empirical potentials and DFT calculations are also listed. 70

4.4 Formation energies for the $\langle 100\rangle$ dumbbell, $\langle 110\rangle$ dumbbell, $\langle 111\rangle$ dumbbell, activated crowdion, octahedral, and tetrahedral interstitials in Nb [in eV]. 72

4.5 Low-index surface energies of BCC Nb [J/m^2] 73

4.6 Maximum stress, the corresponding critical strain and elastic modulus $E_{\langle 100\rangle}$ defined in Equation 4.12 in $[100]_{BCC}$ ideal tensile along TP and OP [197, 265] by MEAM potential and DFT calculations 78

4.7 Maximum stress, the corresponding critical strain and elastic shear modulus $G_{\langle 111\rangle}$ defined in Equation 4.13 of ideal shear deformation along $\{110\}\langle 111\rangle$ and $\{211\}\langle 111\rangle$ obtained by the MEAM and DFT PAW-PBE calculations. 82

6.1 Critical engineering tensile strain to failure for heat treated Mg-2.4wt.%Nd alloy in six aging conditions at 250 °C 139

6.2 Line tension Γ and critical shear stress τ_c for dislocations with different angles θ to cut through β_1 precipitate according to Equation 6.1 to 6.7 . . 148

LIST OF ABBREVIATIONS

QM quantum mechanics

CM classical mechanics

DFT density functional theory

MD molecular dynamics

MS molecular statics

VASP Vienna *Ab initio* Simulation Package

CMA-ES Covariance Matrix Adaptation Evolution Strategy

EAM embedded-atom method

MEAM modified embedded-atom method

USPEX Universal Structure Predictor: Evolutionary Xtallography

VCA virtual crystal approximation

PBE Perdew-Burke-Ernzerhof

QE Quantum Espresso

PAW projector augmented wave

DFPT density functional perturbation theory

GSF generated stacking fault

SF stacking fault

USF unstable stacking fault

MT Martins-Troullier

FBZ first Brillouin zone

LEFM linear elastic fracture mechanics

HCP hexagonal close packed

BCC body-centered cubic

FCC face-centered cubic

FDM finite displacement method

TP tetragonal path

OP orthorhombic path

ESI elastic shear instability

MEP minimum energy path

NEB nudged elastic band

DT deformation twinning

MAEAM modified analytical embedded-atom method

PBC periodic boundary conditions

AT anti-twinning

GB grain boundary

TB twin boundary

PK Peach-Koehler

TEM transmission electron microscopy

FS Finnis–Sinclair

BFGS Broyden-Fletcher-Goldfarb-Shanno

CG conjugate gradient

GGA generalized gradient approximation

PDE partial differential equation

LREP long-range empirical potential

SSH solid solution hardening

SSS solid solution softening

CRSS critical resolved shear stress

APB antiphase boundary

CNA common neighborhood analysis

ABF annular bright field

FE Friedel-Escaig

RE rare earth

GP Guinier-Preston

SSSS supersaturated solid solutions

SHT solution heat treated

MC Monte Carlo

EA evolutionary algorithm

STGB symmetric tilt grain boundaries

GB grain boundary

LAMMPS Large-scale Atomic/Molecular Massively Parallel Simulator

ES evolution strategy

EBSD electron backscatter diffraction

DOF degrees of freedom

HP Hall-Petch

DD dislocation dynamics

GBD grain boundary dislocation

STEM scanning transmission electron microscopy

ABSTRACT

In crystalline metallic systems, plastic deformation originates from nucleation and evolution of crystal defects. There are two types of complexity that generate substantial obstacles for the simulations and understanding of these defects at the atomistic scale. One aspect is to precisely describe interatomic bonding characteristics originated from complex electronic structures. Another aspect is to construct the accurate and representative atomistic structures of defects for the investigations of plastic deformation. Thus, the main topic of this thesis is to develop and apply the theoretical and computational methods that can overcome these two types of barriers. For the aspect of the interatomic bonding, BCC refractory metals (W, Mo, Nb, Ta) and their alloys are typical investigation systems, which have partially filled d-band electrons that generate strong and directionally dependent interatomic bonds. Thus, ab initio calculations and continuum models were applied to investigate the occurrence of the elastic and phonon instability at extreme stress conditions, which reveals the characteristics of defects nucleation and the corresponding intrinsic ductility properties from the lattice instability perspective. A potential-fitting package based on a force-matching method was then developed to create a modified embedded atom method (MEAM) potential for these BCC metals. The MEAM potential of Nb was constructed to reflect both its intrinsic interatomic bonding characteristics under extreme stress conditions and its dislocation core attributes. This potential and other accurate MEAM potentials for BCC refractory metals and alloys can be used together to investigate the effects of interatomic bonding characteristics on the plastic deformation at the mesoscale. For the aspect of complex atomistic structures of defects, two-dimensional and three-dimensional defects such as grain boundary (GB) and precipitates are typical investigation systems, since it can

be difficult to obtain their stable and metastable structures, which have significant impacts on the plastic deformation behavior. Thus, an evolution algorithm (EA) based package was developed to explore stable and metastable GB structures in FCC, BCC, and HCP metals. The GB structures generated in this package build a solid foundation for the investigations between GBs and other defects, such as dislocation and deformation twinning, in the future. Finally, collaborating with experimentalists, the effects of the ordered superlattices of precipitates on the precipitate-dislocation interactions in Mg-Nd alloys were investigated. A precipitation hardening model with parameters from ab initio calculations was constructed to predict the strengthening effects of the anti-phase boundaries (APB). Molecular dynamics (MD) simulations were performed to reveal the mechanism of dislocation cutting and cross-slip when interacting with precipitates. Understanding these dislocation-precipitate interaction mechanisms will be helpful in designing precipitate microstructures that can enhance the strength and ductility of Mg alloys simultaneously.

CHAPTER I

Introduction

1.1 Experimental and theoretical background

Metals and alloys are omnipresent to modern human society due to their essential roles in architecture, vehicles, railway, aerospace, electronic devices, medical and nuclear industry, etc. One crucial application for metals and alloys is to serve as structural materials, and it requires metals and alloys of qualified mechanical properties, such as high strength and ductility, to meet various commercial and safety requirements. Metals and alloys are solid-state crystal materials, so their mechanical properties and deformation mechanism rely on lattice properties and behaviors of crystal defects such as dislocations, deformation twining, grain boundaries, cracks, and precipitates.

Crystal defects, as the source of crystal plasticity, have complicated evolution and interaction behaviors in different metallic systems under various thermodynamic and chemical conditions. The complexity increases for metals and alloys that have interatomic bonds with partially directional characteristics originated from d-orbital electrons and for defects with sophisticated atomistic structures. Therefore, it is a scientifically critical and challenging task to understand, upon simulations and experiments, the lattice and defects behaviors during the plastic deformation of advanced metallic systems, like refractory and light-weight metals and alloys.

Refractory metals with body-centered cubic (BCC) lattice, such as W, Mo and Nb, have nearly half-filled d-band electrons to form strong interatomic bonds with directional characteristics, so deformation defects in these metals have complicated behaviors. Refractory metals have critical engineering applications, such as fusion reactors and turbine engines, due to their high melting point, strength, and excellent high-temperature mechanical properties. However, some refractory metals (W and Mo) have limited formability due to their room-temperature brittleness [281, 208, 55, 82, 263], which is related to the deformation mechanism at crack tips. Both the crack propagation and dislocation emission can occur at the preexisting crack tip to release the strain energy by bond breaking and shear along stacking fault layers, respectively. A ductile material tends to emit dislocations at crack tips, and these dislocations blunt the crack to prevent the cleavage failure. Quantitative descriptions of these deformation defects depend on lattice properties, the geometry of crack tips, and the external loading conditions [12, 201, 228, 276, 123, 261, 9]. Recently it was found these deformation mechanisms at crack tips may depend on d-band filling [197]. Thus, to investigate the effects of electronic structures on bonding characteristics and defect behavior is one of two main topics of this thesis.

Another main topic of this thesis is to investigate the deformation defects with sophisticated atomistic structures, such as dislocations on non-close packed planes, general grain boundaries (GBs) without a high degree of symmetry, precipitates with special ordered lattices, and their interactions. These examples of defects can be frequently found in Mg and Mg alloys with hexagonal close-packed (HCP) structure. As light-weight metals, Mg and Mg alloys have increasing applications in automotive, aircraft, electronic devices, and biomedical industries [192, 153]. However, common Mg alloys have low yield strengths due to the easy basal slip and poor formability due to the development of basal textures during mechanical processing [72, 254]. Grain boundary strengthening (Hall-Petch (HP) strengthening) and precipitate strengthening, are applicable techniques to improve the mechanical performance of Mg and Mg alloys. For HP strengthening, different Mg alloys show significant discrepancies in HP parameters, and it is unclear how the HP strengthening related to dominant deformation modes, including different slips and twinning, and grain boundary structures [251]. For precipitate strengthening, Mg rare earth (RE) alloys are of interest because of their excellent age-hardening response, high creep resistance, and good castability [170, 71, 211]. β_1 precipitates are strengthening phases in the commercial WE43 and WE54 Mg-RE alloys [168]. Thus, it is necessary to understand the interaction mechanisms between dislocations and β_1 precipitates given loading conditions and the size, shape and distribution of β_1 precipitates [280, 169, 96].

To comprehend mechanical properties in advanced metallic systems, many studies rely on computational simulation methods, such as density functional theory (DFT), molecular dynamics (MD), Monte Carlo (MC), and dislocation dynamics (DD). From the electronic scale, methods such as DFT can reveal fundamental physics based on the interpretations of electronic structures and interatomic bonding characteristics. For example, DFT calculations showed that at low temperatures the poor ductility of BCC refractory metals is related to the low dislocation mobility that relies on d valence electrons [238, 154, 155, 139, 140]. At the atomistic scale, techniques such as MD can simulate lattice and defect evolution during external loading. For example, atomistic modeling plays an important role to study structures and properties of GBs [203, 30, 252, 199, 243, 241, 131, 178, 187, 114] and interactions between GBs and other defects [212, 251, 69]. Atomistic simulations showed that GBs of low static energies tend to resist slip transmission and nucleation at GBs [212]. A combined MC and MD approach revealed atomistic details of Ag-segregation-induced structural transition at asymmetric Cu GBs [187].

In general, first-principles calculations based on DFT, despite reflect physics from electronic structures, can usually handle at most thousands of atoms, which is difficult to represent complex defect structures such as grain boundaries, crack tips, and precipitates, or multiple defects. Atomistic modeling, which can handle millions of atoms, is a primary technique to simulate the evolution of crystal defects such as dislocation nucleation from crack tips, dislocation interactions with grain boundaries, or second-phase particles. Reliable atomistic modeling of crystal defects requires accurate descriptions of interatomic interactions and atomic structures of these defects. Therefore, to advance atomistic simulations on the study of the evolution of defects in plastic deformation of advanced metallic systems, the research work plan had two parts. The first phase is to develop methods to generate accurate interatomic potentials and atomic structures of complex defects. The second phase is to implement atomistic simulations to analyze crystal defects behaviors in plastic deformations of advanced metallic systems. In the two phases, we fulfilled four research projects correlated with different aspects of atomistic simulations on crystal defects.

1.2 Outline

In Chapter II, the fundamental concepts related to mechanical deformations and the computational methods are reviewed. The main computational methods used in this thesis are DFT based first-principles calculations and MD. The key concepts related to mechanical deformation and defects are lattice instability of the perfect crystal under increasing homogeneous distortion and the corresponding ideal strength. The concepts and the fundamental features of dislocations and grain boundaries are also reviewed.

In Chapter III, our first work concentrates on the investigation of interatomic bonding characteristics and intrinsic deformation mechanisms for perfect lattices of BCC refractory metals and alloys [265]. These studies can reveal the defect properties at crack tips and the ductility of real materials. We performed DFT and phonon calculations to study the ideal tensile strength and lattice instability under $\langle 100 \rangle$ tension for the perfect crystals of W based alloys. Anisotropic linear elastic fracture mechanics (LEFM) and Rice's criterion were applied to analyze the mechanical instability at the crack tip under $\langle 100 \rangle$ tension. We showed that intrinsic ductility by promoting shear deformation and dislocation activities exists in both W-Ta and W-Re crystals due to different mechanisms. The intrinsic ductility of W-Ta alloys originates from elastic shear instability (ESI), which occurs before cleavage failure. The intrinsic ductility of W-Re alloys comes from unstable transverse phonon waves, which are related to the generation of $\langle 111\rangle\{\bar{2}11\}$ dislocation in BCC crystals.

Our second work, in Chapter IV, is to promote atomistic simulations to accurately reflect the mechanical properties of BCC refractory metals by generating interatomic potential(s) that can correctly describe the bonding characteristics and defect properties consistent with those from DFT calculations [266]. We applied evolutionary algorithm (EA) to build a modified embedded-atom method (MEAM) spline-interpolation potential able to reproduce the intrinsic ductility of perfect Nb lattice during ideal tensile deformation. This MEAM potential also enables atomistic simulations of Nb to exhibit similar-to-DFT characteristics of deformation behavior, such as ideal shear strengths, generalized stacking fault energies, twin boundary energies, phonon spectrum, etc. This potential outputs the structures, energetic stability and glide mechanism of $\frac{1}{2}\langle 111\rangle$ screw dislocations, such as dislocation core structures, core energies, migration barriers, and dislocation core trajectories, consistent with DFT calculations. We also demonstrated that large-scale MD simulations based on this MEAM Nb potential and another MEAM potential of Mo [179] can produce different types of dislocation activities near crack tips, which are consistent with their macroscopic mechanical behavior.

Our third work, in Chapter V, focuses on the construction of proper atomistic structures of complex crystal defects, such as grain boundary (GB), because the accurate GB structures lay the solid foundation for the further studies of the mechanical properties due to the interactions between GBs and deformation defects. General GBs without a high degree of symmetry can have complex atomistic structures. In addition, GBs can exhibit phase-like behaviors at the atomistic level under different chemical and thermodynamic conditions such as temperature, pressure, and chemical potential. We developed a new mutation operator that can induce abrupt internal structure changes to boost the search efficiency of exploring GB structures at grand canonical ensembles with EA [267]. We implemented the new mutation methods along with selection and crossover techniques to form an EA package to explore defect structures with atomistic simulations. Our EA based defect structure package provides a qualified grand canonical search of atomistic structures at GBs in different metallic systems, including face-centered cubic (FCC), BCC, and HCP crystals. Further MD simulations reveal the influence of GB structures on the nucleation mechanisms of dislocations and deformation twinning in pure HCP Mg.

In Chapter VI, the last work focuses on the interactions between dislocations and β_1 precipitates during the plastic deformation of Mg-Nd alloys [105, 106]. The β_1 precipitates have a special ordered lattice structure, which increases the complexity of their effects on dislocation motions. We began with a theoretical estimation of critical resolved shear stress (CRSS) of dislocations cutting through a single β_1 precipitate with inputs from DFT calculations. The CRSS explained the TEM observation of dislocation pile-ups. Then we performed MD simulations to confirm and understand the dislocation cross-slip when interacting with β_1 precipitates. Our atomistic simulations revealed details of structure evolution at dislocation cross-slip.

In Chapter VII, the conclusions of each work mentioned above are summarized. The possible future study directions are also proposed to advance atomistic modeling of defects in plastic deformation of metallic crystalline materials.

CHAPTER II

Fundamental Concepts and Modeling Methodologies

2.1 Materials modeling techniques

One purpose for materials modeling is to simulate the evolution of atoms of a material system in a fixed period of time. We may describe the adiabatic potential energy surface as $E(\mathbf{R}_1, \ldots \mathbf{R}_N)$, a function of N atom positions $\mathbf{R}_1, \ldots \mathbf{R}_N$, and our task is to evaluate $E(\mathbf{R}_1, \ldots \mathbf{R}_N)$ given atom positions and update atom positions from $E(\mathbf{R}_1, \ldots \mathbf{R}_N)$ of the system. The density functional theory (DFT) provides an effective approach to solve $E(\mathbf{R}_1, \ldots \mathbf{R}_N)$ in quantum mechanics, and the molecular dynamics (MD) is a technique to simulate the evolution of system in classical mechanics.

2.1.1 Density functional theory (DFT)

Quantum mechanics describes an atom by both its nucleus and electrons. Since each proton or neutron in a nucleus is 1800 heavier than an individual electron in mass, the Born-Oppenheimer approximation breaks the challenge of solving states of an atom into separate problems of finding the states of nuclei and electrons [26]. The estimation of $E(\mathbf{R}_1, \ldots \mathbf{R}_N)$ requires solving the many-electron time-independent Schrödinger equation [56, 78]

$$\left[-\frac{\hbar}{2m} \sum_{i=1}^{M} \nabla_i^2 + \sum_{i=1}^{M} V(\mathbf{r}_i) + \sum_{i=1}^{N} \sum_{j<i} U(\mathbf{r}_i, \mathbf{r}_j) \right] \Psi = E\Psi \tag{2.1}$$

where Ψ is the electronic wave function, which is dependent on the spatial coordinates of each of the M electrons of electron mass m, and E is the ground-state energy of the M electrons. The first Hamiltonian term describes kinetic energy of electron, the second is the interaction energy between the atomic nuclei and each electron, and the last is interaction energy between different electrons. However, the electron position $\mathbf{r}_i$ is not observable, stead, the physically interesting variable is the density of electrons at a particular position in space $n(\mathbf{r})$ defined as

$$n(\mathbf{r}) = 2\sum_{i} \Psi_i^*(\mathbf{r})\Psi_i(\mathbf{r}) \tag{2.2}$$

where $\Psi_i^*(\mathbf{r})\Psi_i(\mathbf{r})$ equals the probability of an electron in an individual wave function $\Psi_i(\mathbf{r})$ at position $\mathbf{r}$, and the total probability is the summation for all individual electron wave functions occupied by electrons.

The DFT is the methodology to approximately solve the Schrödinger equation of many-body system based on decoupling of many-body wave-functions by theorem related to electron density [102, 125, 180, 152]. The Hohenberg-Kohn theorem says that the ground-state energy is unique to the electron density, and only true electron density that is the full solution of the Schrödinger equation. Accordingly, the process of solving Schrödinger equation can become an optimization problem of finding the true electron density $n(\mathbf{r})$ at the ground-state [102]. Kohn and Sham convert the task of solving the Schrödinger equation 2.1 to solving the Kohn-Sham equation [125, 180]

$$\left[-\frac{\hbar^2}{2m}\nabla^2 + V(\mathbf{r}) + e^2\int \frac{n(\mathbf{r}')}{|\mathbf{r}-\mathbf{r}'|}d^3r' + V_{xc}(\mathbf{r})\right]\Psi_i(\mathbf{r}) = \varepsilon_i\Psi_i(\mathbf{r}) \tag{2.3}$$

Compared with the complete Schrödinger equation 2.1, the electron-electron interaction is dependent on the third and fourth term in the Equation 2.3. The third term is Hartree potential that describes the Coulomb interaction between the single electron and the total electron density from all electrons in the system. The last term $V_{xc}(\mathbf{r})$ is an exchange-correlation functional term that covers the electron-electron interactions beyond the Hartree potential [125, 180]. The Kohn-Sham equation, as a single-electron wave function, only has three variables for $\Psi(\mathbf{r})$; therefore, by decoupling interactions between electrons, the ground-state energy becomes solvable.

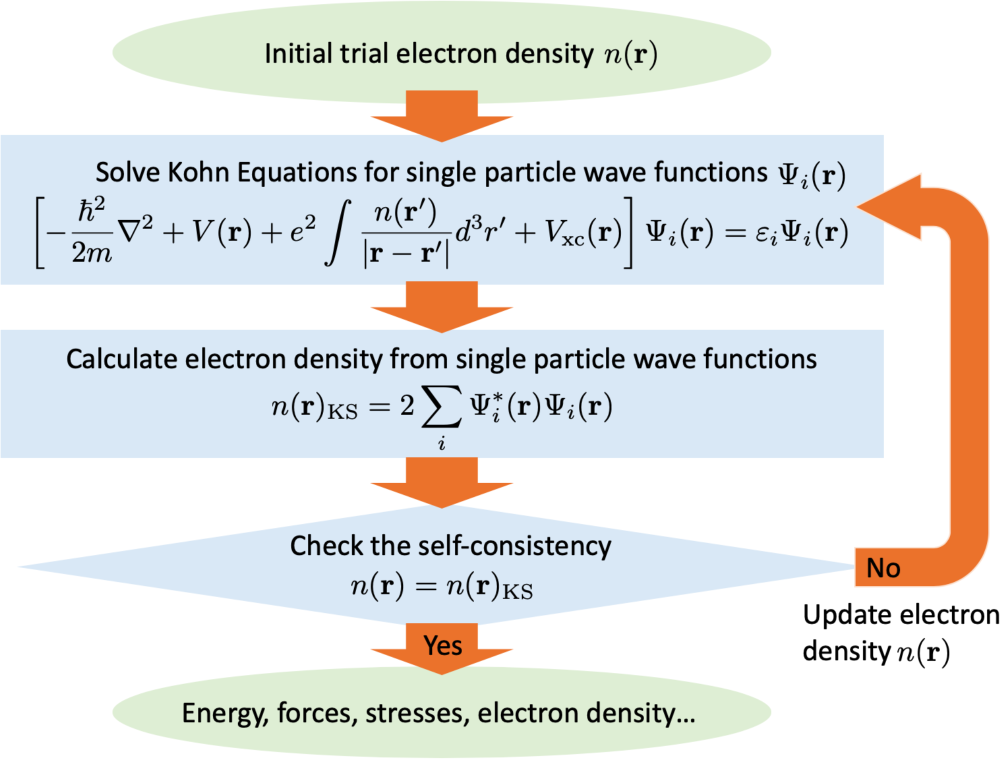

Figure 2.1: Schematic representation of the self-consistent cycle for solving of DFT based Kohn–Sham equations.

In the DFT based Kohn-Sham equation, the Hartree potential is dependent on the electron density, and the electron density comes from the single electron wave function that is the solution of the Kohn-Sham equation. This self-consistent loop indicates an iterative way of solving the Kohn-Sham equation, as shown in Figure 2.1. With the development of computational powers, numerical methods can solve the DFT based Kohn-Sham equation for a system of up to a thousand atoms. The DFT based Kohn-Sham equation becomes a useful and reliable technique to solve many-body electron problems in chemistry, physics, and materials science [132, 152].

2.1.2 Molecular dynamics (MD)

Unlike quantum mechanics (QM) that aims to solve many-body interactions upon electron wave function, classical mechanics (CM) abstracts away the variance of electronic band structure and depicts an atom to be an independent object of fixed mass. In classical mechanics, Molecular dynamics (MD) is a widely-used computer simulation technique that reproduces the interactions and movements of atoms in a confined materials system within a fixed period [66].

MD solves Newton's equations of motion for a system of interacting physical particles to predict the evolution and thermodynamics of the system. Forces on each atom depend on the derivative of the adiabatic potential energy surface $E(\mathbf{R}_1, \ldots \mathbf{R}_N)$ for distribution of atoms. Different from quantum mechanics that solves $E(\mathbf{R}_1, \ldots \mathbf{R}_N)$ upon Schrödinger equation or its variations, MD obtains $E(\mathbf{R}_1, \ldots \mathbf{R}_N)$ with interatomic potentials, which are materials-dependent mathematical or numerical functions to estimate potential energies with information of atom positions [8]. Upon forces calculated from atom positions and empirical potentials, MD integrate Newton's equation of motion on atoms, and the most common integration method is the Verlet algorithm [245]. If we use $\mathbf{F}_i(t)$ to indicate forces on the i-th atom at time t, and $\mathbf{V}_i(t)$ for velocity of the i-th atom. The Tayler expansion of position $\mathbf{R}_i(t)$ of atom at time t with forward Δt and backward Δt is

$$\mathbf{R}_i(t+\Delta t) = \mathbf{R}_i(t) + \mathbf{V}_i(t)\Delta t + \frac{\mathbf{F}_i(t)}{2m}\Delta t^2 + \frac{\Delta t^3}{3!}\frac{\delta^3 \mathbf{R}_i(t)}{\delta t^3} + O(\delta t^4) \tag{2.4}$$

$$\mathbf{R}_i(t-\Delta t) = \mathbf{R}_i(t) - \mathbf{V}_i(t)\Delta t + \frac{\mathbf{F}_i(t)}{2m}\Delta t^2 - \frac{\Delta t^3}{3!}\frac{\delta^3 \mathbf{R}_i(t)}{\delta t^3} + O(\delta t^4) \tag{2.5}$$

Combining Equation 2.4 and Equation 2.5, atom position in next time step is dependent on its trajectory and the forces on the atom

$$\mathbf{R}_i(t+\Delta t) \approx 2\mathbf{R}_i(t) - \mathbf{R}_i(t-\Delta t) + \frac{\mathbf{F}_i(t)}{2m}\Delta t^2 \tag{2.6}$$

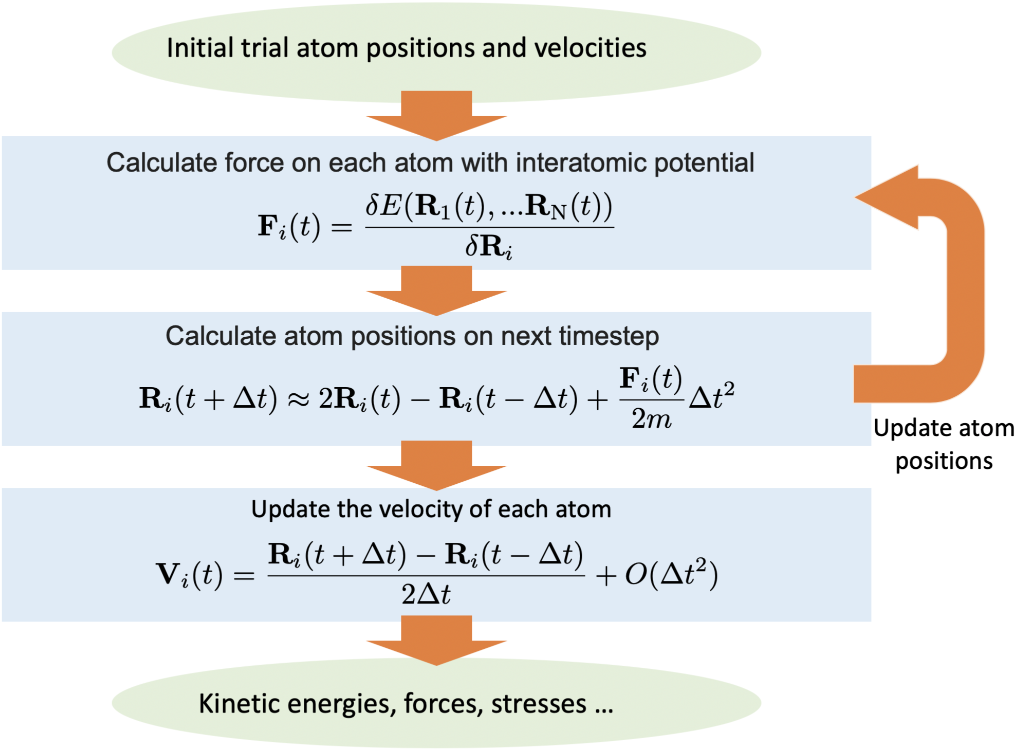

Figure 2.2: Schematic representation of the iteration cycle MD based on the Verlet algorithm

And to make the force implicit, Equation 2.4 and Equation 2.5 also show the $\mathbf{V}_\mathrm{i}(\mathrm{t})$

$$\mathbf{V}_\mathrm{i}(\mathrm{t}) = \frac{\mathbf{R}_\mathrm{i}(\mathrm{t}+\Delta\mathrm{t}) - \mathbf{R}_\mathrm{i}(\mathrm{t}-\Delta\mathrm{t})}{2\Delta\mathrm{t}} + \mathrm{O}(\Delta\mathrm{t}^2) \tag{2.7}$$

Figure 2.2 shows the workflow of MD with the Verlet algorithm. In the Verlet algorithm, the velocity $\mathbf{V}_\mathrm{i}(\mathrm{t})$ is a single time step behind the position of atom, as in Equation 2.7. Therefore, most MD programs apply the Velocity Verlet algorithm [230] to explicit include velocities during updates of positions to avoid time step lags for velocity.

In atomistic simulations, a confined system of atoms requires statistical thermodynamics descriptions, and in statistical thermodynamics, statistical ensembles rely on macroscopically observable variables such as volume (V), pressure (P), temperature (T), etc. Gibbs defined three important thermodynamic ensembles [74]:

- A microcanonical ensemble (NVE ensemble) is a statistical ensemble representing an isolated system of no particles and energy exchange with its environment. The system keeps micro-states quantities constant, such as the number of particles in the system (N), the volume of the system (V), and the total energy of the system (E).

- A canonical ensemble (NVT ensemble) is a statistical ensemble that describes a closed system in thermal equilibrium with a constant-temperature heat bath. The number of particles (N) in the system, the volume of the system (V), and the temperature of the system (T) are constant in the canonical ensemble.
- A grand canonical ensemble (μVT ensemble) is a statistical ensemble that describes an open system in thermal and chemical equilibrium with a reservoir. μVT refer to the constant values of the chemical potential of particles in the system (μ), the volume of the system (V), and the temperature of the system (T).

2.2 Concepts in materials mechanics

2.2.1 Lattice instability

Metals and alloys are crystalline materials that have the lattice structure corresponding to the global minimum of the potential energy landscape $\mathrm{E}(\mathbf{R}_1, \ldots \mathbf{R}_\mathrm{N})$ at thermal equilibrium. Each atoms oscillates on its equilibrium lattice site, and phonon is the lattice wave to describe vibrational motion of atoms in collective mode. And phonon vibration modes are obtained by solving eigenvalue problem

$$\mathrm{D}(\mathbf{q})\mathbf{e}_{\mathbf{q}\mathrm{l}} = \omega^2_{\mathbf{q}\mathrm{l}}\mathbf{e}_{\mathbf{q}\mathrm{l}} \tag{2.8}$$

where $\mathbf{q}$ is phonon wave vector, l is phonon band index, and $\mathbf{e}_{\mathbf{q}\mathrm{l}}$ is phonon polarization vector that indicates atomic displacements. $\omega^2_{\mathbf{q}\mathrm{l}}$ frequency of wave mode, and $\mathrm{D}(\mathbf{q})$ is the dynamical matrix that can be approximated by second-order force constants in harmonic approximation as

$$\mathrm{D}_{\mathrm{ij}}^{\alpha\beta}(\mathbf{q}) = \sum_{\mathrm{k}} \frac{1}{\sqrt{\mathrm{m_i m_j}}} \frac{\delta^2 \mathrm{E}(\mathbf{R}_1, \ldots \mathbf{R}_{\mathrm{N}})}{\delta \mathrm{U}_{\mathrm{i}}^{\alpha} \delta \mathrm{U}_{\mathrm{j}}^{\beta}} \mathrm{e}^{\mathbf{iq}[\mathbf{R}_{\mathrm{j}} - \mathbf{R}_{\mathrm{i}}]} \tag{2.9}$$

α and β indicates Cartesian indices. i and j are indices of atoms with mass $\mathrm{m_i}$ and $\mathrm{m_j}$ respectively, $\mathrm{U}_{\mathrm{i}}^{\alpha}$ and $\mathrm{U}_{\mathrm{j}}^{\beta}$ are displacements for atom-i and atom-j, and k indicates the label of unit cells. At equilibrium

$$\omega_{\mathbf{q}\mathrm{l}}^2 > 0 \tag{2.10}$$

when the lattice becomes unstable, $\omega_{\mathbf{q}\mathrm{l}}$ at certain polarization becomes negative, and the corresponding polarization $\mathbf{e}_{\mathbf{q}\mathrm{l}}$ indicates atomic displacement toward an equilibrium state.

2.2.2 Ideal strength

These inherent properties largely depend on the ideal strength behaviors, which describe the deformation and failure of perfect crystals under the extreme stress without any influences of precursor defects [210, 75]. From the stress perspective, the nucleation of specific deformation defects (dislocation and crack) requires the local stress reach the corresponding ideal tensile or shear strength [119, 79].

The first-principles calculations have been extensively used to investigate ideal tensile and shear strengths of different perfect crystals [224, 210, 197, 148, 165, 75]. For single crystals of BCC metals like W, the cleavage mostly occurs on the low index $\{100\}$ plane, especially at relatively low temperatures [108, 124, 202, 224, 161, 82, 83], so their ideal tensile strengths under tension along $\langle 100\rangle$ directions have been well studied. Perfect crystals of the group-V transition metals vanadium (V) and niobium (Nb) fail by a shear deformation under the increasing $\langle 100\rangle$ tensile strain [148, 165, 197]. The tetragonal symmetry of the strained V or Nb crystal becomes orthorhombic symmetry by a shear deformation, known as elastic shear instability (ESI), as illustrated in Figure 2.3, where vectors $\mathbf{a}_2$ and

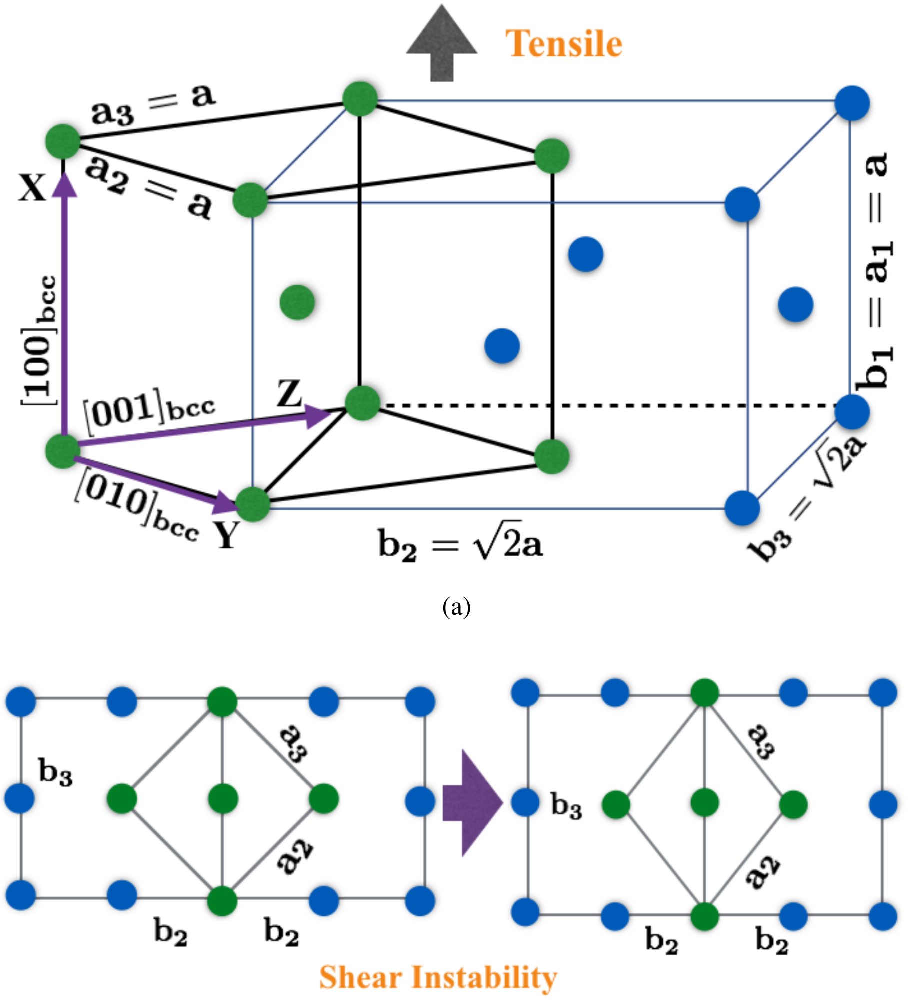

(a)

(b)

Figure 2.3: (a): Sketch of two types of supercells of BCC crystals in the ideal strength calculations. The Cartesian coordinate system is defined along $\langle 100\rangle_{\mathrm{BCC}}$. $\mathbf{a}_{1,2,3}$ indicates the base vector of a 2-atom BCC supercell applied for tetragonal tensile path, and $\mathbf{b}_{1,2,3}$ indicates base vector of a 4-atom BCC supercell applied for orthorhombic tensile path. (b) Illustration of supercell geometry changes due to ESI under $[100]_{\mathrm{BCC}}$ tensile strain. The sketch includes the BCC lattice before/after shear instability viewed from [001] direction.

$\mathbf{a}_3$ of the original cubic unit cell become non-perpendicular to each other. These materials prefer to shear plastic deformation, and they are intrinsically ductile. In opposite, the strained BCC crystals remains tetragonal symmetry even when the tensile stress reaches the ideal tensile strength for both molybdenum (Mo) and W. These materials prefer to generate cleavage fracture along $\{100\}$ plane, and they are intrinsically brittle [210, 148, 197].

2.2.3 Dislocation

Dislocation is a linear crystallographic defect that represents a local mismatch of crystal lattices in a one-dimensional pattern. In the theory of dislocation, the Burgers vector **b** denotes the direction and amount of the atomic misfit of the crystal lattice, and it is estimated by plotting Burgers circuit around the dislocation core, as shown in Figure 2.4. The dislocation line vector η indicates the tangent vector of the lattice misfit line. An edge dislocation is a dislocation that its Burgers vector is perpendicular to its dislocation line direction, and a screw dislocation is a dislocation that its Burgers vector is parallel to its dislocation line, as shown in Figure 2.4. In general, dislocations are mixed of edge and screw components when the Burgers vector forms an angle that is neither 0° or 90° [98]. Dislocations move under external loading, and the force **F**, acting on dislocation to drive it to move, satisfy the Peach-Koehler (PK) equation [98, 109]

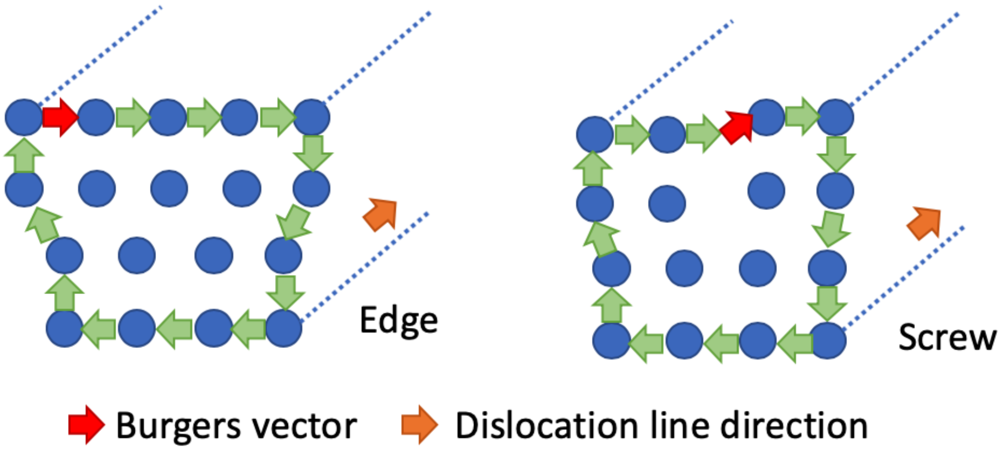

Figure 2.4: A schematic illustration of atomic arrangement for an edge (left) and screw (right) dislocation in simple cubic crystal. Green arrows form the Burgers circuit for edge and screw. The Burgers vector is perpendicular and parallel to the dislocation line direction in edge and screw, respectively.

$$\mathbf{F} = (\sigma \cdot \mathbf{b}) \times \eta \tag{2.11}$$

where the **b** is the Burgers vector and η is the dislocation line direction. Forces resolved on slip plane can drive dislocations to glide on the slip plane, and the dislocation glide (or slip) is the primary source to generate plastic deformations in metals and alloys.

To generate dislocations in atomistic simulations, we solve the dislocation displacement in anisotropic elasticity and apply it to atoms in the simulation system. The target is to solve the displacement field by the partial differential equation (PDE) [62, 226, 15, 98]

$$\mathrm{C_{ijkl}} \frac{\partial^2 \mathrm{u_k}}{\partial \mathrm{x_i} \partial \mathrm{x_j}} = 0 \tag{2.12}$$

The $\mathrm{i, j, k, l}$ equals $1, 2, 3$ in Voigt contraction scheme, $\mathrm{C_{ijkl}}$ is elastic constants, $\mathrm{u_k}$ is displacement along k-th axis, and $\mathrm{x_i}$ is spatial coordinates along i-th axis. Dislocation is a one-dimensional defect; thus conventional simulations apply infinite periodicity of dislocation along the z-axis, and in this case, the displacements, strain, and stress are invariant along the z-direction, so assuming

$$\mathrm{u_k} = \mathrm{A_k f(x_1 + p x_2)} \tag{2.13}$$

Equation 2.12 becomes

$$(\mathrm{C_{i1k1}} + \mathrm{pC_{i1k2}} + \mathrm{pC_{i2k1}} + \mathrm{p^2 C_{i2k2}})\mathrm{A_k} = 0 \tag{2.14}$$

For $\mathrm{A_k}$ not all zeros, the variable p can be solved by

$$|\mathrm{C_{i1k1}} + \mathrm{pC_{i1k2}} + \mathrm{pC_{i2k1}} + \mathrm{p^2 C_{i2k2}}| = 0 \tag{2.15}$$

And a general displacement field in Stroh's form is [226, 15]

$$\mathrm{u_k} = \sum_{\alpha} \mathrm{A_{k\alpha} f_{\alpha}(z_{\alpha})} + \sum_{\alpha} \overline{\mathrm{A}}_{\mathrm{k}\alpha} \overline{\mathrm{f_{\alpha}(z_{\alpha})}} \tag{2.16}$$

where $z_\alpha = x_1 + p_\alpha x_2$ In addition, define stress vector ϕ such that

$$\sigma_{i1} = -\frac{\partial \phi_i}{\partial x_2} \; \sigma_{i2} = -\frac{\partial \phi_i}{\partial x_1} \tag{2.17}$$

and ϕ_i satisfies

$$\phi_i = \sum_\alpha L_{i\alpha} f_\alpha(z_\alpha) + \sum_\alpha \overline{L}_{i\alpha} \overline{f_\alpha(z_\alpha)} \tag{2.18}$$

where

$$L_{i\alpha} = (C_{i2k1} + p_\alpha C_{i2k2}) A_{k\alpha} \tag{2.19}$$

To calculate $A_{k\alpha}$ and $L_{k\alpha}$, use the notation

$$(\mathbf{ab})_{jk} = \mathbf{a}_i C_{ijkl} \mathbf{b}_k \tag{2.20}$$

for tensor multiplication, and the six-dimensional eigenvalue equation becomes [15, 98]

$$-\left\{\begin{matrix} (\mathbf{nn})^{-1}(\mathbf{nm}) & (\mathbf{nn})^{-1} \\ (\mathbf{mn})(\mathbf{nn})^{-1}(\mathbf{nm}) - (\mathbf{mm}) & (\mathbf{mn})(\mathbf{nn})^{-1} \end{matrix}\right\} \left\{\begin{matrix} A_\alpha \\ L_\alpha \end{matrix}\right\} = p_\alpha \left\{\begin{matrix} A_\alpha \\ L_\alpha \end{matrix}\right\} \tag{2.21}$$

where the $\mathbf{m}$, $\mathbf{n}$ and $\mathbf{m} \times \mathbf{n}$ are three orthogonal vectors that defines the system, and the eigenvalues and eigenvectors are q_α, $A_{k\alpha}$ and $L_{k\alpha}$.

2.2.4 Grain boundary (GB)

Dislocation glide releases stress in a single crystal; however, most metals and alloys are multi crystals, as shown in Figure 2.5. The electron backscatter diffraction (EBSD) grain map shows that an extruded Mg-Al alloy consists of grains of size in μm as well as the GBs in black lines. The GB, the interface that separates adjacent crystals (grains) of the same phase, plays an essential role in the mechanical deformation in metals and alloys [229].

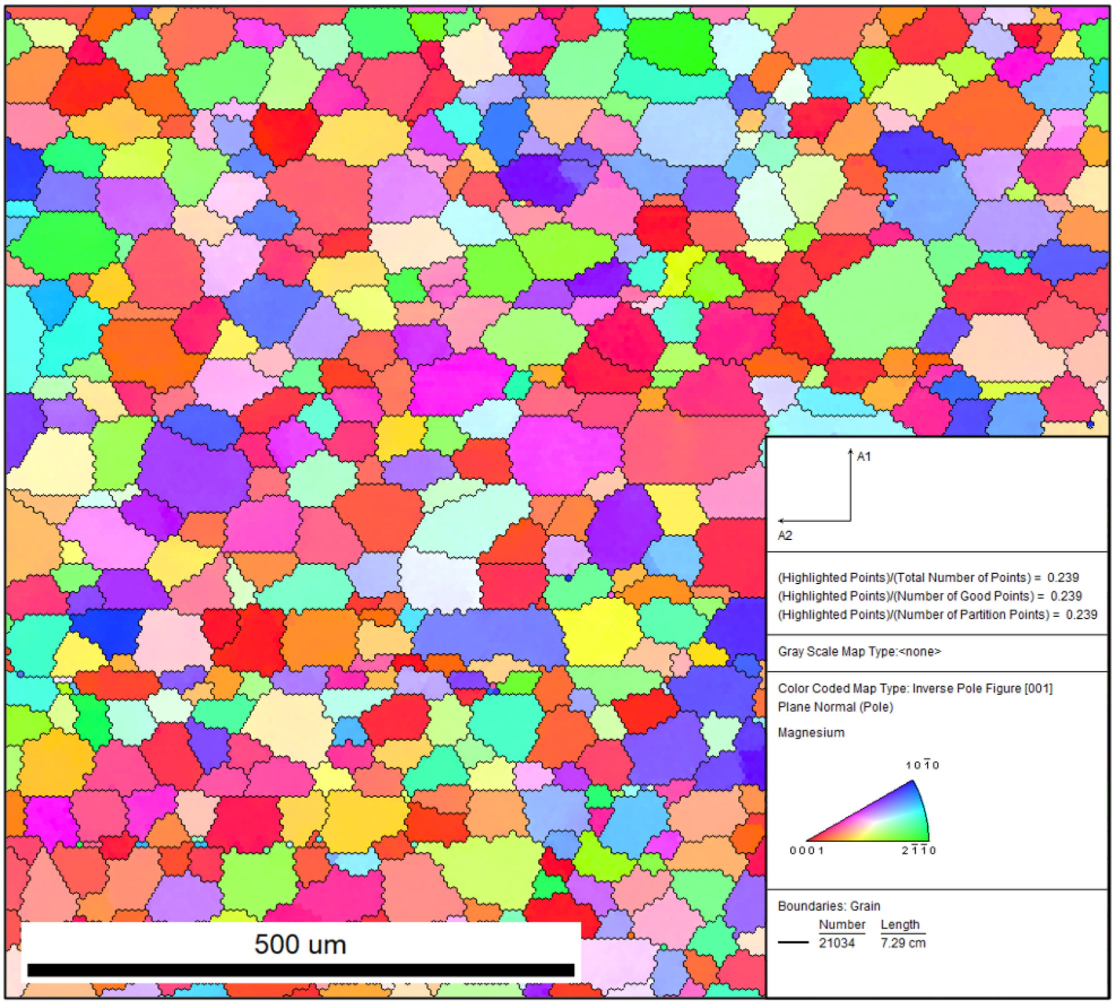

Figure 2.5: electron backscatter diffraction (EBSD) grain map for extruded Mg-Al alloy. Random colour indicates different GBs. The image is from Mohsen Andani.

We can characterize a grain boundary geometrically using five independent parameters (macroscopic degrees of freedom (DOF)) [229, 259, 136] that specifies the information to construct a bicrystal from given single crystals. Among the five variables, three indicate mutual misorientation of the adjoining two grains, as grain-A and grain-B shown in Figure 2.6. This misorientation consists of rotation or tilt by a rotation axis that is dependent on two parameters and a rotation/tilt angle of a single variable. The other two variables form the normal **n** to the grain boundary plane to describe the plane orientation between these two misoriented grains, as shown in Figure 2.6. In convention, symmetrical GBs represent

GBs when two adjoining grains form mirror symmetry, and the GB plane is the mirror plane of the same Miller indices in both adjoining grain, and other GBs are asymmetrical.

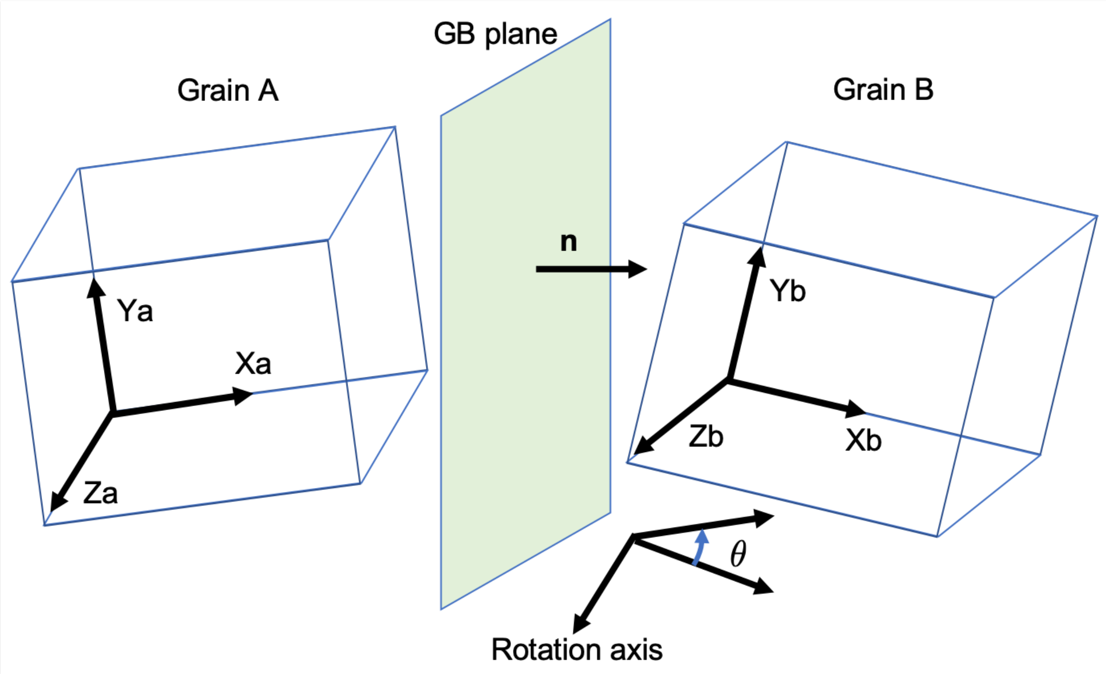

Figure 2.6: Sketch to show variables to define a grain boundary. Xa, Ya, Za and Xb, Yb, Zb are the axes of the coordinates to represent crystallographic directions in grains A and B, respectively. The rotation axis and the rotation (misorientation) angle θ represent the translation between two grains. **n** determines the orientation of the grain boundary plane.

Besides, the creation of a GB structure requires microscopic variables to characterize a rigid body translation of both grains relatively one to the other, parallel and perpendicular to the GB plane. Despite independent of macroscopic DOFs, these microscopic DOFs rely on the thermodynamics of the system. Some mutual translations only exist if they produce equilibrium atomic GB structures under certain thermodynamic conditions like temperature, pressure, and chemical composition [229, 259, 136].

CHAPTER III

Lattice Instability and Intrinsic Ductility of W and W Alloys

In solid-state crystals, the intrinsic mechanical properties of the perfect lattices are determined by interatomic bonding characteristics that originate from electronic structures. These intrinsic properties are often related to lattice instability, defect nucleation/evolution, and phase transformation. All of these phenomena are critical for accurate atomistic simulations of crystal defects and the evaluation of mechanical properties. Therefore, this chapter focuses on our study of intrinsic mechanical properties of refractory alloys with *ab initio* calculations and multiple theoretical analysis techniques [265].

3.1 Introduction

As a refractory metal, tungsten (W) has the highest melting point of all pure metals and excellent high-temperature mechanical properties, making it critical material in many engineering applications, such as fusion reactors and turbine engines. However, its formability and mechanical properties are severely limited by the room-temperature brittleness [281, 208, 55, 82, 263], which is related to the low dislocation mobility at low temperature. Theoretical studies revealed that the energetic of the dislocation motion is related to the filling of d valence electrons [238, 154, 155, 139, 140] in BCC refractory metals. The extra d valence electrons in W alloys can enhance the double-kink nucleation of screw dislocations in BCC lattice, which can increase dislocation mobility and result in solid-solution softening, and decreasing d valence electrons leads to hardening and embrittlement [154, 155].

To fully capture the essential mechanism of ductility, it is also necessary to analyze the competition between crack propagation and dislocation emission behaviors [12, 201, 228, 276, 123, 261, 9]. Both the crack propagation and dislocation emission can occur at the preexisting crack tip to release the strain energy by bond breaking and shear along stacking fault layers, respectively. A ductile material emits dislocations more efficiently at the crack tips, and these dislocations blunt the crack to prevent the cleavage failure. The competition between crack propagation and dislocation nucleation is dependent on intrinsic mechanical properties such as lattice instability under extreme stress conditions.

Our recent studies [197] show that the intrinsic ductility is tunable for Mo and W by alloying them with elements, such as Nb, of less number of valence electrons, due to the occurrence of ESI before the cleavage ideal tensile strength. The ESI originates from the Jahn-Teller distortion effect depending on the electronic banding filling level [134], where the tendency to break the symmetry of electronic band structures increases due to the downward shift of Fermi level under the tensile strain. Oppositely, the increase of valence electrons in Mo and W alloys inhibit elastic shear instability (ESI), keeping them intrinsically brittle. However, rhenium (Re), despite has one more valence electron than W, can substantially improve the ductility of W in engineering applications, and theoretical studies attribute these changes to the increase of dislocation mobility [154, 155, 184, 208].

Instead of ESI, the intrinsic ductility of W-Re alloys may originate from *phonon instability*, in which unstable phonon modes with imaginary frequencies emerge before the elastic instability, and the propagation of unstable phonon modes generate different displacements for individual atoms and destroy the integrity of the perfect crystal [55, 184, 185]. Both elastic instability and phonon instability belong to lattice instability that can be the initial step of either phase transformation or nucleation of deformation defects (crack, dislocation, or deformation twin) [38, 141, 79].

The intrinsic ductility of a material can also be evaluated by the LEFM analyses [201]. The critical stress intensity factor for cleavage fracture propagation near a crack tip is related to elastic constants and surface energies of cleavage planes in Griffith theory [77]. The critical stress intensity factor for dislocation emission near the crack tip depends on elastic constants and unstable stacking fault energies γ_{usf} of specific slip systems in Rice theory [201]. The intrinsic ductility of this material can be determined based on the ratio between these two types of stress intensity factors [201, 9]. These approaches have been examined and modified in cooperation with many atomistic simulations based on empirical interatomic potentials or first-principles calculations for different materials [276, 123, 156, 231, 120, 44, 45, 9], including BCC metals [201, 228].

In this work, we investigated ideal tensile strengths and lattice instabilities of W, W-Ta, and W-Re alloys under [100] tensile strain by DFT based first-principles calculations. W alloys are simulated by using both the standard superlattice method and the virtual crystal approximation (VCA) method [208, 184]. In addition, we applied anisotropic LEFM and Rice's criterion to analyze the mechanical instability at the crack tip under $\langle 100 \rangle$ tension.

3.2 Computational methods

3.2.1 Ideal tensile strength and phonon instability

We performed DFT ideal tensile calculations on pure W in BCC lattice, WRe and WTa in B2 structure, $\mathrm{W_{15}Re_1}$ and $\mathrm{W_{15}Ta_1}$ in $2 \times 2 \times 2$ BCC supercells, as well as $\mathrm{W_xTa_{1-x}}$ and $\mathrm{W_xRe_{1-x}}$ (x = 0.05, 0.10, 0.15, 0.20, 0.25, and 0.50) alloys based on pseudopotentials generated by VCA. We applied two types of supercell structures, as shown in 2.3 (a). The two-atom cell is the conventional BCC supercell composed by vectors $\mathbf{a}_{\mathrm{i}=1,2,3}$; the four-atom cell is the tetragonal supercell composed by vectors $\mathbf{b}_{\mathrm{i}=1,2,3}$. The $[100]_{\mathrm{BCC}}$ axis $\mathbf{a}_1$ in the BCC supercell is the same as [100] axis $\mathbf{b}_1$ in the tetragonal supercell. $\mathbf{b}_2$ and

$\mathbf{b}_3$ in the tetragonal supercell are $[011]_{\mathrm{BCC}}$ and $[0\bar{1}1]_{\mathrm{BCC}}$, respectively. An increasing tensile strain along [100] direction was applied on the two supercells. We used σ_{11} and ε_{11} = ($\mathbf{a}_1(\sigma_{11})/\mathbf{a}_1(\sigma_{11} = 0)-1.0$) to denote the true tensile stress and the engineering tensile strain along [100], respectively. In each quasi-static step, we added ε_{11} = 2.0% along [100] and relaxed the supercell along other directions until all stress tensor components $\sigma_{\mathrm{ij}} < 0.05$ GPa except σ_{11}. During supercell relaxation, the lengths of $\mathbf{a}_2 = [010]_{\mathrm{BCC}}$ and $\mathbf{a}_3 = [001]_{\mathrm{BCC}}$ of the BCC supercell vary independently, the same for the $\mathbf{b}_2 = [011]_{\mathrm{BCC}}$ and $\mathbf{b}_2 = [0\bar{1}1]_{\mathrm{BCC}}$ of the tetragonal supercell, as shown in Figure 2.3 (a). If the relaxed supercells under the fixed non-zero ε_{11} constraint maintain tetragonal symmetry, the tensile deformation follows the TP, where two types of supercells generate the same stress-strain (σ_{11}-ε_{11}) relations. Besides, the original tetragonal lattice can transform into orthorhombic lattice ($|\mathbf{b}_2| \neq |\mathbf{b}_3|$), as shown in Figure 2.3 (b)), and this tensile deformation is along the OP. TP and OP have different stress-strain relations, and the ideal tensile strength $\sigma_{11}^{\mathrm{IT}}$ is the minimum value of σ_{11} to satisfy the condition of $\mathrm{d}\sigma_{11}/\mathrm{d}\varepsilon_{11} = 0$ along both paths.

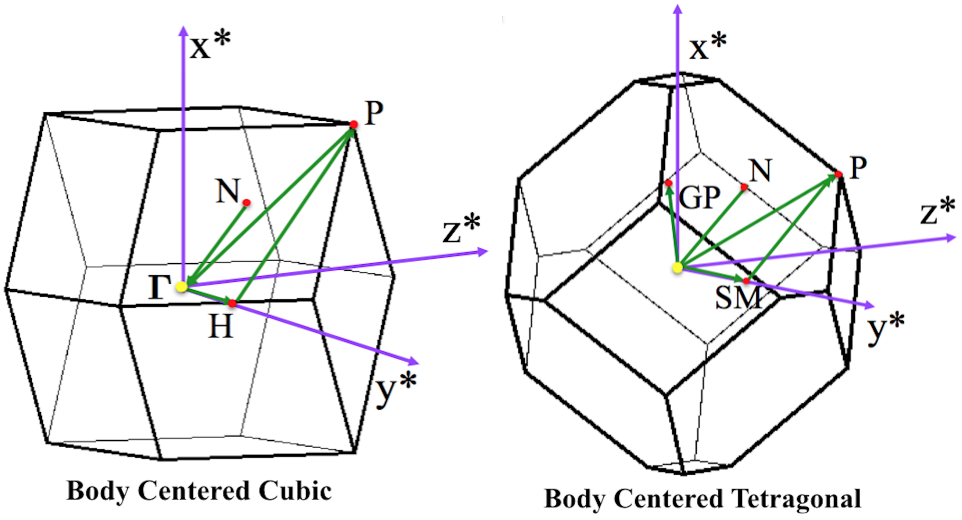

(a) (b)

Figure 3.1: (a) Paths (green lines) along high-symmetry points in the first Brillouin zone (FBZ) of BCC primitive cell for phonon calculations. (b) Changes of FBZ and the symmetric paths under $[100]_{\mathrm{BCC}}$ tension along TP. The reciprocal coordinate system (x^*-y^*-z^*) is defined based on the Cartesian coordinate system defined in Figure 2.3 (a).

We calculated phonon dispersion relations based on one-atom primitive cells for pure W and VCA W_xRe_{1-x}/W_xTa_{1-x} alloys. The lattice parameters of the primitive cells in phonon calculations were obtained by the above relaxation methods under fixed ε_{11} along TP. The wave vectors used in phonon calculations were along the paths following the selected high-symmetry points in the first Brillouin zone (FBZ) of the primitive cell. The coordinates of these high-symmetric points in reciprocal space are listed in Table 3.1 and plotted in Figure 3.1 for primitive cells without and with the tensile deformation, respectively.

Table 3.1: Coordinates of the high-symmetry k-points in FBZ of BCC and BCT (body-centered tetragonal) primitive cells shown in Figure 3.1. The reciprocal coordinate is defined as the unit length equal to $2\pi/|\mathbf{a_{i=1,2,3}}|$. Here $\mathbf{a_i}$ as labeled in Figure 2.3 can have different lengths due to the ideal tensile deformation.

BCC	BCT	Reciprocal coordinates
N	N	[0.5 0.5 0]
H	SM	[0.0 0.5 0.0]
P	P	[0.5 0.5 0.5]
	GP	[0.5 0.25 -0.25]
Γ	Γ	[0 0 0]

3.2.2 Details of DFT calculations

DFT calculations were performed by using Vienna *Ab initio* Simulation Package (VASP) [85] and Quantum Espresso (QE) [73] in non-spin-polarized conditions. In VASP calculations, the applied pseudopotentials were based on projector augmented wave (PAW) method [130] and Perdew-Burke-Ernzerhof (PBE) exchange-correlation functional [183]. We sampled the k-points using the Monkhorst-Pack method [163] by a $21 \times 21 \times 21$ grid for 2-atom BCC supercells, a $21 \times 19 \times 19$ grid for 4-atom tetragonal supercells, a $13 \times 13 \times 13$ grid for 16-atom BCC supercell, and a $13 \times 11 \times 11$ grid for 32-atom tetragonal supercell, respectively. The partial occupancies of each orbital were in the first-order Methfessel-Paxton scheme with a smearing of 0.4 eV [159]. The kinetic cutoff energy was 380 eV. We applied Phononpy [236] for phonon spectrum calculations using the finite displacement method (FDM) with force constants from VASP calculations.

In QE calculations, the VCA scheme was employed to produce pseudopotentials of the virtual $\mathrm{W_xRe_{1-x}}$ and $\mathrm{W_xTa_{1-x}}$ elements. These VCA pseudopotentials were generated by the Martins-Troullier (MT) approach [239] using the PBE exchange-correlation functional [182], and they were constructed by modifying the number of valence electrons per atom for the virtual chemical element using the program FHI98PP [70]. The k-points were sampled using the Monkhorst-Pack method by a 25 × 25 × 25 grid and a 25 × 21 × 21 grid for the BCC and tetragonal supercells. The kinetic cutoff energy was 615 eV. Phonon dispersion curves and modes of atomic movements were calculated by the density functional perturbation theory (DFPT) [20], which was implemented in QE. DFPT calculations used 6 × 6 × 6 Monkhorst-Pack grid and $1\mathrm{e}^{-13}$ eV for energy convergence.

3.2.3 Stacking fault and surface energies

A stacking fault (SF) is formed by shifting one part of a crystal relative to the rest part along a slip vector on a slip plane [246, 201, 45]. The energy increment as a function of the slip vector is the generated stacking fault (GSF) energy or γ surface. The maximum energy increment along the minimum energy path (usually the same direction as the Burgers vector for BCC metals) of the γ surface is the unstable stacking fault (USF) energy γ_{usf}, which represents the energy barrier to shift two neighboring parts of the crystal on the slip plane.

We performed DFT calculations to obtain GSF energies in the Burgers vector direction $\langle 111\rangle$ of stacking fault planes $\{\bar{2}11\}$ and $\{\bar{1}10\}$ for pure W, $\mathrm{W_xTa_{1-x}}$, and $\mathrm{W_xRe_{1-x}}$ alloys in VCA scheme. The supercell geometry was $[\bar{1}11]\times[0\bar{1}1]\times[211]$ and $[\bar{1}11]\times[1\bar{1}2]\times[110]$ along x-y-z axes with the periodicity of 1 × 1 on the x-y plane. The k-points were sampled using the Monkhorst-Pack method by a 17 × 9 × 1 grid and a 20 × 7 × 1 grid in $\langle 111\rangle\{\bar{2}11\}$ and $\langle 111\rangle\{\bar{1}10\}$ γ surface calculations, respectively, and both types of supercells contained 12 layers of atoms and a vacuum layer along the z-axis. We evenly sampled 25 points along each slip path, and fixed the movement of atoms along x and y directions on the slip plane for a given slip vector during the relaxation. The γ_{usf} was measured by the maximum GSF value along the slip path.

Cleavage is mostly on the low index $\{100\}$ planes for W [83], so we calculated $\{100\}$ surface energies of pure W, $\mathrm{W_xTa_{1-x}}$, and $\mathrm{W_xRe_{1-x}}$ alloys in VCA scheme by DFT with the same VCA pseudopotentials for the LEFM analyses based on Griffith theory [77]. The supercell was [100] × [010] × [001] along x-y-z axis with the periodicity of 1 × 1 on the y-z plane, and it contained 14 layers of atoms and a thick vacuum layer along the x-axis to create surfaces. The k-points were sampled using the Monkhorst-Pack method by a 1 × 16 × 16 grid. The energy relaxation was based on conjugate gradient (CG) method in the DFT calculations.

3.2.4 Linear elastic fracture mechanics (LEFM)

Anisotropic LEFM theory was applied to analyze the competition between crack propagation and dislocation emission on a semi-infinite crack in a homogeneous system [77, 226, 201, 228]. A systematic summary of this method can be found in recent publications [261, 9]. According to this method, the strain energy release rate G of the crack growth is

$$\mathrm{G} = \mathrm{K^T \Gamma K} \tag{3.1}$$

K is the stress intensity factor given by

$$\mathrm{K} = [\mathrm{K_I}, \mathrm{K_{II}}, \mathrm{K_{III}}]^{\mathrm{T}} \tag{3.2}$$

where $\mathrm{K_I}$, $\mathrm{K_{II}}$ and $\mathrm{K_{III}}$ denote the stress intensity factors of the basic fracture mode I, II and III, respectively. Γ is defined as

$$\Gamma = 1/2\mathrm{Re}\{\mathrm{iAB^{-1}}\} \tag{3.3}$$

where A and B originate from the eigenvectors of Stroh's formulas in solving defect problems for dislocations and cracks in a continuous medium under 2D plane strain conditions [226]. According to Griffith theory [77], the cleavage fracture happens when the strain energy release rate G equals the surface energy of the cleavage plane γ_s. The corresponding critical stress intensity factor $\mathrm{K_c}$ is given by solving the following equation

$$\mathrm{G_c} = \mathrm{K_c^T} \Gamma \mathrm{K_c} = 2\gamma_\mathrm{s} \tag{3.4}$$

Rice analyzed the critical stress intensity factor $\mathrm{K_e}$ for the dislocation nucleation and emission on the crack tip in isotropic elasticity [201]. Sun and Beltz [228] extended it to an anisotropic formula as the following

$$\mathbf{s}(\phi)\mathrm{K^{eff}} = \sqrt{\gamma_\mathrm{usf}\Gamma_\mathrm{s}(\theta, \phi)} \tag{3.5}$$

$\mathrm{K^{eff}}$ is effective stress intensity factor defined by the following equation [201]

$$\mathrm{K^{eff}} = \mathrm{F}(\theta)\mathrm{K_e} \tag{3.6}$$

where $\mathrm{F}(\theta)$ represents the angular-related matrix in the stress function of the crack tip resolved in a given slip plane. The critical stress intensity of dislocation emission is obtained by solving Equation 3.6, as reviewed by Wu and Curtin [261]. γ_usf is the unstable stacking fault energy, and ϕ is the angle between the Burgers vector and the crack front orientation projected to the slip plane; θ is the angle between the cleavage plane and the slip plane. $\mathbf{s}(\phi)$ is the slip vector based on the constrained path approximation [201] given by

$$\mathbf{s}(\phi) = (\cos\phi, 0, \sin\phi)$$

$\Gamma_s(\phi, \theta)$ is the resolved Γ based on

$$\Gamma_s(\phi, \theta) = \mathbf{s}(\Omega\Gamma\Omega^T)^{-1}\mathbf{s}^T \tag{3.7}$$

where Ω is the rotation matrix

$$\Omega = \begin{bmatrix} \cos\theta & \sin\theta & 0 \\ -\sin\theta & \cos\theta & 0 \\ 0 & 0 & 1 \end{bmatrix} \tag{3.8}$$

For pure W, W_xTa_{1-x}, and W_xRe_{1-x} alloys in VCA scheme, we applied LEFM analyses to calculate the critical stress intensity factors for the dislocation nucleation on $1/2\langle 111\rangle\{\bar{2}11\}$ / $1/2\langle 111\rangle\{\bar{1}10\}$ slip systems and the cleavage propagation along $\{100\}$ plane under Mode I loading along [100] direction. As shown in Figure 3.2 of the LEFM setup, a semi-infinite crack sits in the y-z plane, and its front is along the z direction. The K_I, K_{II}, K_{III} are defined in [100], $[01\bar{1}]$ and [011] directions of the BCC crystal, respectively. The critical stress intensity factor K_{Ic} for the cleavage propagation was calculated by Equation 3.4, and the critical stress intensity K_{Ie} for dislocation emission was calculated by Equation 3.6. The parameters for W and W_xTa_{1-x}/W_xRe_{1-x} alloys (including elastic constants, γ_s, and γ_{usf}) were obtained by the DFT calculations described in Section 3.2.2 and 3.2.3.

LEFM analyses are based on the energetic stability of possible dislocation nucleation events at the crack tip [201]. Figure 3.2 exhibits the potential dislocation slip systems that include the Burgers vector and the slip plane. However, there is no explicit limitation on the dislocation line directions in this 3-dimensional crystal. After the nucleation events, dislocation lines can propagate on the slip planes according to the strain field near the crack tip, and they can evolve to contain screw, edge, and mixed components with different values of dislocation mobility. Both these dislocation nucleation and propagation processes make significant contributions to improve the ductility of the material. To quantitatively evaluate

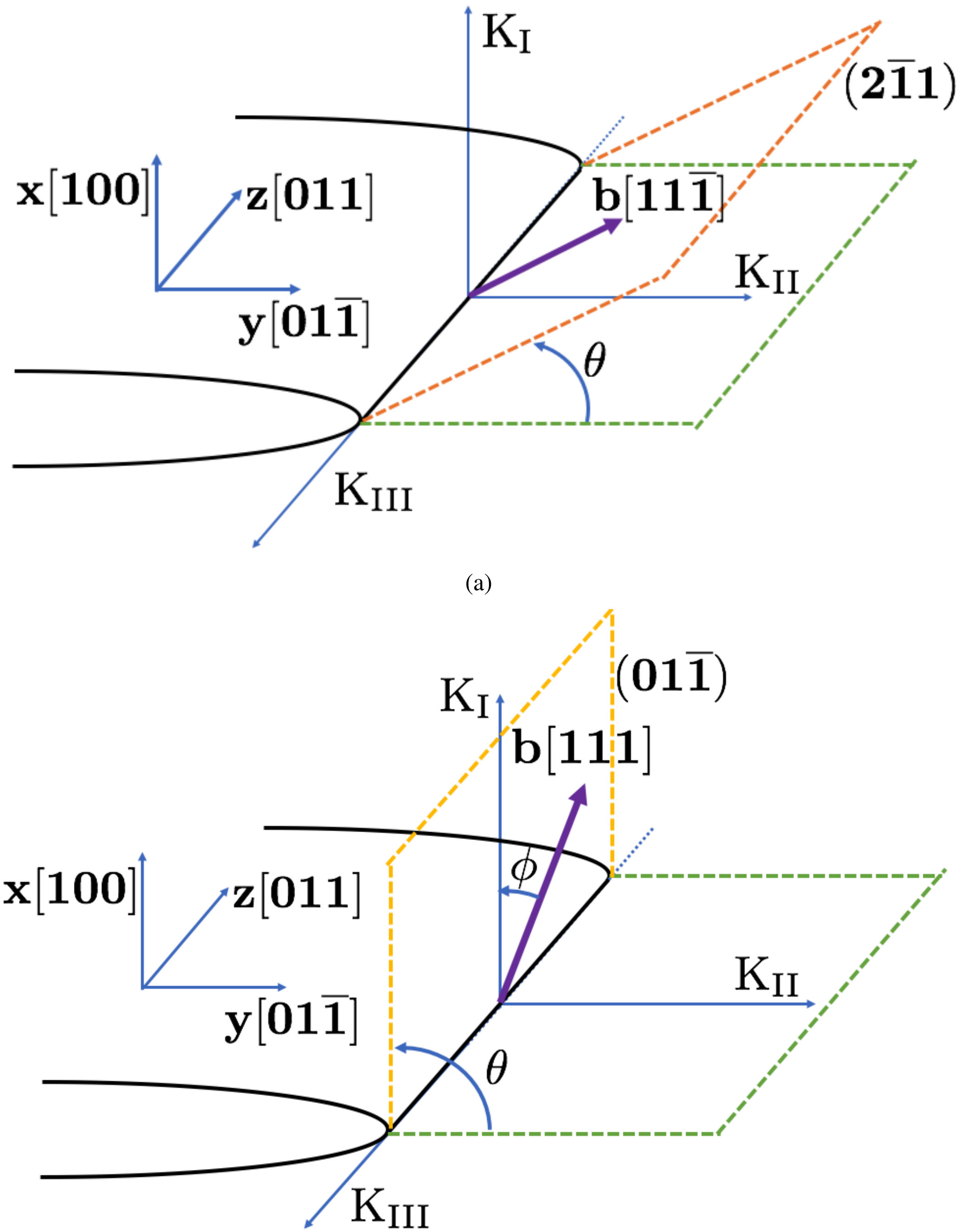

(a)

(b)

Figure 3.2: Schematic diagram of the semi-infinite crack orientation and the dislocation slip system at the crack front for LEFM analyses. (a) $[11\bar{1}](2\bar{1}1)$ dislocation with $(\theta, \phi) = (54.73°, 0.00°)$; (b) $[111](01\bar{1})$ dislocation with $(\theta, \phi) = (90.00°, 35.27°)$, where θ and ϕ are defined in Equation 3.5.

their overall effects is beyond the scope of this study.

3.3 Results and discussion

3.3.1 Benchmarks of ideal strength and phonon calculations

The structural and mechanical properties of pure W from this work and previous studies are summarized in Table 3.2. The lattice constant a, bulk modulus B, and shear modulus C' (defined as $1/2(C_{11}-C_{12})$) obtained in this work are consistent with their counterparts from previous studies (the relative differences are no more than 5%). The ideal tensile strength σ_{11}^{IT} and the corresponding critical strain ε_{11}^{IT} along TP are in Table 3.2. The differences in σ_{11}^{IT} between our results and those from recent studies are no more than 3%. The phonon dispersion relations of pure W without strain from our benchmark calculations are plotted in Figure 3.3. The FDM method using VASP and the DFPT method using QE show similar phonon spectrum along the sampled paths, and both are consistent with previous studies [55]. These results confirm that our calculations are representative of perfect W crystals.

Table 3.2: Lattice constant a (Å), bulk modulus B (GPa), shear modulus $C'(=1/2(C_{11}-C_{12}))$ (GPa), the ideal tensile strength σ_{11}^{IT} (GPa), and the critical tensile strain ε_{11}^{IT} (%) for pure W from our calculations and previous studies.

	a	B	C'	ε_{11}^{IT}	σ_{11}^{IT}
VASP-PAW-PBE	3.171	284	164	14	29.6
QE-PBE	3.171	307.3	168	16	30.1
DFT-LDA [210]	3.17	331	161	13	29.5
FLAPW [224]	-	-	-	12.3	28.9
CPMD-PBE [75]	3.23	294	-	11.7	26.7
QE, VASP [208]	3.187, 3.189	300, 330	160, 159	-	-
Exp [14]	3.165	316	165	-	-

For the validity of the VCA pseudopotentials in describing the mechanical properties of W-Re/W-Ta alloys, we first check the accuracy of lattice and elastic constants with VCA. The lattice constant, bulk modulus, C_{44}, and C' of the VCA $W_xTa_{1-x}/W_xRe_{1-x} (0.5 \leq x \leq 1.0)$ alloys are shown in Figure 3.4 and 3.5, where the number of valence electrons

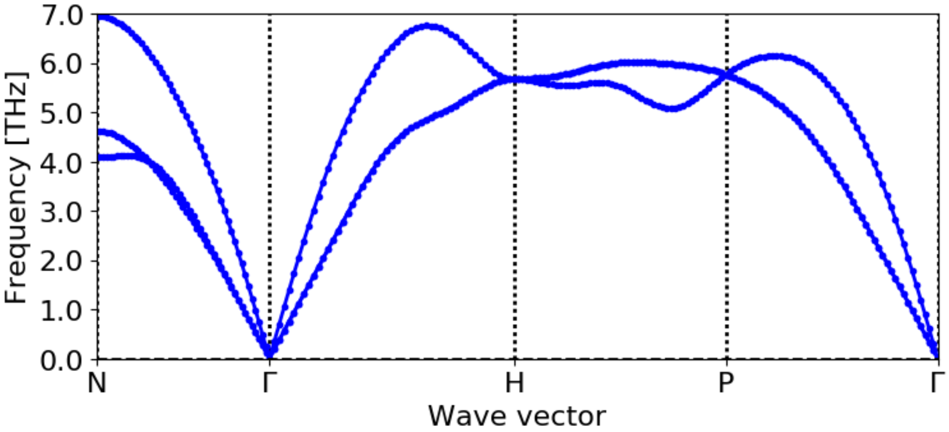

Figure 3.3: The phonon dispersion relations of pure W along high-symmetry points of FBZ of the primitive unit cell calculated by the DFPT method using QE, which are consistent with results from the FDM method using VASP (these results are not shown here).

per atom is determined by the alloy composition in the VCA. For example, $W_{0.50}Ta_{0.50}$, W, and $W_{0.50}Re_{0.50}$ have 5.5, 6.0, and 6.5 valence electrons per atom, respectively. The lattice constant decreases and the bulk modulus increases with increasing valence electrons, consistent with the prediction based on the d-band filling and experimental measurements [14]. C_{44} monotonously increases with the addition of electrons, which agrees with the experiments as well [14]. Notably, the C' of W-Re alloys monotonously decreases with increasing d electrons, which manifests that the BCC W-Re alloy becomes structurally unstable due to the increment of Re concentration [14]. In summary, all these parameters change smoothly with the solid solute concentrations, and they coincide with the recent results of W-Ta/W-Re alloys using the VCA pseudopotentials [139]. So it is a reasonable approximation to apply these VCA pseudopotentials to investigate the effects of Ta/Re solutes on the ideal strengths and lattice instability mechanisms of W alloys.

3.3.2 Ideal strength and shear instability

The ideal strength behaviors of W, W-Re, and W-Ta alloys were investigated based on different methods, including standard PAW-PBE pseudopotentials by VASP, MT-PBE pseudopotentials by QE, and VCA pseudopotentials by QE. All results are mutually consis-

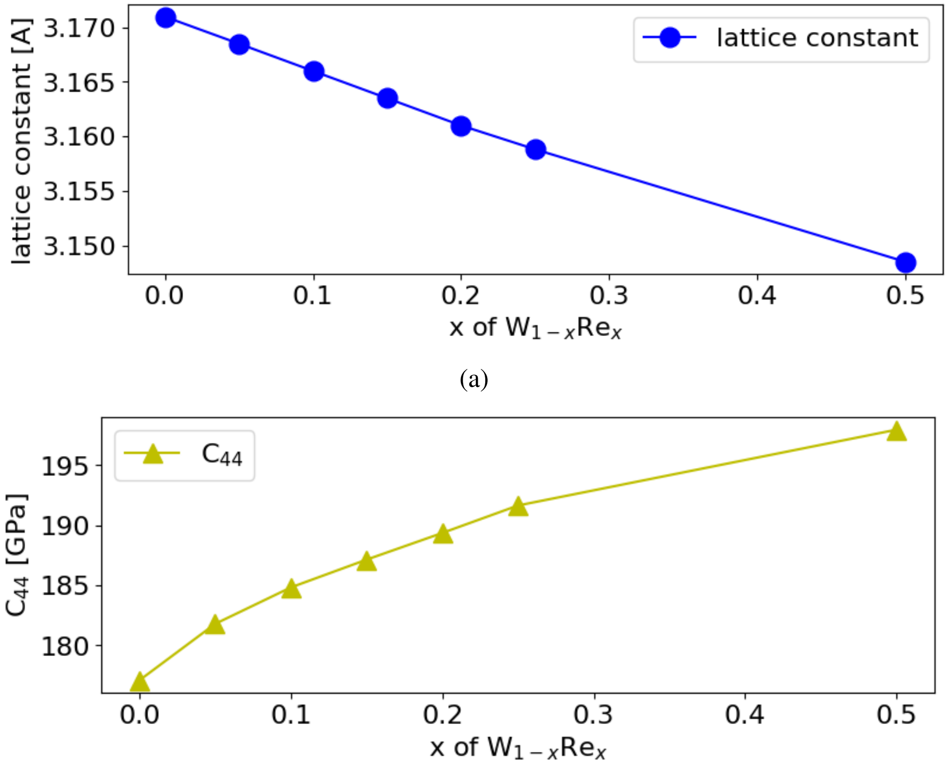

(a)

(b)

Figure 3.4: The correlation of lattice constant (a), C_{44} (b) with the concentration of Re in $W_{1-x}Re_x$, respectively, calculated in VCA scheme.

tent. Pure W exhibits intrinsically brittle behaviors because the ESI along OP only occurs after the stress reaches the ideal tensile strength along TP. Alloying W with a large amount of Ta can generate intrinsically ductile behavior because fewer valence electrons promote ESI along OP before the stress reaches the ideal tensile strength along TP. Alloying W with Re can create ideal tensile behavior with more severe brittle characteristics because more valence electrons inhibit ESI along the OP.

3.3.2.1 Ideal tensile strength of W-Ta alloys

The ideal tensile behavior of W and W-Ta calculated by standard PAW-PBE pseudopotentials using VASP is summarized in Figure 3.6. The stress-strain relations for pure W behave identically in both TP and OP when $\varepsilon_{11} < 18\%$ as shown in Figure 3.6 (a). In both TP and OP, σ_{11} reaches the ideal tensile strength $\sigma_{11}^{\mathrm{IT}}$ = 29.6 GPa when ε_{11} reaches

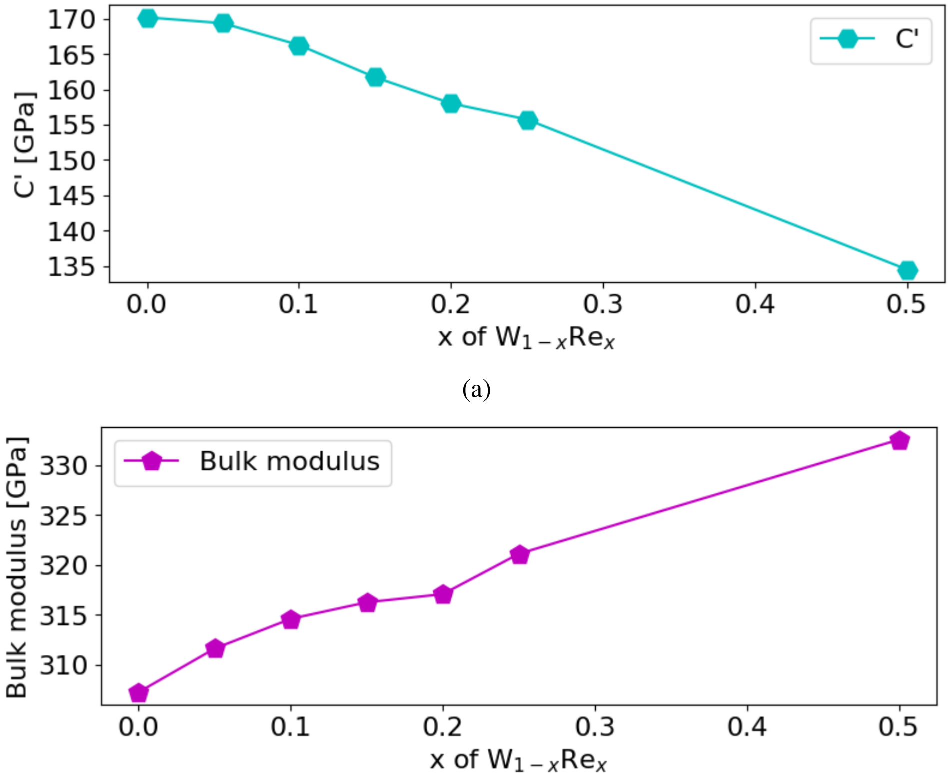

(a)

(b)

Figure 3.5: The correlation of C' (a) and bulk modulus (b) with the concentration of Re in $W_{1-x}Re_x$, respectively, calculated in VCA scheme.

the ideal tensile strain $\varepsilon_{11}^{IT} = 14\%$. When ε_{11} is larger than a critical value (nearly 18% for pure W), σ_{11} along OP drops dramatically compared with σ_{11} along TP. Above the same critical strain, the lattice constants of $\mathbf{b}_2$ along $[011]_{BCC}$ and $\mathbf{b}_3$ along $[0\bar{1}1]_{BCC}$ start to be divergent along OP as shown in Figure 3.6 (b). This transition of lattice constants is also described by ESI illustrated in Figure 2.3 (b). Thus, the critical strain for ESI, marked as ε_{11}^{ESI} in the following sections, is approximately 18%. However, such ε_{11}^{ESI} is at least 4% larger than ε_{11}^{IT} along TP. It means the perfect W crystal should still fail by cleavage fracture deformation and pure W is intrinsically brittle.

Our recent investigations of ideal tensile behavior suggest that ESI is induced by the Jahn-Teller distortion of electronic structures [197]. Jahn-Teller distortion splits the degenerate energy levels of symmetry-related and partially occupied electronic band structures

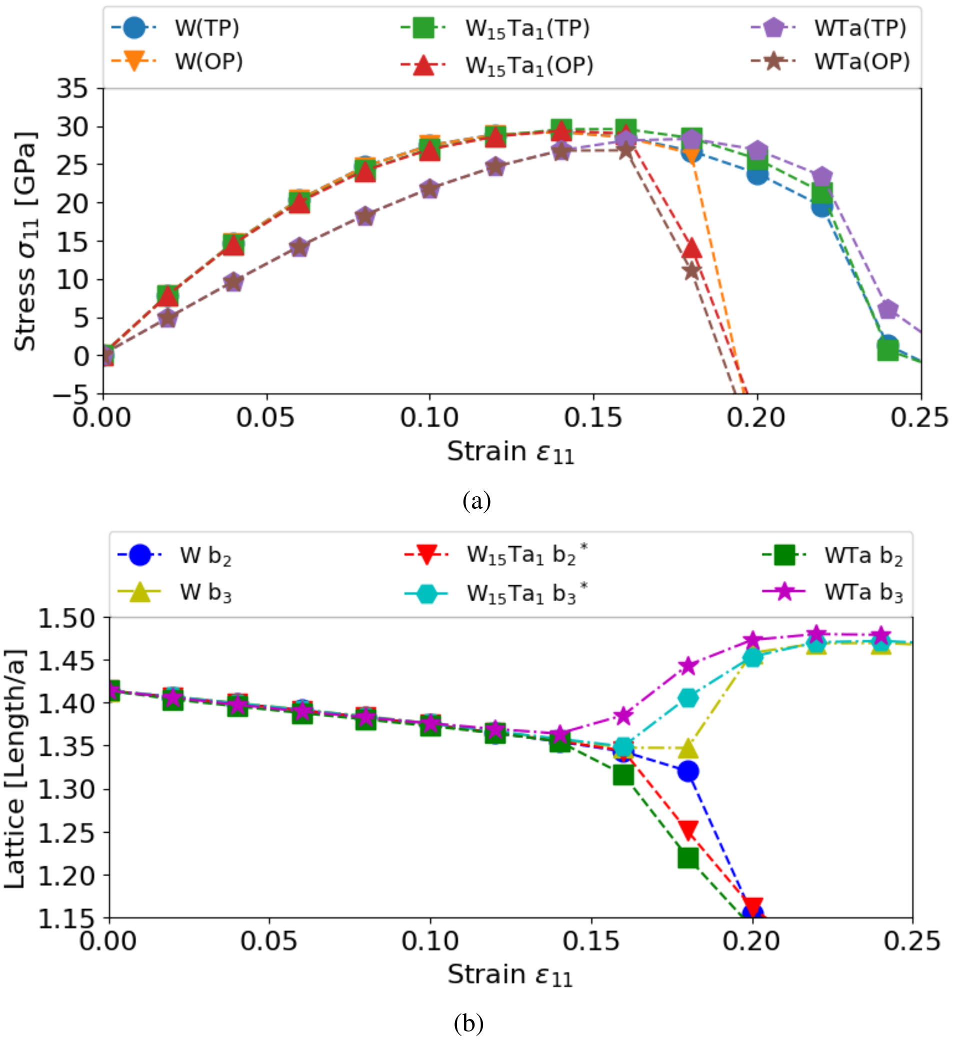

(a)

(b)

Figure 3.6: The ideal tensile strength behaviors of the perfect W and W-Ta alloy systems under [100] tensile strain. (a): The stress-strain curves along both TP and OP of W, $W_{15}Ta_1$ supercell and WTa in B2 supercell from VASP calculations; (b): The corresponding variations of the lattice constants of the tetragonal supercells under [100] tensile strain along the OP from VASP calculations, where $\mathbf{b}_2$ and $\mathbf{b}_3$ are defined in Figure 2.3.

near the Fermi level [112]. This distortion activates symmetry-breaking structural transformation and ESI along OP, so the reduction of valence electrons can shift down the Fermi level and induce ESI with smaller ε_{11} [197]. For alloy $W_{15}Ta_1$ in conventional $2 \times 2 \times 2$ BCC supercell shown in Figure 3.6 (a), σ_{11} along TP and σ_{11} along OP are different when ε_{11} is above the critical strain 16 %. In Figure 3.6 (b), lattice constants of $\mathbf{b}_2$ and $\mathbf{b}_3$ for $W_{15}Ta_1$ also become significantly divergent when ε_{11} is above 16%. So $\varepsilon_{11}^{\text{ESI}}$ is 16% for

$W_{15}Ta_1$. It confirms that a slight decrease in the number of valence electrons can induce ESI with smaller $\varepsilon_{11}^{\mathrm{ESI}}$(16% for $W_{15}Ta_1$ vs. 18% for pure W) [197]. However, because $\varepsilon_{11}^{\mathrm{ESI}}$ of $W_{15}Ta_1$ is still larger than $\varepsilon_{11}^{\mathrm{IT}} = 14\%$ corresponding to its $\sigma_{11}^{\mathrm{IT}}$ along TP shown in Figure 3.6 (a), $W_{15}Ta_1$ should still fail by cleavage mode along TP and it is intrinsically brittle, which is consistent with that W-Ta alloys are brittle when Ta concentration is small [139].

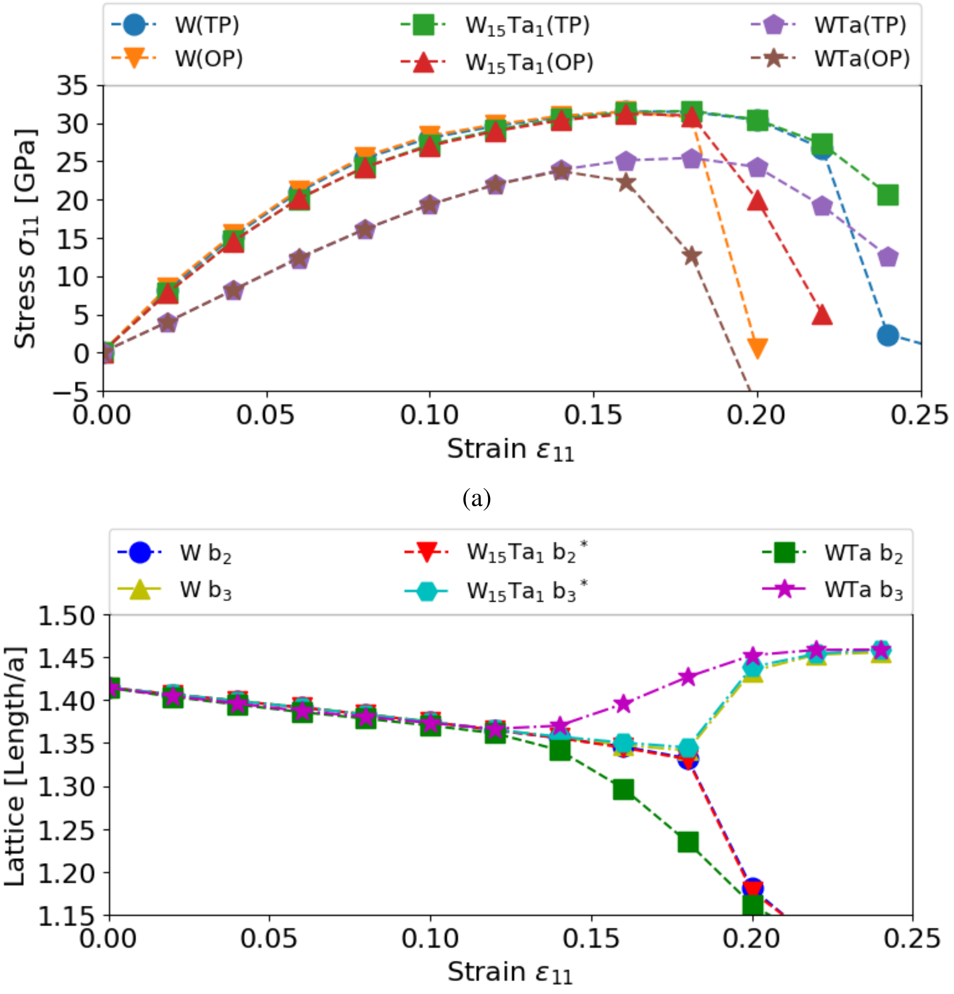

(a)

(b)

Figure 3.7: The ideal tensile strength behaviors of the perfect W and W-Ta alloy systems under [100] tensile strain. (a): The stress-strain curves along both TP and OP of W, $W_{15}Ta_1$ supercell and WTa in B2 supercell from QE calculations; (b): The corresponding variations of the lattice constants of the tetragonal supercells under [100] tensile strain along the OP from QE calculations, where $\mathbf{b}_2$ and $\mathbf{b}_3$ are defined in Figure 2.3.

The number of valence electrons further decreases for WTa in B2 structure. As shown in Figure 3.6 (a), the difference between σ_{11} along TP and σ_{11} along OP emerges when ε_{11} >14% for B2 WTa; its σ_{11} along OP reaches its $\sigma_{11}^{\mathrm{IT}}$ with the corresponding $\varepsilon_{11}^{\mathrm{IT}}$ at a certain value between 14% and 16%, since the σ_{11} has almost the same values at these two strain states. Meanwhile, $\sigma_{11}^{\mathrm{IT}}$ along TP can only be reached at $\varepsilon_{11}^{\mathrm{IT}}$ = 18%. In addition, the small divergence of lattice constants $\mathbf{b}_2$ and $\mathbf{b}_3$ for B2 WTa starts from $\varepsilon_{11} \sim$ 14% and becomes evident when ε_{11} = 16% as shown in Figure 3.6 (b), indicating $\varepsilon_{11}^{\mathrm{ESI}}$ should be approximately 14%. Thus, WTa in B2 structure should fail by ESI along OP and is intrinsically ductile. These results further confirm that the decrease of valence electrons in group VI BCC transition metal can transform its mechanical properties from intrinsically brittle to intrinsically ductile behavior under ideal tensile deformation [197].

All the above these calculations on W and W-Ta alloys are repeated by standard MT-PBE pseudopotentials using QE, and the results are plotted in Figure 3.7. For pure W, the difference between σ_{11} along TP and σ_{11} along OP emerges when $\varepsilon_{11} >$ 18%. This critical strain is larger than $\varepsilon_{11}^{\mathrm{IT}}$ = 16% for its $\sigma_{11}^{\mathrm{IT}}$ along TP, so it is still intrinsically brittle. For WTa in B2 structure, ESI occurs at ε_{11} = 14% illustrated by lattice constants $\mathbf{b}_2$ and $\mathbf{b}_3$ shown in Figure 3.7 (b). Correspondingly, σ_{11} reaches its $\sigma_{11}^{\mathrm{IT}}$ along OP at $\varepsilon_{11}^{\mathrm{IT}}$ = 14%, which is smaller than its counterpart $\varepsilon_{11}^{\mathrm{IT}}$ = 18% along TP, so it is intrinsically ductile. These results are almost the same as those from VASP calculations with different types of pseudopotentials. This consistency provides strong evidence that the intrinsic brittle-to-ductile transition is the fundamental material property insensitive to calculation methods.

3.3.2.2 Ideal tensile strength of W-Re alloys

Our recent studies suggest that the addition of valence electrons into group VI BCC transition metal inhibits its ESI along OP [197]. This prediction is confirmed by our current calculations of W-Re alloys by standard PAW-PBE pseudopotentials using VASP. Figure 3.8 (a) shows $W_{15}Re_1$ show slightly lower ideal tensile strength compared with pure W. σ_{11} along TP and σ_{11} along OP for $W_{15}Re_1$ are different when ε_{11} is above the critical strain

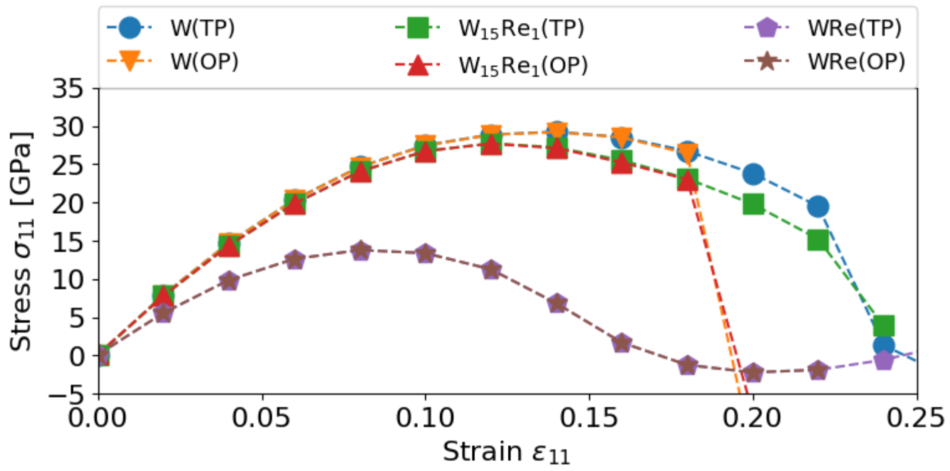

(a)

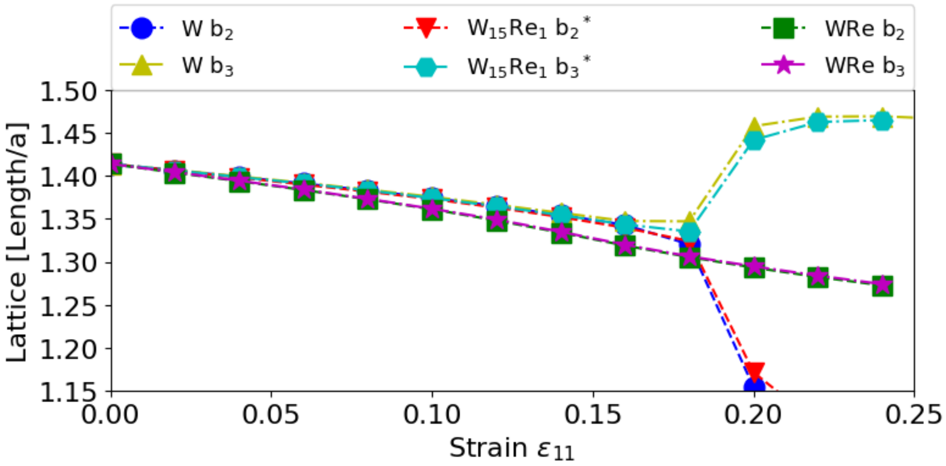

(b)

Figure 3.8: The ideal tensile strength behaviors of the perfect W and W-Re alloys under [100] tensile strain. (a) The stress-strain curves along both TP and OP of W, $W_{15}Re_1$ supercell and WRe in B2 supercell from VASP calculations; (b) The corresponding variations of the lattice constants of the tetragonal supercells under [100] tensile strain along OP from VASP calculations, where $\mathbf{b}_2$ and $\mathbf{b}_3$ are defined in Figure 2.3.

18 %, similar to the case of pure W. At the critical strain ε_{11} = 18%, the difference between $\mathbf{b}_2$ and $\mathbf{b}_3$ for $W_{15}Re_1$ is slightly smaller than its counterpart of pure W at the same strain, indicating less tendency for ESI for $W_{15}Re_1$. Such tendency is further enhanced as the Re concentration raises. For B2 WRe alloy, TP and OP show the same stress-strain responses when $\varepsilon_{11} \leq 25\%$ as shown in Figure 3.8 (a), and the $|\mathbf{b}_2|$ and $|\mathbf{b}_3|$ always have the same values as shown in Figure 3.8 (b), indicating no ESI in the whole deformation path.

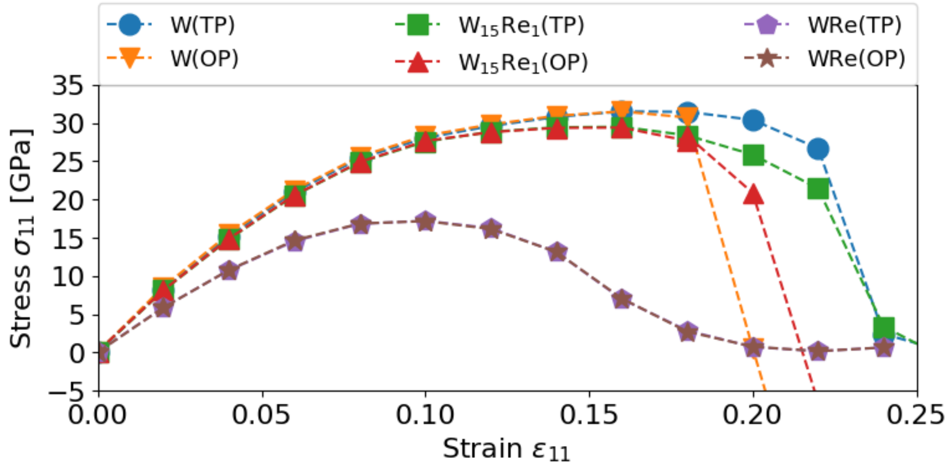

(a)

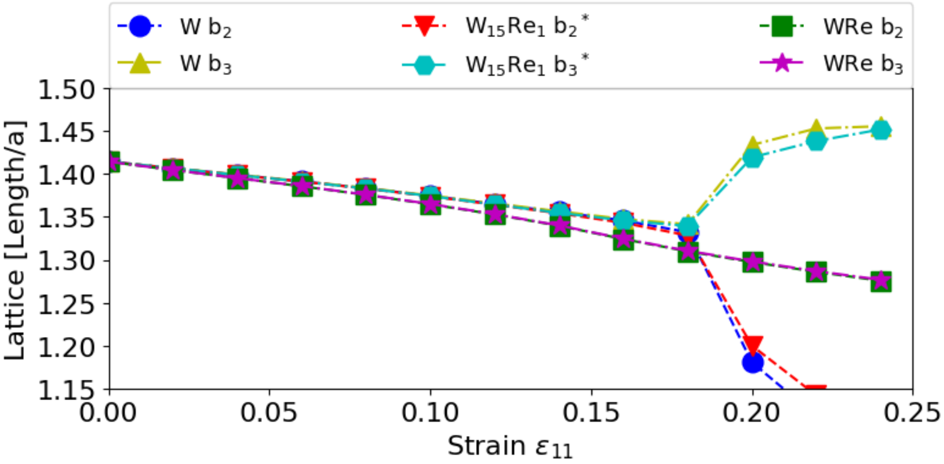

(b)

Figure 3.9: The ideal tensile strength behaviors of the perfect W and W-Re alloys under [100] tensile strain. (a) The stress-strain curves along both TP and OP of W, $W_{15}Re_1$ supercell and WRe in B2 supercell from QE calculations; (b) The corresponding variations of the lattice constants of the tetragonal supercells under [100] tensile strain along OP from QE calculations, where $\mathbf{b}_2$ and $\mathbf{b}_3$ are defined in Figure 2.3.

The calculations for W-Re alloys performed using QE provide essentially the same results as VASP calculations. When Re concentration increases, the differences of σ_{11} between OP and TP decrease and vanish eventually, as presented in Figure 3.9. The supercell for B2 WRe alloy keeps tetragonal symmetry throughout the deformation path, so it can completely inhibit ESI along OP due to the increment of the valence electrons.

The above calculations are based on the conventional supercells and standard pseu-

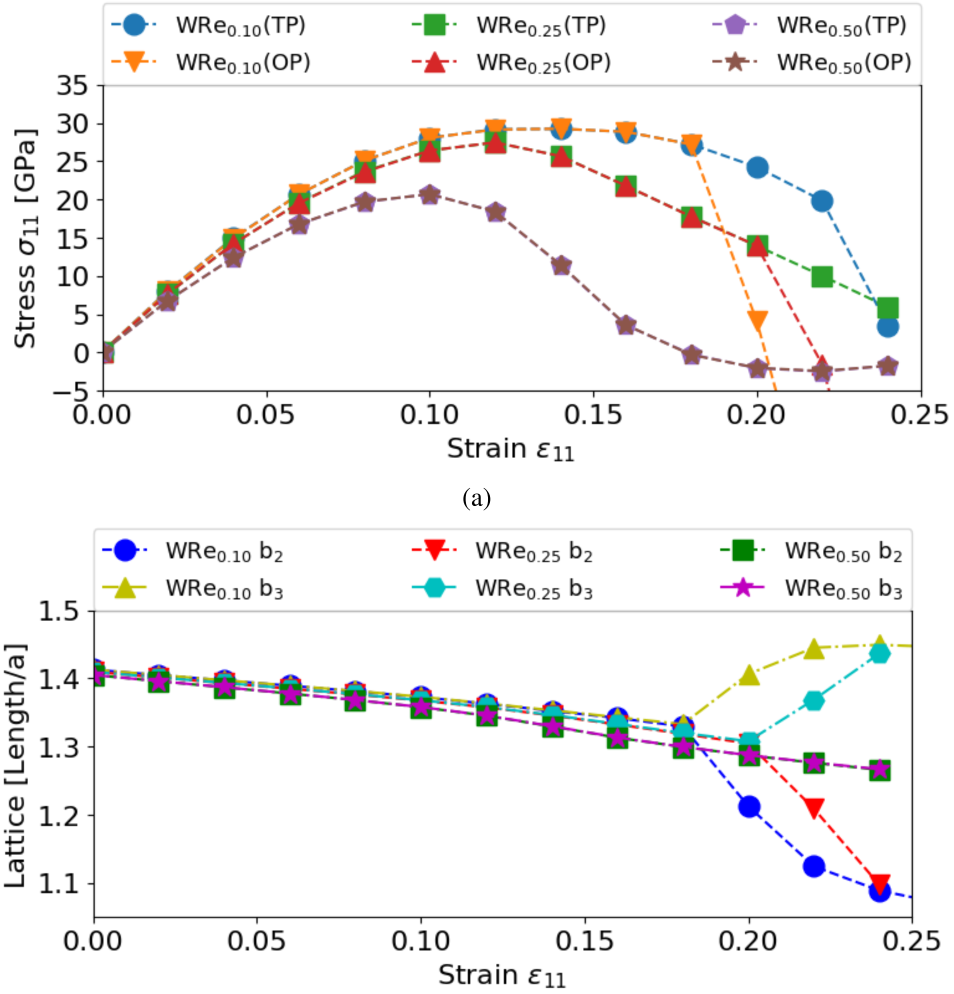

(a)

(b)

Figure 3.10: The ideal tensile behavior of $W_{1-x}Re_x$ in the VCA scheme under [100] tensile strain. (a): Stress-strain curves along both TP and OP. (b): The corresponding variations of the lattice constants of the tetragonal supercells under [100] tensile strain along OP. Here $\mathbf{b}_2$ and $\mathbf{b}_3$ are defined in Figure 2.3.

dopotentials so that the ideal tensile behavior could be affected by the artificial order in supercells. The ideal tensile behavior and lattice constant variations of $W_{1-x}Re_x$ alloys based on the VCA pseudopotentials are presented in Figure 3.10. These results contain no artificial-order effects so that they are more representative of the random binary solid solution alloys. When the concentration of Re increases from 10% ($W_{0.9}Re_{0.1}$) to 25% ($W_{0.75}Re_{0.25}$), the ideal tensile strength $\sigma_{11}^{\mathrm{IT}}$ decreases and the critical strain $\varepsilon_{11}^{\mathrm{ESI}}$, above which the stress and lattice constant divergences between the TP and OP emerge, increases from 18% to 20%. As Re concentration increases to 50 % for $W_{0.5}Re_{0.5}$, $\sigma_{11}^{\mathrm{IT}}$ further decreases, and the two deformation paths become identical throughout the deformation path, the same as B2 WRe alloy in Figure 3.9. Because VCA method ignores the variations of cation characteristics at different lattice sites, it further confirms that ESI along OP is inhibited for W-Re alloys mainly due to the d-band filling effect.

3.3.3 Ideal strength and phonon instability (PI)

According to Section 3.3.2, Re can inhibit ESI along OP and keep W-Re alloys in brittle failure mode under [100] ideal tensile deformation. This brittleness tendency is inconsistent with the experimental facts that the addition of Re can improve the ductility of W-based alloys [154, 155, 184, 208]. However, the above investigations of W alloys only consider *elastic instability*(EI), which means the identical motion occurs to each atom of the crystal in a homogenous tensile or shear distortion until σ_{11} reaches $\sigma_{11}^{\mathrm{IT}}$ along either TP or OP. Besides, crystals can become dynamically unstable due to heterogeneous motions of atoms when there are imaginary frequencies for specific phonon modes, also called *phonon instability* (PI). Polarization vectors of these unstable phonon modes usually correspond to defects nucleation or structural transformation, such as dislocation emission or deformation twinning [38, 141]. Therefore, analyses of phonon instability mechanisms for W, W-Ta, and W-Re alloys under [100] ideal tensile deformation are explained in this section.

3.3.3.1 Phonon instability in Pure W

Figure 3.11 exhibits the evolution of phonon dispersion curves for pure W under increasing tensile strain along [100]. For a particular value of ε_{11}, only the phonon branch with the lowest frequencies of the phonon dispersion relations is plotted along a specific high-symmetry path in k-space defined in Figure 3.1. By convention, imaginary frequencies are plotted as the negative values. Figure 3.11 (a) exhibits that PI with imaginary frequencies first appears near the Γ point at ε_{11} = 15% in the FDM calculations using

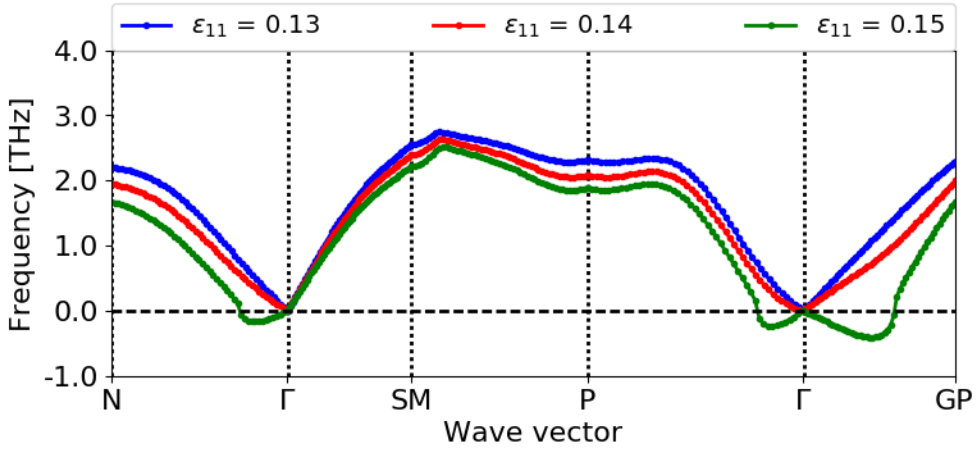

(a)

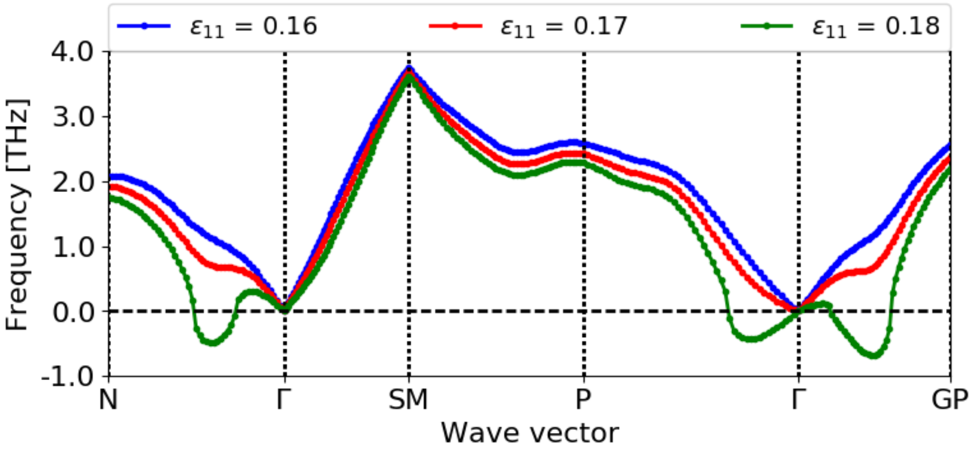

(b)

Figure 3.11: Phonon frequencies of pure W under different ε_{11} along TP during the [100] ideal tensile deformation. Only the branches with the lowest frequencies of the phonon dispersion relations are plotted. (a) Phonon dispersion curves calculated by FDM methods using VASP. (b) Phonon dispersion curves calculated by DFPT method using QE.

VASP, but the critical strain $\varepsilon_{11}^{\mathrm{IT}} \approx 14\%$ for ideal tensile strength $\sigma_{11}^{\mathrm{IT}}$ along TP for pure W as shown in Figure 3.6 (a). In the DFPT calculations of QE, PI happens near the Γ point at ε_{11} = 18%, and pure W also reaches $\sigma_{11}^{\mathrm{IT}}$ when ε_{11} = 18% along TP, as shown in Figure 3.7 (a). If the critical ε_{11} for the appearance of PI under [100] ideal tensile deformation is defined as $\varepsilon_{11}^{\mathrm{PI}}$, $\varepsilon_{11}^{\mathrm{PI}}$ equals to $\sigma_{11}^{\mathrm{IT}}$ for pure W (the small mismatch should be the consequence of different discrete step sizes for strain increments in ideal tensile and phonon calculations). The unstable phonon modes at $\varepsilon_{11}^{\mathrm{PI}}$ are located at the Γ point, corresponding to the limit of long-wavelength motions that are equivalent to the homogenous elastic deformation. Therefore, for pure W, the phonon modes only become dynamically unstable when the system reaches its elastic limit under the ideal tensile strength. The phonon analyses verify that it is the elastic instability that leads to the brittle fracture of W.

3.3.3.2 Phonon instability in W-Ta alloys

For W-Ta and W-Re alloys, since the atomic mass and valence electron number of Re/Ta differ from those of W, the artificial order in the superlattice structures (B2 WTa/WRe or $W_{15}Ta_1$/$W_{15}Re_1$ in a conventional $2 \times 2 \times 2$ BCC unit cell) may significantly underestimate $\varepsilon_{11}^{\mathrm{PI}}$, the critical strain for the phonon instability [141]. We have verified that $\varepsilon_{11}^{\mathrm{PI}}$ for B2 WTa/WRe superlattice is indeed much smaller than $\varepsilon_{11}^{\mathrm{PI}}$ for VCA $W_{0.5}Ta_{0.5}$/$W_{0.5}Re_{0.5}$. Such artificial ordering of lattice structure usually does not exist in real W alloys. Therefore, We only focus on the phonon instability of W alloys in the VCA scheme.

For VCA $W_{0.5}Ta_{0.5}$ alloy, the stress-strain behavior and the corresponding phonon dispersion curves are plotted in Figure 3.12. The stress-strain behavior for the VCA $W_{0.5}Ta_{0.5}$ calculated by QE in Figure 3.12 (a) is almost equal to the results for B2 WTa calculated by VASP in Figure 3.6 (a) and those by QE in Figure 3.7 (a). The VCA $W_{0.5}Ta_{0.5}$ is also intrinsically ductile under [100] tensile, since $\sigma_{11}^{\mathrm{IT}}$ is first obtained when ε_{11} increases to $\varepsilon_{11}^{\mathrm{IT}} \approx 14\%$ along OP before $\varepsilon_{11}^{\mathrm{IT}} \approx 18\%$ along TP. DFPT method is applied to calculate the phonon dispersion relations of the VCA $W_{0.5}Ta_{0.5}$ using the primitive unit cell under an increasing ε_{11} along TP. Figure 3.12 (b) shows the Γ-X phonon branch along $[0\ \xi\ 0]$ first becomes negative near the Γ point when $\varepsilon_{11} \approx 15\%$, close to its $\varepsilon_{11}^{\mathrm{IT}}$ along OP (the small mismatch is the consequence of different discrete step sizes for strain increments in ideal tensile and phonon calculations). Thus, similar to the pure W, VCA $W_{0.5}Ta_{0.5}$ becomes dynamically unstable due to the phonon modes corresponding to the limit of long-wavelength motions when the system reaches its elastic limit under the ideal tensile strength.

Analyses of the polarization and wave vectors of the unstable phonon mode further

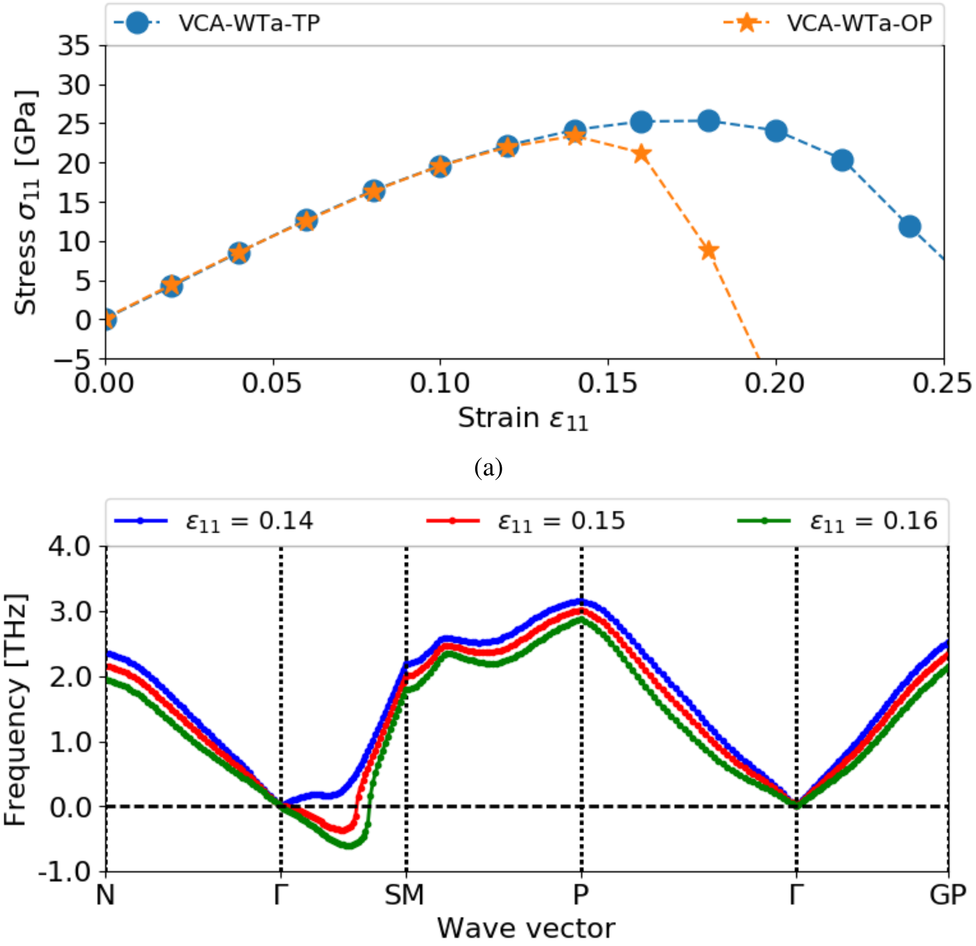

(a)

(b)

Figure 3.12: (a) The ideal tensile behavior of $W_{0.5}Ta_{0.5}$ in the VCA scheme under [100] tensile strain. (b) Phonon frequencies of VCA $W_{0.5}Ta_{0.5}$ under different ε_{11} along TP during the [100] ideal tensile deformation calculated by DFPT method using QE. Only the branches with the lowest frequencies of the phonon dispersion relations are plotted.

confirm that the phonon instability in VCA $W_{0.5}Ta_{0.5}$ is equivalent to ESI along the OP. As shown in Figure 3.13 (a), the wave vector $\mathbf{k}$ is along [010] direction, and the polarization vector $\mathbf{p}$ is along [001] direction. Since $\mathbf{k}$ is near the Γ point and perpendicular to $\mathbf{p}$, the phonon has a long-wavelength transverse wave mode, denoted by $T_{[001]}[0\ \xi\ 0]$, and it should induce elastic shear deformation. In fact, the phonon mode $T_{[001]}[0\ \xi\ 0]$ near the Γ point is regarded as the elastic shear deformation that is closely related to the elastic constant C_{44} [55, 185]. Figure 3.13 (b) illustrates that the transverse waves of the $T_{[001]}[0\ \xi\ 0]$

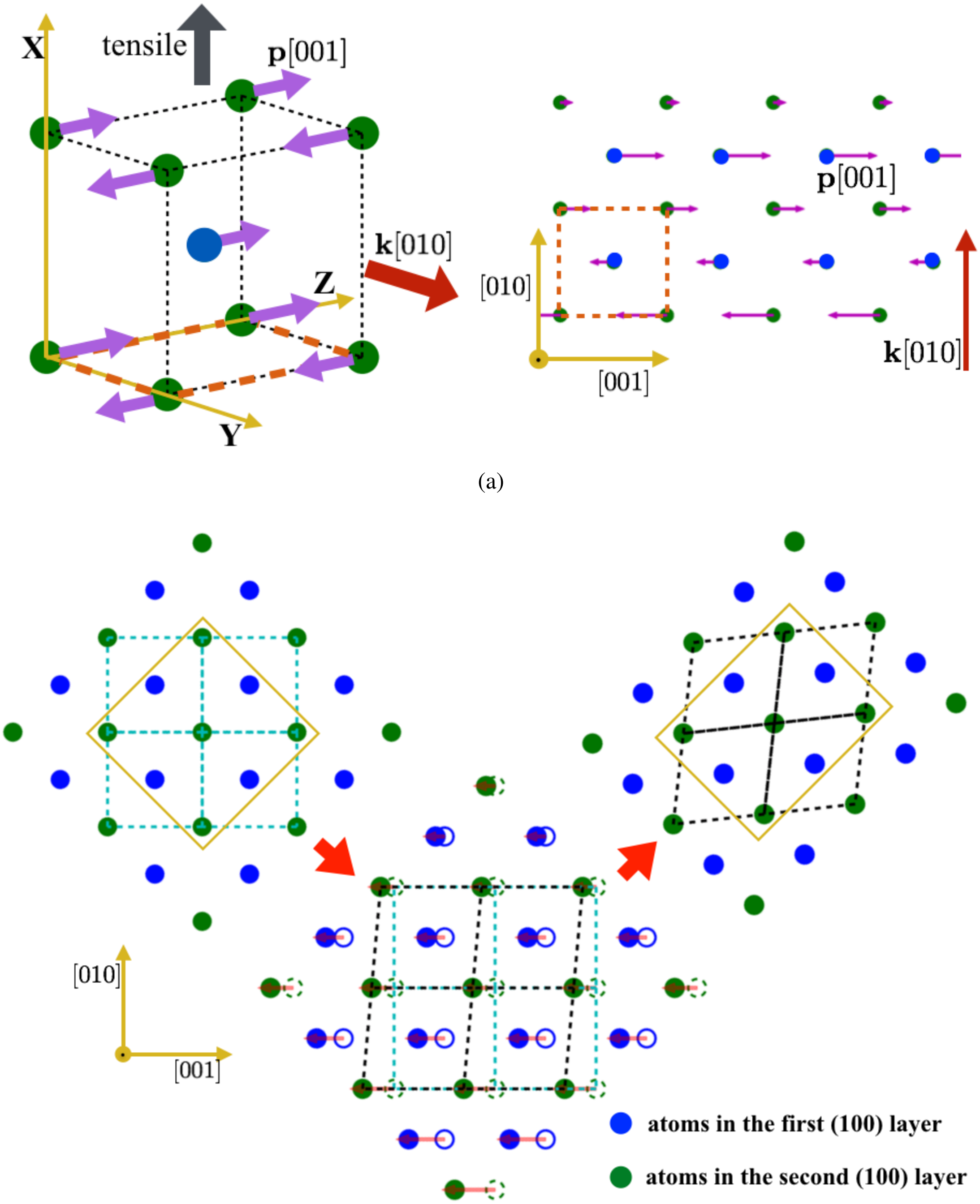

(a)

(b)

Figure 3.13: A sketch of the unstable $T_{[001]}[0\ \xi\ 0]$ phonon mode in VCA $W_{0.5}Ta_{0.5}$ alloy:(a) The polarization vector **p** and the wave vector **k** of the unstable phonon mode. (b) Projection of the crystal structure on $(100)_{BCC}$ plane to illustrate the phonon instability is equivalent to the ESI in Figure 2.3 (b).

mode shear the neighboring (010) atomic planes. As a result, one of the unit cell vectors ($[010]_{\mathrm{BCC}}$ and $[001]_{\mathrm{BCC}}$) in the 2D square lattice of (100) plane is tilted relative to the other. This deformation geometrically transforms the 2D square lattice to a rhombus structure. Thus, the whole 3D lattice changes from the tetragonal to orthorhombic symmetry in the same ESI mechanism illustrated in Figure 2.3 (b) when the unstable phonon propagates.

3.3.3.3 Phonon instability in W-Re alloys

The phonon dispersion curves for VCA $\mathrm{W_{1-x}Re_x}$ alloys under different ε_{11} during the [100] ideal tensile deformation are plotted in Figure 3.14. For VCA $\mathrm{W_{0.9}Re_{0.1}}$ alloy in Figure 3.14 (a), the imaginary frequencies appear first near the Γ point when ε_{11} increases to the critical value $\varepsilon_{11}^{\mathrm{PI}}$ = 15%, which is close to $\varepsilon_{11}^{\mathrm{IT}} \approx 14\%$ for its ideal tensile strength $\sigma_{11}^{\mathrm{IT}}$ shown in Figure 3.10 (a). So this long-wavelength phonon instability is equivalent to its elastic instability, similar to the case of pure W discussed in Section 3.3.3.1.

For VCA $\mathrm{W_{0.75}Re_{0.25}}$ alloy in Figure 3.14 (b), the critical strain $\varepsilon_{11}^{\mathrm{PI}}$ for the emergence of imaginary frequencies is 11%, smaller than $\varepsilon_{11}^{\mathrm{IT}}$ = 12% for its $\sigma_{11}^{\mathrm{IT}}$ shown in Figure 3.10 (a), so the imaginary phonon frequencies appear before the stress reaches its $\sigma_{11}^{\mathrm{IT}}$ to induce the elastic tensile failure. Figure 3.14 (b) also reveals the unstable phonon modes are along the Γ-GP branch ($\mathbf{k} = [2\xi\ \ \xi\ \ \bar{\xi}]$) at the critical strain $\varepsilon_{11}^{\mathrm{PI}}$ = 11% for VCA $\mathrm{W_{0.75}Re_{0.25}}$. Notably, when the phonon mode of the wave vector $\mathbf{k}=[0.2\ 0.1\ \overline{0.1}]$ along the Γ-GP branch first becomes negative (imaginary) at $\varepsilon_{11}^{\mathrm{PI}}$ = 11%, other phonon branches, including long-wavelength modes near the Γ point, are still positive. It means this phonon instability is not triggered by a long-wavelength phonon mode equivalent to homogenous elastic deformation. Instead, the crystal becomes dynamically unstable due to the phonon instability with a wavelength of several atomic layers. This short-wavelength phonon instability becomes further visible when the Re concentration increases. For VCA $\mathrm{W_{50}Re_{50}}$ alloy in Figure 3.14 (c), the imaginary phonon frequencies first appear at the critical strain $\varepsilon_{11}^{\mathrm{PI}}$ = 9% before the stress reaches $\sigma_{11}^{\mathrm{IT}}$ at $\varepsilon_{11}^{\mathrm{IT}}$ = 10% as shown in Figure 3.10 (a). The corresponding

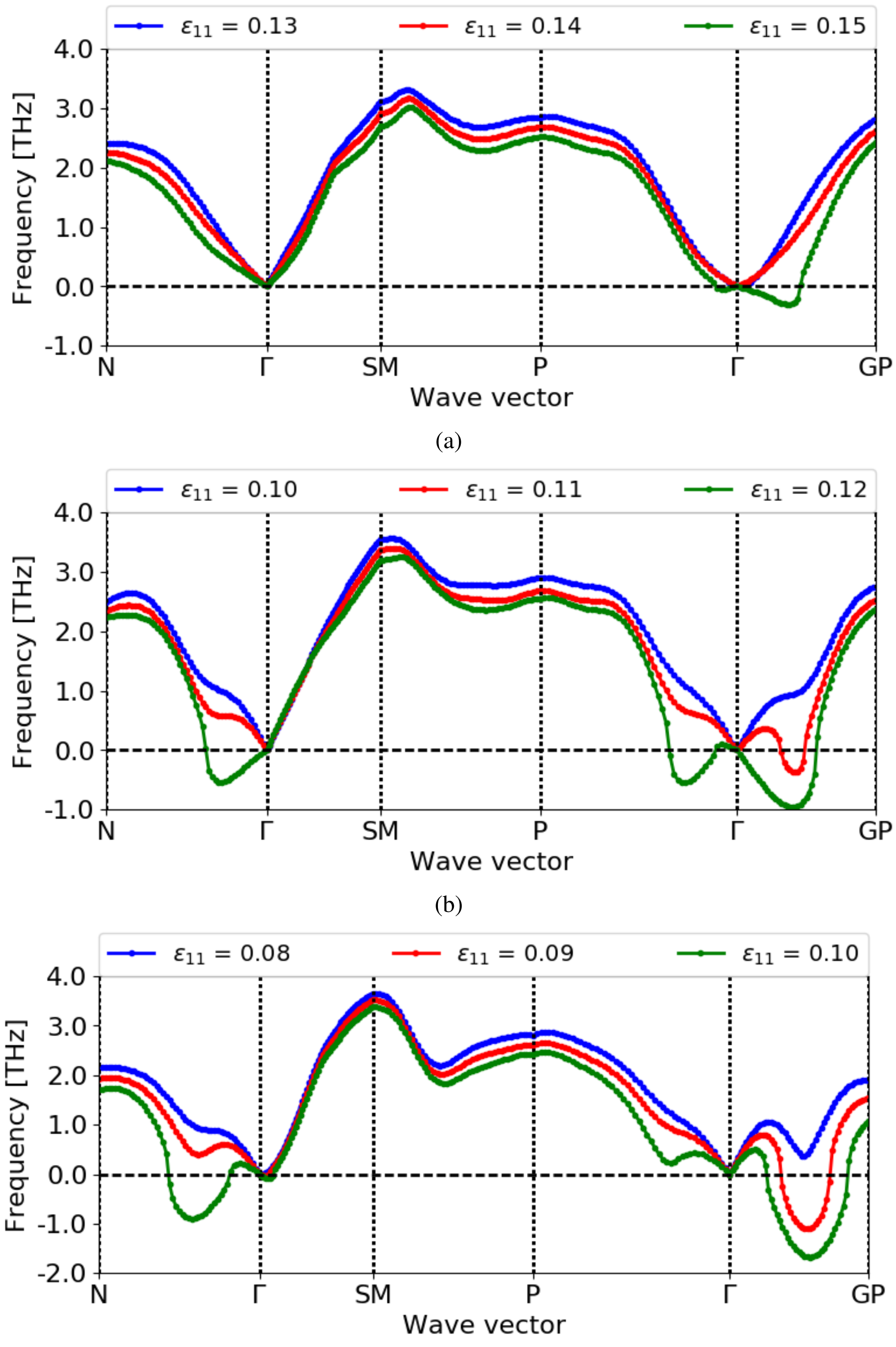

(a)

(b)

(c)

Figure 3.14: Phonon frequencies of VCA $W_{1-x}Re_x$ under different ε_{11} along TP during the [100] ideal tensile deformation calculated by DFPT method using QE. (a): $W_{0.9}Re_{0.1}$. (b): $W_{0.75}Re_{0.25}$. (c): $W_{0.5}Re_{0.5}$.

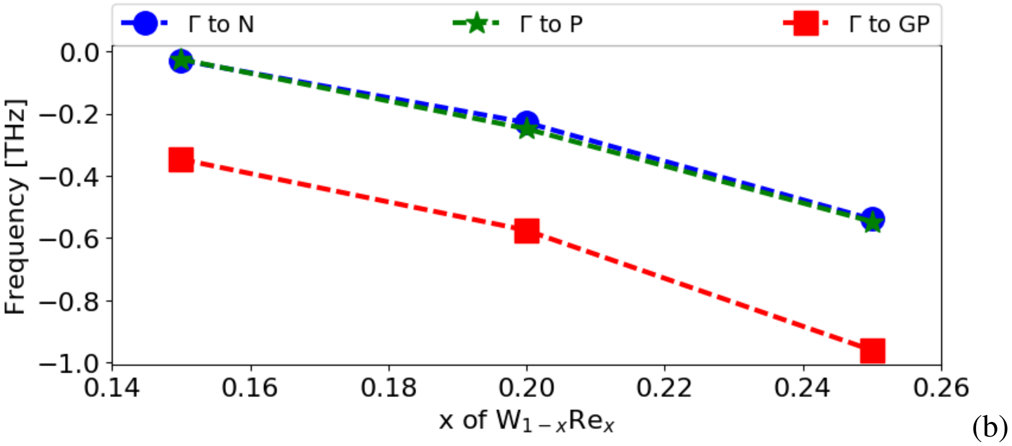

Figure 3.15: The most negative phonon frequencies along different branches of phonon dispersion curves for different VCA $W_{1-x}Re_x$ alloys at ε_{11} = 12% during the [100] ideal tensile deformation.

wave vector **k** is $[0.29\ 0.14\ \overline{0.14}]$ along the Γ-GP branch, also away from the Γ point.

The ideal tensile behavior and phonon spectrums of $W_{0.85}Re_{0.15}$, $W_{0.80}Re_{0.20}$, and $W_{0.75}Re_{0.25}$ alloys in VCA scheme are also investigated to further confirm the effect of Re on the phonon instability of W-Re alloys. For all these three compositions, the critical strain $\varepsilon_{11}^{\mathrm{IT}}$ corresponding to the ideal tensile strength $\sigma_{11}^{\mathrm{IT}}$ is close to 12%. Meanwhile, the most negative (imaginary) frequencies along different branches (Γ-N, Γ-P, and Γ-GP) as functions of Re concentration are plotted in Figure 3.15. It reveals that the Γ-GP branch always has the most negative value for these alloys, suggesting the first imaginary frequency always appears along Γ-GP branch. With the increment of Re concentrations, the imaginary phonon modes always produce more negative frequencies. For example, the most negative frequency along Γ-GP branch changes from ∼-0.4 THz for $W_{0.85}Re_{0.15}$ to ∼-1.0 THz for $W_{0.75}Re_{0.25}$, suggesting the critical strain $\varepsilon_{11}^{\mathrm{PI}}$ for the emergence of imaginary frequencies should decrease with the increase of Re concentration. Thus, phonon instability along Γ-GP branch for W-Re alloys is promoted by the increments of Re concentration and the number of valence electrons per atom.

Figure 3.16 illustrates the analyses of the polarization and wave vectors of the unstable phonon modes in VCA $W_{0.75}Re_{0.25}$ alloy. When the critical strain of phonon instability

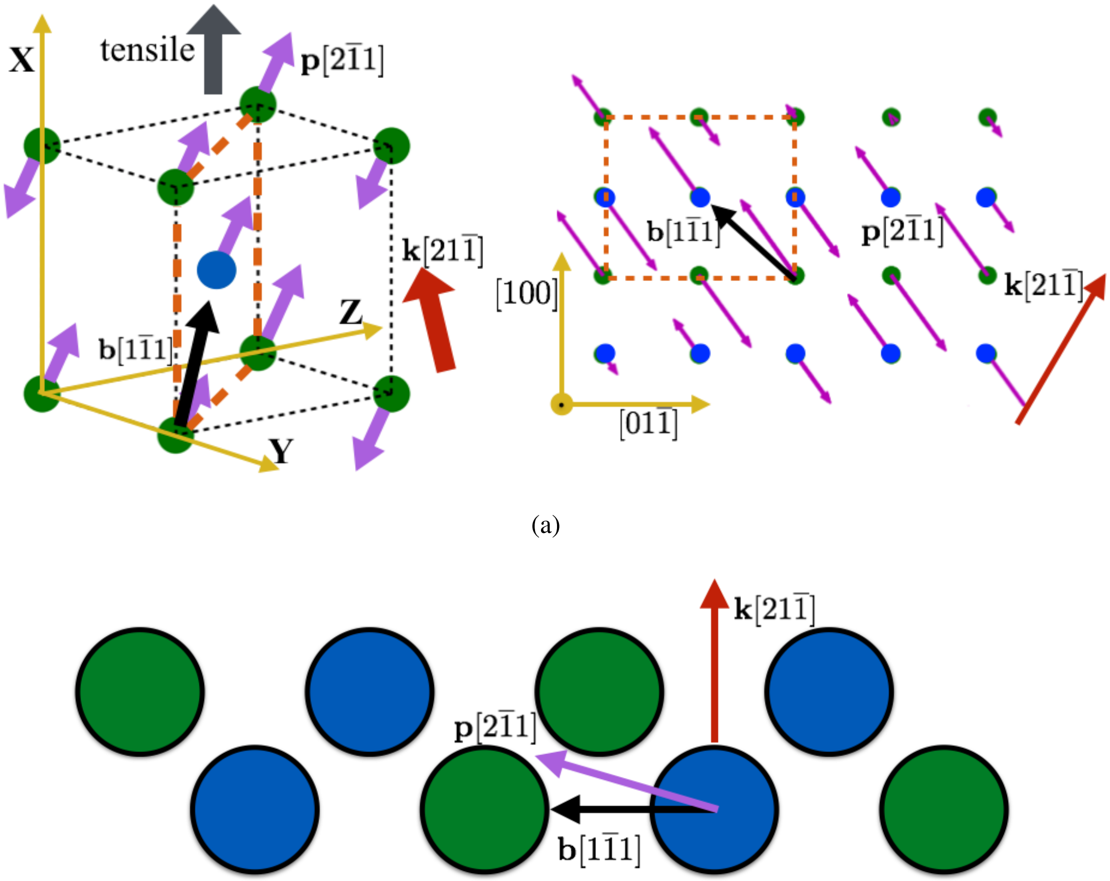

(a)

(b)

Figure 3.16: A schematic illustration of the dynamic instability of $T_{[2\bar{1}1]}[2\xi\ \xi\ \bar{\xi}]$ phonon mode in VCA $W_{0.75}Re_{0.25}$ alloy. (a): The polarization vector **p** and the wave vector **k** of unstable phonon mode shown in the 3D lattice (left) and on the projection of atoms on (011) plane (right). (b): Sketch of the hard sphere "*roll over*" model [141]. The polarization vector **p** is the instantaneous tangent direction along the transition path of the dislocation nucleation event, and it has a small angle with Burgers vector b. Here the green/blue circles stand for atoms at the corner/center of BCC unit cells.

$\varepsilon_{11}^{\mathrm{PI}}$ is applied, the unstable phonon propagates along the wave vector **k** perpendicular to $(21\bar{1})$ planes, and atoms oscillate along the direction of the polarization vector **p** close to $[2\bar{1}1]$ with different phase factors. This unstable phonon mode can promote dislocation nucleation on $1/2[1\bar{1}1](21\bar{1})$ slip system, which is among the most typical slip systems for BCC crystals. The angle between the polarization vector $\mathbf{p} \parallel [2\bar{1}1]$ and the Burgers vector $1/2[1\bar{1}1]$ is about 18°. This deviation between **p** and the Burgers vector is consistent with previous dynamics stability analyses [141], which indicates that the nucleation of certain dislocation due to phonon instability requires the atoms on the potential slip plane to *roll over* their neighbor atoms to minimize the dislocation nucleation barrier. The phonon polarization direction **p** responds to the instantaneous *rolling* direction [141] as illustrated in Figure 3.16 (b). Thus, the unstable phonon for $\mathrm{W_{1-x}Re_x}$ VCA alloys under the critical strain before the elastic tensile failure can activate the emission of $1/2\langle 111\rangle\{\bar{2}11\}$ dislocations and enhance the preference of ductile plastic deformation to the brittle fracture under the extremely high-stress condition, like the local region near the crack tip.

3.3.4 LEFM analyses

The ideal strength, elastic and phonon instability criteria emphasize the stress/strain evolution, and the LEFM theory emphasizes the energetic variations. This section covers LEFM analyses on the intrinsic brittleness/ductility in circumstances similar to the deformation of real metals/alloys. Our LEFM analyses output the critical stress intensity factors $\mathrm{K_{Ic}}$ for the cleavage propagation along the $\{100\}$ plane and $\mathrm{K_{Ie}}$ for the emission of dislocations in $1/2\,\langle 111\rangle\,\{\bar{2}11\}$ and $1/2\,\langle 111\rangle\,\{\bar{1}10\}$ slip systems for different $\mathrm{W_{1-x}Ta_x}$ and $\mathrm{W_{1-x}Re_x}$ VCA alloys under Mode I loading along $\langle 100\rangle$ directions. The parameters in LFFM analyses listed in Table 3.3 are the elastic constants, surface energies $\gamma_{\mathrm{s}\,(100)}$, and unstable stacking fault energies ($\gamma_{\mathrm{usf}\,(211)}$ and $\gamma_{\mathrm{usf}\,(110)}$) calculated using VCA pseudopotentials by QE. The results of $\mathrm{K_{Ic}}$ and $\mathrm{K_{Ie}}$ for different alloys are summarized in the Figure 3.17, where the number of valence electrons per atom indicates the chemical composition of VCA $\mathrm{W_{1-x}Ta_x}$ and $\mathrm{W_{1-x}Re_x}$ alloys.

The individual values of $\mathrm{K_{Ic}}$ and $\mathrm{K_{Ie}}$ for $1/2\,\langle 111\rangle\,\{\bar{2}11\}$ and $1/2\,\langle 111\rangle\,\{\bar{1}10\}$ slip systems are plotted in Figure 3.17 (a). Starting from pure W (the number of valence electrons per atom equals to 6.0), $\mathrm{K_{Ic}}$ and $\mathrm{K_{Ie}}$ of two slip systems both decrease with the increment of valence electrons per atom by adding more Re into W. These trends are consistent with the variations of $\gamma_{\mathrm{s}\,(100)}$, $\gamma_{\mathrm{usf}\,(211)}$m and $\gamma_{\mathrm{usf}\,(110)}$ listed in Table 3.3. A parameter $\mathrm{K_{Ie}/K_{Ic}}$

Table 3.3: Parameters in LEFM analyses: lattice constant a [Å], elastic constants [GPa], and unstable stacking fault energy γ_{usf} and surface energy γ_{s} [J/m^2]. The deviations between the values of pure W from our DFT calculations and those from previous results [151] should result from the usage of different pseudopotentials.

	a	C_{11}	C_{12}	C_{44}	$\gamma_{\mathrm{usf}\,(211)}$	$\gamma_{\mathrm{usf}\,(110)}$	$\gamma_{\mathrm{s}\,(100)}$
$W_{0.50}Ta_{0.50}$	3.250	344	187	92	1.599	1.276	3.941
$W_{0.75}Ta_{0.25}$	3.209	436	189	123	2.182	1.859	4.65
$W_{0.80}Ta_{0.20}$	3.199	467	190	136	2.191	1.992	4.771
$W_{0.85}Ta_{0.15}$	3.189	487	191	148	2.241	2.083	4.862
$W_{0.90}Ta_{0.10}$	3.178	512	191	160	2.258	2.095	4.935
$W_{0.95}Ta_{0.05}$	3.172	532	193	170	2.245	2.133	4.992
W	3.171	534	193	177	2.120	2.021	4.847
W [151]	3.165	523	203	160	1.978	1.762	4.630
$W_{0.95}Re_{0.05}$	3.168	537	199	182	2.025	1.944	4.749
$W_{0.90}Re_{0.10}$	3.166	536	203	184	1.930	1.867	4.643
$W_{0.85}Re_{0.15}$	3.163	531	208	187	1.832	1.768	4.534
$W_{0.80}Re_{0.20}$	3.161	527	211	189	1.738	1.687	4.426
$W_{0.75}Re_{0.25}$	3.159	529	217	191	1.647	1.610	4.323
$W_{0.50}Re_{0.50}$	3.149	512	243	198	1.243	1.132	3.905

is introduced to evaluate the intrinsic ductility of alloys because K_{Ie}/K_{Ic} can quantitatively describe the preference of dislocation emission over the crack propagation to release the strain energy at the crack tip [201, 9]. Figure 3.17 (b) shows that K_{Ie}/K_{Ic} decreases for both $1/2\,\langle 111\rangle\,\{\bar{2}11\}$ and $1/2\,\langle 111\rangle\,\{\bar{1}10\}$ slip systems when pure W is alloyed with higher Re concentrations in the VCA scheme. It means to increase valence electrons in W promotes the dislocation emission near the crack tip under Mode I loading along $\langle 100\rangle$ and leads to more ductile deformation. This result is consistent with the ideal tensile results that alloying Re solutes can induce short-wavelength phonon instability for W alloys to raise the tendency of dislocation nucleation under the extremely high-stress condition.

Noticeably, K_{Ie}/K_{Ic} of both $1/2\,\langle 111\rangle\,\{\bar{2}11\}$ and $1/2\,\langle 111\rangle\,\{\bar{1}10\}$ slip systems are larger than 1.0 for pure W. It means the propagation of $\{100\}$ cleavage fracture occurs under less stress intensity factors than dislocation emissions at the crack tip under Mode I loading described as Figure 3.2, so pure W is intrinsically brittle. K_{Ie}/K_{Ic} of $1/2\,\langle 111\rangle\,\{\bar{2}11\}$ becomes smaller than 1 when Re concentration is above a critical value slightly larger than 0.25 ac-

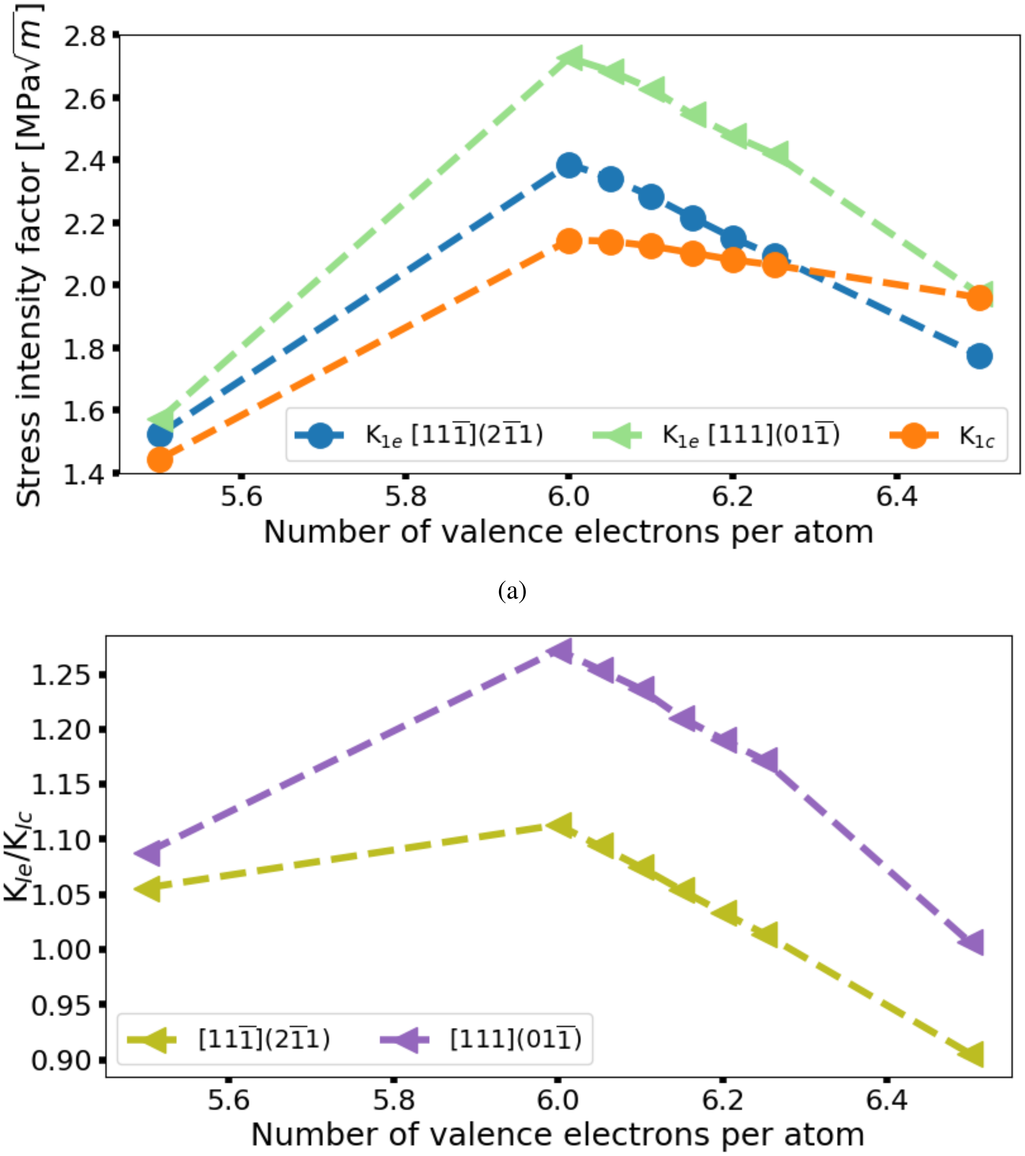

(a)

(b)

Figure 3.17: Cleavage and dislocation emission competition for different W alloys in the VCA scheme predicted by anisotropic LEFM analyses based on crack tip geometry in Figure 3.2. The number of valence electrons per atom is 6.0 for pure W, and it decreases/increases linearly in variance of Ta/Re concentration. (a): The variations of critical stress intensity factor K_{Ic} for Griffith cleavage and K_{Ie} for dislocation emissions of $1/2 \langle 111 \rangle \{\bar{2}11\}$ and $1/2 \langle 111 \rangle \{\bar{1}10\}$ slip. (b): The variation of the ductility parameter K_{Ie}/K_{Ic} for both slip systems.

cording to Figure 3.17 (b). It means that the $1/2 \langle 111 \rangle \{\bar{2}11\}$ dislocation emission occurs under less stress intensity factors than the cleavage fracture, so $W_{1-x}Re_x$ VCA alloys are intrinsically ductile above this critical Re concentration [201, 9]. Interestingly, this critical Re concentration is close to its counterpart to induce unstable phonon modes to activate dislocation nucleation before elastic tensile failure predicted in Figure 3.14 (b).

Figure 3.17 (b) also unveils that, when a small amount of Ta (less than 25%) is added to pure W, K_{Ie}/K_{Ic} first increases to some extent for both 1/2 $\langle 111 \rangle$ $\{\bar{2}11\}$ and 1/2 $\langle 111 \rangle$ $\{\bar{1}10\}$ slip systems. These changes demonstrate that to slightly decrease valence electrons of W inhibits the dislocation emission near the crack tip under Mode I loading along $\langle 100 \rangle$ so that $W_{1-x}Ta_x$ VCA alloys prefer to more brittle deformation. This result matches with the previous DFT calculations [139] and experiments [263], both of which show that Ta reduces the ductility of W alloys when Ta concentration is smaller than 10%. However, when Ta concentration is higher than a specific value between 25 % and 50 %, K_{Ie}/K_{Ic} of both slip systems for $W_{1-x}Ta_x$ VCA alloys decline to values smaller than their counterparts of pure W. These W alloys with high Ta concentration become more ductile compared with pure W, consistent with the ESI revealed by ideal tensile calculations in Section 3.3.2.1.

Another interesting result of these LEFM analyses is the change of the preferable slip system in W alloys. A comparison of K_{Ie} between two slip systems in Figure 3.17 (a) indicates that 1/2 $\langle 111 \rangle$ $\{\bar{2}11\}$ slip system is more favorable for the dislocation emission at the crack tip than 1/2 $\langle 111 \rangle$ $\{\bar{1}10\}$ in pure W and W-Re alloys, but adding a significant amount ($\sim$ 50%) of Ta solutes into W generates a preference to 1/2 $\langle 111 \rangle$ $\{\bar{1}10\}$ dislocation emission. This transformation of the preferable slip system by the variation of valence electrons is consistent with our phonon analyses in $W_{1-x}Ta_x$ and $W_{1-x}Re_x$ VCA alloys as shown in Figure 3.13 and 3.14. It also agrees with the results of DFT-based dislocation core structure calculations and microcantilever bending experiments [140], which show that adding Re in W facilitates the 1/2 $\langle 111 \rangle$ $\{\bar{2}11\}$ dislocations while alloying Ta in W favors the 1/2 $\langle 111 \rangle$ $\{\bar{1}10\}$ dislocations.

3.4 Conclusion

Tuning the d-band filling by chemical alloying can make the brittle BCC W metal more ductile due to different lattice instability mechanisms [197]. W-Ta alloys of small Ta concentration prefer to brittle cleavage fracture during [100] ideal tensile deformation so that they are intrinsically brittle, as pure W. The addition of high-concentration ($\sim$ 50 %) Ta makes ESI occur before brittle cleavage fracture during [100] ideal tensile deformation so that these W-Ta alloys are intrinsically ductile. Consistently, LEFM analyses reveal that small amount of Ta (less than $\sim$ 25%) in W-Ta alloys increase the preference of $\{100\}$ cleavage fracture propagation than dislocation emissions near the crack tip under Mode I loading along $\langle 100 \rangle$, so these W-Ta alloys should be more brittle than pure W. Higher Ta concentrations (above a specific value between 25 % and 50 %) in W-Ta alloys induce the preference of dislocation emissions, especially for those of 1/2 $\langle 111 \rangle$ $\{\bar{1}10\}$ slip systems.

Re inhibits ESI in W-Re alloys during [100] ideal tensile deformation. However, Re above a critical concentration ($\sim$ 25%) in W-Re alloys provokes the phonon instability with $\mathrm{T}_{[2\bar{1}1]}[2\xi\ \ \xi\ \ \bar{\xi}]$ phonon mode before the W-Re alloys reach elastic instability. The propagation of this unstable phonon mode correspond to the initialization of $1/2[1\bar{1}1](21\bar{1})$ dislocation nucleation, so these W-Re alloys are still intrinsically ductile. Consistently, LEFM analyses show that, when Re concentration is above a similar critical concentration, the emission of dislocations in 1/2 $\langle 111 \rangle$ $\{\bar{2}11\}$ slip system is mostly favorable than $\{100\}$ cleavage fracture propagation and 1/2 $\langle 111 \rangle$ $\{\bar{1}10\}$ dislocation emission near the crack tip under Mode I loading along $\langle 100 \rangle$, so these W-Re alloys are intrinsically ductile also according to LEFM analyses.

In general, for the BCC refractory metals and alloys, the differences in ductility behaviors found in the real materials indeed are consistent with the differences in their lattice instability behavior in this work [281, 58]. These lattice instability criteria provide valuable and easily obtainable indicators of material ductility without considering other factors at a larger scale or from the external environment.

CHAPTER IV

Accurate Interatomic Potential of Nb for Studies on Deformation Defects

In BCC refractory alloys, with interesting intrinsic crystal deformation properties revealed in Chapter III, this work is to promote atomistic simulations to accurately reflect the intrinsic mechanical properties and interatomic bonding characteristics for the study of defects nucleation and evolution during plastic deformation. We created an interatomic potential that can reproduce bonding characteristics and defect properties for Nb consistent with those from DFT calculations [266]. This potential combined with and other accurate MEAM potentials for BCC refractory metals and alloys can assist our large-scale MD simulations to investigate the effects of interatomic bonding characteristics on the plastic deformation at mesoscale, such as the ductility difference between Nb and Mo.

4.1 Introduction

Niobium (Nb) as a refractory metal has many promising properties, such as outstanding high-temperature mechanical performances and suitable biocompatibility. Moreover, Nb shows excellent ductility and formability at room temperature, although its non-close packed body-centered cubic (BCC) lattice and directional chemical bonding due to d electrons that usually result in brittle deformation at relatively low temperatures (room temperature or lower) for other similar transition metals, such as molybdenum (Mo), tungsten (W), and iron (Fe) [5, 116, 52, 52]. On the other hand, first-principles calculations based on DFT revealed [128, 197] that Nb is intrinsically ductile due to its ESI during $\langle 100 \rangle$ ideal tensile deformation before cleavage fracture along the typical $\{100\}$ cleavage plane.

It is tempting to build clear and quantitative connections between the intrinsic ductility revealed in perfect crystals by DFT calculations and the ductile properties of realistic materials revealed by macroscopic experiments. A fundamental step is to correlate the intrinsic ductility and ideal strength of perfect Nb crystal to the characteristics of individual deformation defects, such as the nucleation and motion of dislocations and deformation twinning. Nevertheless, for mesoscopic mechanical processes involving dislocation network evolution or crack propagation, their length/time scales lie beyond the domain achievable by the nowadays computational power to fulfill DFT calculations. One remedy is to develop mesoscale models using deformation defect characteristics obtained from large-scale molecular dynamics/statics simulations, where the empirical interatomic Nb potential should represent the fundamental ductile essentials consistent with DFT calculations.

To describe many-body interactions, embedded-atom method (EAM) [43] and Finnis–Sinclair (FS) [64, 4] potentials treat each atom embedded in a host environment consisted of other neighboring atoms, and the embedding energy is a function of the “electronic density” contributed by all its neighboring atoms. EAM and F-S potentials are efficient in computations, but they have limitations to represent directional bonding properties. For directional bonding features to represent the inherent ESI in Nb, we applied a MEAM that is based on EAM but included three-body interactions in its “electron density”. The MEAM model was first proposed by Baskes [21] to describe various bonding characteristics including s, p, d, and f type angular contributions, and later successfully applied to study advanced metals and alloys of complex atomic interactions [133, 138, 196, 179, 273, 54].

In this work, we applied MEAM spline form in the development of Nb potential with emphasis on the simulations of its deformation behaviors under extreme and anisotropic loading conditions [197, 47]. We fitted the MEAM potentials using force matching method [60] based on data from DFT calculations, and we employed a cubic spline interpolation scheme of tabulated parameters rather than analytic formulas [138]. To minimize force difference between the MEAM potential and DFT calculations, we applied an evolution strategy (ES) and a model selection during the fitting and validating process. We applied the MEAM potential to calculate structural, thermal and mechanical properties of Nb and compared them with results from DFT calculations and/or experiments. We demonstrated the difference of ductility during MD tensile test with Nb and Mo MEAM potentials.

4.2 Computational methods

4.2.1 Modified embedded-atom method

In MEAM, the total energy E_{tot} of the system is in the form

$$E_{tot} = \frac{1}{2} \sum_{i,j(j \neq i)} \phi(r_{ij}) + \sum_{i} U(n_i) \tag{4.1}$$

where $\phi(r_{ij})$ represents pair interactions between atoms i and j of a distance r_{ij}. $U(n_i)$ is embedding function of n_i, which is the total "electron density" at atom i's position. This background "electron density" in MEAM model combines both two-body and three-body interactions for the atom i with all its neighboring atoms as

$$n_i = \sum_{j} \rho(r_{ij}) + \frac{1}{2} \sum_{jk} f(r_{ij}) f(r_{ik}) g[\cos(\theta_{jik})] \tag{4.2}$$

where both $\rho(r_{ij})$ and $f(r_{ij})$ are functions of a distance r_{ij} between atoms i and j. $g[\cos(\theta_{jik})]$ is a function of θ_{jik}, the angle between the bond connecting atoms j and i and the bond connecting atoms i and k. Unlike the EAM, the embedding function in MEAM has an angular term $f(r_{ij})f(r_{ik})g[\cos(\theta_{jik})]$ and loses the physics as a uniform electron density [21]. Equation 4.2 is equivalent to Baskes' model [21] that $g[\cos(\theta)] = A_1 \cos(\theta) + A_2 \cos^2(\theta) +$

$A_3 \cos^3(\theta)$. In Equation 4.1 and Equation 4.2, the functions $\phi(r)$, $U(n)$, $\rho(r)$, $f(r)$ and $g[\cos(\theta)]$ are described by cubic spline interpolations [196], which add more flexibility to fit forces obtained by the first principle calculations.

4.2.2 Force matching method

We adopted the force-matching method [60] to determine the five functions $\phi(r)$, $U(n)$, $\rho(r)$, $f(r)$ and $g[\cos(\theta)]$ in the MEAM. We minimized differences between energies/forces generated by DFT calculations and those calculated by the MEAM potential for the same atomic configurations. Thus, the optimization target is the error function Z_{total} as

$$Z_{total} = w_f Z_{force} + w_e Z_{energy} \tag{4.3}$$

where w_f and w_e are weighting factors of the error function for forces Z_{force} and energies Z_{energy}, respectively. Some previous studies incorporated stress terms in the target function [63]. In our cases, we noticed that incorporating stresses did not significantly improve the quality of fitting results despite more time spent for stress calculations during iterations. Thus we skipped fitting stresses for each data and incorporated more force data if necessary. The error functions for the forces Z_{force} and energies Z_{energy} are

$$Z_{force} = \sum_{i=1}^{C} w_i \sum_{j}^{N_i} \sum_{\alpha \in x,y,z} H_{pen}(u_{ij\alpha}) \tag{4.4}$$

$$Z_{energy} = \sum_{i=1}^{C} w_i H_{pen}(u_i) \tag{4.5}$$

where C is the total number of configurations included in the dataset. N_i is the total number of atoms in the configuration i, and w_i is the weighting factor for configuration i. u_i and $u_{ij\alpha}$ are residuals of energies and forces between DFT and MEAM potential calculations.

$H_{pen}(u)$ is the Huber penalty function (also called robust least-squares) [27],

$$H_{pen}(u) = \begin{cases} u^2 & \text{if } |u| < M \\ M(2|u| - M) & \text{if } |u| \geq M \end{cases} \tag{4.6}$$

M is a parameter to be determined. This penalty form agrees with the least-squares penalty function when residuals are smaller than M. The penalty grows linearly in l_1-norm form for residuals larger than M, which ensures that our fitting is less perturbed by ourliers since l_1-norm approximation is the most robust to outliers among (convex) penalty function approximation methods. The residuals of forces $u_{ij\alpha}$ and energies u_i are calculated by

$$u_{ij\alpha} = \frac{|F_{ij\alpha}^{MEAM} - F_{ij\alpha}^{DFT}|}{|F_{ij\alpha}^{DFT}| + \epsilon} \tag{4.7}$$

$$u_i = |E_i^{MEAM} - E_i^{DFT}| \tag{4.8}$$

We measured the relative error of forces, and add a parameter ϵ to prevent errors of small forces render the penalty to be extreme large.

4.2.3 Fitting procedures

To build the Nb MEAM potential, we first applied DFT calculations to generate the force and energy dataset. Next, we implemented a ES for the optimization and a k-fold model selection to choose the parameters of the five functions $\phi(r)$, $U(n)$, $\rho(r)$, $f(r)$ and $g[\cos(\theta)]$. Finally, we examined the accuracy, transferability, and limitations of the MEAM potential by MS / MD calculations with DFT or experiment results.

In the first step, we built a DFT dataset with 4217 energies and 32601 force components. We employed four types of atomic configurations in the DFT dataset: one-atom BCC primitive cells under different types and magnitudes of strain exerted on the cell (including those from ideal tensile/shear deformation); FCC and hexagonal close packed (HCP) unit cells with varying lattice constants near the equilibrium states; 5×5×5 duplicated BCC primitive supercells of 125 atoms that record atomic trajectories using ab initio MD simulations; 16-atom supercells generated by USPEX, a crystal structure prediction software [173, 174, 149], based on crystal symmetries randomly selected from Space Groups of Number 2-230. Our DFT data were purely based on strained/unstained simple phases (BCC, HCP and FCC), their thermally activated atomic trajectories, and crystal structures with randomly selected symmetric structures.

- Elastic strain: We added one-atom BCC primitive cells with various types of elastic strains, including volumetric strains, volume-conserving orthorhombic strains and volume-conserving monoclinic strains.
- Ideal tensile/shear deformation and phase transformation: We added atomic configurations generated by applying extremely large strains and/or atomic shuffles, including BCC crystals under $\langle 100 \rangle$ ideal tensile deformation along TP and OP [197, 265], ideal shear along $\langle 111 \rangle$ on $\{211\}$ and $\{110\}$ planes, elastic strains and atomic shuffle in Burgers model of BCC-to-HCP transformation [57].
- HCP and FCC phases: We added one-atom FCC primitive cells and two-atom HCP unit cells, and the lattice constants were sampled near the equilibrium FCC and HCP states without applied stress by DFT calculations.
- Thermal activated atomic trajectory: Upon a 5×5×5 BCC conventional supercell, we run ab initio MD simulations for 1500 fs with temperatures from 400 K to 4000 K (one configuration per 200 K) and chose the last configuration of each run.
- Random chosen symmetric structures: We applied routines of USPEX to generate multiple 16-atom configurations that have symmetries of space groups randomly chosen from space group Number 2 to Number 230, such as P4/mmm, P2/m, C2/m etc.

We applied VASP [129] for DFT calculations with the 10^{-4} eV/atom energy convergence threshold for all electronic self-consistent calculations. The pseudopotentials were based on the PAW method [130] and the PBE exchange-correlation functional [182]. Γ-centered k-point were applied with meshed by 31×31×31 for the primitive cell, and the number of k-point for other supercells change inverse proportionally to the supercell size. We used 450 eV plane-wave cutoff energy and first-order Methfessel-Paxton smearing of 0.2 eV smearing width [159] for partial occupancies of each wave function.

In the fitting procedure, we implemented the Covariance Matrix Adaptation Evolution Strategy (CMA-ES) algorithm [92, 91] to minimize the error function Z_{total}. CMA-ES is a stochastic method that can tackle continuous domain optimization of non-linear, non-convex functions. The CMA-ES belongs to the class of evolutionary algorithms that are normally based on an interleaving of variation (including recombination and mutation) and selection processes. In our implementation, the fitting variables are spline knots of the five MEAM functions ϕ(r), U(n), ρ(r), f(r) and g[cos(θ)], and pairwise dependencies between variables exist due to knots are connected together to describe one empirical potential curve. During the optimization iteration, new candidate individuals are sampled according to a multivariate normal distribution based on a moving mean vector and covariance matrix which are internal state variables of the algorithm. The force penalty function Equation 4.6 is applied to measure the fitness of each solution. Then a new mean value is selected for the distribution as the recombination step, and a random perturbation vector is added to each candidate solution with zero mean as the mutation step. In general, the whole optimization loop includes sampling of new candidate solutions, sorting sampled solutions upon their fitness, and updating internal state variables including covarance matrix and step-size variables. We refer our initial values of spline knots to parameters of a Mo MEAM potential [179] since Mo and Nb are adjacent elements in the periodic table.

Although the CMA-ES is efficient and robust even for rugged search landscape and local optima, the initially fitted potentials may not be robust since some configurations that

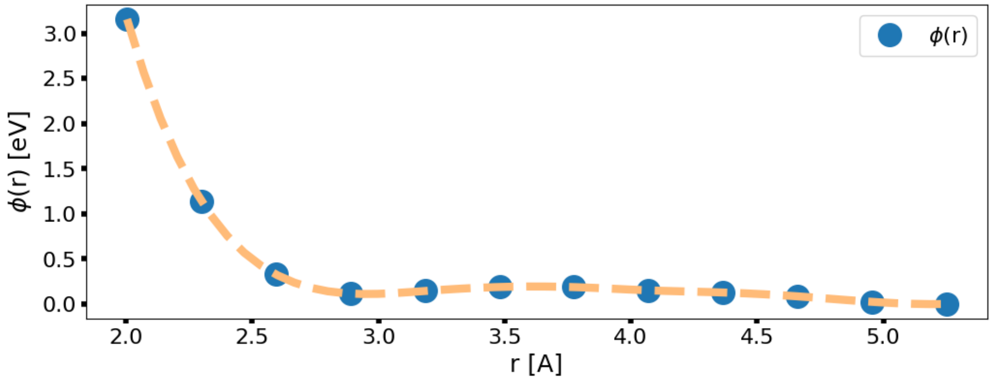

Figure 4.1: The cubic splines function of ϕ(r) in the MEAM Nb potential.

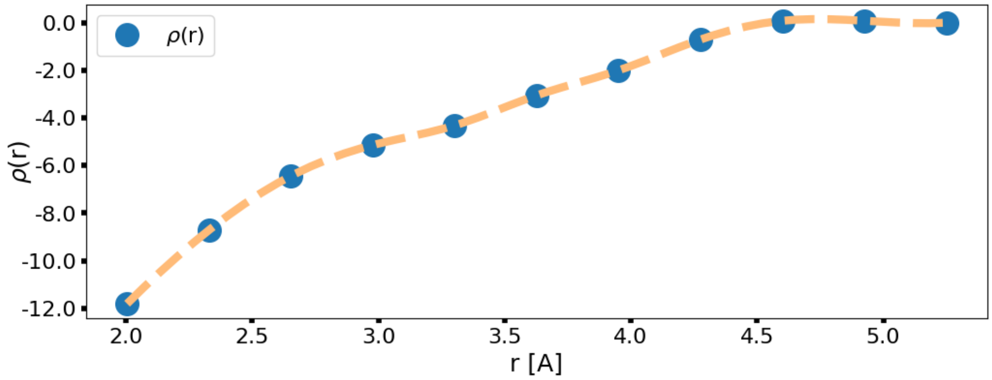

Figure 4.2: The cubic splines function of ρ(r) in the MEAM Nb potential.

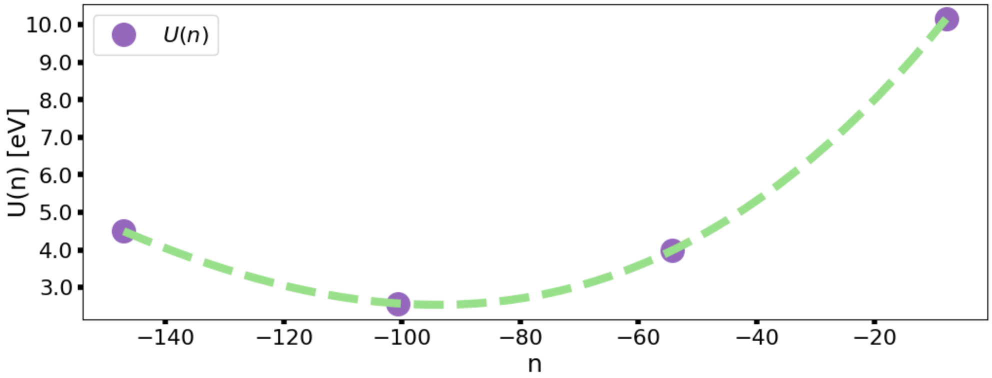

Figure 4.3: The cubic spline function of f(r). in the MEAM Nb potential.

have large errors may dominate the optimization path. The quality of a potential is also dependent on the number of spline knots, since too many/fewer knots may lead to overfitting/underfitting. We therefore applied a k-fold model selection to tune hyper parameters such that weight parameters in the dataset were balanced to represent the material features properly. Parameters we managed to select include: ε (in Equation 4.7) that limits the errors of small forces; M (in Equation 4.6) that controls the effects of large residuals; $\mathrm{w_e}$ (in Equation 4.3) that determines the weights of energies relative to the weights of forces, and $\mathrm{w_i}$ (in Equation 4.4) that specifies the weight of each configuration. For $\mathrm{w_i}$, we assigned a specific value to a group of similar configurations as classified in the section C. To prevent the configurations with large values of forces and high energies to dominate the fitting processes compared with those near the equilibrium conditions, we added a correction by

$$\mathrm{w_i} = \mathrm{w_i^0} \exp\left(\frac{-|\mathrm{E_i} - \mathrm{E_0}|}{\lambda}\right) \tag{4.9}$$

where λ is the parameter to be determined by our model selection. $\mathrm{E_i}$ and $\mathrm{E_0}$ are energy per atom in configuration i and in equilibrium BCC phase, respectively. We applied a 3-fold model selection to determine parameters from Equation 4.3 to Equation 4.9. For each parameter among $\mathrm{w_e}$, $\mathrm{w_i^0}$, M, ϵ, we divided our dataset to four disjoint subsets, then trained the model using just three of them, leaving the fourth subset for the cross-validation purpose [29]. We then applied the selected parameters to re-train the five spline functions on the whole DFT dataset. For the number of spline knots, our tests showed a bias-variance trade-

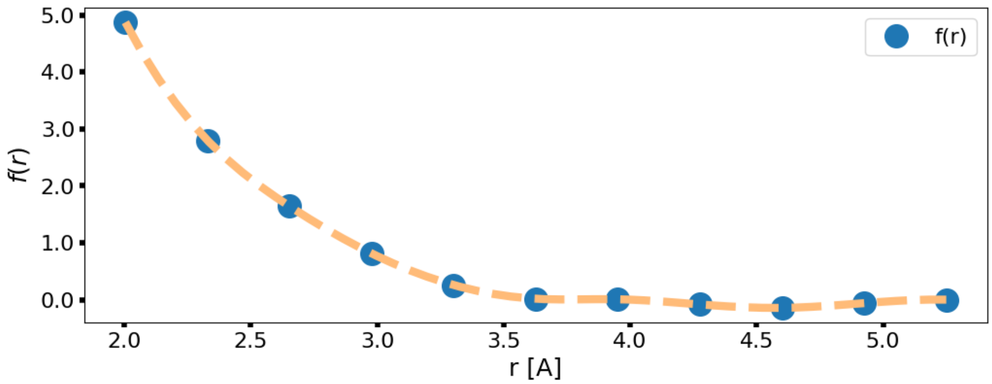

Figure 4.4: The cubic spline function of U(n) in the MEAM Nb potential.

off: if we increased the number of the spline knots, the bias decreased but the variances

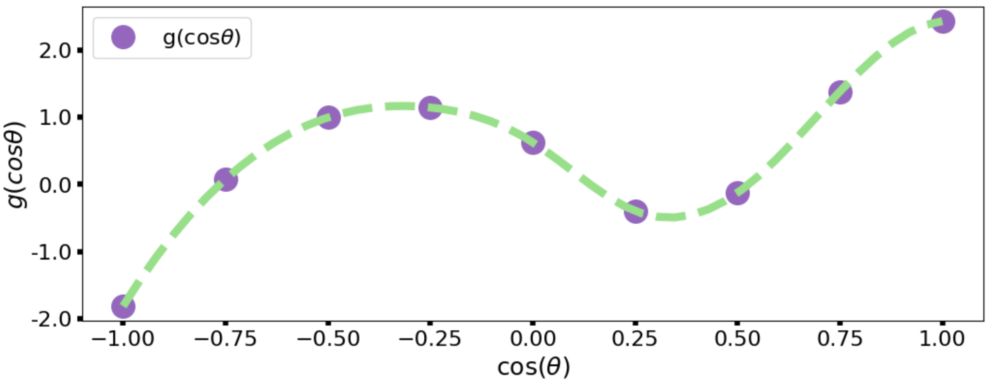

Figure 4.5: The cubic spline function of g[cos(θ)] in the MEAM Nb potential.

grew. We thus followed the principle of parsimony as the following [29]. We started using a few spline knots and kept accepting additional knots if the newly introduced trial knots could significantly decrease force errors. For the evaluation of the potential, we focused on the smoothness of the five spline functions and whether the potential reproduced certain materials constants obtained from the DFT calculations with small bias. We repeated the fitting process of adding or deleting knots in the five spline functions then re-fitting and validating the potential. The final optimal MEAM potential was shown in Figure 4.1. In this potential, ϕ(r) contain 12 knots, ρ(r) and f(r) are consisted of 11 knots, U(n) and g[cos(θ)] have 4 and 9 knots respectively.

4.3 Results and discussion

To examine accuracy, robustness and usability of the MEAM potential, we evaluated structural, thermal, mechanical and defect properties of the MEAM potential to compare with DFT calculations and experiments. MD and MS calculations with the MEAM potential were implemented by Large-scale Atomic/Molecular Massively Parallel Simulator (LAMMPS) [191], which supported a new style multicomponent MEAM [273].

4.3.1 Structural and elastic properties

We used Universal Structure Predictor: Evolutionary Xtallography (USPEX) [173, 174, 149] to perform crystal structure predictions based on the Nb MEAM potential. In USPEX, we used LAMMPS for force calculations with supercells of 16 atoms. We optimized crystal structures by minimizing the total enthalpy with 50 generations and 30 individual atomic configurations per generation. The USPEX prediction confirmed that the most stable structure of the MEAM potential was indeed BCC.

Table 4.1: The cohesive energy E_{cos}, lattice parameters, elastic constants, bulk modulus $B = 1/3(C_{11} + 2C_{12})$, shear modulus $C' = 1/2(C_{11} - C_{12})$ calculated by Nb MEAM potential and DFT calculations in this work, previous DFT calculations [63] and experiment values [33]. The experimental lattice parameter and elastic constants were measured at 4.2 K. The MEAM values for the energies and lattice parameters of meta-stable phases for BCC metals are compared to DFT results. The energies are denoted by their relative value to the cohesive energy. Units: Lattice [Å], Elastic constants [GPa], Energies [meV/atom]

	MEAM	PAW-PBE	GGA-PBE[63]	Experiment [25, 33]
E_{cos}	7.00	7.00	7.10	7.57 [122]
a_{BCC}	3.322	3.322	3.309	3.303 [205]
B	173	173	172	173, 172
C’	58	59	59	60, 56
C_{11}	250	251	251	253, 246
C_{12}	135	134	133	133, 135
C_{44}	21	20	22	31, 29
a_{FCC}	4.232	4.234	4.217	-
$\Delta E_{FCC\text{-}BCC}$	321	319	324	-
a_{HCP}	2.850	2.891	2.867	-
c_{HCP}	5.339	5.266	5.238	-
$\Delta E_{HCP\text{-}BCC}$	290	298	297	-
a_{A15}	5.358	5.316	5.296	-
$\Delta E_{A15\text{-}BCC}$	226	103	104	-
$a_{\beta Ta}$	10.398	10.231	10.184	-
$c_{\beta Ta}$	5.282	5.386	5.371	-
$\Delta E_{\beta Ta\text{-}BCC}$	208	82	83	-
$a_{\omega Ti}$	4.902	4.907	4.905	-
$c_{\omega Ti}$	2.700	2.710	2.765	-
$\Delta E_{\omega Ti}$	181	202	201	-

We collected cohesive energy, equilibrium lattice parameters, elastic constants and lattice parameters (and energies) of meta-stable phases including FCC, HCP, β-W (A-15), β-Ta and ω-Ti, from DFT calculations, the MEAM potential and experiments [25, 33]. As shown in Table 4.1, the MEAM potential matches the cohesive energy 7.00 eV per atom from DFT calculations. BCC lattice parameter of the MEAM is 3.322 Å, the same as the DFT result. The elastic constants C_{11}, C_{12} and C_{44} from the MEAM potential differ at most 1 GPa from the DFT calculations. The bulk modulus B is identical to the DFT value, and the shear modulus C' differs only 1 GPa. For meta-stable phases, the energy per atom of the meta-stable FCC phase is 321 meV higher than the equilibrium BCC phase in the MEAM, differing 1% from the DFT 319 meV. Energy per atom for the difference between BCC and HCP phases is 290 meV, 2-3% lower than the DFT. These excellent matches may result from the elastically strained BCC, FCC and HCP configurations in the DFT dataset. For other metastable phases, the MEAM potential overestimates energies of A-15 phase and β-Ta by $\sim$100 meV compared with DFT calculations. Similar overestimation occurs in the MEAM potential of Mo [179], which also overestimates energies of A-15 and β-Ta phase by $\sim$100 meV. As for ω-Ti phase, the MEAM potential reproduce the lattice constants with less than 1% difference and the energy with 10% difference.

4.3.2 Phonon, volume-pressure and thermal expansion

4.3.2.1 Phonon

With experimental measurements, phonon dispersion relations are useful to estimate dynamical properties of the interatomic potentials. We computed phonon band structures along high-symmetry directions using the MEAM potential and DFT. We sampled high symmetry phonon paths in BCC first Brillouin zone (FBZ), as shown in Figure 4.6. Table 4.2 summarized the meaning of k-point notations in BCC FBZ plotted in Figure 4.6.

We obtained the phonon band structures via FDM, and atomic forces in the FDM came from both DFT and MS. We applied Phonopy [235] for phonon spectrum calculations

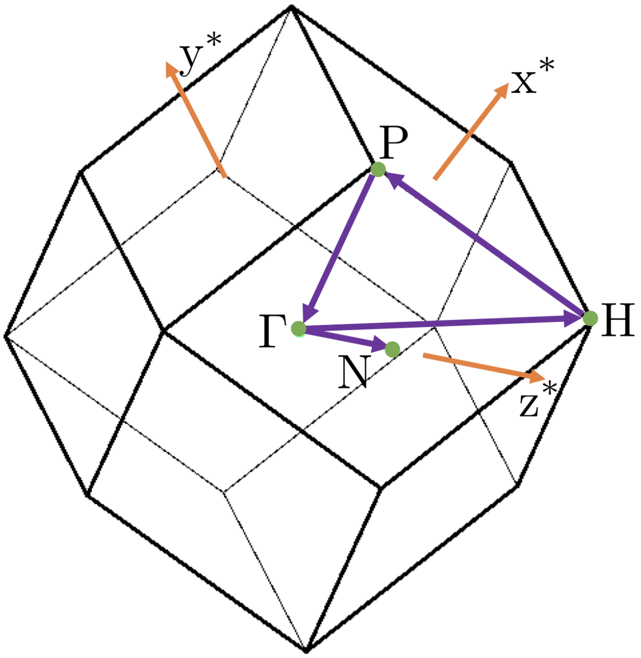

Figure 4.6: Schematic illustration of sampled phonon paths in the primitive cell of BCC reciprocal lattice.

Label	**x***	**y***	**z***
Γ	0	0	0
H	1/2	-1/2	1/2
P	1/4	1/4	1/4
N	0	0	1/2

Table 4.2: Sampled high-symmetry k-points in the primitive cell of BCC reciprocal lattice.

with additional efforts to modify Phonopy for reading force data generated by LAMMPS. In phonon calculations, we duplicated a one-atom BCC primitive cell by 6×6×6 and exerted finite displacements to calculate induced forces. DFT calculations for phonon band structure converged till the energy difference was below 10^{-8}eV.

As shown in Figure 4.6, in which we refer experimental results for comparisons [195], the MEAM potential reproduces degenerates of phonon bands in the spectrum. It matches the DFT and experiments in long wavelength regime. Despite small deviations occur in the middle of the Γ-H branch, H point, the middle of H-P branch and N point, the MEAM can generally reproduce all phonon modes revealed by DFT and experiments.

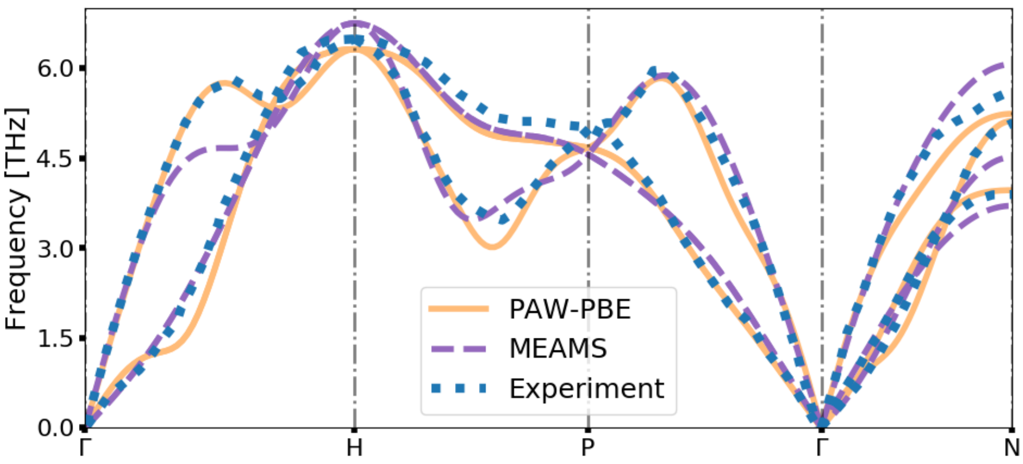

Figure 4.7: Nb phonon band structures obtained by the MEAM potential (MEAM), DFT (PAW-PBE) and experiments [195]

4.3.2.2 Pressure-volume curve and thermal expansions

Volumetric compression can show qualities of a MEAM potential in high "electron" density regime, which is related to the shape of the embedding function U(n). We measured static pressure variation in response to the volume change by the MEAM potential and DFT calculations. We used V_0 to denote the equilibrium volume at 0 K and V/V_0 for the volume change. As shown in Figure 4.8, where the MEAM potential accurately replicates the static pressure-volume relations obtained from DFT calculations. This match may result from that the fitting dataset incorporates atomic configurations under hydrostatic strains.

On the other hand, we measured thermal expansions of MEAM potentials at 1 atm pressure and temperatures from 0 K to 2500 K. We applied MD simulations in isothermal–isobaric (constant-NPT) ensemble to 12 × 12 × 12 conventional BCC supercell with 3456 atoms. The MD timestep was 1.0 femtosecond, and a Nose-Hoover barostat and thermostat were applied to maintain the target pressures and temperatures. We simulated the system in the constant-NPT ensemble for three nanoseconds, and we determined the lattice constant by averaging the frames in the last 0.3 nanoseconds. As shown in Figure 4.9, the

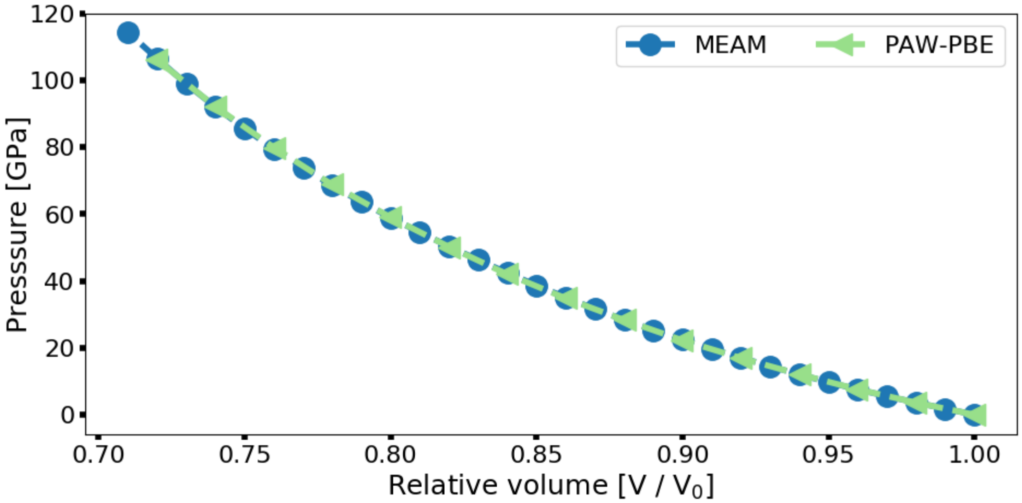

Figure 4.8: Nb 0K pressure-to-volume curve calculated by the MEAM potential and DFT.

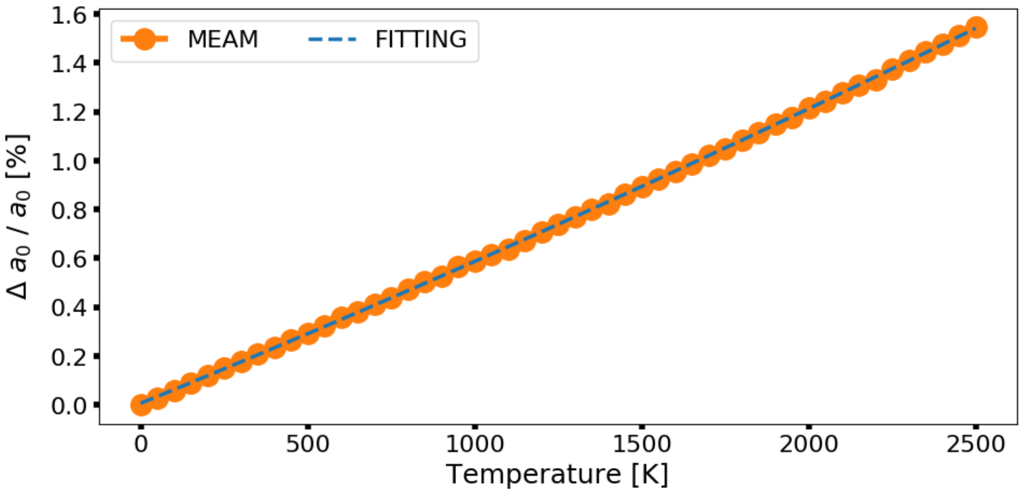

Figure 4.9: Nb thermal expansion curve from 0K to 2500 K by the MEAM potential calculations.

potential shows linear thermal expansions and it can be fitted by

$$\frac{\Delta a_0}{a_0} = 2.23 \times 10^{-10}T^2 + 5.59 \times 10^{-6}T + 6.28 \times 10^{-5} \tag{4.10}$$

The MEAM potential results show almost linear expansion characteristics (the quadratic term coefficient is much smaller than the linear term coefficient) the same as experiments. But its linear term coefficient is 5.59×10^{-6}, which is 19% smaller than linear expansion coefficients 6.96×10^{-6} reported by experiments [237]. The constant term is 6.28×10^{-5}, which is not exactly zero. This may come from statistical errors, and will not significantly affect the thermal expansion property shown by Figure 4.9.

4.3.3 Point defects

Due to a low capture cross-section for thermal neutrons, Nb is used in the nuclear industries for building neutron transparent structures [113, 172]. However, point defects commonly occur due to radiation damage in nuclear industries. We thus verified our MEAM potential on the formation and motion of point defects [117, 93, 104, 133].

4.3.3.1 Vacancy

We calculated single-vacancy formation energy $\mathrm{E}^{\mathrm{f}}_{\mathrm{vac}}$, its migration energy $\mathrm{E}^{\mathrm{m}}_{\mathrm{vac}}$ and the activation energy of vacancy diffusion $\mathrm{Q}_{\mathrm{vac}} = \mathrm{E}^{\mathrm{f}}_{\mathrm{vac}} + \mathrm{E}^{\mathrm{m}}_{\mathrm{vac}}$. We applied a $16 \times 16 \times 16$ conventional BCC supercell of 8192 atoms, and deleted one atom near the center of the supercell to generate a single vacancy. Energy minimization was performed by CG descent algorithm and the vacancy formation energy $\mathrm{E}^{\mathrm{f}}_{\mathrm{vac}}$ was measured by

$$\mathrm{E}^{\mathrm{f}}_{\mathrm{vac}} = \mathrm{E}^{\mathrm{vac}}_{\mathrm{tol}} - \mathrm{N}\mathrm{E}_{\mathrm{coh}} \tag{4.11}$$

where $\mathrm{E}^{\mathrm{vac}}_{\mathrm{tol}}$ is the optimized total energy of the system that contains a single vacancy. N is the total number of atoms in the supercell and $\mathrm{E}_{\mathrm{coh}}$ is the cohesive energy of BCC Nb.

Vacancy migration energy was determined by the maximum energy increment in the minimum energy path (MEP) of the vacancy migration. We applied the nudged elastic band (NEB) method [118] to search the MEP. Our NEB calculations were performed upon the $\langle 111 \rangle$ migration path, and its two ends were optimized equilibrium configurations before/after vacancy migration. We used eight interpolated images and a damped dynamics method [24] in the calculations. We listed the vacancy formation, migration and activation

Table 4.3: Single vacancy formation energy E^{f}_{vac}, migration energy E^{m}_{vac} and diffusion activation energy Q_{vac} in Nb [in eV] by the MEAM and DFT (PAW-PBE) calculations in this work (first three rows in the table). Results from previous empirical potentials and DFT calculations are also listed.

	E^{f}_{vac}	E^{m}_{vac}	Q_{vac}
MEAM	2.10	0.92	3.02
PAW-PBE	2.46	-	-
GGA-PBE [63]	2.72	0.55	3.27
EAM [63]	3.10	0.77	3.87
EAM [81]	2.88	0.97	3.85
EAM [104]	2.76	0.64	3.40
FS [93]	2.48	0.91	3.39
MEAM [18]	2.75	0.54	3.29
MEAM [133]	2.75	0.57	3.32

energies obtained by the MEAM potential and the reference data in Table 4.3. The 2.1 eV vacancy formation energy for the MEAM potential is 0.36 eV (14-15%) lower than the DFT calculation of 2.46 eV. The total diffusion activation energy of 3.02 eV is 0.25 eV (7-8%) lower than the DFT result of 3.27 eV [63]. Thus, although we did not apply any vacancy-relevant configurations in our DFT training data to replicate the coordinate environments of atoms near a vacancy, the MEAM potential shows acceptable transferability for the simulation of vacancy formation and migration in Nb.

4.3.3.2 Interstitials

We also assessed energies of interstitial point defects by the MEAM potential. There are six equilibrium self-interstitial configurations in BCC lattice due to symmetry as shown by Johnson [117]. The six configurations are $\langle 100\rangle$ split interstitial, $\langle 110\rangle$ split interstitial, $\langle 111\rangle$ split interstitial, activated crowdion, octahedral interstitial and tetrahedral interstitials, as shown in Figure 4.10. The interstitial energy can be defined as the energy increment of the interstitial structure compared with a corresponding perfect crystal lattice with the same number of atoms. Therefore, the interstitial formation energy ΔE^{f}_{int} can be

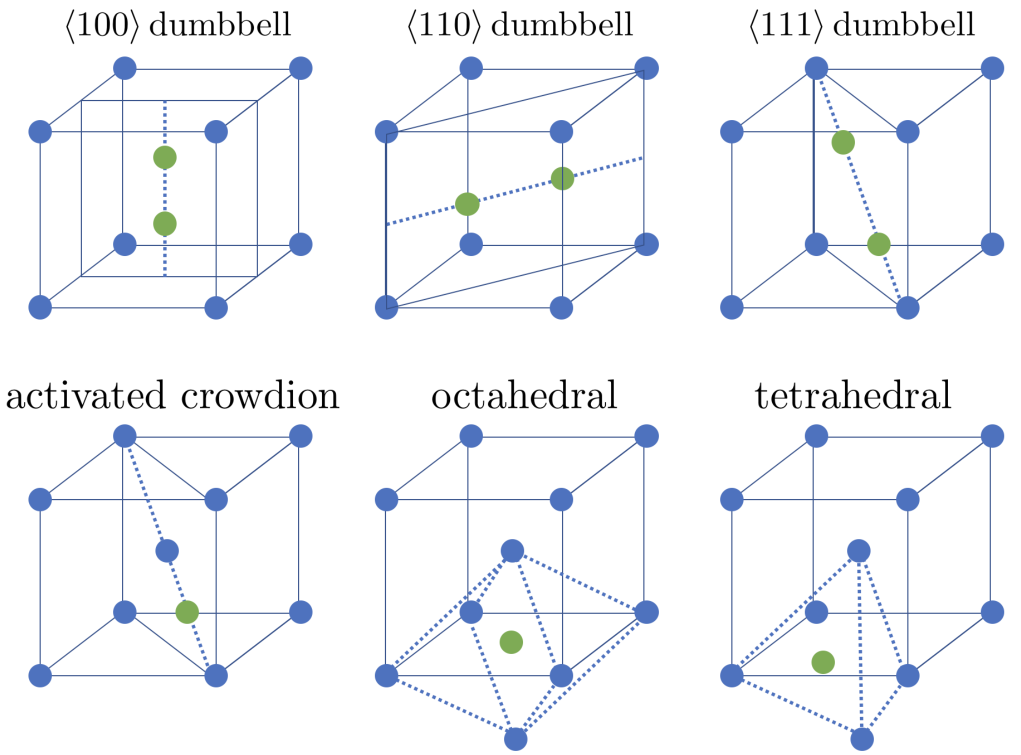

Figure 4.10: Schematic illustration of six interstitial configurations in BCC lattice.

measured by the form [115]

$$\Delta E^{f}_{int} = E^{ini}_{tol} - \frac{N+1}{N} E_{coh}$$

where E^{ini}_{tol} is the total relaxed potential energy of the system with N atoms occupying perfect lattice position and one interstitial atom. In our modular static implementation, we employed a 25 × 25 × 25 conventional supercell of 31250 atoms and inserted one extra atom to form a self-interstitial point defect. Interstitial formation energies for the six symmetric positions calculated by the MEAM potential are summarized in Table 4.4. We also list values obtained from DFT calculations [63], calculations based empirical potentials including EAM [63, 104], FS [200, 3, 93] and MEAM [133] potentials.

Compared with DFT calculations [63], the largest difference of self-interstitial formation energy for our MEAM potential is ∼15%, which occurs in the ⟨100⟩ split interstitial. The smallest difference is ∼3% for the ⟨110⟩ split interstitial. The differences are accept-

Table 4.4: Formation energies for the ⟨100⟩ dumbbell, ⟨110⟩ dumbbell, ⟨111⟩ dumbbell, activated crowdion, octahedral, and tetrahedral interstitials in Nb [in eV].

	E^f_{100}	E^f_{110}	E^f_{111}	E^f_{crd}	E^f_{oct}	E^f_{tet}
MEAM	4.02	4.43	4.18	4.18	4.41	4.12
GGA-PBE [63]	4.76	4.31	3.95	3.99	4.89	4.56
EAM [63]	4.50	3.83	4.09	4.02	4.36	4.37
EAM [104]	4.44	4.39	4.74	4.93	4.43	4.73
FS [200]	4.13	3.99	-	4.10	4.23	4.26
FS [3]	4.82	4.49	4.80	4.86	-	-
FS [93]	4.85	4.54	4.88	4.95	4.91	4.95
MEAM [18]	-	2.56	-	-	-	-

able, while our MEAM potential does not duplicate the lower-to-higher energy sequence among the six self-interstitial in the DFT. Our MEAM potential exhibits the most energetic favorable one is the ⟨100⟩ split interstitial, different from the DFT [63] that reveals the ⟨111⟩ has the lowest self-interstitial formation energy. Our MEAM potential shows formation energies for ⟨111⟩ split interstitial E^f_{111} and crowdion interstitial E^f_{crd} are similar, which is consistent with the DFT [63]. The DFT predicts the highest self-interstitial formation energy is in octahedral interstitial but the MEAM potential shows E^f_{oct} of octahedral interstitials similar to E^f_{110} of ⟨110⟩ split interstitial. In general, the MEAM potential may not be suitable for interstitial problems relying on the accurate energies of different types of interstitials. However, it should be reliable for the study of the general effects of self-interstitial defects since their average formation energies are close to DFT results. In addition, the differences between the MEAM potential and DFT calculations may also result from different supercell configurations used in each calculation method.

4.3.4 Surfaces, twin boundaries and generalized staking faults

Surface atoms have low coordination numbers so it can reflect robustness of a MEAM potential in the low “electron” density regime. Twinning and slip are primary deformation modes that characterize how the system deform beyond the elastic deformation. Accordingly, to examine the quality of the MEAM potential for application in 2D defects, we calculated energies of low-indexed surfaces, deformation twinning (DT) and the GSF.

4.3.4.1 Surface energies

We verified the $\{110\}$, $\{100\}$ and $\{111\}$ surface energies of Nb MEAM potential by MS and DFT calculations, and the MS calculations were based on a 24-layer-slab supercell with a 12-15 Å vacuum layer to create surfaces. The smearing, energy cutoff and k-point meshing in DFT calculations were the same as those for generating force dataset. As shown in Table 4.5, we compared Nb surface energies with previous calculations including DFT (generalized gradient approximation (GGA)-PBE) [63], EAM [63, 81, 104], FS [2], a long-range empirical potential (LREP) [42], MEAM [21, 133] as well as modified analytical embedded-atom method (MAEAM) [257].

Table 4.5: Low-index surface energies of BCC Nb [J/m^2]

	E_{surf}^{110}	E_{surf}^{100}	E_{surf}^{111}
MEAM	1.64	2.12	2.43
PAW-PBE	1.98	2.22	2.30
EAM [63]	2.04	2.36	2.47
GGA-PBE [63]	2.10	2.34	2.39
EAM [81]	1.81	1.97	-
EAM [104]	1.73	1.93	-
FS [2]	1.67	1.96	-
LREP* [42]	1.79	2.10	2.34
MEAM* [21]	1.87	2.79	2.02
MEAM [133]	2.49	2.72	2.92
MAEAM [257]	1.77	2.00	2.28

* indicates unrelaxed surface energies

As shown in Table 4.5, our MEAM potential exhibits the same lower-to-higher energy sequence as $E_{surf}^{110} < E_{surf}^{100} < E_{surf}^{111}$ as the DFT results. The largest difference between the MS and DFT occurs in the $\{110\}$ surface since the MEAM potential underestimates the $\{110\}$ surface energy by 17% than the DFT results. For the $\{100\}$ and $\{111\}$ surfaces, the MEAM potential shows less than 5% differences with the DFT. It was difficult to improve the energy difference among the $\{110\}$, $\{100\}$, and $\{111\}$ surfaces, as we did not include any surface or vacancy in fitting dataset such that the potential could not reproduce the exact low "electron" density of the DFT. We consider the 17% differences in $\{110\}$ surface is acceptable regarding of surface energies measured by referred empirical potentials. In general, the potential can serve to study mechanical problems that incorporate surfaces. Due to the 17% difference of $\{110\}$ surface energies between the MEAM and the DFT results, the MEAM potential may result in artificial effects to study problems that demand accurate surface energies specifically.

4.3.4.2 Deformation twinning

Deformation twins form by a homogeneous simple-shear of the parent lattice, which corresponds to highly coordinated individual atomic displacements, in contrast to the chaotic slip band generations and growths [35]. Deformation twinning was observed in polycrystalline Nb under low temperature and high strain-rate loading conditions [5], and the activation energy to nucleate a deformation twin is higher than to initiate a dislocation slip [35, 176]. Compared with Fe, Nb is less inclined to form deformation twinning since a deformation twinning requires an above-critical stress concentration on the head of a rapidly piled-up array of dislocations produced by a burst of slip [5]. Initial formation of the first layer of a twin is more difficult than the subsequent growth of twin layers since the area of misfit between a twin and matrix stays invariant during the twinned growth [40]. Once a deformation twin is nucleated, it can instantly generate substantial inelastic strain since the growth of twins has low energy barriers. Therefore, in BCC, the twinning formation energy dominates mechanical behaviors under low-temperature, large-strain rate conditions.

We calculated the twinning formation energy by DFT and the MEAM potential by applying a 24-layer-slab supercell of three basis vectors $\mathbf{e_1} = a_0/2[111]$, $\mathbf{e_2} = a_0[011]$ and $\mathbf{e_3} = a_0[211]$. The twinning formation energy was obtained by measuring energy increment between a reference matrix and a matrix-twinning-matrix sandwich structure. The twinning elements in BCC metals was experimentally verified by Paxton et al. [181], and we built a

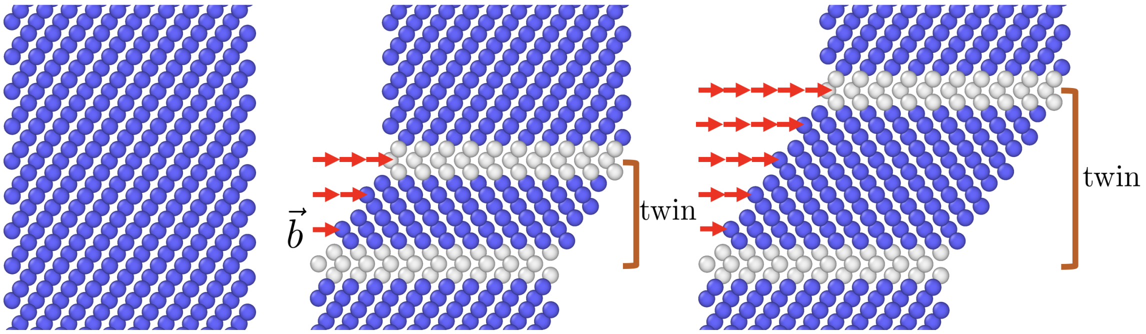

Figure 4.11: Schematic illustration of deformation twinning pathway. A single red arrow indicates one $\langle 111\rangle$ Burgers vector magnitude. Atoms are visualized by the software OVITO [227] with color assigned by common neighbor analysis. Blue corresponds to BCC crystal and white corresponds to defects.

$\langle 111\rangle$ $(2\overline{1}\overline{1})$ deformation twinning [176]. The twinning pathway was shown in Figure 4.11. Our DFT calculation shows for Nb a single twin boundary formation energy $\mathrm{E}^{\mathrm{f}}_{\mathrm{twin}}$ is 273.94 mJ/m^2 and the MEAM potential shows $\mathrm{E}^{\mathrm{f}}_{\mathrm{twin}}$ is 292.50 mJ/m^2, which just deviates 6-7% from the DFT result. Therefore, the potential is useful in low-temperature, large-strain rate conditions where deformation twinning may occur, for example, the onset of deformation twinning nucleation from a crack tip.

4.3.4.3 Generalized stacking faults (GSF)

GSF energy (γ-surface) is a function of energy increment as displacing two parts of a crystal relative to each other along a crystal plane, and it aims to study the existence of stacking faults in BCC metals [246]. Since GSF is related to screw dislocation core properties and the non-Schmid behavior in BCC metals [51], we calculated GSF using the MEAM potential and DFT to validate the performance of the MEAM potential to simulate the slip along the closed packed direction in BCC.

We calculated GSF energy by shifting the equilibrium BCC crystal along $\langle 111\rangle\{211\}$ and $\langle 111\rangle\{110\}$ slip system, and the calculations were based on a 24-layer-slab supercell for the $\{211\}$ slip and a 12-layer-slab for the $\{110\}$ slip. To measure the γ-surface, we

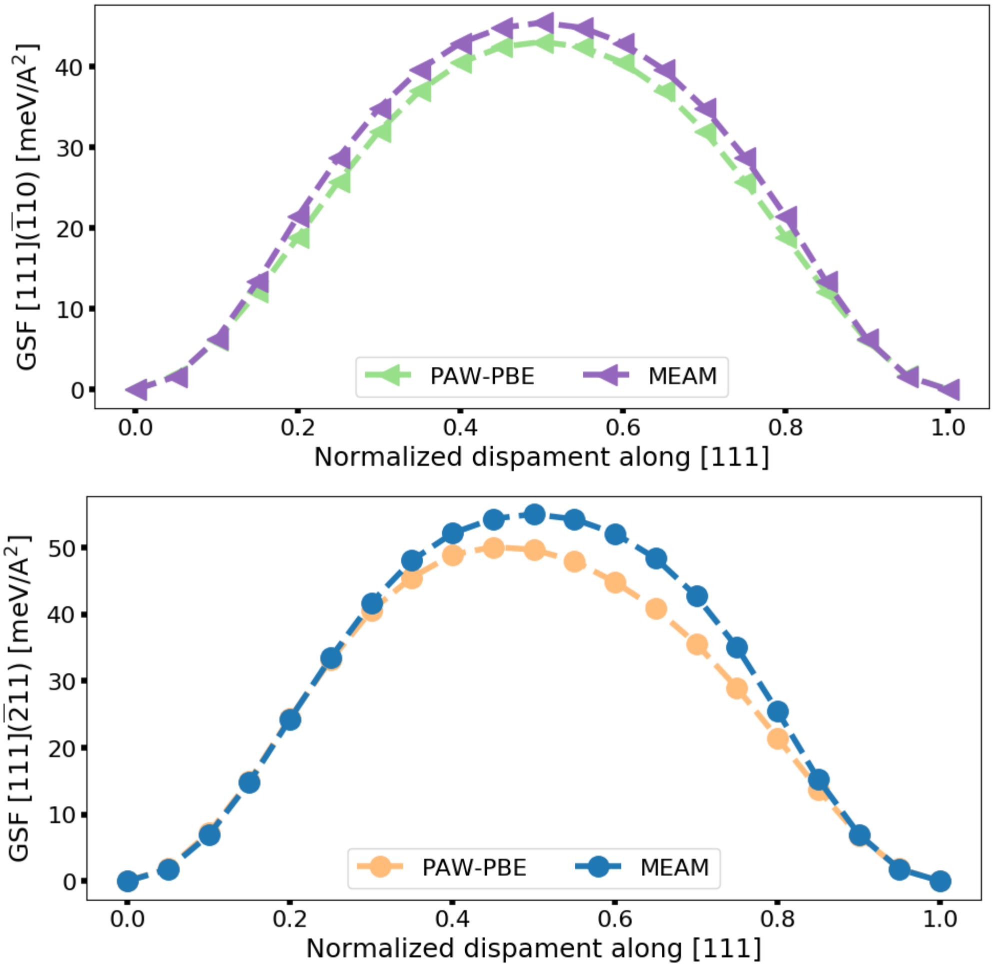

Figure 4.12: Generalized stacking fault energies obtained by the Nb MEAM potential and DFT calculations along $[111](\bar{1}10)$ and $[111](\bar{2}11)$ slip.

allowed each atom to relax only perpendicular to the fault plane since the displaced configurations were energetically unstable and a full relaxation of three directions would eliminate the stacking fault. The $\langle 111\rangle\{211\}$ and $\langle 111\rangle\{110\}$ GSF calculated from DFT and MEAM potential are shown in Figure 4.12. The MEAM potential reproduces the shapes of GSF energy curves consistent with the DFT calculations. There is no local minima in the $\langle 111\rangle\{211\}$ and $\langle 111\rangle\{110\}$ GSF for both the MEAM and DFT calculations, therefore, no metastable stacking faults exists. This is consistent with that in BCC metals a full $\langle 111\rangle$ dislocation cannot dissociate into partial dislocations. For the $\langle 111\rangle\{211\}$ GSF, the maximum energy in MEAM potential is 54.9 meV/Å^2, which deviates 9-10% from

50.0 meV/Å^2 in the DFT. For the $\langle 111\rangle\{110\}$ GSF, MEAM potential shows the maximum energy is 45.4 meV/Å^2, differing 5-6% from 43.1 meV/Å^2 in the DFT. The MEAM reproduces the fact that the $\langle 111\rangle\{211\}$ unstable stacking fault energy (USFE) 53.9 meV/Å^2 is larger than USFE in $\langle 111\rangle\{110\}$ which is 45.4 meV/Å^2. Since the DFT dataset does not include any slip or GSF configurations, the MEAM potential shows a potential based on fitting intrinsic deformation properties can be extended to study slip and dislocations.

4.3.5 Ideal strengths

The ideal strength, as a consequence of bonding and electronic structures, reveals the intrinsic mechanical behavior of materials under strain that is far beyond linear elastic regime [197, 210]. To examine intrinsic mechanical behaviors, we applied ideal strength test on the Nb MEAM potential.

4.3.5.1 Ideal tensile strengths

As shown in Figure 2.3, the ideal tensile deformation was applied by fixing tensile engineering strain along the x-direction and relaxing other strain components of the supercell so that $\sigma_{\mathrm{ij}} = 0$ (except σ_{xx}) [210, 197, 265]. In the TP we constrained the calculation supercell to conserve tetragonal symmetry by using a two-atom normal BCC unit cell. In the OP we employed a four-atom supercell to release additional tetragonal constrain on the system. During ideal tensile deformation, we increased 2% tensile strain ($\varepsilon_{\mathrm{xx}}$) for each run and performed Broyden-Fletcher-Goldfarb-Shanno (BFGS) method to optimize external strain matrix until that the absolute value of all stress components, except σ_{xx}, $<$ 0.05 GPa. In BCC transition metals, the nearest extremes of the total energy variation during the ideal tensile deformation along $\langle 100\rangle$ TP is a maximum point that corresponds to a FCC structure (so-called Bain path) [128, 209]. However, for Nb, in $\langle 100\rangle$ OP, an elastic shear on the $\{211\}$ plane occurs before the inflection point in the TP. The failure is intrinsically triggered by an elastic shear along the $\langle 111\rangle\{211\}$ [148, 197, 265]. This

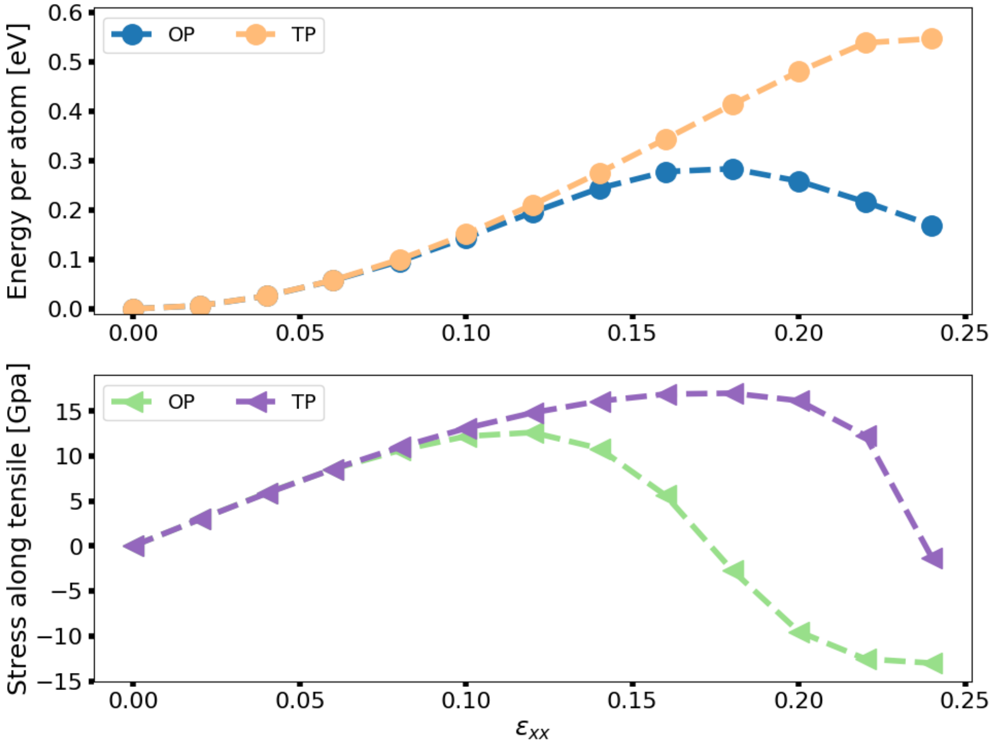

Figure 4.13: The curves of energy and tensile stress in response to ideal tensile strain along [100] direction, calculated by DFT using a PAW-PBE pseudopotential.

tetragonal-to-orthorhombic shear originates from shifts of electron band structures and induces a significant decrease of the ideal tensile strength [197]. Our ideal tensile of Nb by

Table 4.6: Maximum stress, the corresponding critical strain and elastic modulus $E_{\langle 100\rangle}$ defined in Equation 4.12 in $[100]_{BCC}$ ideal tensile along TP and OP [197, 265] by MEAM potential and DFT calculations

Stresses	PAW-PBE		MEAM	
in [GPa]	OP	TP	OP	TP
$\sigma^{m}_{\langle 100\rangle}$	12.6	17.0	13.8	17.5
$\varepsilon^{m}_{\langle 100\rangle}$	0.12	0.18	0.10	0.16
$E_{\langle 100\rangle}$	158	158	155	155
$\sigma^{m}_{\langle 100\rangle}$ / $E_{\langle 100\rangle}$	0.08	0.11	0.09	0.11

DFT and MEAM potential calculations are shown in Figure 4.13, Figure 4.14 and Table 4.6. Both our DFT and MEAM potential calculations show the tetragonal-to-orthorhombic shear occurs when the tensile strain ε_{xx} is 0.10, where the energy and stress along tensile

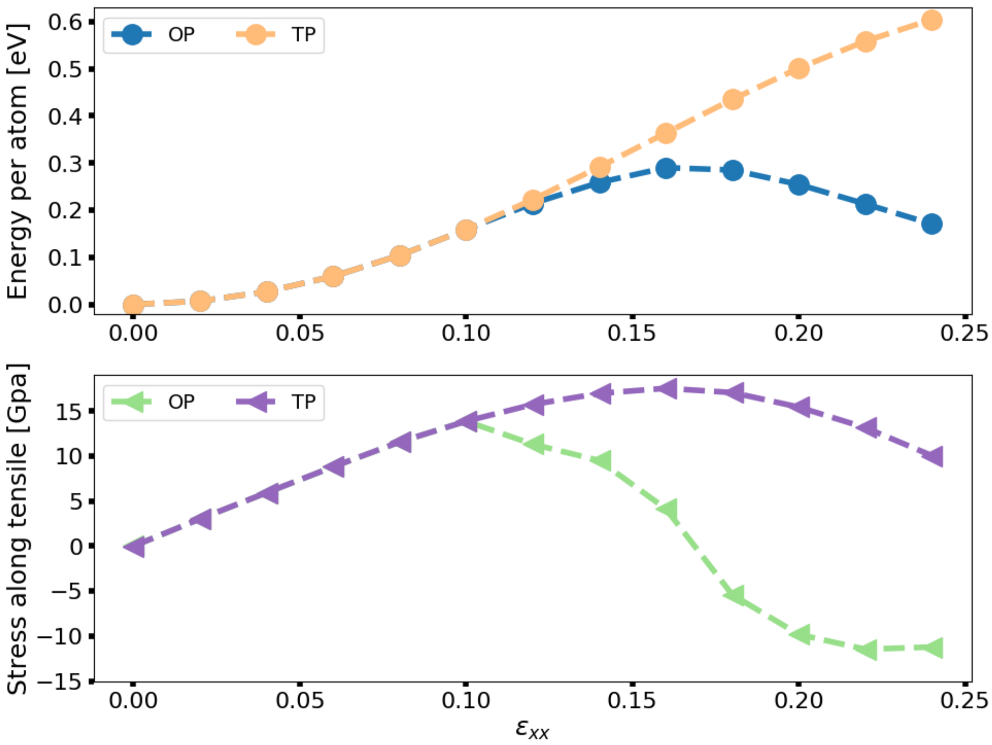

Figure 4.14: The curves of energy and tensile stress in response to ideal tensile strain along [100] direction, calculated by MS with the Nb MEAM potential.

direction drop significantly along OP. The relaxed tensile modulus along $\langle 100\rangle$ [148, 128] is estimated as

$$E_{\langle 100\rangle} = \frac{(C_{11} + 2C_{12})(C_{11} - C_{12})}{(C_{11} + C_{12})} \tag{4.12}$$

where C_{11} and C_{12} are elastic modulus. As shown in Table 4.6, the maximum tensile stress of TP and OP and the relaxed tensile modulus calculated from MEAM are less than 5% deviation from the DFT. The maximum stress in OP occurs at $\varepsilon_{\langle 100\rangle} = 0.10$ from MEAM simulations, 0.06 before the $\varepsilon_{\langle 100\rangle}$ that corresponds to the maximum stress in TP. This difference of the critical strain in OP and TP paths is identical to the DFT results that shows in OP the maximum stress occurs 0.06 of $\varepsilon_{\langle 100\rangle}$ before the maximum stress occurs in TP. Therefore, the MEAM potential reproduces the inherent ESI in Nb.

4.3.5.2 Ideal shear strengths

We calculated the $\langle 111\rangle\{110\}$ and $\langle 111\rangle\{211\}$ ideal shear strength by the MEAM potential and DFT based on one-atom BCC primitive cell. We applied the true strain [209] and determined the stresses by the DFT Hellmann-Feynman stresses and virial stress tensor [234] generated by the MEAM potential. Applied shear strain increased 2% for each run, and BFGS optimization was utilized on strain components except for the fixed shear strain component until the system evolved to its minimum energy state [148].

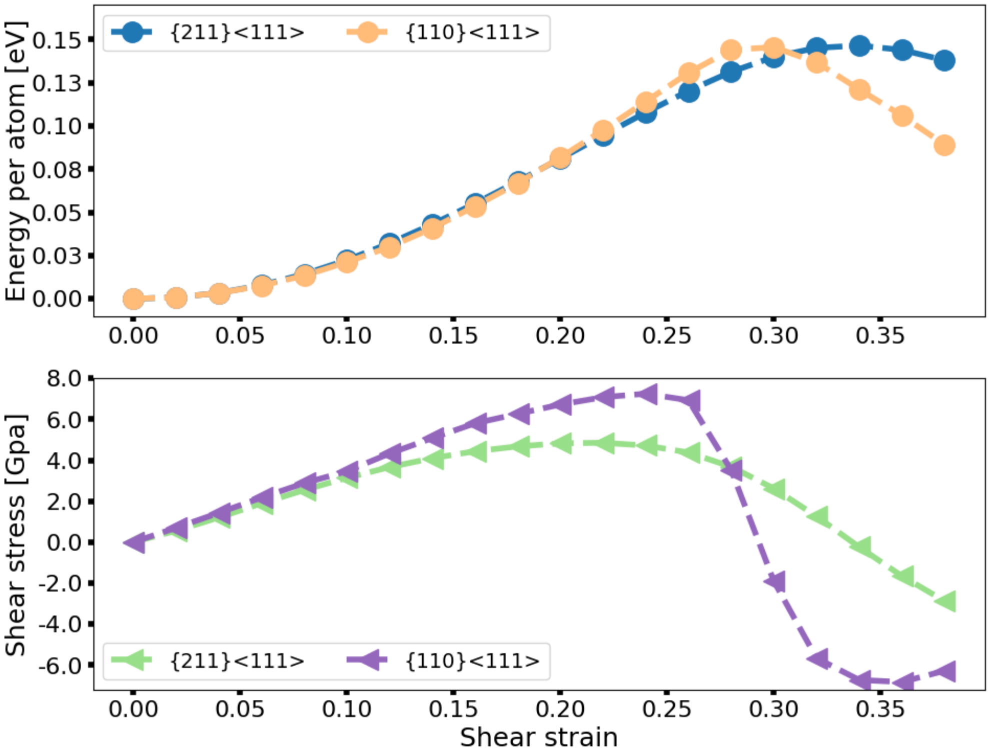

Figure 4.15: Energy and shear stress of ideal shear by MS with the Nb MEAM potential.

As shown in Figure 4.15 and Figure 4.16, the maximum energy during both $\langle 111\rangle\{110\}$ and $\langle 111\rangle\{211\}$ shear deformation in the MEAM potential calculations is the same as 0.15 eV, which exactly matches the DFT calculations. The MEAM potential calculations exhibit that the maximum energy during shear deformation in both slip systems corresponds to the tetragonal saddle-point structure, which is a stress-free tetragonal structure that defines a saddle point in the strain-energy surface [148]. Consistent with DFT calculations, the

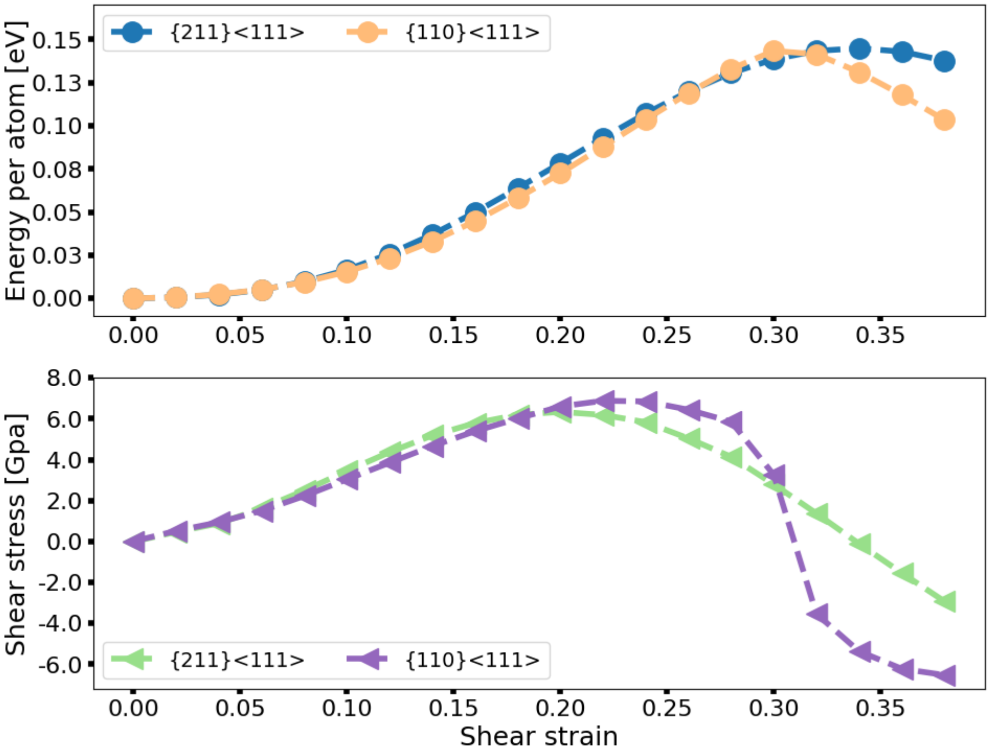

Figure 4.16: Energy and shear stress of ideal shear calculated by DFT with PAW-PBE pseudopotential.

MEAM potential unveils that the $\langle 111\rangle\{110\}$ shear reaches its saddle point sooner than the $\langle 111\rangle\{211\}$ shear due to the difference of relaxations of the two slipped structures [148]. Moreover, similar to DFT calculations, the MEAM potential calculations exhibit that the stress-strain curves for ideal shear deformation in two slip systems are the same in small strain regime, and their slopes were related to the relaxed shear modulus [209, 148, 128]

$$G_{\{110\}\langle 111\rangle} = G_{\{211\}\langle 111\rangle} = \frac{3C_{44}(C_{11} - C_{12})}{C_{11} - C_{12} + 4C_{44}} \tag{4.13}$$

where C_{11}, C_{12} and C_{44} are elastic constants.

In high strain regime, the MEAM potential calculations show the stress-strain curve of $\langle 111\rangle\{211\}$ system reaches its peak at shear strain ∼0.22, consistent with 0.20 of our DFT calculations and 0.20 in previous work [148] that shows for $\langle 111\rangle\{211\}$ shear in Nb deviates from the sinusoidal shape toward a higher strain. The same as our DFT results,

Table 4.7: Maximum stress, the corresponding critical strain and elastic shear modulus $G_{\langle 111\rangle}$ defined in Equation 4.13 of ideal shear deformation along $\{110\}\langle 111\rangle$ and $\{211\}\langle 111\rangle$ obtained by the MEAM and DFT PAW-PBE calculations.

Stresses	PAW-PBE		MEAM	
in [GPa]	{211}	{110}	{211}	{110}
$\tau^{m}_{\langle 111\rangle}$	6.3	6.9	4.9	7.2
$\varepsilon^{m}_{\langle 111\rangle}$	0.20	0.22	0.22	0.24
$G_{\langle 111\rangle}$	36	36	36	36
$\tau^{m}_{\langle 111\rangle}$ / $G_{\langle 111\rangle}$	0.18	0.19	0.14	0.20

the stress-strain curve of $\langle 111\rangle\{110\}$ shear in the MEAM potential calculations starts to deviate from $\langle 111\rangle\{211\}$ shear before it reaches its saddle point, and the $\langle 111\rangle\{110\}$ shear evolves to a higher shear strength. The MEAM calculations shows the maximum shear stress in $\langle 111\rangle\{211\}$ is 4.9 GPa, which is $\sim$20% lower than the DFT result. In general, the MEAM potential reproduces the features of $\langle 111\rangle\{211\}$ and $\langle 111\rangle\{110\}$ ideal shear deformation in Nb consistent with DFT calculations.

4.3.6 Screw dislocation cores

Screw dislocation dominated plastic deformations in BCC metals. A temperature and strain-rate dependent plastic flow are due to high lattice resistance of screw dislocation so that the movement of screw dislocations in BCC is thermally activated to overcome the Peierls barriers [11]. Solid solution hardening solid solution hardening (SSH) and solid solution softening (SSS) in BCC are due to the interaction between solid solutes with screw dislocations and changes of Peierls barriers induced by increasing/decreasing valence electrons [154]. In addition, the violations of Schmid's law are also widely observed in BCC metals [255, 47]. The non-Schmid effects originate from that the movement of the screw dislocation in BCC is affected by stress components beyond the resolved shear stresses [80]. We thus calculated the structure and motion of screw dislocation to verify whether the screw dislocation simulated by this MEAM potential can have these characteristics.

4.3.6.1 Dislocation Core structures

In BCC crystal, there are two types of screw dislocation core structures. A compact screw dislocation core structure (non-degenerate) presents a full D_3 symmetry in the $\{111\}$ zone. A polarized core (degenerate) exhibits C_3 symmetry and it has two degenerate structures related along the $\langle 110\rangle$ diad [51]. DFT studies evidenced that all BCC pure metals have non-degenerate core structures without external stress [51, 65, 244]. The core configuration may evolve from non-degenerate to degenerate due to changes of electron band structures that can be induced by applied stresses or alloying [11, 154].

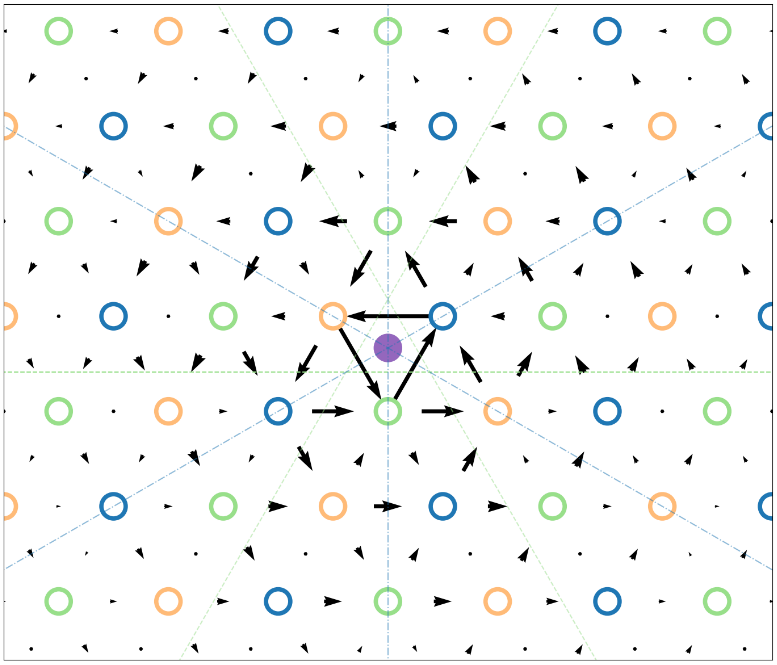

Figure 4.17: Equilibrium screw dislocation core structure given by the MEAM potential calculation. Arrows indicate the differential-displacement of atoms along the [111] Burgers vector direction [247].

To simulate a single screw dislocation core under zero external stress, we applied a cylindrical slab oriented as the x-axis along $[1\bar{2}1]$, y-axis along $[\bar{1}01]$ and z-axis along [111]. The cylindrical slab had a radius of ~30 nm and a thickness of ~2 nm. We generated the dislocation by the anisotropic elasticity screw displacement field [226, 98], and we implemented periodic boundary conditions (PBC) along the z-direction to make an infinitely long straight screw dislocation. We fixed atoms in several outer layers of the slab at initial positions during MS. The characterization of the screw core by the differential displacement map [247] is shown in Figure 4.17. In Figure 4.17, atomic coordinates are projected onto the (111) plane normal to the viewing direction and the differential displacement (DD) map for this dislocation core is also plotted [247]. Circles of different colors represent atoms in three successive (111) layers, and the same color denotes atoms in the same stacking layer. Three longest arrows in the center for the DD map correspond to the relative displacement vector $a_0/6[111]$, and together they form a $a_0/2[111]$ screw. Around any circuit that encompasses the dislocation core, the net sum of the arrows is equal to the length of 1/2[111] Burgers vector. Relaxed by the MEAM potential, the screw dislocation core is non-degenerate, invariant to the [111] threefold screw axis and the 1/2[101] diad, the same as the DFT results [256].

4.3.6.2 Dislocation core energy

We calculated the energy of a straight screw dislocation per unit length using the MEAM potential. The dislocation energy is consisted of atomistic dislocation core energy E_{core} and elastic energy E_{elas} [19, 98]

$$E_{tot} = E_{core} + \alpha \ln \frac{R}{r_0} \tag{4.14}$$

α is dislocation prelogarithmic energy factor. R is outer cutoff and r_0 is defined as inner cutoff. r_0 is artificially defined dislocation core radius, and in convention it is from 1 to 4 $|\mathbf{b}|$. We calculated the dislocation core energy by various outer cutoffs. As shown in Figure 4.18, the dislocation core energy as a function of R can be represented by $r_0 = 2|\mathbf{b}|$ as

$$E_{tot} = 0.3667[\mathrm{eV/Å}] + 0.1637 \ln \frac{R}{r_0} \tag{4.15}$$

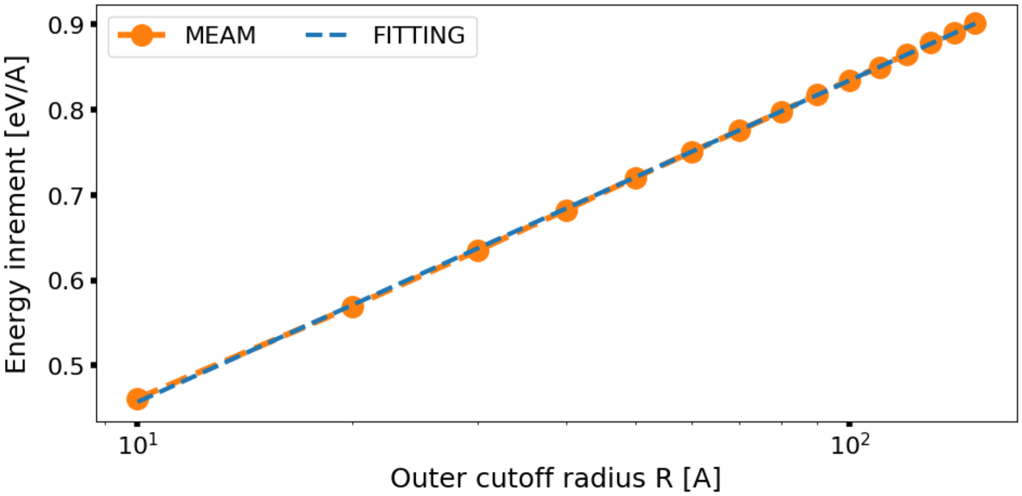

Figure 4.18: Dislocation core energy calculated by the MEAM potential.

The dislocation prelogarithmic energy factor in continuum mechanics solution is [226, 19]

$$\alpha = \frac{\mathrm{b_i K_{ij} b_j}}{4\pi} \tag{4.16}$$

where $\mathrm{K_{ij}}$ is the energy coefficient tensor obtained by solving a six-dimensional framework by Stroh [226], and the $\mathrm{b_i}$ is i-th component of Burgers vector. Based on elastic constants calculated by the MEAM potential as listed in Table 4.1 and Equation 4.16, α is 0.1651 eV/Å, which is consistent with the value 0.1637 eV/Å in our fitting results. Thus, the MEAM potential can show the relaxed screw dislocation energy amounts to the superposition of a core energy and linear elastic energy.

4.3.6.3 The Peierls barrier

For the migration of the screw dislocation core in the MEAM potential calculations, we measured dislocation trajectory [244] and the energy barrier (the Peierls barrier) in the MEP of a screw dislocation core moving from one equilibrium position (the Peierls valley) to an adjacent equilibrium position. To avoid surface, we applied a dislocation dipole setup [142, 111], as shown in Figure 4.19, a 231-atom supercell dipole configuration based on the periodic boundary condition image sum formula [31]. Using three basis vectors are $\mathbf{e_1} = a_0[11\bar{2}]$, $\mathbf{e_2} = a_0[\bar{1}10]$ and $\mathbf{e_3} = a_0/2[111]$, three edges of the supercells are defined as $\mathbf{h_1} = 7\mathbf{e_1}$, $\mathbf{h_2} = 3.5\mathbf{e_1} + 5.5\mathbf{e_2} + 0.5\mathbf{e_3}$ and $\mathbf{h_3} = \mathbf{e_3}$. We applied the NEB method with 19 images to find the minimum energy path for a [111] screw dipole gliding in a $\{110\}$ plane. The initial configurations were generated by interpolating initial and final configurations of a screw dipole translating from a stable core position to an adjacent stable core position.

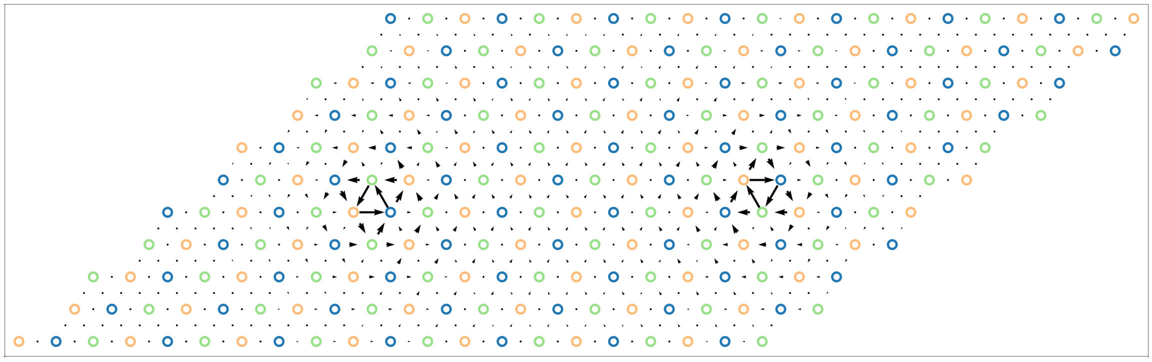

Figure 4.19: Schematic representation of the unit cell and periodicity vectors within the quadrupolar arrangement [142, 111]. Atomic belong to three different $\langle 111 \rangle$ planes in BCC crystal are represented by three different colors. The dislocation dipole is visualized by its differential displacement map.

Dependent on the direction of the screw Burgers vector, or the orientation of the triangle formed by the three $\langle 111 \rangle$ columns near the core center, there exist two types of cores by centering the dislocation in three $\langle 111 \rangle$ atomic columns: easy core (E) and hard core (H) [111, 256, 244, 46, 47], as shown in Figure 4.20. An easy core is a stable dislocation configuration where the chirality of $\langle 111 \rangle$ columns is reversed. A hard core is a metastable or unstable dislocation configuration where the $\langle 111 \rangle$ columns are at the same level. We can also denote a middle point position (M) in the middle between two easy core positions and a split core position (S) by the midpoint in the linear extrapolating between a hard core position and a middle point position [111, 47].

By applying the NEB method on the dislocation dipole setup, we can identify additional metastable states along the path of dislocation movement, which may not be revealed by a

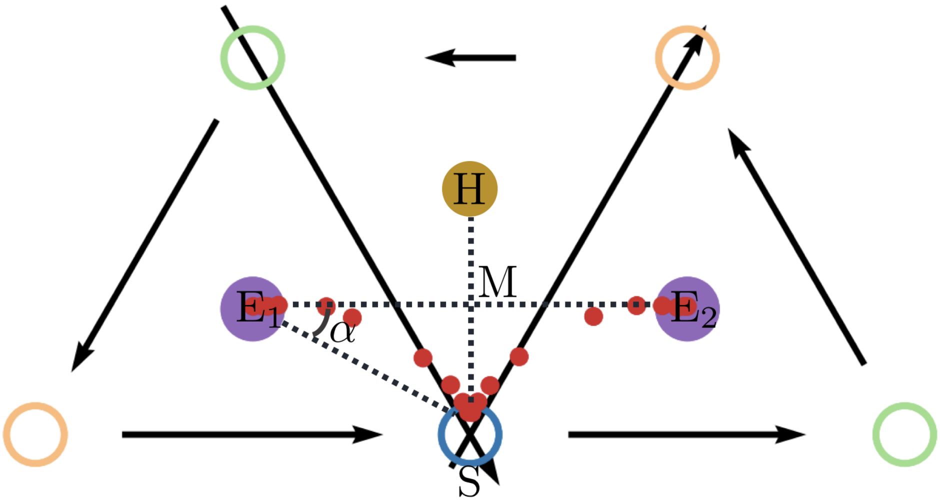

Figure 4.20: Screw dislocation trajectory of moving from one easy core to an adjacent easy core. E: easy core, H: hard core, S: split core, M: the middle point between two easy cores. The red dots are the dislocation core positions extracted from the cost-function method based on Equation 4.17 [244].

drag method [94] in which the reaction coordinate used is the vector from the initial to the final position for the dipole or by the NEB method upon an isolated dislocation [256]. If the Peierls barrier shows a "double-humped" shape with a local minimum between adjacent Peierls valleys, the hard core or split core configuration is metastable. On the other hand, the Peierls barrier becomes "single-humped" and neither of the intermediate configurations is metastable [111]. As shown in Figure 4.21, our MEAM potential exhibits a single hump along the MEP so that neither the hard core or split core is stable, which agrees with the DFT results [256]. Moreover, the Peierls barrier from the MEAM potential for a dislocation dipole is 58.13 eV/b (b is the length of the Burgers vector), which only deviates 1-2% from 59.25 eV/b by the DFT [256] (based on the same VASP and PAW type pseudopotentials with PBE exchange-correlation functional as employed in present work).

To show the dislocation trajectory in the movement along the minimum energy path, we determined the dislocation core position with a cost-function method [244], which was upon the difference between the Volterra field solution of periodic distribution of dislocation dipoles and the configuration of each NEB calculation image based on the MEAM potential. Denoting (x_1, y_1) and (x_2, y_2) as centers of the two dislocations in the the dislo-

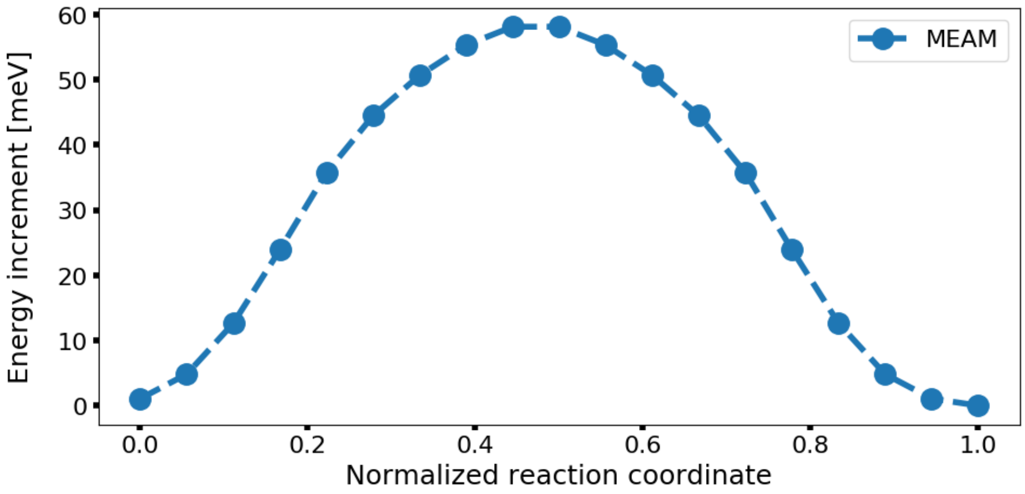

Figure 4.21: The energy path of the infinite straight screw dipole moving between adjacent easy core positions in (110) plane by the NEB calculations based on the MEAM potential.

cation dipole setup, the cost function is

$$C(x_1, y_1, x_2, y_2) = \sum_{i=1}^{N}(\delta_i^{MEAM} - \delta_i^{ELAS(x_1,y_1,x_2,y_2)})^2 \tag{4.17}$$

The calculation loops over the displacement field of N atoms in the five most displaced $\langle 111 \rangle$ atomic columns. $\delta_i^{ELAS(x_1,y_1,x_2,y_2)}$ is the anisotropic elastic displacement of each atom i induced by the dislocation dipole (positioned at (x_1, y_1) and (x_2, y_2)) and its periodic images along the x and y directions. δ_i^{MEAM} is the displacement of each atom i obtained by the NEB calculations using the MEAM potential. For each NEB image frame we obtained dislocation core positions (x_1, y_1) and (x_2, y_2) of two dislocations in the dislocation dipole by minimizing Equation 4.17. We recorded the positions of one dislocation core (x_1, y_1), as shown by the red dots in Figure 4.20. The positions of the other dislocation core (x_2, y_2) is symmetrically equivalent and not plotted here.

In Figure 4.20, the black arrows represent DD map near the saddle point of the transition when the dislocation core position is in between the middle point of two easy cores (M) and split-core point (S), consistent with Figure 2 in previous work [111], and red points are dislocation trajectories by minimizing the quadratic cost function method in Equation 4.17 [244]. The dislocation trajectory deviates towards the split core from a straight line that connects two easy cores, and it is well consistent with DFT calculations [47]. The MEAM potential shows the maximum deviation occurs in half of the path when the dislocation is in the saddle state that corresponds to the maximum energy in the Peierls potential. This saddle state is reached when the dislocation crosses the line connecting the hard and split core positions (so-called the "hard-split line"). We use the angle α to characterize the deviation of a dislocation core migration path from the straight line connecting two easy cores (so-called the "easy-easy line"), as shown in 4.20. The maximum deviation angle α from the MEAM potential calculation is 25.3°, which only deviates 3.6° from the DFT calculations [47]. The screw dislocation trajectory is important to accurately describe plastic anisotropy and non-Schmid effect in BCC metals, since the twinning (T) and anti-twinning (AT) asymmetries are linked to how the dislocation trajectory deviates from the $\{110\}$ slip plane [47]. Applying the Schmid law to the actual dislocation trajectory can generate the predictions of T/AT asymmetries that qualitatively agree with experiments and DFT calculations of Peierls stress [47]. Therefore, our MEAM potential is a good candidate to study dislocation behaviors and mechanical problems that are related to plastic anisotropy and non-Schmid effect in BCC Nb.

4.3.7 Simulations of crack evolution under tensile loading

We applied MD tensile simulations on crack evolution in bulk Nb to investigate whether our MEAM potential can correctly describe the ductility behavior of Nb. In comparison, we also employed the MD tensile test with the same setup with a Mo MEAM potential[179]. [100] ideal tensile strength calculations based this Mo potentials suggest that elastic shear instability (ESI) is not preferred over cleavage during the ideal tensile test consistent with DFT results[197, 148]. As shown in Figure 4.22, the energy and tensile stress ideal tensile generated by the Mo MEAM potential agree with DFT results of ideal tensile stress-strain curves along TP and OP[197, 148]. Thus, both the empirical potentials and DFT calculations suggest that Nb is intrinsically ductile but Mo is intrinsically brittle. The next question is whether large-scale atomistic simulations can describe their difference in ductility, which is the main topic of this subsection.

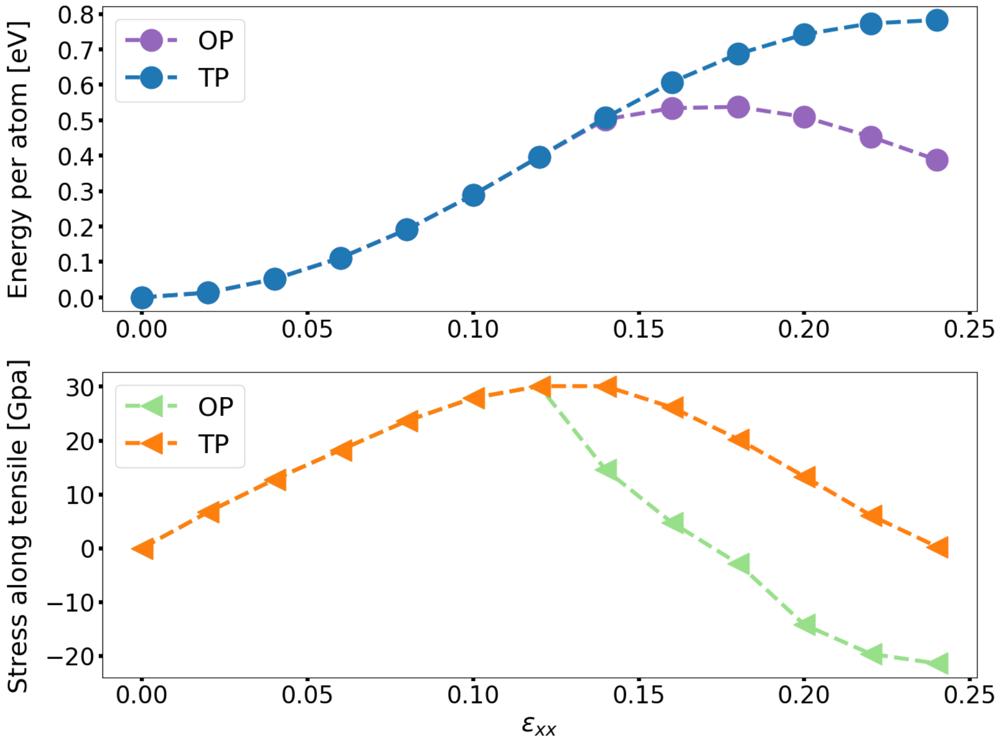

Figure 4.22: Energy and tensile stress in response to ideal tensile strain along [100] direction from MS calculations using the Mo MEAM potential [179].

The simulation box contained 539580 atoms and was oriented as x-axis || [110], y-axis || [001] and z-axis || [1$\bar{1}$0]. It has the dimension of approximately 470 Å × 460 Å × 470 Å for Nb and 450 Å × 440 Å × 450 Å for Mo, respectively. The periodic boundary condition was applied along the three axes. A microcrack was created by cutting a layer of (001) atoms in a width of 50 Å in the center of the simulation box, and the microcrack was periodic along the z-axis. The simulation started in the NPT ensemble with zero pressure to increase the system temperature to 300 K, then a tensile loading along [001] was applied on the system simulated in the NVT ensemble with a constant tensile strain rate is 5×7 s^{-1}.

Figure 4.23 shows the tensile stress-strain curve during the MD tensile test on the mi-

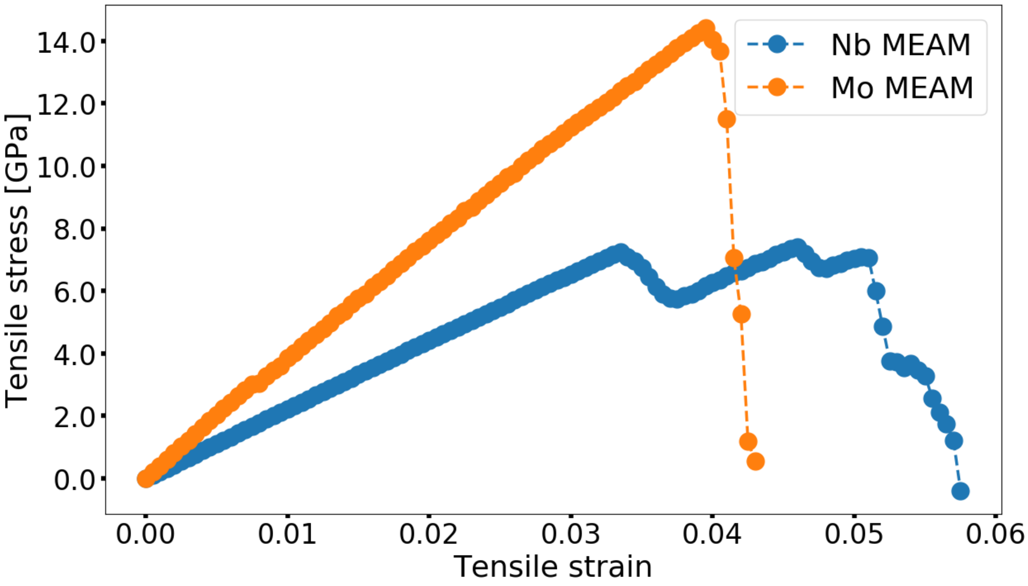

Figure 4.23: The stress-strain curve of [001] tensile on the BCC crystal bulk with a microcrack from MD simulations using Nb and Mo MEAM potential, respectively.

crocrack configurations. The maximum tensile stress is 7.2 GPa and 14.4 GPa for using the Nb MEAM and Mo MEAM potentials, respectively. Both of the maximum stress values are approximately 50% of the corresponding [001] ideal tensile strength in DFT calculations[197]. The critical strain corresponding to the maximum tensile stress is 0.0335 for the Nb MEAM result, which is 85% of the critical strain 0.0395 for the Mo MEAM result. This ratio between critical strains is similar to the ratio of the critical strains for Nb and Mo in the DFT ideal tensile calculations[197].

Since both MEAM potentials are generated from DFT calculations, our MD $\langle 100 \rangle$ tensile on BCC bulk crystal of microcrack show a correlation between the DFT ideal tensile and MD tensile simulations. The tensile stress has a significant drop at the critical strain for the Mo MEAM, which indicates the possible propagation of the preexisting microcrack as the brittle deformation. In comparison, the tensile stress generated by the Nb MEAM potential fluctuates after the maximum tensile stress, which indicates the dislocation nucleation and propagation as the ductile deformation.

Figure 4.24 shows the atomistic structure evolution during the initial stage of the plastic

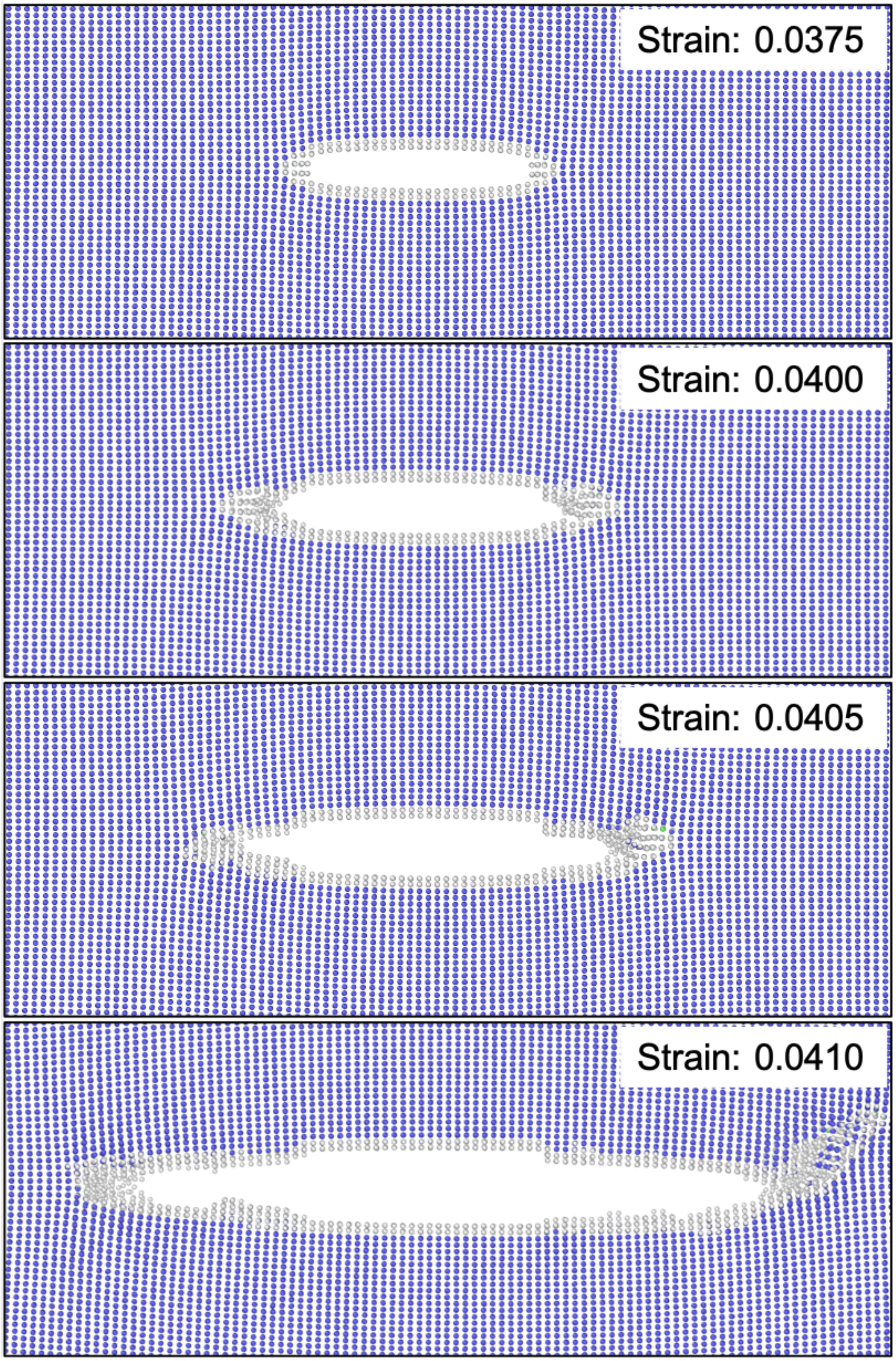

Figure 4.24: The atomistic structure evolution of a microcrack under [001] tensile in MD simulations using the Mo MEAM potential [179].

deformation of the MD simulation using the Mo MEAM potential. Atoms are colored with common neighborhood analysis (CNA) that uses blue to indicate the atoms in the perfect BCC lattice. Right before the activation of plastic deformation, at the strain of 0.0375, when the tensile stress is approaching maximum value, stress concentrates at two crack tips to induce four to five layers of atoms at the crack tips to deviates from equilibrium BCC lattice sites, as shown as the white atoms of defect structure at two crack tips. At the strain of 0.04, the plastic deformation starts as the crack tip propagates approximately 1 nm along the (001) plane, which is the cleavage plane of BCC lattice. Atoms of 2 nm (110) layers at the crack tip shuffle such that the crack tip becomes sharper, which facilitates the crack tip to propagate further, and the stress starts to drop, as shown in Figure 4.23. At the strain of 0.0405, the crack tip propagates quickly along the (001) plane, and during the propagation, the crack tip remains cleavage and induces lattice distortion on atoms close to the crack tip within 2 nm. At the strain of 0.0410, the microcrack grows to the width of nearly 160 nm, that is three times of its initial width, and one crack tip induces deformation twinning along the $(2\overline{11})$ plane. Therefore, Mo is brittle at $\langle 100 \rangle$ tensile loading since its plastic deformation only originates from the propagation of crack tips at the preexisting microcracks.

Figure 4.25 shows the atomistic structure evolution at the initial stage of the plastic deformation during the MD tensile using the Nb MEAM potential. Before the plastic deformation, at the strain of 0.0325, the microcrack is wider along the [001] direction so that the crack tip is blunt, compared with the case of Mo MEAM. At the strain 0.0335 that activates the plastic deformation, the crack tip generates stacking fault along the $(2\overline{11})$ plane. When tensile strain increases, $\langle 111 \rangle$ $(2\overline{11})$ edge dislocation is nucleated from the crack tip and glides on the $(2\overline{11})$ plane away from the crack tip, as shown at the strain of 0.0338, where the black dashed lines indicates the trajectory of dislocation glides. The dislocation nucleation and glide induce the plastic deformation that causes the tensile stress drops at the strain of 0.0335 in Figure 4.23, and the whole process is consistent with one of our the-

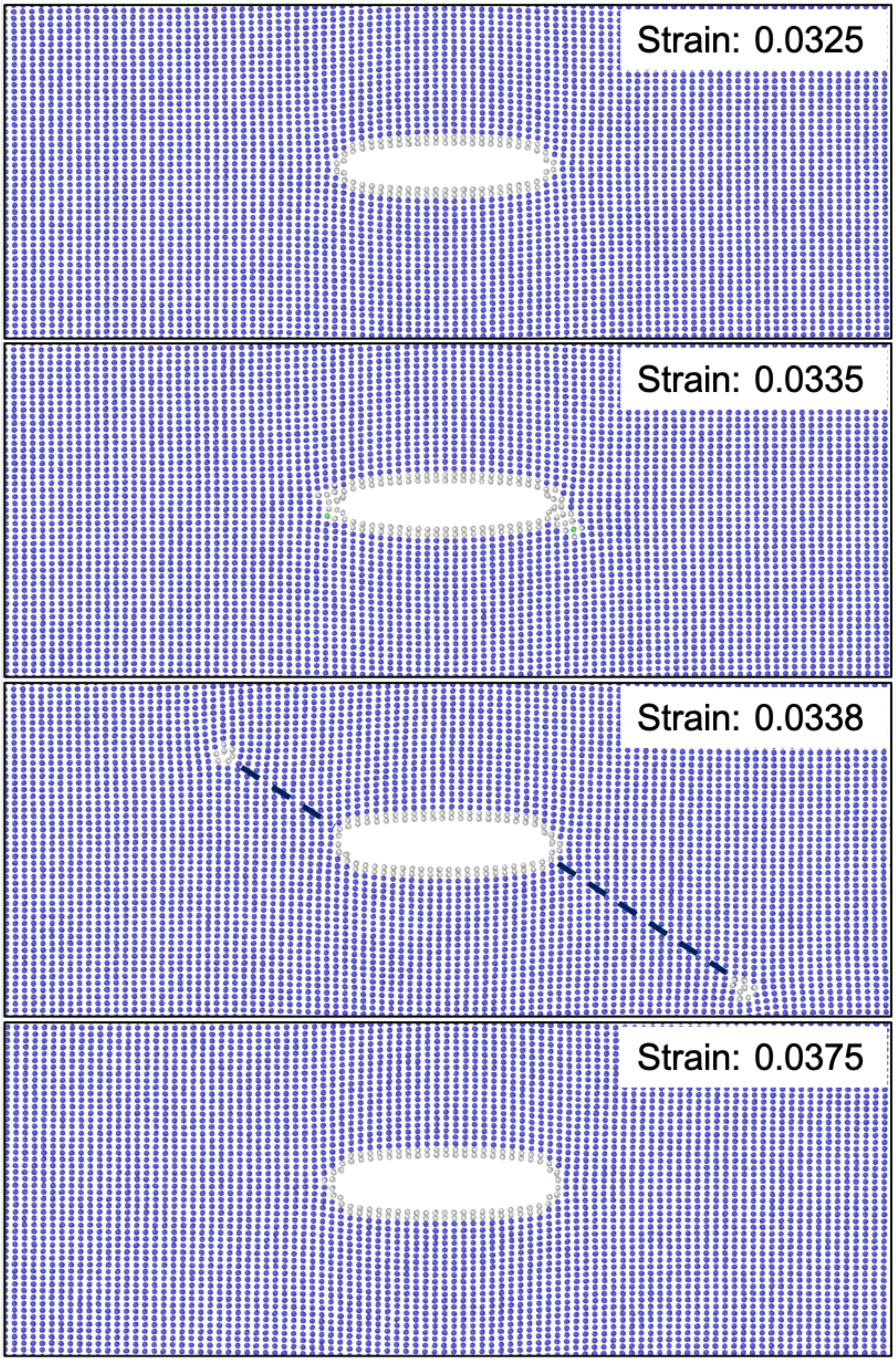

Figure 4.25: The atomistic structure evolution of a microcrack under [001] tensile in MD simulations using our Nb MEAM potential.

oretical picture in the ideal LEFT analysis in Chapter III. Due to the dislocation nucleation and glide, the two crack tips become blunt, as shown at the strain of 0.0375, compared with those at the strain of 0.0325 in Figure 4.23. Another interesting feature is that there are significant lattice misfits at crack tips in Mo at the tensile strain of 0.0375, while the crack tips in the Nb are more blunt and coherent compared with the bulk lattice under the same tensile strain. As more plastic deformation achieved by dislocations nucleation and glide from the crack tips, the Nb system starts to fail by cleavage fracture at the strain over 0.05, which is $\sim$25% larger than Mo, as shown in Figure 4.23.

4.4 Conclusion

Using the force-matching method and first-principles calculations, we applied an ES based optimization process to build a MEAM potential for Nb. The MEAM potential can reproduce structural, thermal, mechanical, and defect features of Nb consistent with DFT calculations and experimental results. The Nb MEAM potential exhibits the intrinsic ductile characteristics of the pristine Nb lattice that originates from its electronic structures, and the Nb potential also gives appropriate descriptions of the energetic stability of various types of crystalline defects, such as vacancies, self-interstitials, surfaces, and deformation twinning. Besides, this MEAM potential can generate accurate properties of $a_0/2\,\langle 111\rangle$ screw dislocation, such as dislocation core structures, core energies, migration barriers and dislocation core trajectories that are related to plastic anisotropy and non-Schmid effect. In our large-scale MD tensile simulations on the infinite bulk crystal with periodic arrays of microcracks, Nb represented by our MEAM potential showed deformation with more ductile features as its plastic deformation mainly originated from dislocation nucleation and glides, while Mo represented by the MEAM potential [179] showed deformation with more brittle features due to the occurrence of cleavage fracture propagation on the initial stage of plastic deformation.

Therefore, by exploiting data that included unit cells contain few numbers of atoms with small/large strains, thermal trajectories and randomly chosen symmetric phases, we constructed a semi-empirical potential that successfully bridged the intrinsic mechanical characteristics of Nb pristine crystal to the mesoscopic physics of deformation defects. Our work built an example of extending the ideal and quantum-mechanical physics to an applicable model of solving realistic and complex mechanical problems, especially those under extreme and anisotropic loading conditions.

CHAPTER V

Complex Grain Boundary Structures from Evolutionary Algorithm

Besides suitable interatomic potentials for precise descriptions of bonding characteristics, atomistic simulations of mechanical properties also demand the construction of accurate and representative atomistic structures of complex crystal defects, such as stable and metastable grain boundary (GB), which is the foundation for the studies of the interactions between GBs and deformation defects. This chapter covers the development and application of our method for the search of GB structures, as well as large-scale MD simulations that demonstrate a correlation between GB structures and deformation mechanisms in Mg.

5.1 Introduction

Grain boundaries (GBs) strongly affect mechanical [135, 97, 221] properties of polycrystalline metals and alloys. GBs can impede dislocation motion and result in dislocation pile-up, and further induces stress concentration and dislocation generations in neighboring grains [87, 186, 251]. The dislocation can react with GBs to generate residual dislocations, causing further nucleation or transmission of dislocations through GBs [97].

Although it is an active research area to study the influence of GBs on materials properties with experimental techniques, it is still challenging for experiments to characterize atomic structures, thermodynamic properties, phase transformations, and deformation behaviors of GBs [158, 279, 214]. Accordingly, atomistic modeling plays an important role to study structures and properties of GBs [203, 30, 252, 199, 243, 241, 131, 178, 187], and the interactions between GBs and other defects [212, 251, 69]. For example, Janssens etc. computed the mobility for different types of symmetric GBs based on MD simulations [114]. Sangid etc. employed atomistic simulations to show that GBs with a low static GB energy tends to resist slip transmission and nucleation at GBs [212]. Peter etc. examined the atomistic details of Ag-segregation-induced structural transition at asymmetric Cu GBs with a combined Monte Carlo (MC) and MD approach [187].

For light-weight metals like Mg with HCP structure, atomistic simulations showed that reactions of dislocations with grain boundaries depend on the structure and misorientation of grain boundaries [251]. MD based study of the interaction between basal slip and $\{10\bar{1}2\}$ twin boundary (TB) revealed the absorption of dislocations in the twin boundary [59]. Besides GBs in pure Mg, GBs in Mg alloys may have different behavior due to the changes in GB structures and compositions. For example, experiments showed that the clustering and segregation of Gd in GBs may contribute to the modifications of GB evolution during the mechanical processing and the overall texture in Mg alloys [84].

In atomistic simulations, a typical setup to construct a GB is to join two perfect crystals with given orientations on a specific grain boundary plane. Based on this setup, the γ-surface method is a conventional technique to examine a variety of microscopic degrees of freedom by sampling all possible translations of the grains relative to each other to find the most stable structure among sampling configurations [204, 240, 177, 251, 213]. Recent studies show that GBs are essentially interface-stabilized structures that may be chemically and structurally distinct from any bulk phases [49, 222, 147, 67, 32]. Since the GB structures could vary by the structural transformations at various thermodynamic and chemical conditions, the conservation of the total number of atoms in the simulation cell and the periodic boundary conditions limit the search of all possible configurations

[53, 188, 272, 67, 32].

Many methods based on stochastic search demonstrated novel results of GB structures in the grand canonical ensemble [248, 249, 272, 278, 69, 17], and among them, the evolutionary algorithm (EA) is a practical and effective method to be coupled with atomistic simulations to investigate GB structures [272, 150, 36, 278, 69]. EA adopts bio-inspired operators such as reproduction, mutation, recombination, and selection to traverse a fitness energy landscape of structural configurations. Due to the high DOF in the crystal structure optimization problem [173, 150], it is critical to have proper evolution operators such as mutation and crossover for the EA to be reliable to explore atomistic structures [149, 150, 242]. In prevailing successful EA applications in structure finding, a common mutation operator is to add displacement vectors on atoms based on atomic properties [150, 149, 278, 242, 225, 160, 36]. If displacement vectors have small magnitude, the probability of transformation of an atomistic structure is limited. On the other hand, if displacement vectors have large magnitude, the system may remain trapped in amorphous structures, especially for pure metals with non-directional bonds, which brings no benefits toward the ordered ground states. It is thus tempting to have abrupt internal structure changes in addition to localized and incremental atomic displacements in mutation phase.

In this work, we developed a new mutation method upon the exchange of crystal structure blocks between internal GB structures and symmetric crystal structures seeds. Combined with a series of evolution operators such as selections and crossovers, we incorporated the new mutation method into a parallel EA package to validate our mutation ideas by exploring GB structures based on atomistic simulations. We applied the EA package to examine GB structures in representative face-centered cubic (FCC), body-centered cubic (BCC), and hexagonal close packed (HCP) metals, and we implemented a tensile test to examine structure evolution at the GBs discovered by EA. Our results show that the proposed mutation methods are sufficient and efficient to search GB structures with a variable number of element types and macroscopic degrees of freedom. Finally, we demonstrate benchmark MD simulations of symmetric tilt grain boundaries (STGB) in pure Mg under tensile loading using two different Mg interatomic potentials. The preliminary results suggest the critical stress for the nucleation of dislocations and deformation twinning from Mg GBs may depend on many factors of the detailed GB structures, and it is difficult to correlate the critical stress with one parameter of GB properties, such as GB energies [212].

5.2 Computational methods

In this section, we discuss the workflow of the EA method in GB structure search, our atomistic simulation setup to measure thermodynamic properties of GBs, the design flowchart, and implementation details of evolution operators in the program.

5.2.1 Basics of evolutionary algorithm (EA)

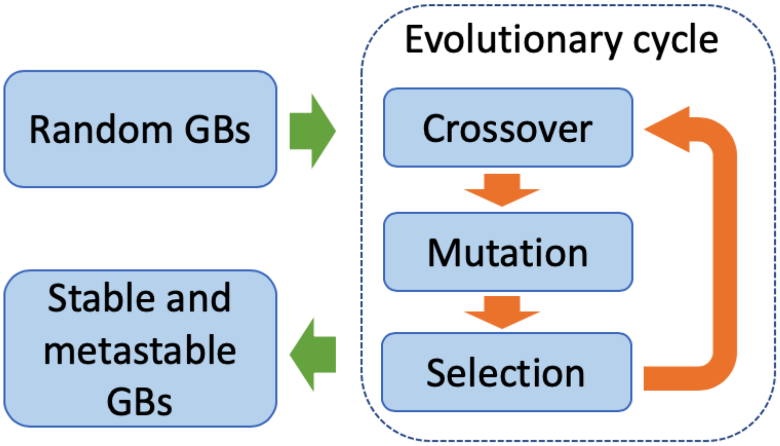

Figure 5.1: The sketch of the basic EA workflow for the search of GB structures.

In our package, we implemented a typical evolutionary algorithm, which involves phases of crossover, mutation, and selection [36, 278], as shown in Figure 5.1. Crossover and mutation are procedures to spread the search scope by creating distinct atomistic structures at GBs. The selection phase is to form a new generation based on the thermodynamic properties of candidate GBs. Our implementation measures the thermodynamic properties of each

GB before the selection phase. To estimate thermodynamic properties, we use LAMMPS [191] to run MD and MS on each GB to reach the state of force equilibrium.

5.2.2 Atomistic simulations of GBs

We apply a sandwich structure setup for GB simulations, as shown in Figure 5.2. The simulation box is periodic along the directions parallel to the GB plane, and it is non-periodic normal to the GB plane due to a vacuum layer of thickness 40 Å that creates two free surfaces. We divide the supercell into several regions based on their distance to the middle line of the simulation box. The region A is the most critical part that contains the mutation and crossover operations, and its thickness is 30-40 Å in our implementation. The region B corresponds to the GB region for the estimation of GB properties, and this region comprises region A and two additional slabs of thickness 10-20 Å. Structure relaxation occurs on the region C, and this domain incorporates a buffer layer of thickness 10-20 Å between the GB zone and the outside region D. The region D simulates the perfect crystal lattice and surfaces, and this region remains rigid throughout molecular dynamics and force

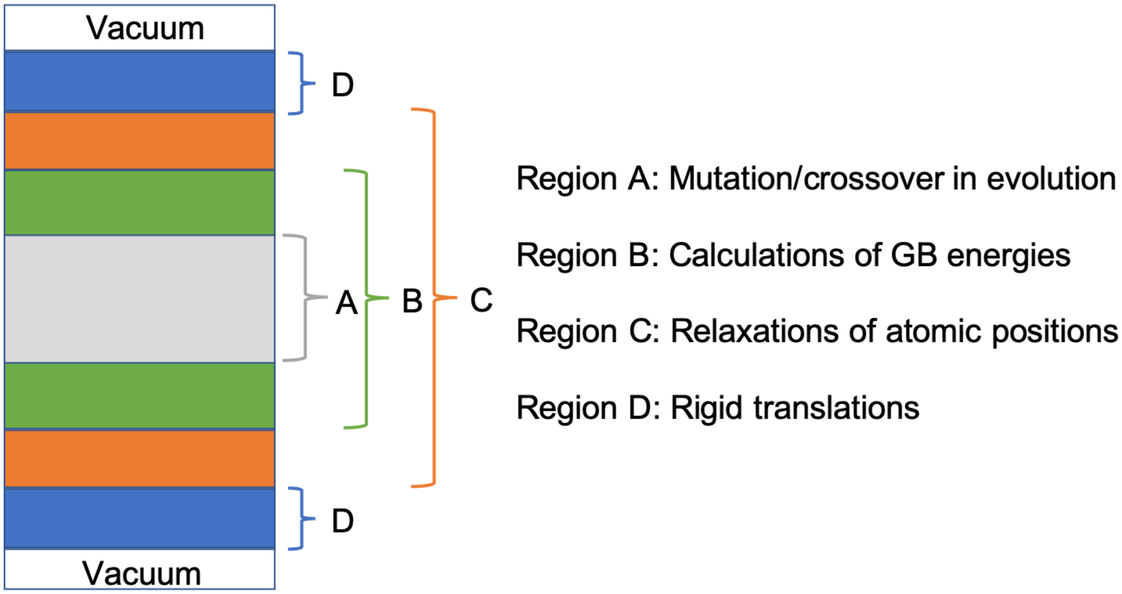

Figure 5.2: The supercell model of GB representation in our atomistic simulations.

minimization. The GB energy γ^{GB} is measured by per unit area as

$$\gamma^{GB} = (E^{GB}_{tot} - E^{Bulk}_{coh} N^{GB}_{tot})/A^{GB} \tag{5.1}$$

E^{GB}_{tot} is the total energy measured at the GB region (the region B), and it equals to the summation of energies of all atoms in the GB region. E^{Bulk}_{coh} is the cohesive energy for an atom in the fully relaxed perfect crystal at 0K. N^{GB}_{tot} is the total number of atoms at the GB region, and A^{GB} is the area of the cutting face that is parallel to the GB plane.

5.2.3 Flowchart of the EA based GB structure search implementation

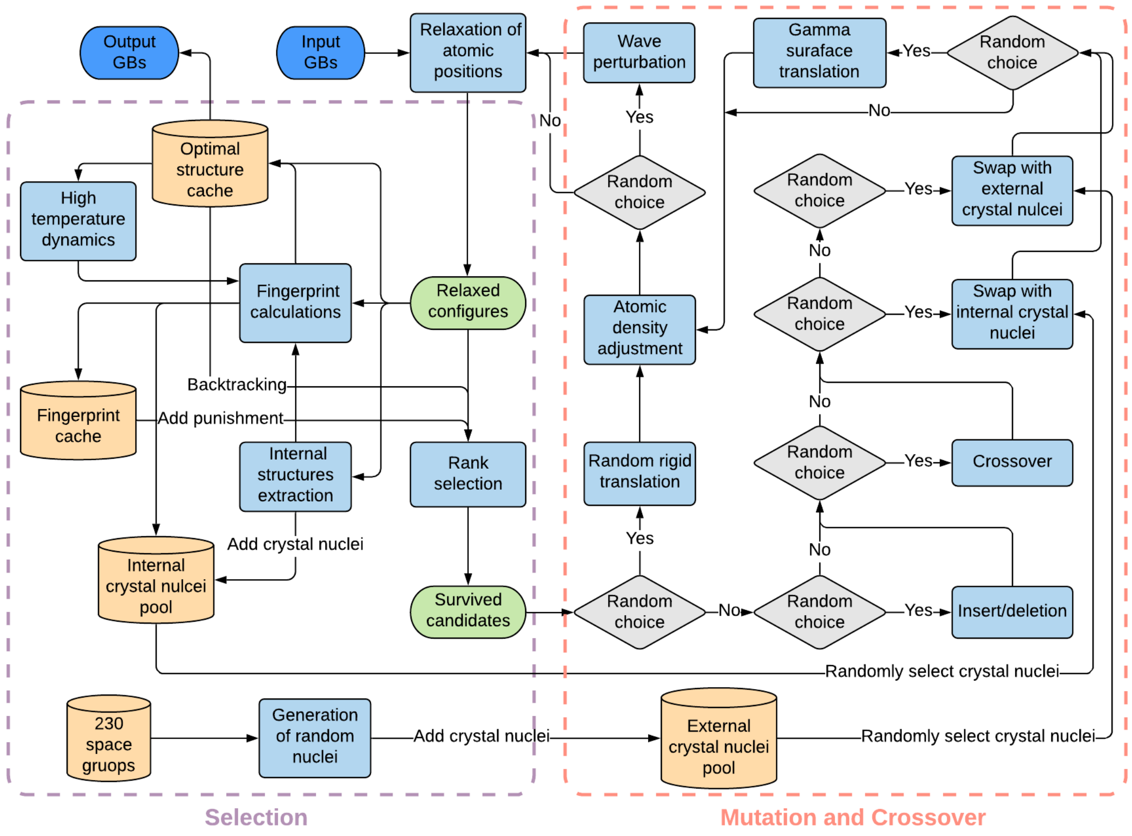

Figure 5.3: Flow chart for finding GB structures by using an evolutionary algorithm with effective mutation methods.

Our implementation of the EA-based GB structure search method contains two stages, including a selection phase and mutation-crossover phase in each evolution cycle. Figure 5.3 shows the flowchart of the implementation of the EA-based GB search method.

In the selection phase, operations aim to ensure an efficient sampling of GB structures by maintaining individual quality and population diversity. Before selections of individuals, we first run a quick dynamics and relax the GB zone to equilibrium states at 0 K. We estimate GB structure properties such as GB energies, virial stress tensor [234] as well as bond orientational order parameter [225, 160] in MD and force relaxation steps. Our next step is to calculate and store a structure fingerprint for each relaxed GB structure. The purpose of the structure fingerprint is to check similarities and duplicates for both GB structures and internal crystal nuclei, both of which are cached for future mutation operations [175]. For each GB structure that resembles identities recorded in the structure fingerprint caches, we exert a duplication punishment on the GB structure during the evaluation of selections. Our definition and calculation of structure fingerprint are discussed in Section 5.2.6. The magnitude of duplication punishments is dependent on the times of duplication of the atomistic structure throughout the history of evolution. Meanwhile, we extract arbitrary amounts of atomistic structure blocks at randomly selected GBs based on local energies and stress states in the selection phase. We establish an optimal structure pool to store GB structures with low GB energy and unique structure fingerprint. The optimal structure pool primarily consists of a priority queue and a hash map of structure fingerprints [39]. The optimal structure pool provides stable and metastable GB structures for outputs and backtracking of search states. The backtracking operation occurs by random chances if any particular GB structures deviate far away from the minimum-energy states at energy landscapes. Our backtracking is to designate random structures from the optimal structure pool to replace a single outlier structure with extreme GB energies. After the series of preprocessing on GB structures at current generations, we apply a rank selection to pick survivals to form the candidates for the next generation of GB structures.

In the mutation and crossover phase, our EA operations intend to spread the search scope by introducing innovative structures and making incremental changes on candidate structures survived from the selection phase. We first apply a random choice to split structure recreation into two routes, and these two routes join before the adjustment of GB atomic densities to a user-predefined range. The first processing route simulates the changes for microscopic degrees of freedom by adding random rigid translations. We first divide randomly selected configurations into two pieces near the GBs, and add three-dimensional rigid-translations on one piece. There may exist atoms that are too close to each other after rigid translations. Due to the pigeonhole principle, the atom-overlapping situation only occurs among pairs of atoms. Therefore, we replace pairs of overlapping atoms with single atoms at the center of the original overlapped pairs.

The second structure re-creation route mainly produces novel local structures (so-called "structure elements" here). Along this path, our first operation is to make a local adjustment on selected configurations by insertion or deletion of a single atom based on local atomic energy and stress. Discussion of insertion and deletion of atoms is in Section 5.2.5. The crossover then happens between randomly selected candidates. The details of crossover implementation are in Section 5.2.4. In the next, we randomly choose GB candidates to exchange their internal structure elements with either an external or internal crystal nuclei pool. The external crystal nuclei pool originates from randomly generated symmetric structures based on 230 space groups. The internal crystal nuclei pool consists of structure blocks extracted from configurations that lived in previous generations. Our final operation is to add γ-surface translation with translation vectors on the grain boundary planes on randomly selected candidates along this route. After two structure recreation routes merge in the mutation and crossover phase, we adjust atomic density by inserting or deleting atoms, and the corresponding details are in Section 5.2.5. To assist the occurrence of phase transformations, we add perturbations to the position of each atom according to a three-dimensional lattice wave on randomly selected GB structures. The direction lattice waves are dependent on random selection from high symmetric crystal orientations. Finally, we performed a few steps of dynamics and structure relaxation on all configurations, and it handed the outputs back to the selection phase to start the next evolution cycle.

5.2.4 Crossover and mutation

Our crossover and mutation intend to promote robustness and effectiveness for the GB structure search with EA. The crossover operation of our implementation resembles the method proposed by Chua etc. [36]. For mutation, inspired by the application of symmetric structures in the first generation [260, 150, 253, 189, 149], we develop a new mutation technique based on swaps of crystal nuclei between GB internal structures and cached symmetric crystal structure seeds, aiming to introduce ordered crystal structure genes into GBs to assist the potential creation of new stable GBs with locally ordered structures. Boosted by structure nuclei at GBs, the GB structure search visit different local minimum states on the energy landscape more effectively by hopping over energy barriers.

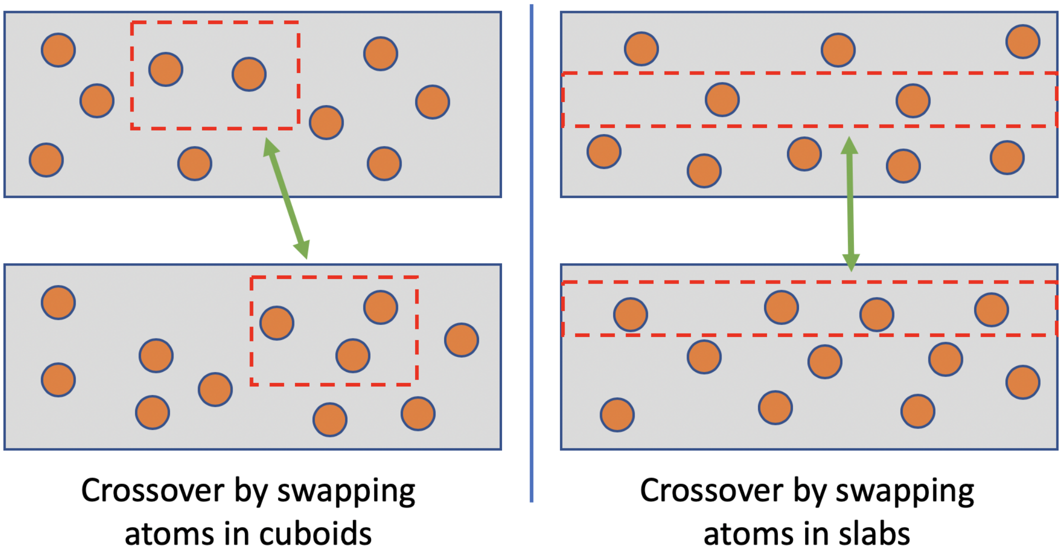

Figure 5.4: The sketch of crossover based on swapping cuboids or slabs of atoms.

In the crossover, we randomly select pairs of configurations from the current generation, and the proportion of selection is a predefined constant, analogous to the work [36]. We generate a random cuboid or slab in each selected pair, and the cuboid or slab has identical size but various center locations in each configuration of pairs, as illustrated in Figure 5.4. We perform wrap-around through the periodic boundary conditions for cuboids at the boundary. Unlike the crossover in the previous work [36], our implementation allows the variation of the number of atoms between exchanged cuboids/slabs in the pair configurations to avoid re-selection of cuboids or slabs for the conservation of atoms.

In mutation, we first randomly choose a subset of configurations, then pick a random crystal nuclei from the crystal nuclei pool for each chosen configuration. A crystal nuclei pool stores the information of the atomistic structure of crystal nuclei and the used times in the ongoing search. As shown in Figure 5.3, our system maintains two crystal nuclei pools: an external pool (shown in Figure 5.5) and an internal pool (shown in Figure 5.6). The next task is to inject the selected crystal nucleus into the selected GB. We define a nuclei-swap to be an operation that copies relative atomic coordinates of a crystal nuclei to an internal structure block at a GB. In a nuclei-swap, we first delimit an internal structure block, which has the same dimension as the to-swapped crystal nucleus cell. We then remove atoms in the internal block and insert the selected crystal nucleus to the internal cell location, as shown in Figure 5.5 and Figure 5.6. A single nuclei-swap step may be inefficient as only

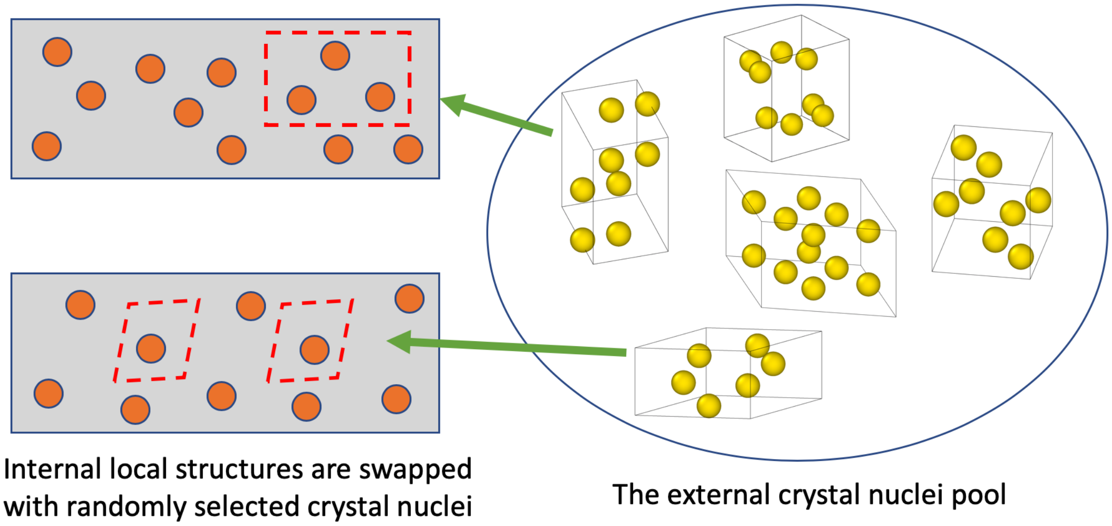

Figure 5.5: The sketch of crossover based on swapping cuboids or slabs of atoms from the crystal nuclei pool generated externally based on 230 space groups.

a single local change introduced in the GB. We hence applied a series of nuclei swaps in a single mutation step. We first calculate the maximum number of candidate crystal nuclei that can simultaneously occupy in the GB region of selected configurations, then use a random choice upon the binomial distribution to determine the number of nuclei-swap steps. A scalar variable serves as a mutation step length to scale the probability of the binomial distribution, and a large mutation step length gives a high possibility of making more nuclei swaps in a single mutation step. The mutation step length depends on the GB energy ranking of the configuration among the previous generation. A GB structure of low ranking in the selection has a more substantial mutation step length than GB structures of high ranking, which is thermodynamically preferred. The location of each nucleus swap is determined after the number of nuclei swaps. Our implementation is to arrange all nuclei swaps near the GB plane with patterns randomly chosen from the plane crystallographic group (also known as wallpaper group) [86] and exert sinusoid perturbations on the center location of swaps with normal along the GB plane normal.

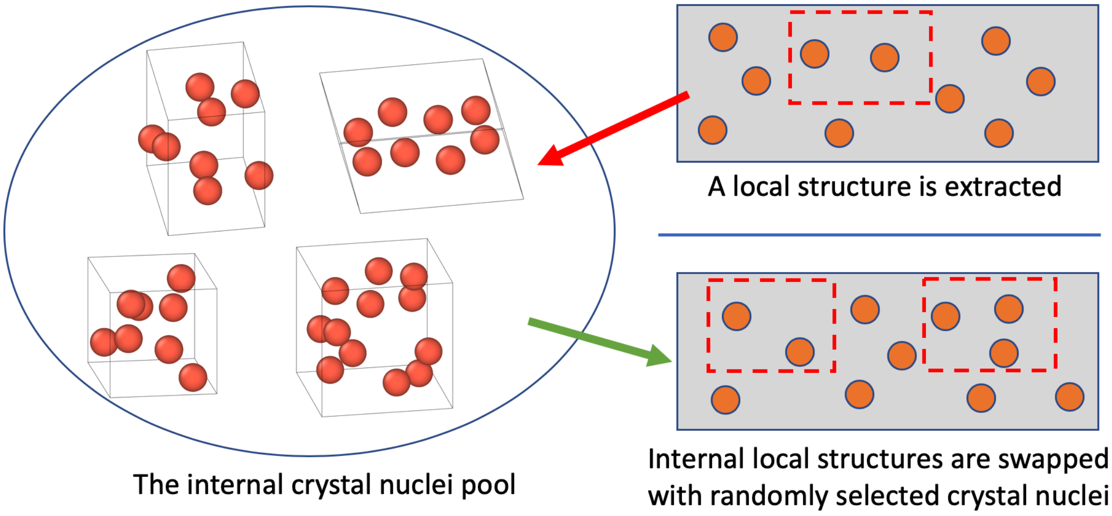

Figure 5.6: The sketch of crossover based on swapping cuboids or slabs of atoms using the crystal nuclei pool generated internally, which means those nuclei are chosen from local structures of GBs in previous generations of EA.

For the effectiveness of nuclei-swap mutation, we consider two requirements for candidate crystal nuclei. The crystal nuclei first should be representative of ordered structures of different symmetries for exhaustive search on the energy landscape. Second, the crystal nuclei should contain high-quality genes to speed up the creation of promising candidates. For the first requirement, we construct the external crystal nuclei pool by generating symmetric crystal structures based on 230 space groups with steps similar the work [149]. We determine the number of atoms in the crystal nuclei by a random choice, then randomly pick one space group that is compatible with the number of atoms in the unit cell. Atoms are placed based on Wyckoff positions with random variable picked, and cells are re-scaled to make atomic volume consistent with equilibrium matrix crystal. We finally apply additional operations such as deletion, insertion, and merge of atomic positions to make atomic positions satisfy the minimum bond length constraints in the periodic boundary conditions along with all three directions. We construct the internal crystal nuclei pool to meet the second requirement. As shown in the flowchart of Figure 5.3, we extract structure blocks at GBs from randomly selected configurations in each EA generation. The probability of a configuration to be picked is proportional to the ranking of this configuration. Next, we define structure blocks that are centered at atoms with high energies and relatively ordered neighboring by evaluating the potential energies and virial stress tensor of atoms. The size of blocks and the number of atoms included in the crystal nuclei are random variables among predefined ranges. Our hypothesis for choosing internal structure blocks into the crystal nuclei pool is that atomistic structure blocks with high energy concentration and ordered local structures contain critical structural signatures of stable GBs. Additionally, we constrain the lifespan of each crystal nuclei during EA by removing a crystal nuclei if its usage surpasses a predefined limit.

5.2.5 Control of atomic density

It is critical to measure and control the variation of the number of atoms at GBs during the GB structure search in the grand canonical ensemble. To quantify the number of atoms at GBs, we first define the excess amount of atoms at GB per unit area $\mathrm{N}_{\mathrm{ex}}^{\mathrm{GB}}$ as

$$\mathrm{N}_{\mathrm{ex}}^{\mathrm{GB}} = \left\langle \mathrm{N}_{\mathrm{tot}}^{\mathrm{GB}} - \mathrm{V}_{\mathrm{tot}}^{\mathrm{GB}}/\Gamma \right\rangle /\mathrm{A}^{\mathrm{GB}} \tag{5.2}$$

The $\mathrm{N}_{\mathrm{ex}}^{\mathrm{GB}}$ is an estimation of the excess number of atoms in the GB. In a single estimation step, we first define a measurement region that contains the GB (region B in Figure 5.2), and the measurement region thickness is a random variable that can make the measurement region incorporating the GB region. The excess number of atoms amounts to the total number of atoms in the region $\mathrm{N}_{\mathrm{tot}}^{\mathrm{GB}}$ subtracting the expected number of atoms, which is the total volume of the region $\mathrm{V}_{\mathrm{tot}}$ dividing equilibrium volume per atom Γ. We take an average of 30 measurements for the estimation of $\mathrm{N}_{\mathrm{ex}}^{\mathrm{GB}}$, and divide it by the effective GB plane area A^{GB}. Mutation and crossover can vary the excess number of atoms at GB $\mathrm{N}_{\mathrm{ex}}^{\mathrm{GB}}$. Random rigid translation can induce both volume and amount of atoms change. Crossover may change $\mathrm{N}_{\mathrm{ex}}^{\mathrm{GB}}$ since it may not be the same for the number of atoms in the cuboids or slabs swapped between two configurations.

Additionally, we have two operations for automatic atom insertion and deletion. The first operation occurs before the crossover, and the target of this insertion/deletion operation is to tune internal crystal structures locally before crossover and mutation. We first take samples of several structure units with high energies and evaluate the virial stress of sampled atoms, then determine whether to proceed with the insertion or deletion of a single atom based on the average volumetric stress field of sampled structures. If the average volumetric stress exceeds an upper bound, we insert a single atom to the system; otherwise, if the average volumetric stress is less than a lower bound, we delete a single atom at GBs. The upper bound and lower bound are materials-dependent constants calculated by expanding and shrinking a perfect crystal with one percent volumetric strain.

As shown in Figure 5.7, to delete a single atom at GB, we first select candidate atoms in high energy and compressive volumetric stress environment. The atom to be deleted is a

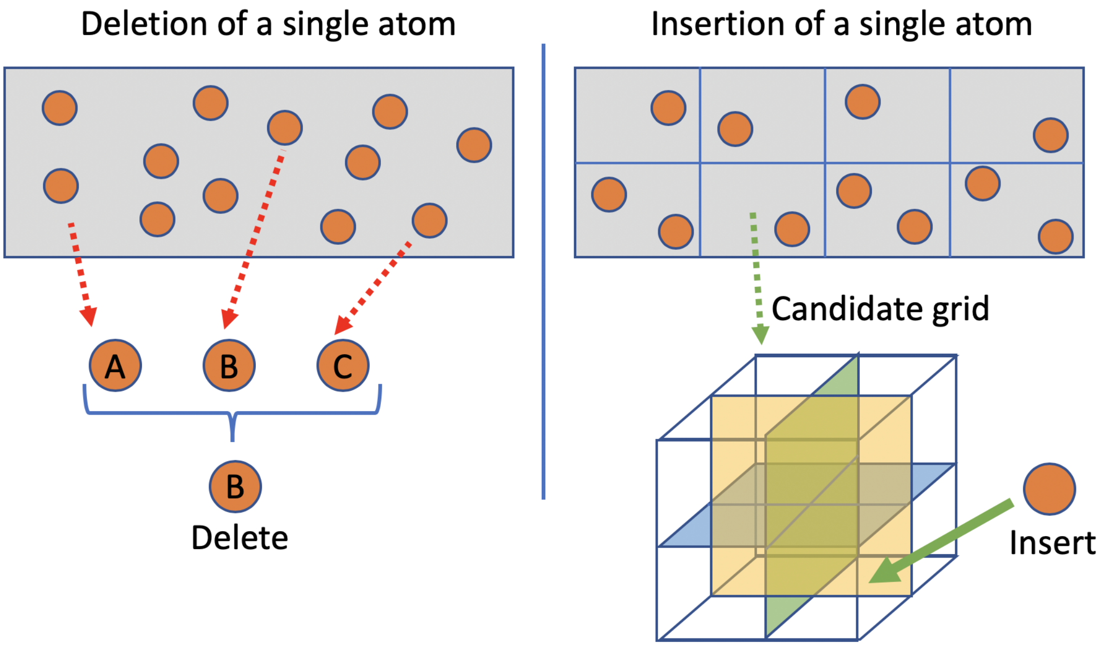

Figure 5.7: The sketch of insertion and deletion of a single atom into/from the GB region.

random choice among candidate atoms with a bias on the atomic energy of each candidate. During the insertion, we divide the GB region into equal-size cubic grids by a 3-D mesh split, and the size of mesh grids is a random choice in each insertion to promote the flexibility of atom insertion. We then measure the energy/stress properties of each mesh grid by summing the properties of atoms of distances to the center of the grid within a critical cut-off value. We choose candidate grids based on the average energy and expansive pressure of atoms in each grid, and among candidate grids, we randomly select a final grid that is further divided into eight sub-grids. We measure the expansive pressure on the sub-grid using the same method applied to the grid. In sub-grids unoccupied by any atoms, we finally insert a single atom at the center of the sub-grid with the highest expansive pressure.

The second automatic insertion and deletion of atoms is for the adjustment of atomic density at GBs, as shown in Figure 5.3. Our EA method is for effective search of metastable states of GB structures with N_{ex}^{GB} inside a range predefined by users. Since the crossover and mutation may vary N_{ex}^{GB} to be outside of the expected scope, we modify N_{ex}^{GB} to a random choice in the expected scope by inserting or deleting atoms at GBs. Since operations have no atomic properties as a reference at this stage, we delete atoms in a high atomic density environment and to insert atoms at locations of low atomic density. Similar to the previous insertion method, we divide the GB region into 3D mesh grids and estimate the atomic density of each mesh grid. To calculate atomic density in each mesh grid, we sum the contribution of atoms with within a cutoff distance to mesh grid centers. We insert or delete a single atom in a random grid among those of the lowest atomic density or the highest atomic density, respectively. After each deletion or insertion of a single atom, we recalculate the atomic density of each grid using the same method for another insertion or deletion. We repeat this process until the $\mathrm{N}_{\mathrm{ex}}^{\mathrm{GB}}$ of all GB structure in one EA generation reaches a uniform distributed random target in the predefined atomic density range.

5.2.6 Selection and structure fingerprints

Selection is to pick qualified candidates to form the next generation that retains both the quality and diversity of the atomistic structure genes of the previous and current generations. For the quality of survival configurations, we apply rank selection [76] upon a comparison of GB energies defined in Equation 5.1. However, configurations may greedily converge to resembling structures of low GB energies, which decreases the diversity of the generation and further traps the generation in a local minimum of the energy landscape. We thus apply a trade-off by adding external punishment for similar or repeated structures to balance between quality and diversity. To estimate the punishment, we introduce structure fingerprint, unique to each atomistic structure and measurable directly from this structure, for filtering duplicated GB structures during the evolution. Many studies have proposed different descriptors to discriminate structures, such as usage of distance metrics [95, 258], bond orientational order parameter [225], topology or statistics of potential energy landscapes [22, 28, 219], and pairwise structure factor [175, 150].

We represent a structure fingerprint with a serial key based on the structural and energetic properties of atoms at GBs. Figure 5.8 exhibits an example of our key-based structure

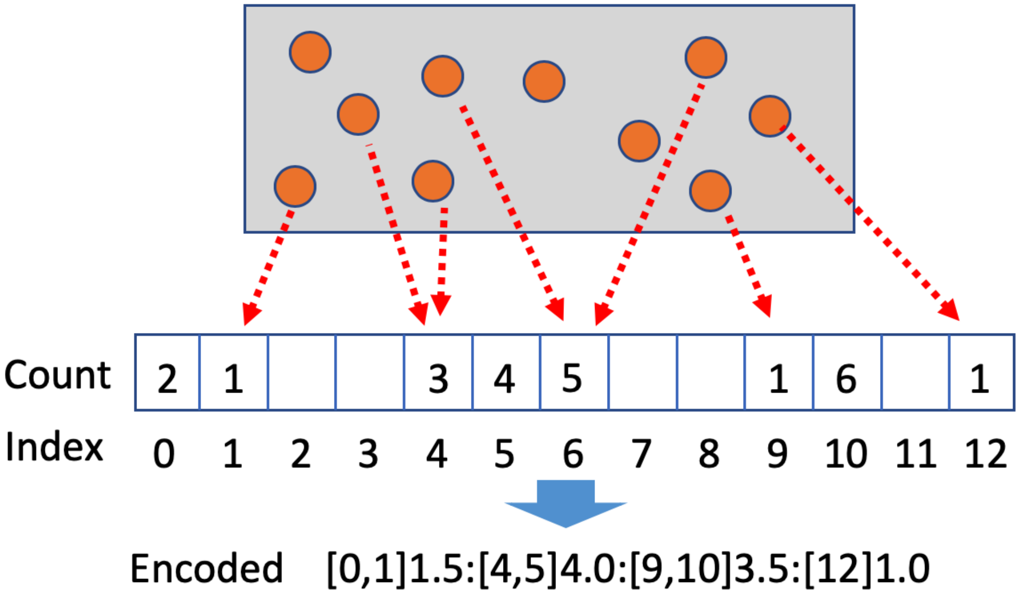

Figure 5.8: A diagram of extraction and calculation of structure fingerprints for each GB structure

fingerprint and the diagram for the calculation of structure fingerprint. Our first step is to select a constant amount of representative atoms of the highest atomic energy and volumetric stress. We define an atomic fingerprint as the inner product between the atomic energy and the bond orientational order parameter, which relies on the structural environment of each atom and the potential energies of the materials. The next is to discretize the atomic fingerprint into discrete bins and assign atoms to bins upon their atomic fingerprints such that atoms of a similar atomic environment in the same atomic fingerprint bin. We group adjacent occupied bins into a large bin and evaluate the average atomic fingerprint for each occupied bin, then measure the structure fingerprint by encoding the index, size, and average atomic fingerprint of each occupied bins. Our key-based structure fingerprint is hashable to achieve the constant time search for the detection of duplication of atomistic structures throughout evolution history during the selection phase, but it prohibits the direct comparison of different atomistic structures. Therefore, it is worth for future studies on the development of methods that balance between key-based fingerprint for structure identification and matrix-based fingerprint for structure comparison.

5.2.7 Details of GB setups and simulations

We apply the EA method to investigate STGBs in pure metals, including the [001] STGBs in FCC copper (Cu), the [110] STGBs in BCC tungsten (W), and the [$1\bar{2}10$] STGBs in HCP magnesium (Mg). Our EA method utilizes empirical potentials to simulate the GBs of each metal, and the potentials in use are a Cu embedded atom method (EAM) potential [43, 162], a W EAM potential [277], and an Mg EAM potential [146]. All empirical potentials applied in this work are previously validated to be suitable for the studies of GBs [30, 240, 67, 278, 217, 213, 69, 252, 251, 167, 178].

Our simulations apply orthogonal simulation boxes to construct STGBs. To build the [001] STGBs in FCC Cu, we align the [100], [010], and [001] lattice orientation along the x- and y- and z- Cartesian axis, respectively. We coordinate the x- and y- and z- Cartesian axis parallel to the [110], [001], and [$1\bar{1}0$] to construct the [110] sets of STGBs in BCC W. We apply the basal-plane tilt to build the [$1\bar{2}10$] STGBs in HCP lattice [279], and the three-axis corresponds to the [$10\bar{1}0$], [0001] and [$1\bar{2}10$] lattice orientation, respectively. Thus, for all the GB simulations, the GB tilt axis is along z-axis and the grain boundary plane is on the x-z plane. In the next, we divide the supercell of the perfect crystal into a top and a bottom half part, respectively. Along the tilt axis, we then rotate the top grain by the tilt angle θ clockwise and tilt the bottom grain by θ counterclockwise. The total misorientation angle ϕ thus equals twice of the tilt angle θ. We determine the tilt angle and the simulation box width (length along the x-axis) based on the constraint of periodicity along the x-axis. We regulate the simulation box width along each dimension at least 20 Å and at least four atomic layers by examining their correlations to the GB energies. Throughout simulations in this work, we display atomic structures with OVITO, an open visualization tool for visualization and analysis of atomistic simulation data [227].

5.3 Results and discussion

5.3.1 The [001] STGBs in FCC Cu

We first apply the EA method to study the [001] STGBs in FCC copper (Cu). Recent investigations of Cu $\Sigma5(210)[001]$ and $\Sigma5(310)[001]$ STGBs reveal an occurrence of phase transformations induced by diffusion of atoms at the GBs [67], which indicates that a conventional method that conserves the number of atoms at GBs impose constraints for potential structure transformations. A recent GB search method demonstrates the possibility of finding new stable and metastable phases at GBs in grand canonical ensembles [278]. Accordingly, our first work is to explore the [001] STGBs in FCC Cu as a benchmark to examine the effectiveness of our mutation operations and EA implementation.

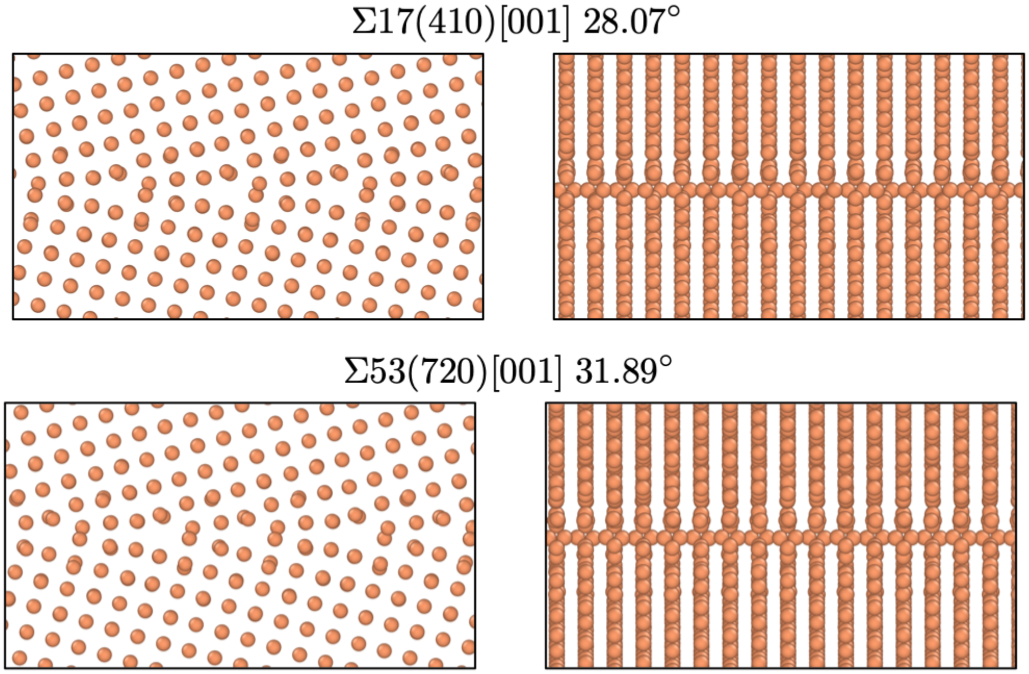

$\Sigma17(410)[001]$ 28.07°

$\Sigma53(720)[001]$ 31.89°

Figure 5.9: Two projected views of the ground-state STGB structures of the $\Sigma17(410)[001]$ and $\Sigma53(720)[001]$ GBs at the misorientation angle of 28.07° and 31.89°, respectively, obtained in the grand canonical ensembles at 0 K. The left images show the view along the z-axis (the tilt axis) and the right images show the view along the x-axis. The grain boundary plane is on the x-z plane. All the following GB images are plotted according to the same orientation setup.

Our GB search starts with low tilt angles, and we discovered the ground-state (GS) structures of Σ17(410)[001] at ϕ = 28.07° and the Σ53(720)[001] at ϕ = 31.89°, as presented in Figure 5.9. The left panel exhibits atomic structures from the view parallel to the [001] tilt axis, and the right panel shows the view along the direction perpendicular to the tilt axis but still on the grain boundary plane. The GB energies are 0.902 J/m^2 and 0.944 J/m^2 for the Σ17(410)[001] and the Σ53(720)[001], respectively. For low tilt-angle STGBs such as the Σ17(410) and the Σ53(720), we find ground-state structures that belong to the Split Kite (SK) family but have non-glide symmetry compared with the typical Split Kite (SK) structure. The finding of Split Kite (SK) with non-glide symmetry is consistent with the GS structures of the Σ17(410) and the Σ53(720) reported by Zhu etc [278].

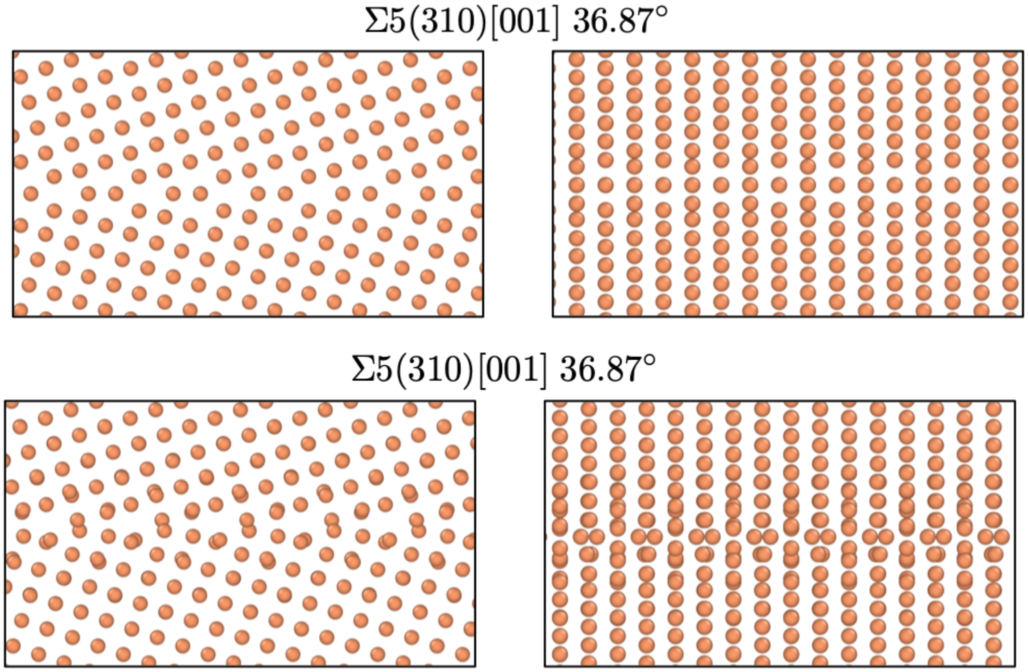

Figure 5.10: The projected views along z-(left images) and x-(right images)axis of the STGB structures of the Σ5(310)[001] with the misorientation angle of 36.87° at the ground state (top images) or a near-ground state (bottom images) obtained in the grand canonical ensembles at 0 K.

We increase the tilt angle for the Σ5(310)[001], Σ29(520)[001] and Σ5(210)[001] GBs that correspond to the misorientation angle at 36.87°, 43.60° and 53.37°, respectively. For the $\Sigma5(310)[001]$, our EA identifies two structures of GB energy equal or close to the ground state, as shown in Figure 5.10. The top one shows the conventional Kite structure GB with GB energy of 0.905 J/m^2, and the bottom one exhibits a GB of the skewed Split Kite (SK) structure with GB energy 0.914 J/m^2. This is consistent with reported results that the Kite structure is the ground-state GB structure for the $\Sigma5(310)[001]$ at 36.87°, and the structure of Split Kite family gives energy close to the ground-state Kite structure [278]. Moreover, the skewed Kite has excess atoms per unit GB area N_{ex}^{GB} of -0.007 Å^{-2}, which indicates its atomic density is close to the perfect FCC Cu lattice. Compared with the N_{ex}^{GB} of -0.041 Å^{-2} for the conventional Kite, the skewed Kite GB has a higher atomic density than the usual Kite GB, which also matches the previous analysis [278].

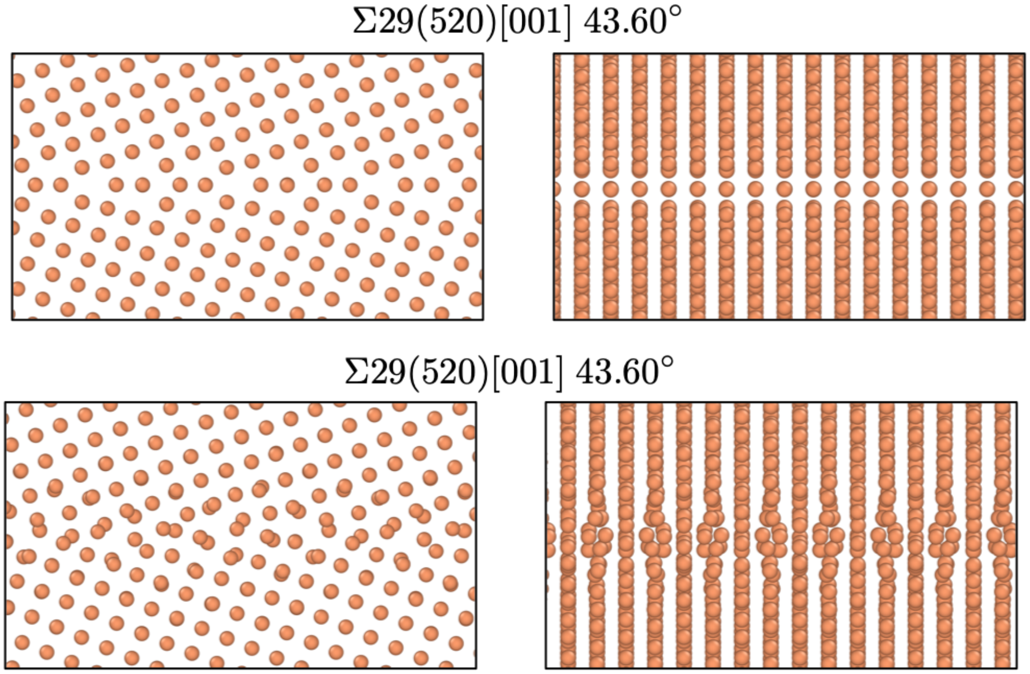
$\Sigma29(520)[001]$ 43.60°

$\Sigma29(520)[001]$ 43.60°

Figure 5.11: The projected views along z-(left images) and x-(right images) of the STGB structures of the $\Sigma29(520)[001]$ with the misorientation angle of 43.60° at the ground states obtained in the grand canonical ensembles at 0 K. Two ground-state structures (top vs. bottom images) are obtained.

At the misorientation angle of 43.60°, we find the $\Sigma29(520)[001]$ has two structures that correspond to the ground-state with the same GB energy of 0.983 J/m^2, as displayed in Figure 5.11. The top GS structure is the typical Kite GB structure with Kite units of alternated size periodically aligning along the GB plane. The second GS is in a Distorted Kite structure, as shown in the bottom penal of Figure 5.11, where atoms are in distorted positions compared with the usual Split Kite structures. The finding of two GS structures agrees with the finding from Zhu etc. [278]. The Distorted Kite structure has N_{ex}^{GB} of -0.016 $Å^{-2}$ that is in-between the -0.024 $Å^{-2}$ for the normal Kite and -0.007 $Å^{-2}$. Therefore, the GB of Distorted Kite has an atomic density in the middle of the split and normal Kite GB, which is consistent with previous examination [278].

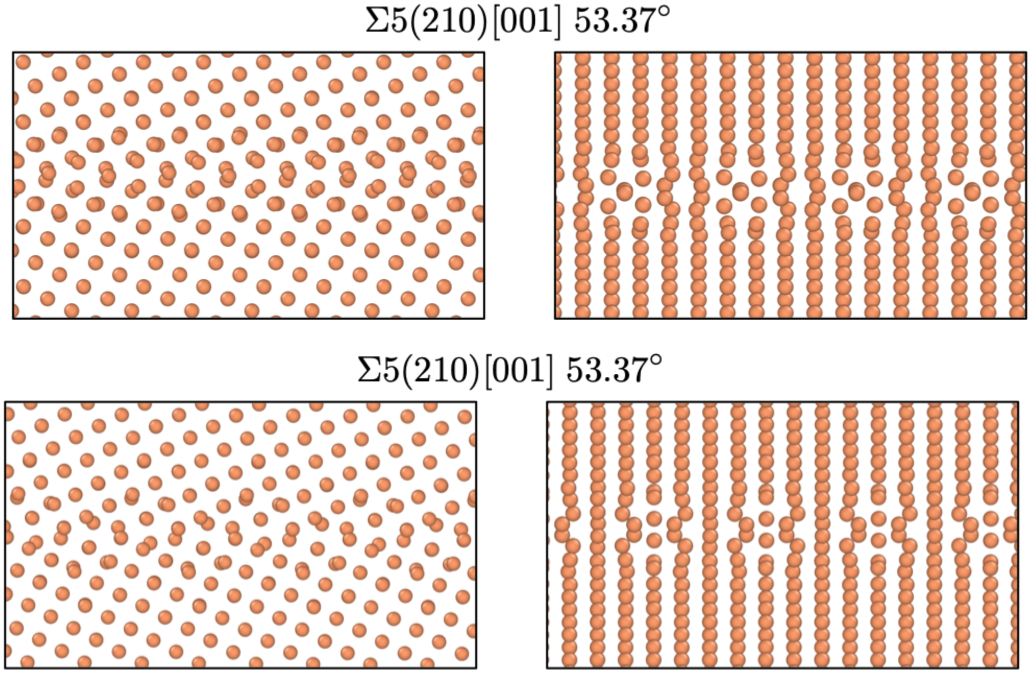

Σ5(210)[001] 53.37°

Σ5(210)[001] 53.37°

Figure 5.12: The projected views along z-(left images) and x-(right images)axis of the STGB structures of the Σ5(210)[001] with the misorientation angle of 53.37° at the ground state (top images) or a near-ground state (bottom images) obtained in the grand canonical ensembles at 0 K.

For the Σ5(210)[001] at the misorientation angle of 53.37°, our GB search obtains two structures at or near the ground-state. As shown in Figure 5.12, the GS is a Split Kite structure (top images in Figure 5.12) of GB energy 0.943 J/m^2, and the second to the GS is a Distorted Kite structure (bottom images in Figure 5.12) of GB energy 0.947 J/m^2. The N_{ex}^{GB}

of Split Kite structure is -0.006 Å^{-2}, higher than the N_{ex}^{GB} of -0.015 Å^{-2} for the Distorted Kite structure. The atomic density of Split Kite GB family is close to perfect the FCC lattice and higher than typical Kite GB family in that extra atoms occupy lattice sites between the [001] planes. Split Kite family also have complex internal structures of distinct subunits compared with the typical Kite family, and this rich structural diversity corresponds to the increase of entropy, which is consistent with the results that most ground-state structures at high temperatures belong to the Split Kite family [278].

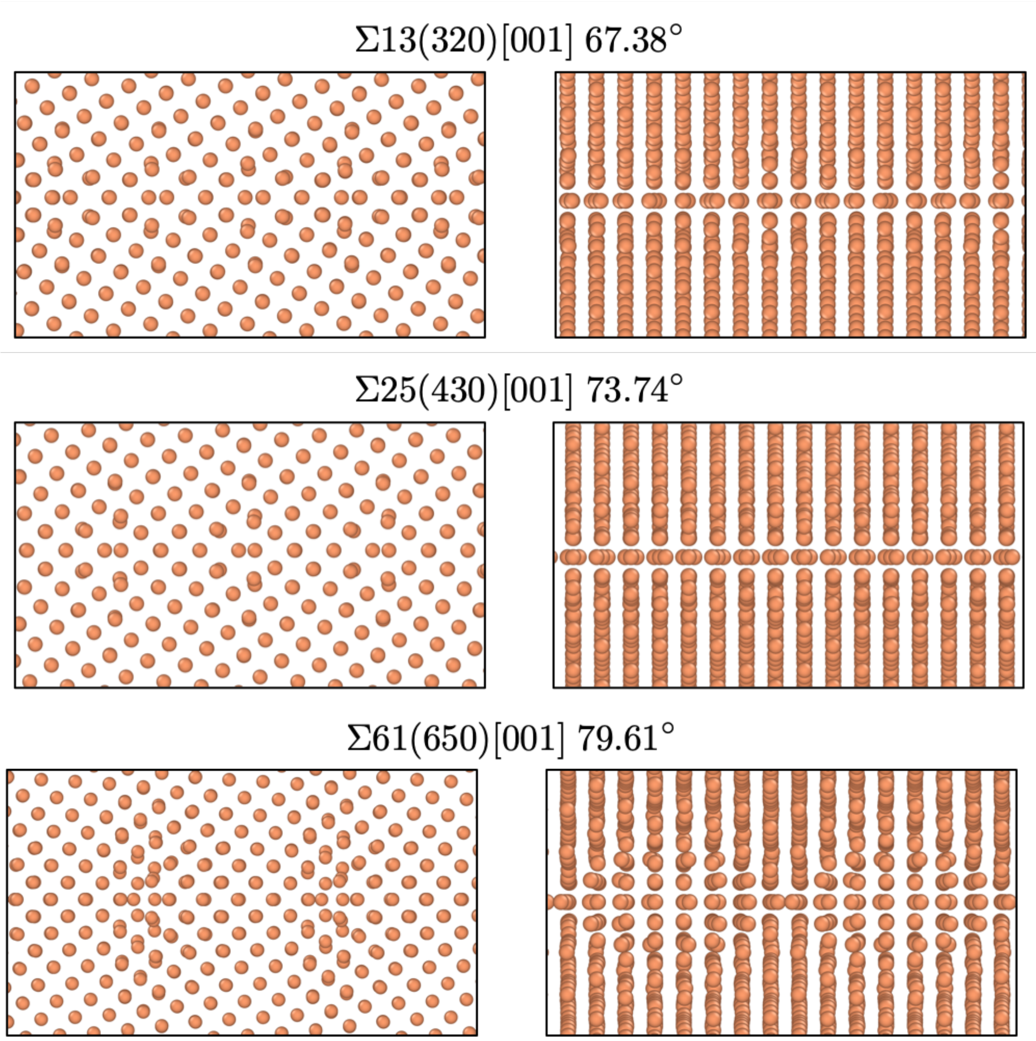
$\Sigma13(320)[001]$ 67.38°

$\Sigma25(430)[001]$ 73.74°

$\Sigma61(650)[001]$ 79.61°

Figure 5.13: The projected views along z-(left images) and x-(right images)axis of the STGB structures of the $\Sigma13(320)[001]$, $\Sigma25(430)[001]$ and $\Sigma61(650)[001]$ with the misorientation angle of 67.38°, 73.74° and 79.61°, respectively, at the ground states obtained in the grand canonical ensembles at 0 K.

At high angles, we perform the structure search on the Σ13(320)[001], Σ25(430)[001], and Σ61(650)[001] for the misorientation angle at 73.74°, 67.38° and 79.61°, respectively. As shown in Figure 5.13, these three GB structures are in the category of Extended Kite family since the structure units at the GBs are [110] edge dislocations with extended dislocation core structures compared with regular Kites [278]. The GB energies are 0.805 J/m^2, 0.666 J/m^2, and 0.509 J/m^2 for the Σ13(320)[001], Σ25(430)[001] and Σ61(650)[001], respectively. When the tilt angle increases, the GB energy of Extended Kites decreases. The Extended Kites become favorable than Normal Kites and Split Kites at high misorientation angles, and this observation is consistent with previous examinations on [001] STGBs [278]. The N_{ex}^{GB} is -0.0263 Å^{-2}, -0.014 Å^{-2} and -0.013 Å^{-2} for the Extended Kite structures at Σ13(320)[001], Σ25(430)[001], and Σ61(650)[001], respectively. Extended Kites, therefore, have atomic densities close to Split Kites and higher than regular Kites, and this estimation also agrees with the previous investigation [278].

5.3.2 The [110] STGBs in BCC W

Our next application of the EA is to study GBs in BCC refractory metals. Unlike many FCC metals, d valence electron in transition metals promotes directional chemical bonding, causing additional complexity on the structures and behaviors of defect [21, 266]. Thus, early studies applied DFT calculations to investigate properties of STGBs at different tilt angles with γ-surface method [217, 218, 213]. Recently, an application of metastable structural unit model demonstrated the variety and multiplicity of states and properties of GBs in BCC W [90], and researches focused on W [001] and [110] tilt GBs discovered novel structures with the number of atoms inconsistent with the number of atoms in the lattice planes of neighbor crystals [68, 69]. Consequently, we employ our EA package to study [110] STGBs in BCC W to validate the quality of our EA GB search method.

Our first examination focuses on GB structures of the Σ3(112)[1$\bar{1}$0] and Σ3(332)[1$\bar{1}$0] at the ϕ of 70.53° and 129.52°, since these two tilt angles correspond to the two deep

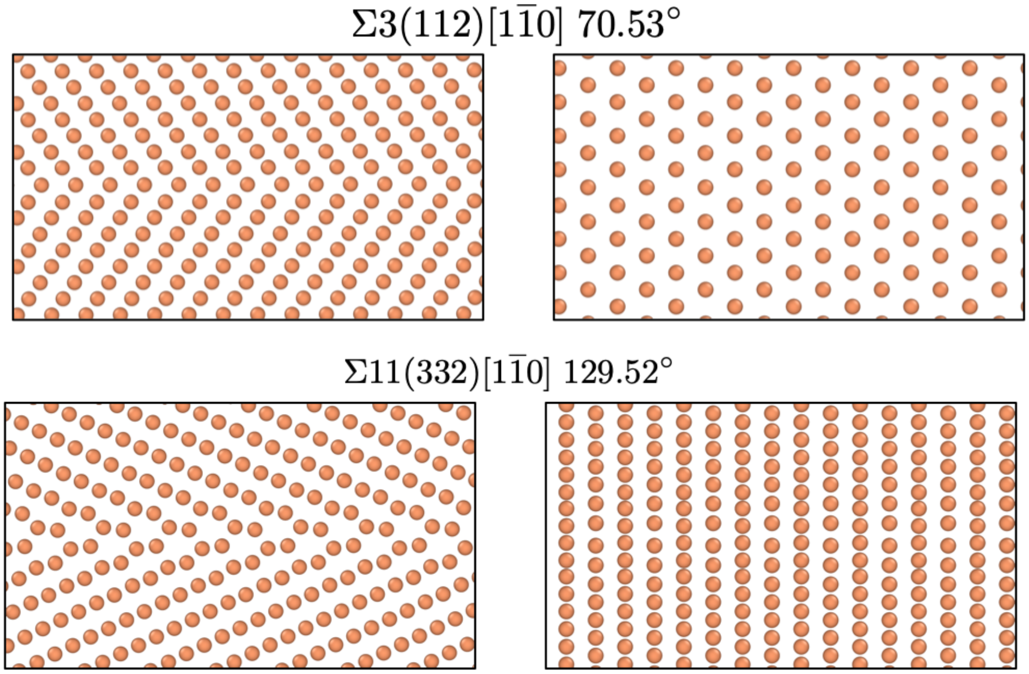

$\Sigma3(112)[1\bar{1}0]$ 70.53°

$\Sigma11(332)[1\bar{1}0]$ 129.52°

Figure 5.14: The projected views along z-(left images) and x-(right images)axis of the ground-state STGB structures of the $\Sigma3(112)[1\bar{1}0]$ at ϕ = 70.53° (top images) and $\Sigma3(332)[1\bar{1}0]$ at ϕ = 129.52° (bottom images) obtained in the grand canonical ensembles at 0 K.

cusps for the GB energy curve [213, 69]. Figure 5.14 shows the ground-state structures of $\Sigma3(112)[1\bar{1}0]$ and $\Sigma3(332)[1\bar{1}0]$ explored by the EA, and their ground-state energy are 0.582 J/m^2 and 2.016 J/m^2, respectively. For the $\Sigma3(112)[1\bar{1}0]$, the lattice at GB is completely symmetric and coherent. The excess atoms per GB area $\mathrm{N}_{\mathrm{ex}}^{\mathrm{GB}}$ is -0.008 Å^{-2}, and it indicates the ground-state structure of the $\Sigma3(112)[1\bar{1}0]$ has almost the same atomic density as the perfect BCC crystal. Due to the consistency of structure and atomic density at the GB, the $\Sigma3(112)[1\bar{1}0]$ has ground-state GB energy much lower than other tilt angles in the $[1\bar{1}0]$ tilt set. As a comparison, $\mathrm{N}_{\mathrm{ex}}^{\mathrm{GB}}$ of $\Sigma3(332)[1\bar{1}0]$ is -0.018 Å^{-2}, and the decrease of atomic density is due to small vacancies spread at the GB plane, as indicated by the bottom images in Figure 5.14. These vacancies increase the GB energy of $\Sigma3(332)[1\bar{1}0]$ to be about three times higher than the $\Sigma3(112)[1\bar{1}0]$. In summary, at the angles of 70.53° and 129.52°, our EA finds both structures and energies that are consistent with previous reports [218, 213, 69], and no novel ground-state structures compared with γ-surface approach.

For misorientation angles between 0° and 70.53°, we apply the EA to examine the $\Sigma33(118)[1\bar{1}0]$ at the angle ϕ of 20.05°. Our result shows a novel structure that is different from the one given by the γ-surface approach [213, 69]. As shown in top images of Figure 5.15, GB atoms shuffle along the z-axis to generate new structure units evenly distributed along the GB plane at a distance of approximately 9 Å. This structure is consistent with a recent finding by a grand canonical GB structure search technique [69]. A high-temperature molecular dynamics simulations with open surfaces also confirms that this structure is equilibrium at high temperature after phase transformations that accompanied with changes of atomic density at GB [69]. Also, this structure is found to be the ground-state GB structure for the $\Sigma33(118)[1\bar{1}0]$ with other W empirical potentials [69].

We next examine the $\Sigma43(335)[1\bar{1}0]$ and $\Sigma3(111)[1\bar{1}0]$ at the misorientation angle ϕ of 80.63° and 109.47°. As shown in Figure 5.15, our EA finds a novel GB structure with novel structure units aligned along the GB plane with spacing of 14.6 Åalong x-axis for the $\Sigma43(335)[1\bar{1}0]$. These local structure units consist of pairs of interstitial atoms at the GB plane, and these structures serve as extended grain boundary dislocation (GBD) to alleviate lattice misfit energy such that the rest atoms at GB are symmetrically coherent. This GB structure has $\mathrm{N}_{\mathrm{ex}}^{\mathrm{GB}}$ of -0.013 Å^{-2}. This new GB structure has not been reported for the STGBs at the misorientation angle of 80.63° in BCC metals. At the misorientation angle of 109.47°, our EA discovers a new GB structure of thickness of three atomic layers along z-axis, as shown in Figure 5.15, and this structure has atoms shifted along the x- and z-axis near the GB plane. This distorted phase exhibits a rich structural diversity in that multiple equivalent structures of different distortion of atoms exist near the ground-state. The GB energy is 2.357 J/m^2 for this GB structure, lower than the GB energy provided by γ-surface method [69]. This structure also matches the stable GB phases at thermodynamic equilibrium in recent high-temperature MD simulations with atom diffusion at GB [69].

We investigate the $\Sigma27(552)[1\bar{1}0]$ at the angle of 148.41° for the misorientation angle above 129.52°. As shown in Figure 5.15, the EA discovers a novel phase that is related to

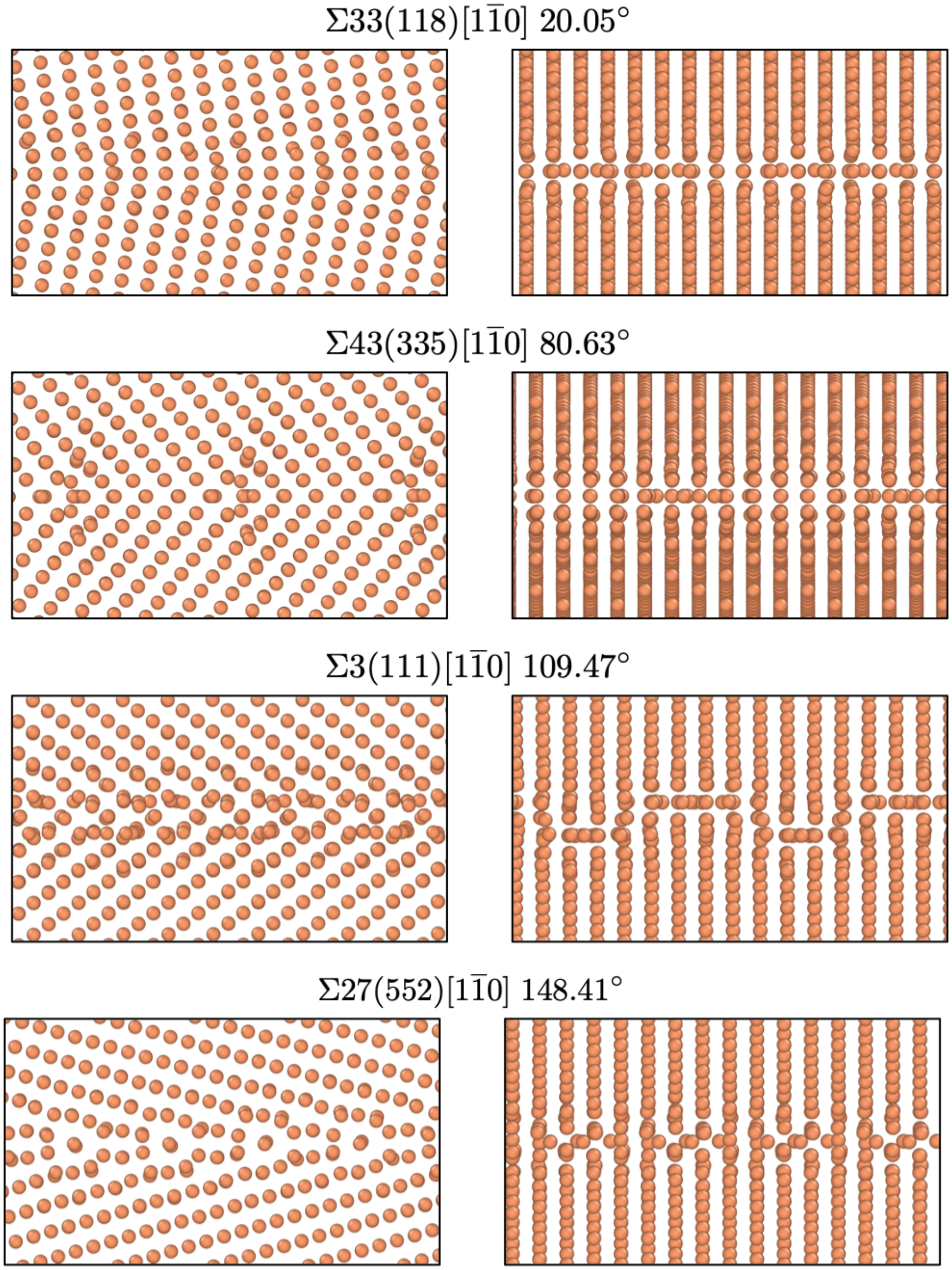

$\Sigma33(118)[1\bar{1}0]$ 20.05°

$\Sigma43(335)[1\bar{1}0]$ 80.63°

$\Sigma3(111)[1\bar{1}0]$ 109.47°

$\Sigma27(552)[1\bar{1}0]$ 148.41°

Figure 5.15: The projected views along z-(left images) and x-(right images)axis of ground-state STGB structures of the $\Sigma33(118)[1\bar{1}0]$ at ϕ = 20.05°, $\Sigma43(335)[1\bar{1}0]$ at ϕ = 80.63°, $\Sigma3(111)[1\bar{1}0]$at ϕ = 109.47°, and $\Sigma27(552)[1\bar{1}0]$ at ϕ = 148.41° obtained in the grand canonical ensembles at 0 K.

a shuffle of atoms along the z-axis. This novel structure has GB energy 2.493 J/m^2 that is 7% lower than the GB energy of 2.67 J/m^2 for structures from γ-surface method [68, 69]. The $\mathrm{N}_{\mathrm{ex}}^{\mathrm{GB}}$ of the GB phase is -0.009 Å^{-2} such that this GB structure has the almost same atomic density as the equilibrium BCC lattice. This GB phase has a high structural diversity since our EA detects multiple structures with similar energies, with the only difference on the local interstitial sites within the GB plane. The same GB structure was found with different potentials, and DFT calculations and high-temperature MD simulations confirmed its energy and thermodynamic stability [68, 69].

5.3.3 The $[1\bar{2}10]$ STGBs in HCP Mg

We apply the EA method to explore $[1\bar{2}10]$ STGBs in Magnesium (Mg). Since GBs perform a fundamental role in plastic deformation [229], many theoretical and experimental work investigated GBs in Mg or Mg alloys [252, 251, 107, 167, 279, 178]. Wang and Beyerlein comprehensively analyzed the correlation between the GB structures and tilt angles for $[1\bar{2}10]$ STGBs. In this work, we revisit the study of $[1\bar{2}10]$ STGB structures with our EA methods to validate the effectiveness of the EA in the HCP crystal structure.

We first examine the GB structures at tilt angles that correspond to the formation of twin boundaries (TBs). The TBs form a particular subclass of STGBs that satisfy mirror symmetry on the twinning plane, and the TBs are coherent with atoms belong to both grains that form the GBs. We applied the EA for the $(10\bar{1}3)[1\bar{2}10]$, $(10\bar{1}2)[1\bar{2}10]$, $(10\bar{1}1)[1\bar{2}10]$ and $(20\bar{2}1)[1\bar{2}10]$ at the misorientation angle of 63.99°, 86.28°, 123.83° and 150.12° respectively, and our EA validates that the TBs are their corresponding ground-state structures, as shown in Figure 5.16. The GB energy is 0.104 J/m^2, 0.122 J/m^2, 0.075 J/m^2 and 0.125 J/m^2 for the $(10\bar{1}3)[1\bar{2}10]$, $(10\bar{1}2)[1\bar{2}10]$, $(10\bar{1}1)[1\bar{2}10]$ and $(20\bar{2}1)[1\bar{2}10]$, respectively, and these energies are consistent with previous studies on the structures of TBs in HCP metals [215, 216, 164, 252, 131]. Moreover, the excess atoms per GB area $\mathrm{N}_{\mathrm{ex}}^{\mathrm{GB}}$ is 0.002 Å^{-2}, 0.001 Å^{-2}, -0.020 Å^{-2}, and 0.004 Å^{-2} for the $(10\bar{1}3)[1\bar{2}10]$, $(10\bar{1}2)[1\bar{2}10]$, $(10\bar{1}1)[1\bar{2}10]$

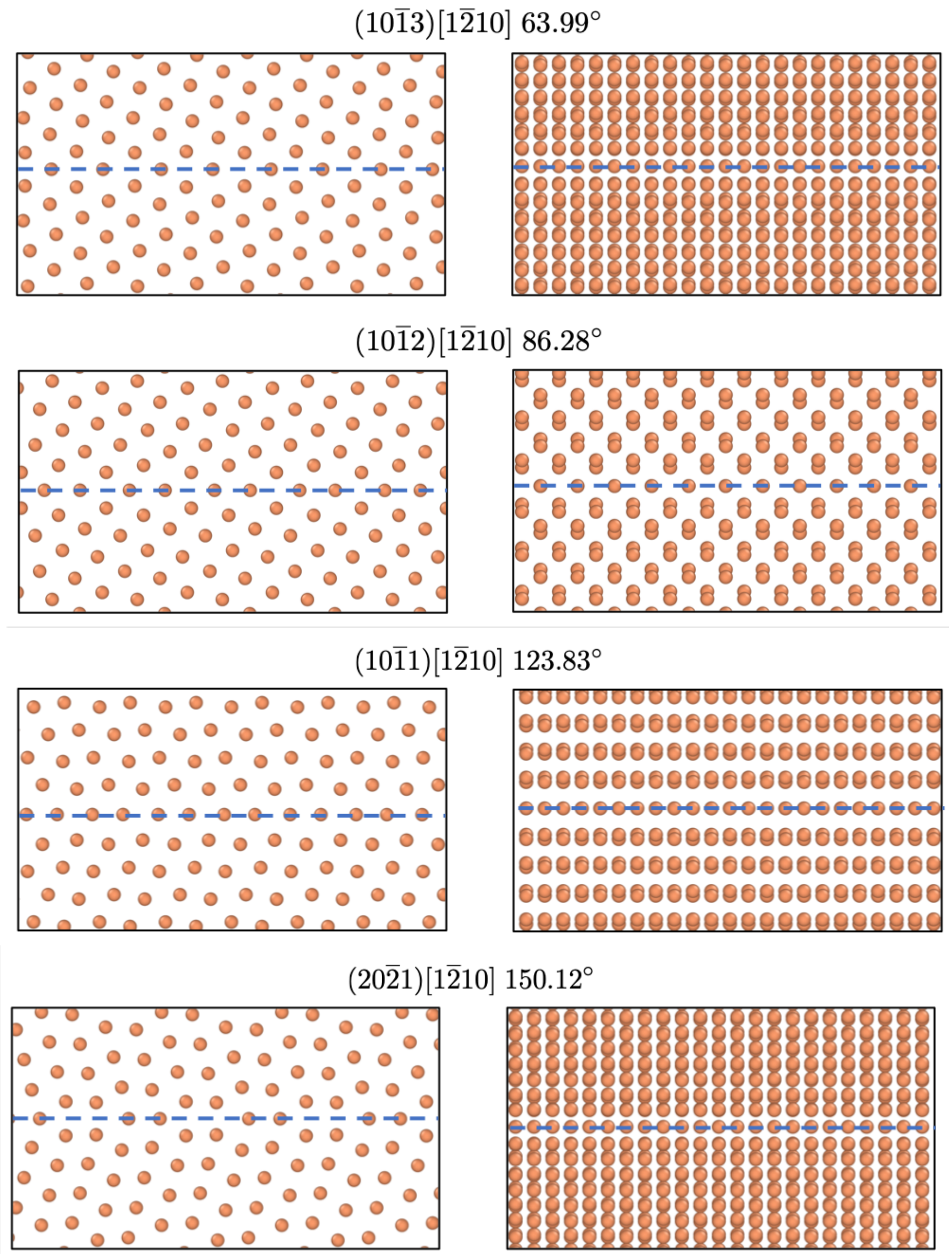

Figure 5.16: Two projected views along z-(left images) and x-(right images)axis of the ground-state STGB structures of the $(10\bar{1}3)[1\bar{2}10]$ at $\phi = 63.99°$, the $(10\bar{1}2)[1\bar{2}10]$ at $\phi = 86.28°$, the $(10\bar{1}1)[1\bar{2}10]$ at $\phi = 123.83°$ and the $(20\bar{2}1)[1\bar{2}10]$ at $\phi = 150.12°$ obtained the grand canonical ensembles at 0 K. All the four GBs have coherent twin boundary structures, and the blue dashed line indicates the twin boundary plane.

and $(20\bar{2}1)[1\bar{2}10]$, respectively. Most TBs have atomic density close to the perfect HCP lattice, except for the misorientation angle at 123.83°. The $(10\bar{1}1)[1\bar{2}10]$, energetically the most favorable GB, has the atomic density lower than the perfect HCP lattice.

$(10\bar{1}\,12)[1\bar{2}10]$ 17.75°

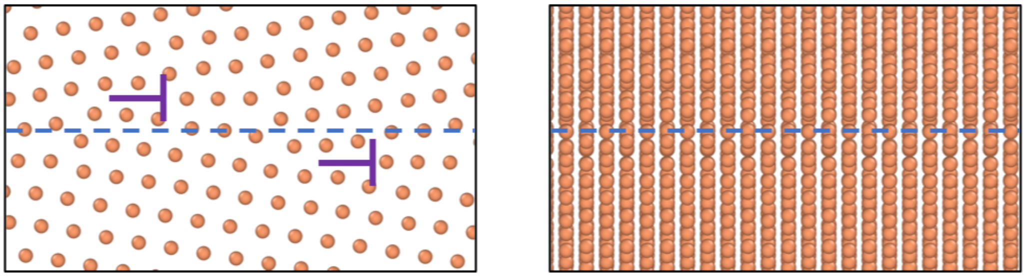

$(10\bar{1}8)[1\bar{2}10]$ 26.37°

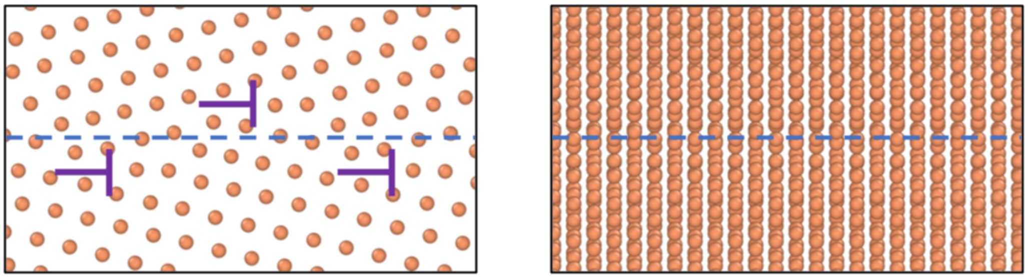

Figure 5.17: Two projected views along z-(left images) and x-(right images)axis of the ground-state STGB structures of the $(10\bar{1}\,12)[1\bar{2}10]$ at $\phi = 17.75^\circ$ and the $(10\bar{1}8)[1\bar{2}10]$ at $\phi = 26.37^\circ$ obtained the grand canonical ensembles at 0 K. Each purple sign indicates a single edge-type grain boundary dislocation, and the blue dashed line highlights the middle plane of each GB.

At low angles, our EA searches the $(10\bar{1}\,12)[1\bar{2}10]$ and $(10\bar{1}8)[1\bar{2}10]$ GBs at the misorientation angle of 17.75° and 26.37°, respectively. Our EA finds the ground-state structure with GB energies of 0.281 J/m^2 and 0.306 J/m^2 for the $(10\bar{1}\,12)[1\bar{2}10]$ and $(10\bar{1}8)[1\bar{2}10]$, respectively, and both GB energies are approximately 0.02 J/m^2 lower than values reported by the conventional γ-surface method [252]. As shown in Figure 5.17, the ground-state of the two low-angle STGBs consists of edge-type grain boundary dislocations (GBD) that form a tilt wall [97]. Moreover, unlike the conventional picture that tilt-wall consists of edge-type GBDs arranged to a straight line, our EA discovered the zigzag distribution of the GBDs along with the tilt GB plane. We consider each displacement along the GB plane normal of adjacent GBDs as a step [99], which is related to the passage of lattice dislocations thorough the GBs [194, 99, 100, 101]. A disconnection is defined as a combined step/dislocation defect [194, 99], and it is related to the interface defects in phase transformations [193, 1] and interactions between GBs and dislocations [100, 101]. It is worth for future research on the thermal and mechanical influence of the arrangement of GBDs at low angle $[1\bar{2}10]$ STGBs in HCP Mg. Our EA shows the N_{ex}^{GB} is -0.001 Å^{-2} for the $(10\bar{1}\ 12)[1\bar{2}10]$ and approximately 0 Å^{-2} for the $(10\bar{1}8)[1\bar{2}10]$. Accordingly, the transverse distribution of GBD at GBs may attribute to conservation of the atomic density at GB.

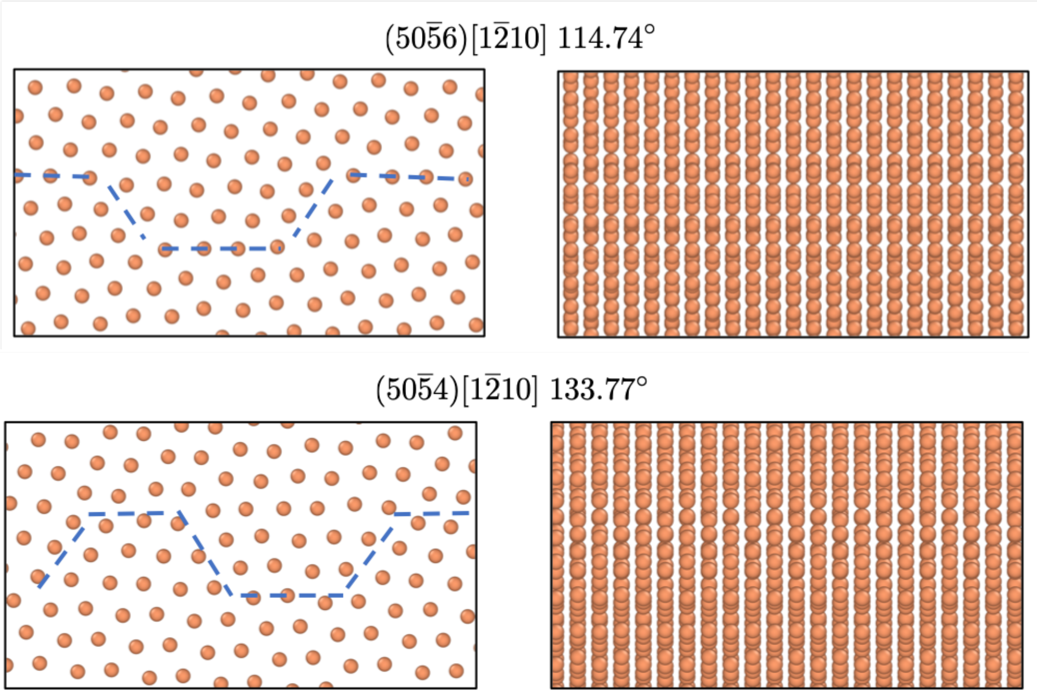

Figure 5.18: Two projected views along z-(left images) and x-(right images)axis of the ground-state STGB structures of the $(50\bar{5}6)[1\bar{2}10]$ and $(50\bar{5}4)[1\bar{2}10]$ at the misorientation angle of 114.74° and 133.77° obtained the grand canonical ensembles at 0 K. The blue dashed line indicates the GB plane that is characterized by the common neighborhood analysis [103].

We next increase the tilt angle to explore the STGB structures of the $(50\bar{5}6)[1\bar{2}10]$ and $(50\bar{5}4)[1\bar{2}10]$ at the misorientation angle of 114.74° and 133.77°, respectively. Our structure search shows the GB energy of their ground-state structure is 0.216 J/m^2 and 0.209 J/m^2 for the 114.74° and 133.77°, respectively. The ground-state structures discovered by our EA have GB energy approximately 0.03 J/m^2 lower than the ground-state GB energy reported by original γ-surface method [252]. The $\mathrm{N}_{\mathrm{ex}}^{\mathrm{GB}}$ is -0.010 Å^{-2} for the $(50\bar{5}6)[1\bar{2}10]$ and -0.012 Å^{-2} for the $(50\bar{5}4)[1\bar{2}10]$. As exhibited in Figure 5.18, the STGB plane is semi-coherent for the GB structures of both $(50\bar{5}6)[1\bar{2}10]$ and $(50\bar{5}4)[1\bar{2}10]$. Identified by the common neighborhood analysis [103], the GB plane consists of pure cleavage steps that are 1-2 nm in height and depth for the GBs with ϕ of 114.74° and 133.77°, as indicated by the blue dashed line in Figure 5.18. The lattice along the step surface parallel to the GB planes resemble the complete coherent $(10\bar{1}1)[1\bar{2}10]$ TB, which has the minimum GB energy for all $[1\bar{2}10]$ STGBs in HCP Mg. Atoms near the step surface normal to the GB plane deviate from equilibrium lattice sites to alleviates the lattice mismatch due to the tilt orientation varying from the perfect twining angle 123.83°. On the other hand, the conventional γ method predicts the GB structures that are straight tilt walls of GBDs aligning along the GB plane [252]. Therefore, our EA shows that the semi-coherent GB consisted of $\sim$ 1 nm thick steps can decrease the GB energy to be lower than a straight interface.

5.3.4 Predictions of metastable GB structures

Our package can output not only optimized ground-state GB structures but also a spectrum of metastable GB structures near the ground state. For example, Figure 5.19 shows GB energies of metastable GB structures recorded in our package during the EA search of the GB $\Sigma27(552)[1\bar{1}0]$ in BCC W. Our EA records GB structures of various atomic densities at GBs, which are evaluated by the average excess number of atoms at GB per unit simulation cell in Figure 5.19. For each value of GB density (the average excess number of atoms labeled in the x-axis of Figure 5.19), there are many variants of metastable structures of GBs with a spectrum of GB energies (labeled in the y-axis of Figure 5.19). These results are consistent with the recent discovery that the vast multiplicity of GB states show statistical properties in the description of GB statistical-mechanics [89]. Beyond pure metals, atomistic simulations showed that the GB segregation concentrations and energies

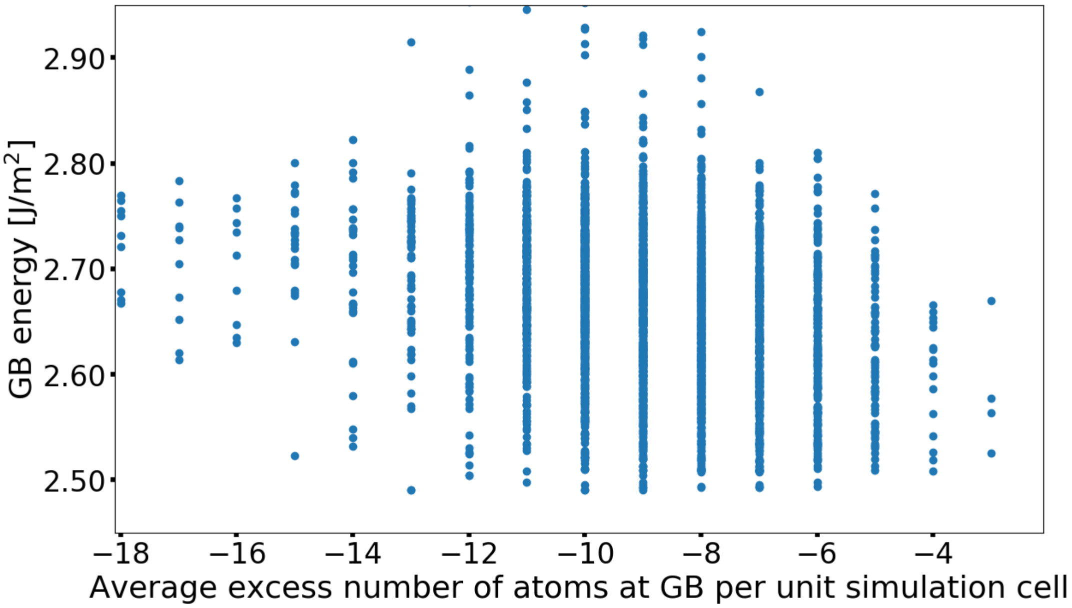

Figure 5.19: A spectrum of stable/metastable GB energies at $\Sigma 27(552)[1\bar{1}0]$ at $\phi = 148.41°$ in BCC W

for solute atoms form a spectrum of normal-like distribution in polycrystals [250]. Our package generates a spectrum of stable or metastable states GB structures that can serve as the foundation for grand canonical Monte Carlo simulations on GB segregation and other GB properties, which have been shown to have a critical influence on ductility and strength [206, 207, 137, 229].

5.3.5 Simulations of Tensile Loading on $[1\bar{2}10]$ STGBs in HCP Mg

To demonstrate the effects of GB structures and properties on plastic deformation, we applied MD simulations of tensile loading on selected Mg $[1\bar{2}10]$ STGBs using both the EAM [146] and MEAM potential [48] that generated the same GB structures as illustrated in the last section. In the MD tensile simulation, we enlarged the GB supercell so that the simulation cell was at least 150 Å along the x-axis, 500 Å along the y-axis and 120 Å along the z-axis. We applied periodic boundary conditions (PBC) along the x- and z-axis, and created free surface along the y-axis.

Before the tensile, we performed thermostatting and barostatting on the system until

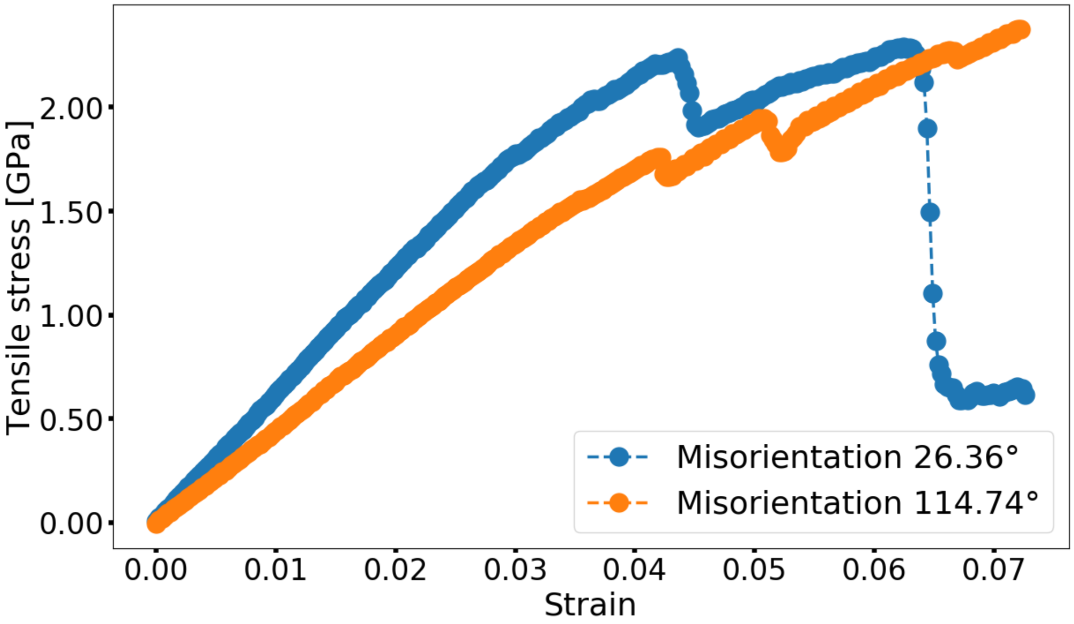

Figure 5.20: The tensile stress strain curve for MD tensile normal to the planes of the GB $(10\bar{1}8)[1\bar{2}10]$ at the misorientation angle ϕ = 26.37° and $(50\bar{5}6)[1\bar{2}10]$ at the misorientation angle ϕ =114.74° based on Mg EAM potential [146].

it reaches NPT ensemble of zero external pressure and 300 K. We then applied tensile of constant strain rate 10^7 s^{-1} along the y-axis at NVT ensemble at 300 K. The simulation timestep is 1 femtosecond throughout the MD simulations.

Figure 5.20 shows the stress-strain curves of MD tensile on the GB $(10\bar{1}8)[1\bar{2}10]$ at ϕ = 26.37° and the GB $(50\bar{5}6)[1\bar{2}10]$ at ϕ =114.74° based on Mg EAM potential [146]. For both GBs, the plastic deformation starts to activate at the strain of between 0.02 to 0.03 indicated by the slope change of stress-to-strain curves. However, the stress curve for the $(10\bar{1}8)[1\bar{2}10]$ GB has a large drop compared with the $(50\bar{5}6)[1\bar{2}10]$ GB, and the stress variation of each curve shows different plastic deformation mechanisms for both GBs. As shown in Figure 5.21 of the atomistic structure evolution at the $(10\bar{1}8)[1\bar{2}10]$ GB, the GB generates the $(10\bar{1}2)$ twin embryos on both sides of the GB, as shown at the strain of approximately 0.024. Similar twin embryos nucleation was observed at low angle STGBs when interacting with external dislocations [251]. The twin embryos formed from the dissociation of GBDs distributed in a zigzag pattern, as shown in Figure 5.17. The

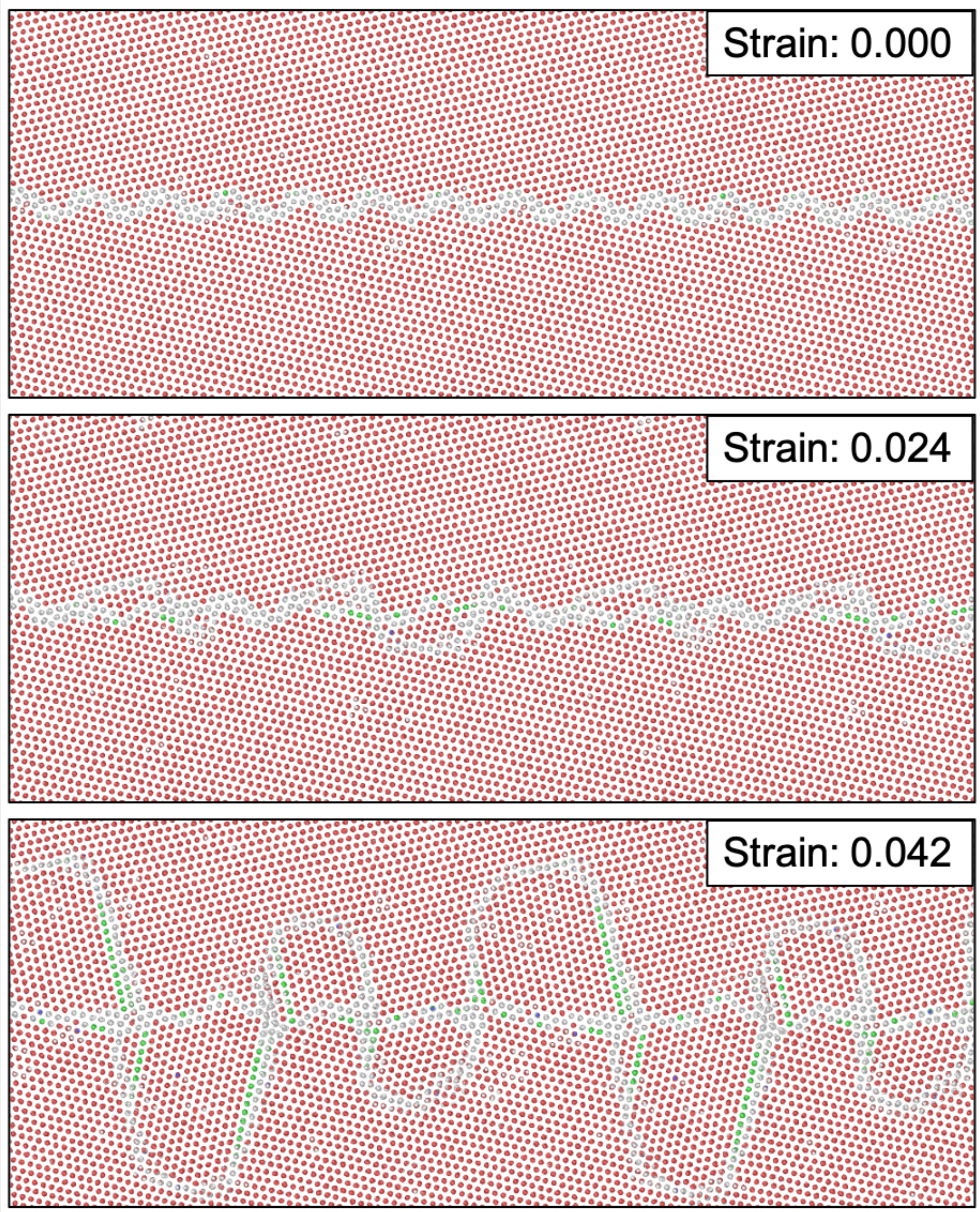

Figure 5.21: Atomistic structure evolution near the GB $(10\bar{1}8)[1\bar{2}10]$ at the misorientation angle of 26.37° during increasing tensile strain normal to the GB plane at 300 K based on Mg EAM potential [146].

twin embryo grows to the twin nucleus that expands further to generate sizeable plastic deformation when the tensile strain increases, as shown at the strain of 0.042 in Figure 5.21. The significant embryo growth is consistent with the stress drop in the stress-strain curve, and the twin nucleation indicates the resolved shear stress for dislocation activation is larger

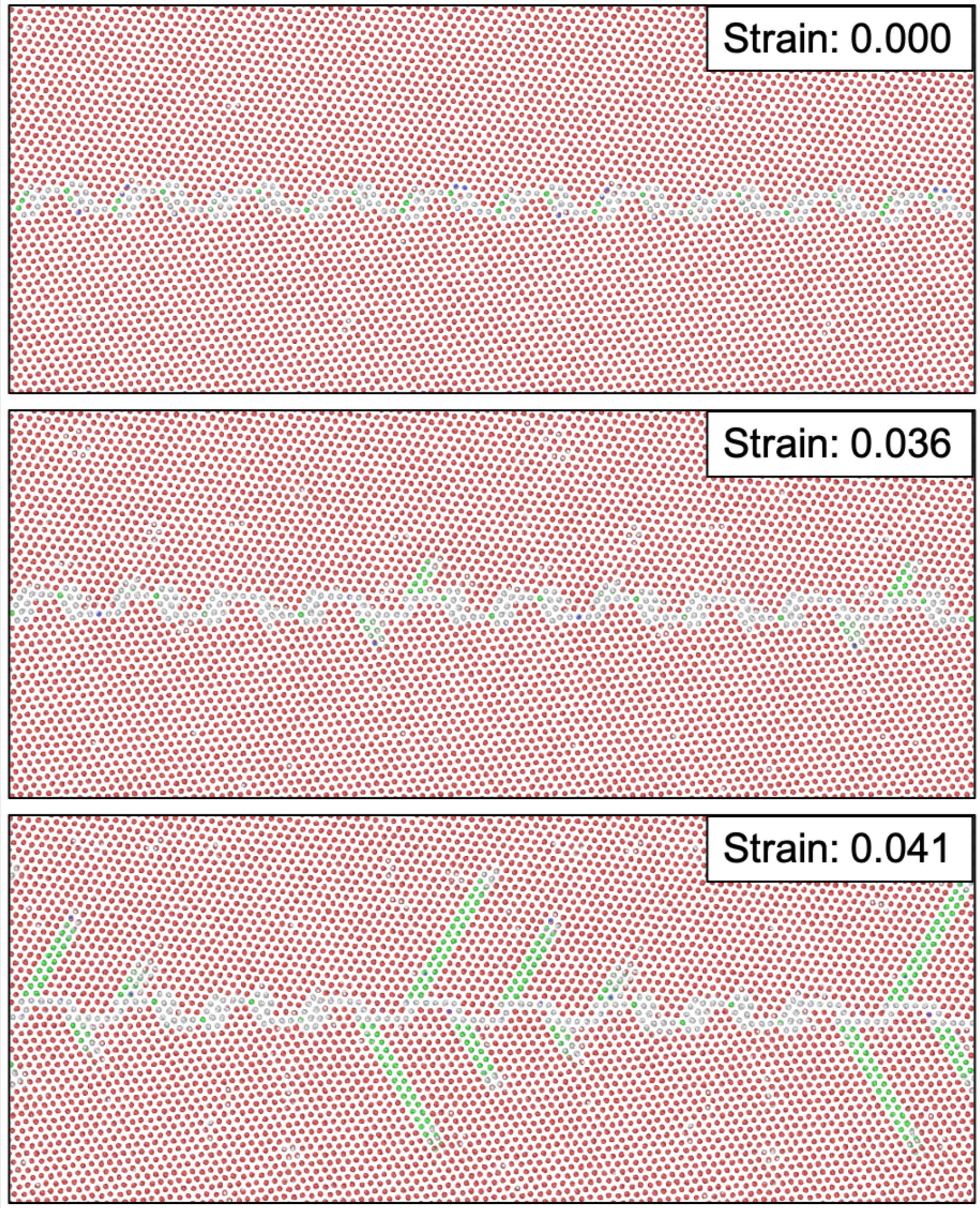

Figure 5.22: Atomistic structure evolution near the GB $(50\bar{5}6)[1\bar{2}10]$ at the misorientation angle of 114.74° during increasing tensile strain normal to the GB plane at 300 K based on Mg EAM potential [146].

than the counterpart for twin nucleation at Mg $[1\bar{2}10]$ STGBs with low misorientation angles. This deformation twinning at GBs relieve inelastic strains and could increase the ductility of polycrystalline hexagonal metals without $\langle c + a \rangle$ pyramidal slip [110].

As shown in Figure 5.18 and 5.22, the $(50\bar{5}6)[1\bar{2}10]$ GB consists of basal stacking faults interleaved with $(10\bar{1}1)[1\bar{2}10]$ twinning boundary segments. At the strain of 0.036, 1/3 $\left\langle 10\bar{1}0 \right\rangle \{0001\}$ partial dislocations nucleates from the GB to glide along the basal plane, leaving FCC stacking fault layers, indicated by atoms in green color. The leading partial dislocations glide on the basal plane away from the GB when the elongation strain increases, leaving an array of stacking fault layers, as shown at the strain of 0.041 in Figure 5.22. In comparison to the low misorientation angle GB $(10\bar{1}8)[1\bar{2}10]$, the $(50\bar{5}6)[1\bar{2}10]$ favors dislocation slip over deformation twinning to release tensile stress normal to the GB plane, partially because the Schmid factor increases for the resolved shear stress on the basal dislocation slip $\left\langle 1\bar{2}20 \right\rangle \{0001\}$ when the misorientation angle increases. The atomistic structure of GBs are also related to the plastic deformation mechanism under tensile loading along the GB plane normal direction. The $(10\bar{1}8)[1\bar{2}10]$, have twin embryo easily nucleated at slight strain, while the $(50\bar{5}6)[1\bar{2}10]$ GB structure contains stacking faults that facilitates the dislocation nucleation from the GB.

Systematic MD simulations on tensile loading of more $[1\bar{2}10]$ STGBs in Mg were performed. Figure 5.23 shows the critical tensile stress at the start of the plastic deformation of these GBs during the MD tensile tests using both the EAM [146] and MEAM potential [48]. Results from both potentials show consistent results that the preferred deformation mechanism at low misorientation angles is deformation twining, as shown in Figure 5.21, and partial dislocation glide on basal planes dominates the plastic deformation at increased misorientation angles. In addition, since it was reported that GBs with a low static GB energy tends to resist slip transmission and nucleation at GBs [212], the critical tensile stress to activate plastic deformation was plot relative to the GB energy variation in Figure 5.23. It shows GBs of relative high GB energies are those with low misorientation angles and they tend to generate deformation twinning, while low energy GBs are those with high misorientation angles and they often induce dislocation slip.

Another remarkable result in Figure 5.23 is that the $(50\bar{5}6)[1\bar{2}10]$ 114.74° GB has a significant lower critical tensile stress in both potentials compared with other GBs with

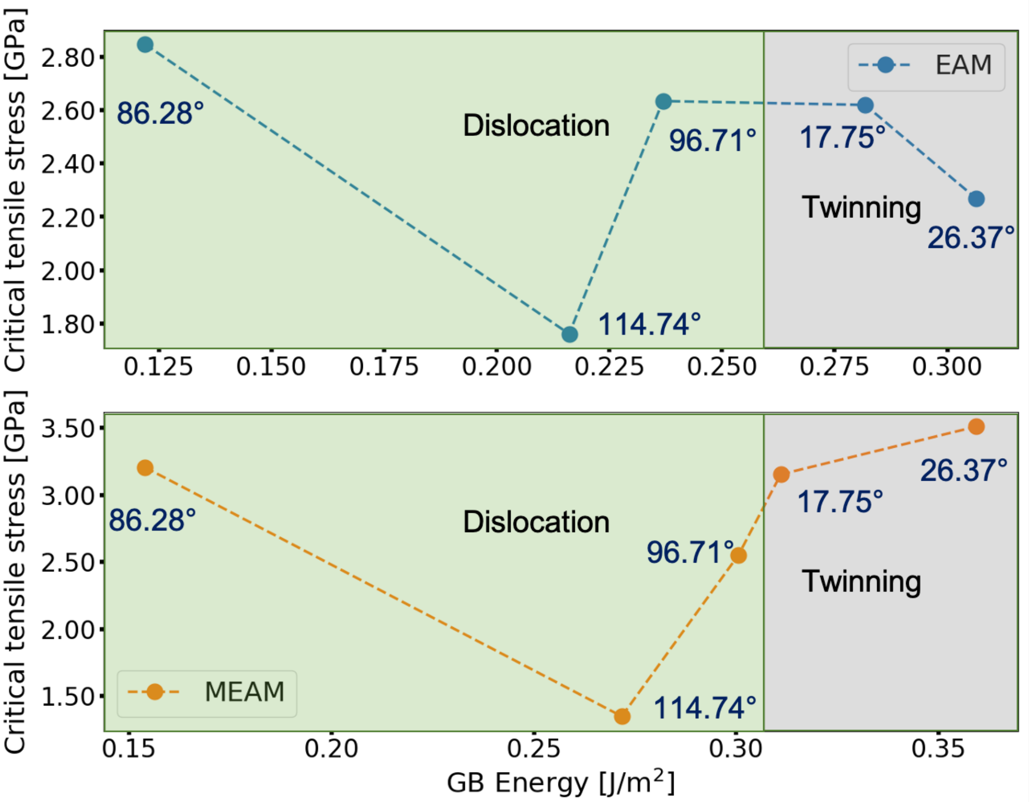

Figure 5.23: The critical tensile stress to activate plastic deformation in relation to the GB energy for [1$\bar{2}$10] STGBs with different misorientation angles using both the EAM [146] and MEAM potential [48]. The value of the misorientation angle for each GB is labeled in the figure.

either lower or higher GB energies. This GB structure has stacking fault segments due to partial dislocations on basal planes, as shown in Figure 5.18, so they have easy sources to generate more basal dislocations. As a result, our MD results suggest that there is no simple correlation between the GB energy and the critical tensile stress for the activation of dislocation and deformation twinning nucleation as suggested by previous MD simulations [212]. Other GB features, like certain GB structures that can enhance dislocation activities, should be considered to comprehensively understand the GB effects on plastic deformation.

5.4 Conclusion

In this work, we created an EA-based GB structure search code of novel mutation methods upon the exchange of internal atomistic structure segments. The package successfully explored symmetric tilt grain boundaries (STGB) in different metallic systems of various crystal structures to produce results consistent with recent progress on GB structures searches [67, 278, 69, 68, 17]. Moreover, our structure search discovered a distinct ground-state structure in the $\Sigma 43(335)[1\bar{1}0]$ for BCC W, GBs with a distribution of grain boundary dislocations (GBDs) at low misorientation angles of the $[1\bar{2}10]$ STGBs, as well as GBs in the shape of 1-nm thick steps, as shown in Figure 5.18, for the $[1\bar{2}10]$ STGBs in HCP Mg with high misorientation angles. Furthermore, our code can output a spectrum of metastable GB structures near the ground state, which is critical to describe the GB properties based on statistical mechanics [89]. In general, this EA-based GB structure search code is efficient and robust. From the efficient aspect, the nuclei-exchange-based structure mutation, as the critical development in our EA package, only employs linear time to scan, insert, and delete atoms. From the robust aspect, the nuclei exchange technique does not exert additional boundary constraints on the material systems. Therefore, beyond the GB structure, our EA based search package can solve general atomistic structure optimization problems such as perfect crystals, dislocations, interphase boundaries, and surfaces.

Finally, we performed benchmark MD simulations of tensile loading on symmetric tilt grain boundaries (STGB) in pure Mg generated by our GB structure search code using two different Mg interatomic potentials. The preliminary results suggest the critical stress for the nucleation of dislocations and deformation twinning from Mg GBs may depend on many factors of the detailed GB structures, such as misorientation angles, GB energies [212], and local GB structures that can enhance dislocation activities. More systematic simulations and analyses are required to obtain a clear and quantitative description on GB effects to dislocation/twinning activities and plastic deformation based on stable and metastable GBs generated by our code.

CHAPTER VI

Simulations of Dislocation-precipitate Interactions in Mg-Nd Alloys

Chapter V focuses on the interactions between deformation defects and typical two-dimensional defects such as grain boundaries. This chapter focuses on the interactions between dislocations and β_1 precipitates as three-dimensional defects during the plastic deformation of Mg-Nd alloys [105, 106]. The β_1 precipitates have a special ordered lattice structure, which increases the complexity of their effects on dislocation motions. We demonstrate a mixed approach of DFT calculations, MD simulations and experiments that reveals novel motion mechanisms for basal dislocations in Mg-Nd alloys. All experimental work in this chapter is from our collaborator Zhihua Huang [105, 106].

6.1 Introduction

Mg-RE alloys such as Mg-Nd, Mg-Nd-Y, Mg-Gd, and Mg-Gd-Y share a similar precipitation sequence, and their dominant strengthening mechanism is precipitation hardening. For Mg-Nd, the precipitation sequence is supersaturated solid solutions (SSSS) - Guinier-Preston (GP) zone - β''' - β_1(Mg_3Nd) - β($Mg_{12}Nd$) - β_e($Mg_{41}Nd$) [280, 190, 166]. β''' is a shearable coherent thin (5 nm) precipitate of nominal dimensions of 10 to 30 nm, as shown in Figure 6.1 [105]. Oppositely, β_1 has FCC structure with a $D0_3$ ordering, and it is

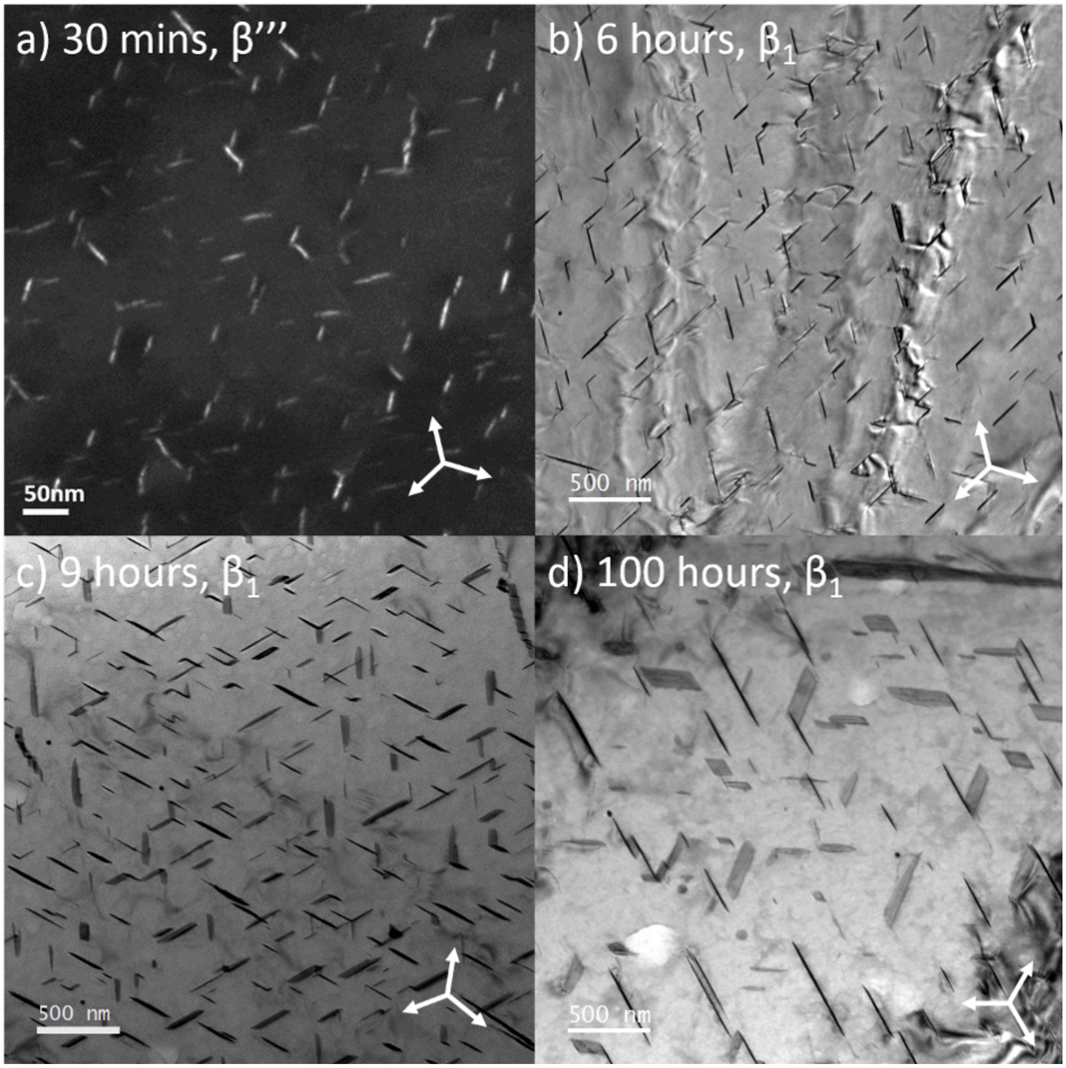

Figure 6.1: Dark field image a) and bright field image b-d) show microstructure and precipitate configuration for 30 minutes a), 6 hours b), 9 hours c) and 100 hours d) aging of Mg-Nd alloy. Fine β''' precipitates dominate the 30-min sample, and β_1 precipitates are profuse in other conditions. The view is close to [0001] direction, and the triad represent $\{1\bar{2}10\}$ direction. All aging is at 250 °C.

regarded as non-shearable precipitate [144]. The orientation between β_1 and Mg matrix is $\langle 111\rangle_{\beta 1} \,||\, \langle 1\bar{2}10\rangle_{\mathrm{Mg}}$ and $\{\bar{1}10\}_{\beta 1} \,||\, \{0001\}_{\mathrm{Mg}}$. β_1 precipitates are in shape of thin-plate with dimensions of approximately 130 nm $\times$ 10 nm $\times$ 310 nm, aligned on a $\{\bar{1}100\}_{\mathrm{Mg}}$ prismatic habit plane, as shown in Figure 6.1. Our recent TEM images show steps on the surface of β_1 precipitates, as shown in Figure 6.2, which indicates dislocations can cut through β_1 precipitates during deformation. Compared with easy-to-shear β''' precipitates,

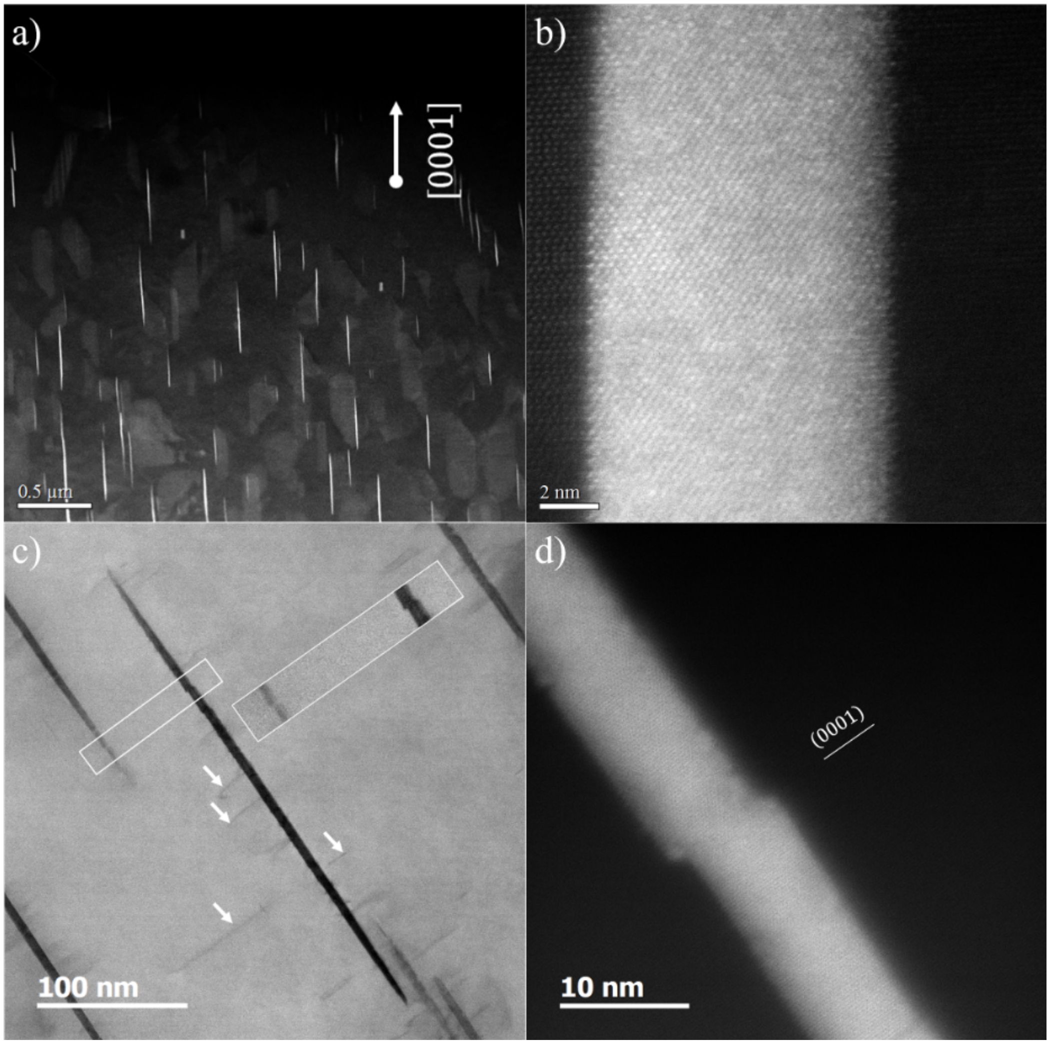

Figure 6.2: Undeformed samples show straight precipitates with an intact interface with the matrix in a) and b). Images c) and d) are taken from samples compressed 5% showing that the precipitate is cut by basal dislocations leaving an offset at the sheared interface. Image c) is an annular bright field (ABF) image and the thin dark lines (marked with arrows) are dislocations impinging on the precipitate. The inset in c) is a high magnification image of interface offsets. All images are viewed from $[1\bar{2}10]$ direction.

it is worthwhile to understand the critical stress for dislocation cutting β_1 precipitates to further estimate the strengthening property of β_1 precipitates.

For ductility, the basal slip is the most active to generate plastic deformation in Mg and Mg alloys [6, 264], it provides only two independent slip systems that are insufficient to satisfy von Mises criterion of five independent slip systems for arbitrary shape change in a random polycrystalline aggregate [232]. Mg and Mg alloys still have measurable ductility with slip systems involving $\langle a \rangle$ type dislocations. The tensile elongation-to-failure of many Mg alloys at room temperature is 15 to 25% [13], significantly higher than many materials with a limited number of slip systems, such as Be and NiAl, both of which rarely achieve greater than 3% tensile elongation-to-failure at room temperature. Koike et al. showed AZ31B alloys of a refined grain size could reach greater than 45% tensile elongation at room temperature with an abundance (40%) of non-basal $\langle a \rangle$ type dislocations [126], suggesting a profuse occurrence of cross-slip in the system. Agnew et al. [6] showed similar results and pointed out that the non-basal cross-slip could provide two extra independent slip systems $\left\langle 1\bar{2}10 \right\rangle \{10\bar{1}0\}$ to activate a total of four independent slip systems, which might account for increased room temperature tensile ductility, particularly under deformation conditions such as unconstrained in-plane tension [6].

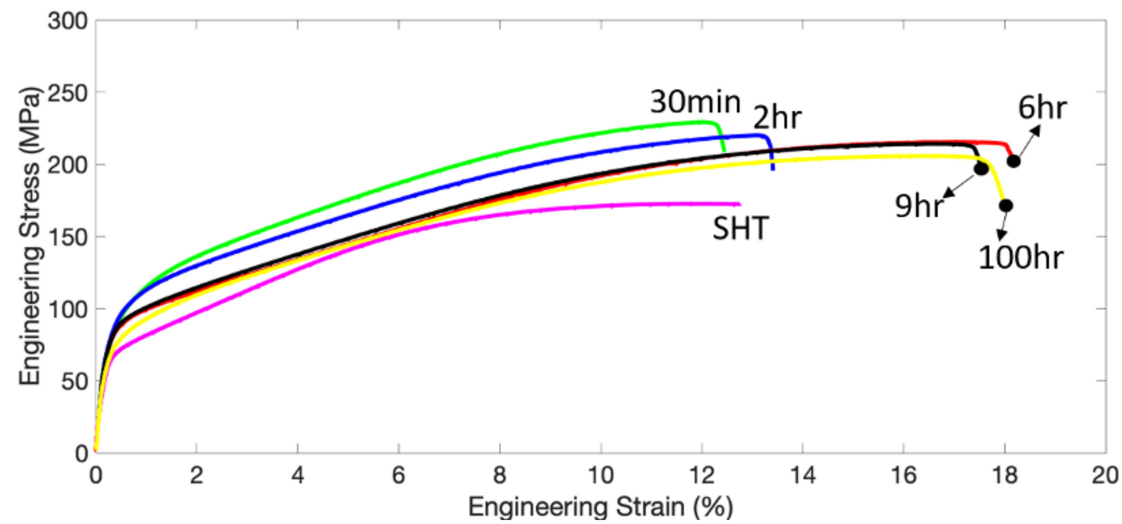

Figure 6.3: Engineering stress-strain curve of heat treated Mg-2.4wt.%Nd alloy in six aging conditions at 250 °C

Our recent tensile experiment and TEM characterization revealed non-basal $\langle a \rangle$ dislocation cross-slip in β_1 dominant microstructure, as shown in Figure 6.4, among Mg-2.4wt.%Nd alloy at six heat treatment conditions including solution heat treated (SHT) and aging at 250 °C for 30 minutes, 2 hours, 6 hours, 9 hours, and 100 hours. As shown in

Table 6.1: Critical engineering tensile strain to failure for heat treated Mg-2.4wt.%Nd alloy in six aging conditions at 250 °C

Microstructure	Sample conditions	Strain to failure
no precipitates	SHT	13.7% ± 1.3%
only β''' precipitates	30 mins	12.4%
only β_1 precipitates	6 hours, 9 hours, 100 hours	17.9% ± 0.3%

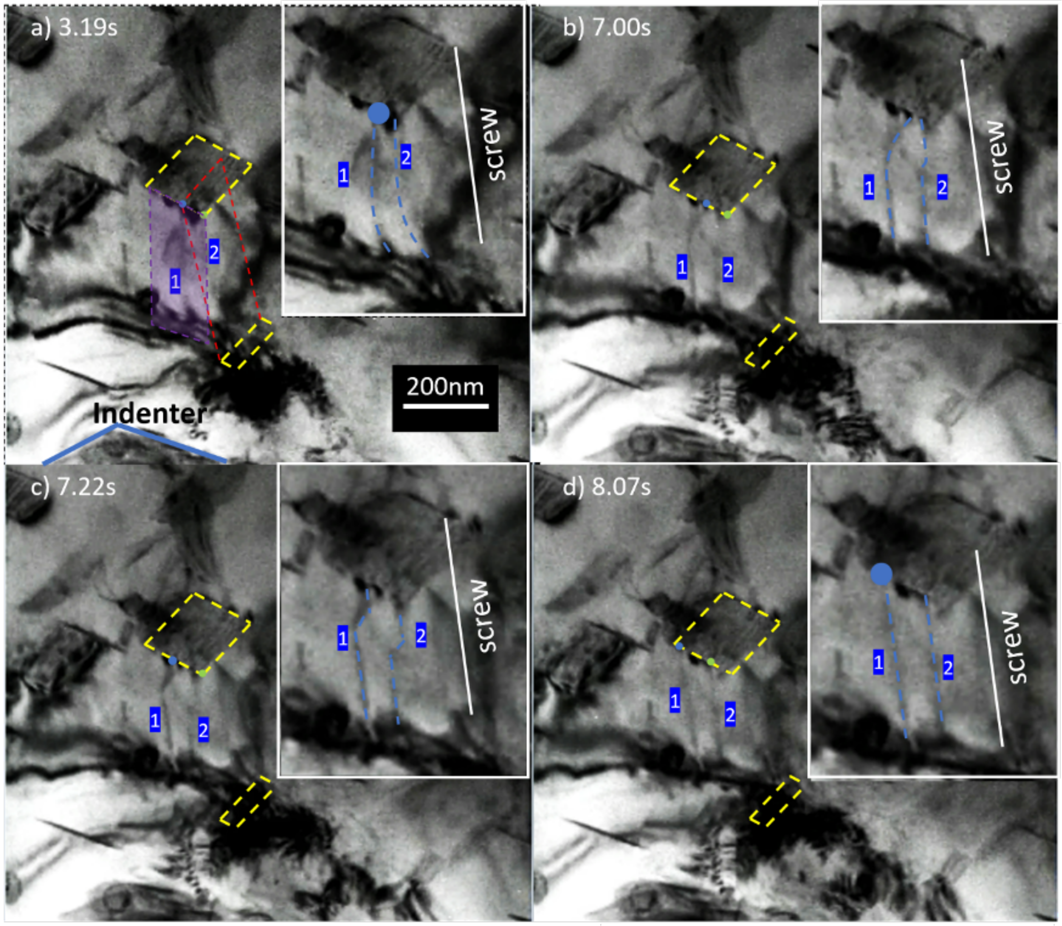

Figure 6.4: Sequence of dislocation interactions with β_1 precipitates from *in situ* experiments, viewed along $[1\bar{2}1\bar{3}]$. The bright field TEM images in a), b), c) and d) show the progression of the interaction at different times. Images show a cross-slipped dislocation pinned at the departure side of the precipitate, The pinning point of dislocations 1 and 2 are marked with blue and green dots. The dislocations of interest are marked by dashed blue line in the enlarged inset at top right of each image.

Table 6.1, the sample of 30-mins aging only has β''' precipitates, and it fails at strain 13.7% ± 1.3%. Samples at 6-, 9-, and 100-hour aging conditions have β_1 dominant microstructure, and they fail at strain 17.9% ± 0.3%, as shown in Figure 6.3. In addition, non-basal $\langle a \rangle$ dislocation cross-slip in Mg and Mg alloys has been observed and studied experimentally [41, 37] and computationally [268, 269]. Couret and Caillard [41] showed that the prismatic glide is controlled by thermally activated motion of rectilinear screw component, known as the FE mechanism [61]. Experiments have exhibited both basal and prismatic slip systems polycrystalline samples, despite the CRSS to activate prismatic slip is two orders of magnitude higher than basal slip at room temperature [6, 126, 127]. Recent MD simulations showed dislocation cross-slip at $Mg_{17}Al_{12}$ precipitate [143]. Experiments showed the precipitation-hardened Mg alloys could exhibit a comparable ductility even better than solutionized alloys [274, 275, 23].

In this work, we start with calculating the CRSS for dislocation cutting the precipitates based on a theoretical model to analyze the dislocation pile-up phenomenon. We then apply MD to directly simulate interactions between the β_0 precipitates and single edge or screw dislocation to understand the mechanism of the dislocation cross-slip.

6.2 Computational methods

6.2.1 DFT calculations for stacking fault energy

We used the VASP [85] based on the PAW-PBE pseudopotentials [130, 182]. Our calculation supercell size was 5.25 Å × 7.41 Å × 114.37 Å, containing with 108 Mg atoms and 36 Nd atoms and 20 Å vacuum along z-direction. The supercell axes were x || $[\bar{1}10]$, y || [001], and z || [110] in Cartesian coordinates. We sampled 13 × 9 × 1 k points by the Monkhorst-Pack method and used 350 eV as the cutoff energy for the plane-wave basis set. Due to crystal symmetry, we built antiphase boundary (APB) by shifting half of the supercell along with $1/4[11\bar{1}]$ and $1/2[11\bar{1}]$ vector on (110) plane in Mg_3Nd precipitates. We applied VASP to calculate the energies of the supercell before and after introducing APB, respectively. Ionic relaxation was performed to all atoms by conjugate gradient algorithm until total energy converges to 1e^{-4} eV. We estimated the APB energy by the total energy difference divided by the x-y plane area of the supercells.

6.2.2 Dislocation line tension in HCP lattice

To estimate dislocation line tension in HCP Mg, we employed anisotropic elasticity by

$$\Gamma(\theta) = \frac{\mathrm{b}^2}{4\pi}\left[\mathrm{K_e}\sin^2\theta + \mathrm{K_s} + \cos^2\theta + 2(\mathrm{K_e} - \mathrm{K_s})\cos 2\theta\right]\ln\frac{\mathrm{R}}{\mathrm{r_0}} \tag{6.1}$$

Where θ is the angle between Burgers vector and the dislocation line. $\mathrm{K_e}$ and $\mathrm{K_s}$ are energy coefficients for edges and screw dislocation. In hexagonal crystals, $\mathrm{K_e}$ and $\mathrm{K_s}$ are related to elastic constants by

$$\mathrm{K_e} = (\mathrm{C}^*_{13} + \mathrm{C}_{13})\left[\frac{\mathrm{C}_{44}(\mathrm{C}^*_{13} - \mathrm{C}_{13})}{\mathrm{C}_{33}(\mathrm{C}^*_{13} + \mathrm{C}_{13} + 2\mathrm{C}_{44})}\right]^{1/2}, \ \mathrm{C}^*_{13} = (\mathrm{C}_{11}\mathrm{C}_{33})^{1/2} \tag{6.2}$$

$$\mathrm{K_s} = \left[\frac{1}{2}\mathrm{C}_{44}(\mathrm{C}_{11} - \mathrm{C}_{12})\right]^{1/2} \tag{6.3}$$

Here, $\mathrm{r_0}$ is a small cut-off length that corresponds to the dislocation core radius, and it is independent of the surroundings of the dislocation and is usually within 1 to 4 Burgers vector length. R depends on surroundings of the dislocation, so it is not well defined [34, 10]. By convention, we adopted the approximation that $\ln(\mathrm{R}/\mathrm{r_0})$ equals 4, which was reported appropriate for alloys aged to near the peak strength condition [10]. The elastic constants we use are c_{11} = 63.5 GPa, c_{12} = 25.9 GPa, c_{33} = 66.4 GPa, c_{13} = 21.7 GPa, and $\mathrm{c}_4 4$ = 18.42 GPa measured by experiments [223].

6.2.3 MD simulations of dislocation-precipitate interactions

We set up two simulation boxes of $\sim$ 2.9 million atoms for dislocations interacting with β_1, one for a screw dislocation, as shown in Figure 6.5, and one for an edge dislocation, as shown in Figure 6.6. The supercell basis vectors for the screw dislocation setup were x || [$10\bar{1}0$], y || [0001] and z || [$\bar{1}2\bar{1}0$] with the size along each dimension as 46.36 nm, 41.90 nm and 33.14 nm, respectively, as shown in Figure 6.5. The basis vectors of the edge dislocation setup were oriented as x || [$1\bar{2}10$], y || [0001] and z || [$\bar{1}0\bar{1}0$], and the simulation box has dimensions of 47.87 nm × 46.53 nm × 33.20 nm, as shown in Figure 6.6. We applied PBC along x- and z-directions of the supercells, and we cut along the y-directions to make free surfaces of $(0001)_{\mathrm{Mg}}$, on which we applied the traction force to make the dislocation glide. In these periodic supercells, we created a periodic array of ⟨a⟩ dislocations on the basal plane in the equilibrium HCP lattice based on Stroh's formula, as

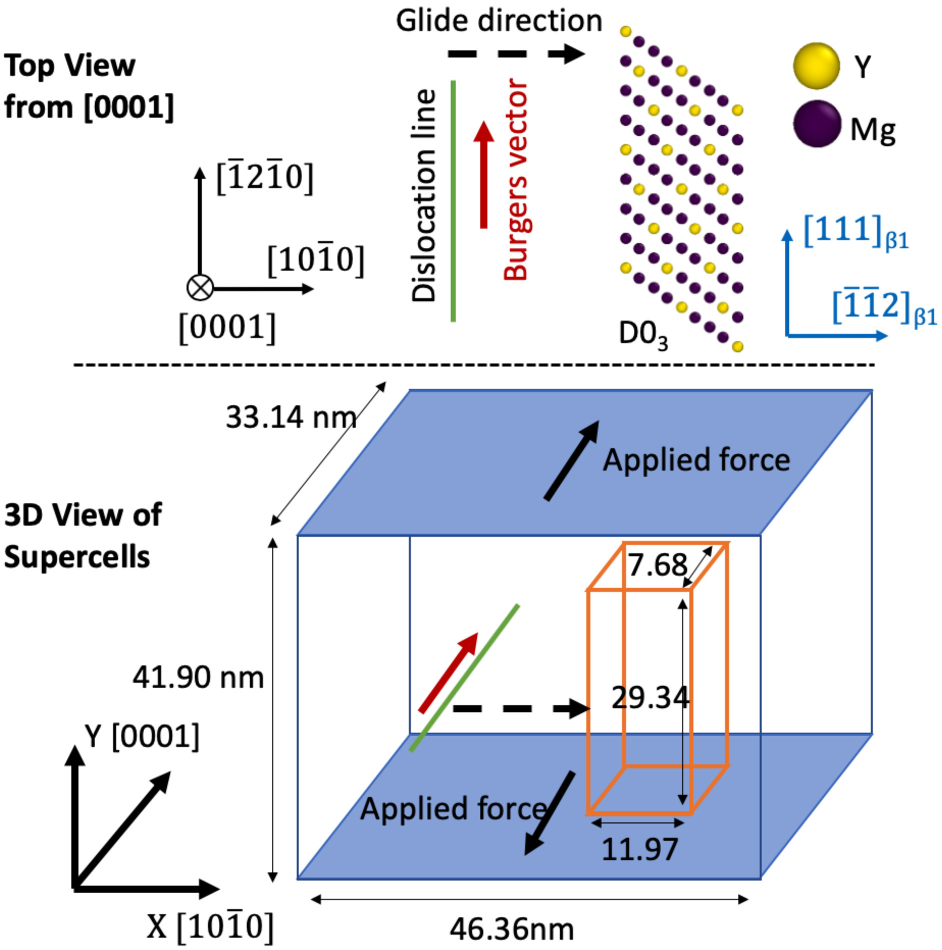

Figure 6.5: MD simulation setups for interactions between a single basal ⟨a⟩ screw dislocation and a β_1 precipitate. The blue dashed vectors indicates the lattice orientation of each β_1 precipitate; an orange cuboid indicates the β_1 precipitate in 3D view of the supercell in the bottom subfigure.

Equation 2.16, and we applied methods described by Bacon [16] to maintain the periodicity along the x-z plane after introducing dislocations. As shown in Figure 6.5 and Figure 6.6, to simulate a precipitate in our system, we cut a cuboid out from each supercell and replaced it by β_1 precipitate (Mg_3Y in $D0_3$ structure) of the same shape and size. The lattice orientation relationships between the Mg matrix and β_1 precipitate were $[111]_{\beta 1} \parallel [1\bar{2}10]_{Mg}$ and $(\bar{1}10)_{\beta 1} \parallel (0001)_{Mg}$, also shown in Figure 6.5. The size of the cuboid was 11.97 nm × 29.34 nm × 7.68 nm in the screw dislocation setup and 12.85 nm × 32.16 nm × 6.74 nm in the edge dislocation setup, respectively, as shown in Figure 6.6.

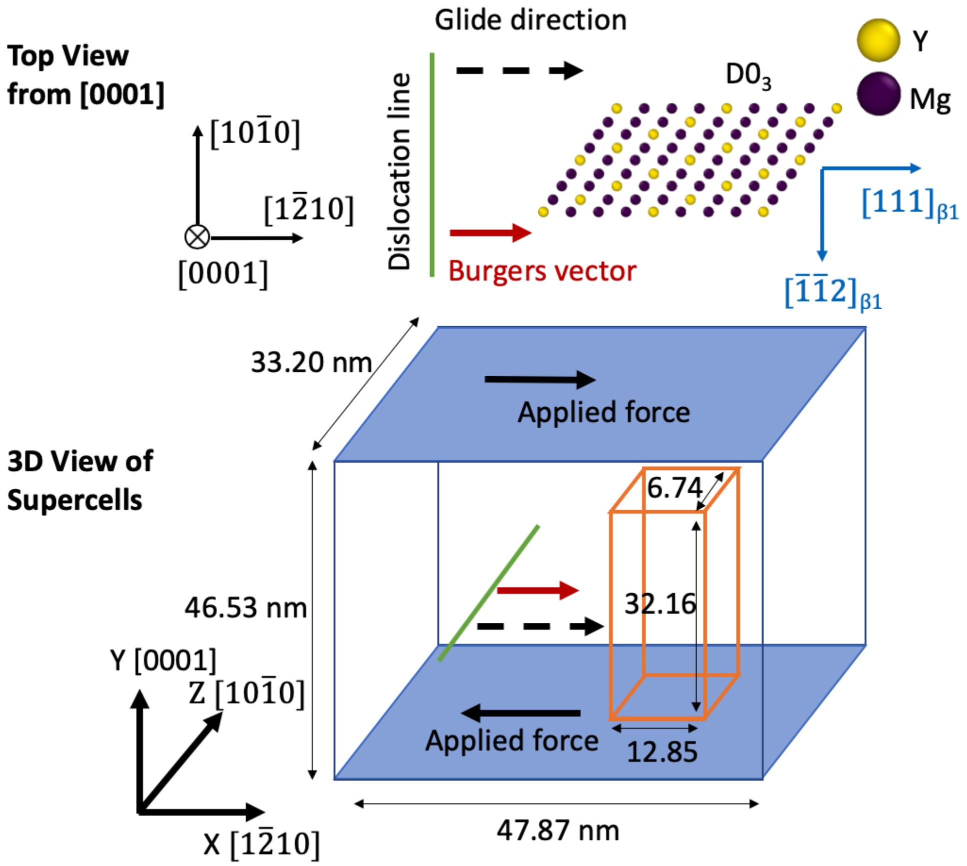

Figure 6.6: MD simulation setups for interactions between a single basal ⟨a⟩ edge dislocation and a β_1 precipitate. The blue dashed vectors indicates the lattice orientation of each β_1 precipitate; an orange cuboid indicates the β_1 precipitate in 3D view of the supercell in the bottom subfigure.

We determined the precipitate sizes by the inter-precipitate spacing estimated from our experiments. Our simulations disregarded the exact shape of precipitates due to the size limitation of the MD simulation supercells. Among six orientation variants of β_1 (Mg_3Nd) precipitates [145], we only simulated one orientation variant of β_1 precipitates to demonstrate the interaction between dislocation and precipices. We fully relaxed our simulation supercells before applied the traction force to make the dislocation glide. The equilibrium edge and screw $\langle a \rangle$ dislocations in the Mg matrix from our simulations exhibited the same core structures compared with those from the recent reportedly work [262].

Our MD simulations started with an isothermal-isobaric ensemble (NPT) based on the Nose-Hoover temperature thermostat and pressure barostat for 50 ps to make the system equilibrium at 300K. The system evolved in the canonical (NVT) ensemble at 300 K with external force applied on its free $(0001)_{\mathrm{Mg}}$ surfaces, as shown in Figure 6.5. To generate the shear stress to drive the dislocation glide, we applied surface traction by adding a constant force on the top and bottom surfaces at each time step. Based on the Peach-Koehler equation (Equation 2.11), the forces were applied along the z-direction in the screw dislocation setup, and along the x-direction in the edge dislocation setup, both along $(1\bar{2}10)_{\mathrm{Mg}}$, as shown in Figure 6.5 and Figure 6.6. The applied forces $\mathrm{F}_{\mathrm{app}}$ per atom is

$$\mathrm{F}_{\mathrm{app}} = \sigma_{\mathrm{shear}} \mathrm{A}_{\mathrm{xz}} / \mathrm{N}_{\mathrm{surf}} \tag{6.4}$$

In Equation 6.4, σ_{shear} is the shear stress component that drives dislocations to move, A_{xz} is the surface area of the x-z plane, and $\mathrm{N}_{\mathrm{surf}}$ is the number of atoms on the surface. Our MD simulations run in a timestep of 1 fs, and we applied constant shear stress of 200 MPa on the simulation box to drive the dislocation move.

6.3 Results and discussion

6.3.1 Theoretical estimation of CRSS for slip transmission across a β_1 precipitate

Interactions between dislocations and coherent precipitates include two forms: hard-contact interactions and soft-contact (or diffuse) interactions [11]. In precipitates that can form superlattice ordering, the hard-contact interactions refer to atomic-order strengthening that when dislocation shearing precipitates they induce antiphase boundaries inside the precipitates. The soft-contact interactions are size-misfit and modulus misfit interactions. Since hard-contact interactions contribute main resistance for dislocation cutting through precipitates, we focus on atomic-order strengthening to estimate the critical resolved shear stress for slip transmission across a β_1 precipitate.

The Mg matrix and β_1 precipitates have coherent lattice with the orientation relationship $[\bar{1}11]_{\beta 1}$ || $[11\bar{2}0]_{\mathrm{Mg}}$, and the 1/4$[1\bar{1}1]$ lattice vector in the β_1 precipitate matches the Burgers vector 1/3$[11\bar{2}0]$ of basal $\langle$a$\rangle$ dislocation in Mg matrix in terms of magnitude and direction. As shown in Figure 6.7 (a), a 1/4$[1\bar{1}1]$ Burgers vector generates an APB in the β_1 precipitate since it only consists 1/4 of a translational-symmetry vector in the β_1 lattice. Once a consecutive dislocation glides through, it adds another 1/4$[1\bar{1}1]$ shift to the precipitate and induces another APB. The whole energy landscape along $\langle 111 \rangle$ shifting requires NEB calculations to handle energy barriers. As our interest centers on APB energies rather than energy barriers, we used MD calculations based on MEAM potential [121, 7] to confirm the shape of energy landscape along $\langle 111 \rangle$ shift, and only applied DFT calculations for configurations near the local/global minimum in the energy landscape. As shown in Figure 6.7 (b), in the sketch landscape the local minimum energies correspond to APB energies, and our DFT calculations show the APB energy γ_{APB} is 0.0158 eV/Å^2 (253.1 mJ/m^2) for 1/4$[1\bar{1}1]$ shift and 0.0103 eV/Å^2 (165.0 mJ/m^2) for 1/2$[1\bar{1}1]$ shift.

For only one dislocation cutting the precipitates, based on average spacing and dislocation bows out model from Ardell, A.J. [10], we estimate the critical shear stress to cut

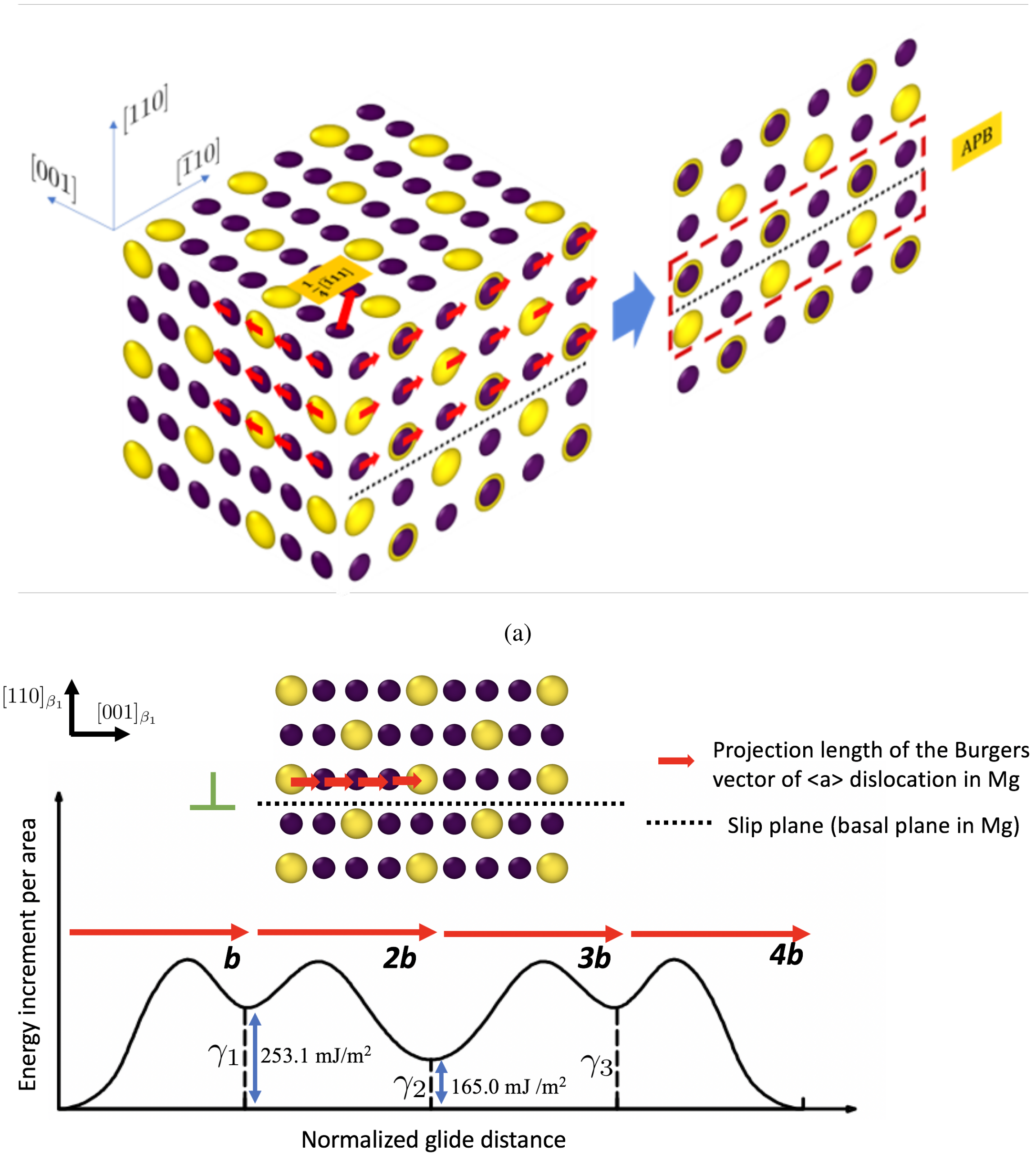

(a)

(b)

Figure 6.7: Illustration of the APB generated by 1/4[1$\bar{1}$1] Burgers vector in the lattice of a β_1 precipitate. Purple and yellow atoms stand for Mg and Nd, respectively. b) Sketch of energy increment when $\langle a \rangle$ basal dislocations consecutively cut the lattice of a β_1 precipitate

through a β_1 precipitate by

$$\tau_c = \frac{\gamma_{APB}}{b}(3\pi^2\gamma_{APB} f \langle r \rangle /(32\Gamma)^{1/2} \tag{6.5}$$

where γ_{APB} is APB energy per unit area for 1/4[$1\bar{1}1$] shift, f is volume fraction of precipitates and $\langle r\rangle$ is the average radius of precipitates and Γ is the dislocation line tension. The volume fraction f is 0.013 measured from TEM and the average radius is calculated by $\sqrt{wt}$, where w is the average width of precipitate (130 nm) and t is the average thickness of precipitate (10 nm). For the dislocation line tension Γ in hexagonal crystals, we adopt anisotropic elasticity, as Equation 6.1 [34] in which the line tension, $\Gamma(\theta)$, is a function of the angle θ between the dislocation line and the Burgers vector.

Furthermore, as shown in Figure 6.7 (b), the influence of second, third, and forth dislocation on CRSS are also profound. When a second dislocation cutting through the precipitates, it decreases APB energy; thus, the APB force assists the dislocation cutting through the precipitates. The multiple dislocation effects are difficult to calculate due to statistical distribution for dislocation-dislocation spacing and different extent of bowing. We consider relatively weakly coupled dislocations. The balanced forces acting on a group of four dislocations satisfy the equation

$$4\tau b = \gamma_1 \frac{d_1}{L_1} + (\gamma_2 - \gamma_1)\frac{d_2}{L_2} + (\gamma_3 - \gamma_2)\frac{d_3}{L_3} + (-\gamma_3)\frac{d_4}{L_4} \tag{6.6}$$

where γ_i (i=1,2,3,4) denotes APB energy after i-th dislocation cutting the precipitate, d_i/L_i denotes the fraction of a i-th dislocation inside precipitates. Due to lattice inverse symmetry along $\langle 111\rangle$, γ_3 equals to γ_1. Based on the energy landscape in Figure 6.7 (a), we apply the assumption that the first and third dislocation bow out due to resistance and the second and forth dislocation remain straight, details of similar analysis can be found in the work [10] (Order Strengthening section). And Based on the assumptions and combine the APB energies calculated by DFT, the CRSS for loosely coupled four dislocations is

$$\tau_{c_4} = \frac{\gamma_1}{4b}\left[\left(\frac{3\pi^2(\gamma_1) f \langle r\rangle}{32\Gamma}\right)^{1/2} - f\right] + \frac{\gamma_1 - \gamma_2}{4b}\left[\left(\frac{3\pi^2(\gamma_1 - \gamma_2) f \langle r\rangle}{32\Gamma}\right)^{1/2} - f\right] \tag{6.7}$$

where γ_1 and γ_2 are ABP energies per unit area for 1/4[$1\bar{1}1$] shift and 1/2[$1\bar{1}1$] shift respectively. Γ is the dislocation line tension and f is precipitate volume fraction. The calculation results for dislocation line tension, CRSS for a single dislocation, and CRSS for four loosely coupled dislocations based on $\langle a \rangle$ dislocation of different mixed angles θ ranging from 0° (for pure screw dislocations) to 90° (for pure edge dislocations) are in Table 6.2.

Table 6.2: Line tension Γ and critical shear stress τ_c for dislocations with different angles θ to cut through β_1 precipitate according to Equation 6.1 to 6.7

θ [degree]	$\Gamma(\theta)$ [eV / Å]	τ_c [MPa]	τ_{4c} [MPa]
0	0.72	250	72
22.5	0.645	264	76
45	0.464	310	91
67.5	0.283	398	117
90	0.208	465	137

On the other hand, our recent *in situ* indentation in TEM showed that basal $\langle a \rangle$ dislocations pile up at β_1 precipitates, and in some regions the pile-up dislocation number was up to six or seven, as shown in Figure 6.8. The *in situ* shows a Frank-Read-type source that generated dislocations that form a single-ended pile-up at the β_1 precipitate facets. We can estimate the number of allowed dislocations of single-ended pile-up [98] by

$$\mathrm{N} = \frac{\pi\sqrt{1-\nu}\,\mathrm{d}\tau}{\mathrm{Gb}} \tag{6.8}$$

where ν is Poisson's ratio of Mg (0.35), G is the shear modulus of Mg (16.5 GPa), b is the Burgers vector of the basal $\langle a \rangle$ dislocation (0.32 nm), τ is the applied shear stress from external force and d is the diameter of the confined space which is equal to 230 nm. With rearrangement of Equation 6.8, the local shear stress τ due to the pile-up is approximately 63 MPa. For comparison, the required shear stress to generate the dislocations bowing out a certain gap is given by the Frank-Read model [109]

$$\tau_{\text{F-R}} = \frac{\mathrm{Gb}}{\lambda} \tag{6.9}$$

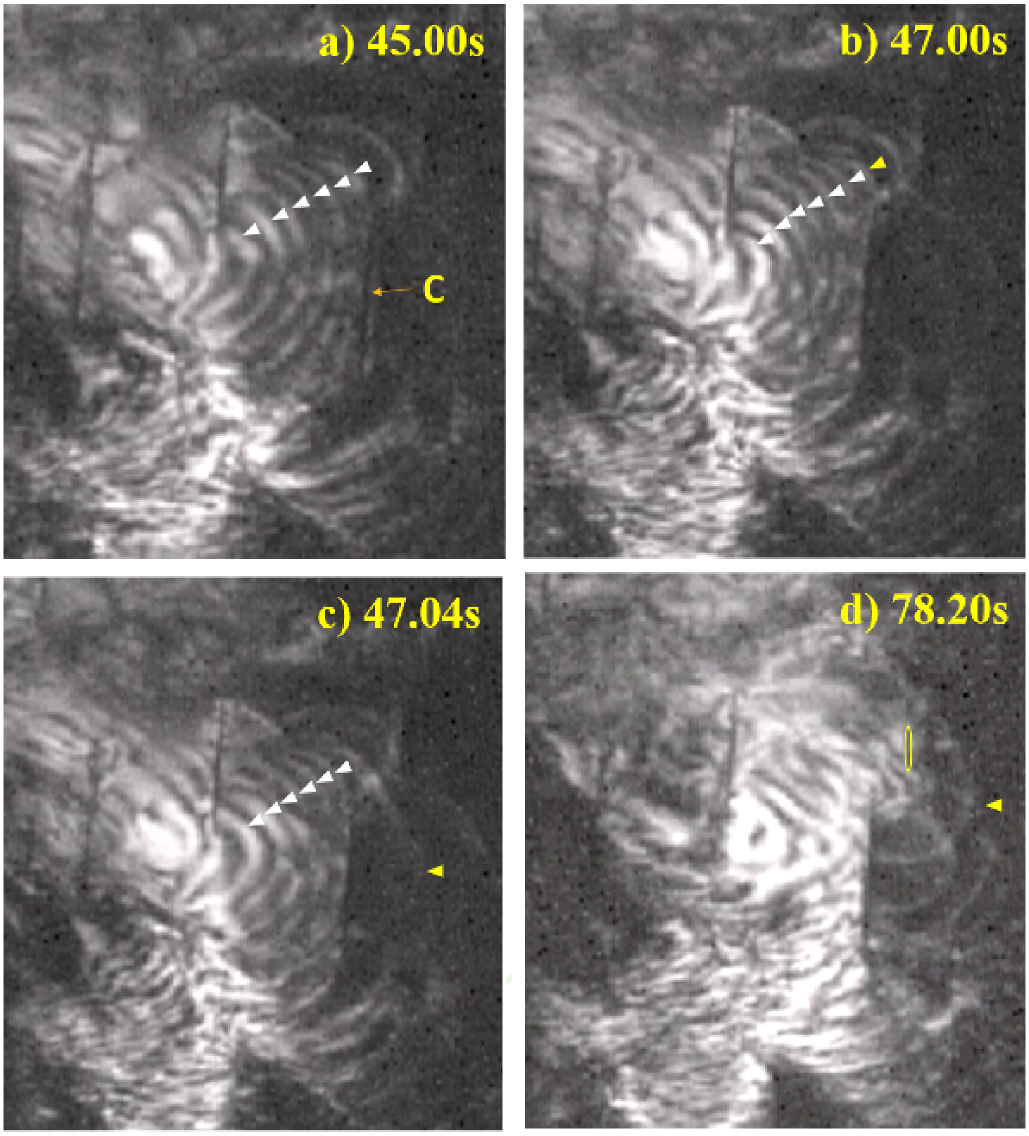

Figure 6.8: Images show how dislocations overcome the blocking precipitates. From a) to c), the number of piled-up dislocations is tracked with white arrowheads. The yellow triangle in b), c) and d) show that the leading dislocation escapes from the confined region.

where λ is the gap distance between two pinning points. For a 182 nm gap, estimated from 6.1, it needs 29 MPa shear stress to bow dislocations inside the confined region. However, the local applied shear stress increases to 63 MPa with the dislocations pile-up. The pile-up mechanism significantly improves the local strength level and indicates a higher strengthening comparing to dislocation looping.

The critical shear stress for shearing a β_1 precipitate is estimated by the stress on the leading dislocation Nτ. When N equals 7, the CRSS for shearing β_1 precipitate is 441 MPa. The experimental result is consistent with simulation result given in Table 6.2, in which the critical stress to shear a precipitate is estimated to range from 250 to 465 MPa depending on the character of the dislocation. The dislocations in the pile-up have both screw and edge components, evident from the curved dislocation lines observed in the in situ experiment. Thus, 441 MPa is a reasonable estimation for a mixed dislocation to shear a β_1 precipitate. This analysis indicates a very high stress at the front of the pile-up.

6.3.2 Verification of empirical potentials in MD simulations

We applied MD simulations with Mg-Y MEAM potential [7] to simulate Mg-Y system due to the lack of accurate Mg-Nd potentials. To validate if the Mg-Y potential can represent basic mechanical behavior of Mg_3Nd in $D0_3$ lattice, we calculated the two dimensional GSF [246] energy on the $(\bar{1}10)_{\beta 1}$ plane, which was parallel to the basal slip plane in Mg matrix in Mg-Nd alloys. As shown in Figure 6.9, a periodic unit cell on $(\bar{1}10)_{\beta 1}$ plane can be made by a vector of $[111]_{\beta 1}$ and a vector of $1/2[\bar{1}\bar{1}2]_{\beta 1}$. A vector of $1/4[111]_{\beta 1}$ is parallel and equal to a Burgers vector $1/3[1\bar{2}10]$ in Mg matrix, so four $\langle a \rangle$ type $1/3[1\bar{2}10]$ dislocations in Mg matrix consist a complete translational symmetry displacement along $[111]_{\beta 1}$ in a β_1 precipitate. Thus, GSF energies on the $(\bar{1}10)_{\beta 1}$ plane, especially those along $[111]_{\beta 1}$, are critical to evaluate the dislocation-β_1 interactions.

In the GSF calculations, we created a simulation box of size 12.63 × 102.50 × 8.93 nm, with three supercell basis vectors oriented as x || $[111]_{\beta 1}$, y || $[\bar{1}10]_{\beta 1}$ and z || $[\bar{1}\bar{1}2]$. We introduced free surfaces by adding 2 nm vacuum layer along y-axis. Atoms were relaxed along with y-direction while fixed displacements along x- and z-axis were applied to all atoms above a $(\bar{1}10)_{\beta 1}$ plane bisecting the y-axis to obtain the GSF energy landscape in Figure 6.9 (b). The GSF energies along $[111]_{\beta 1}$ are highlighted in the plot of Figure 6.10. Consistent with the crystal structure of $(\bar{1}10)_{\beta 1}$ plane in Figure 6.9 (a), a displacement

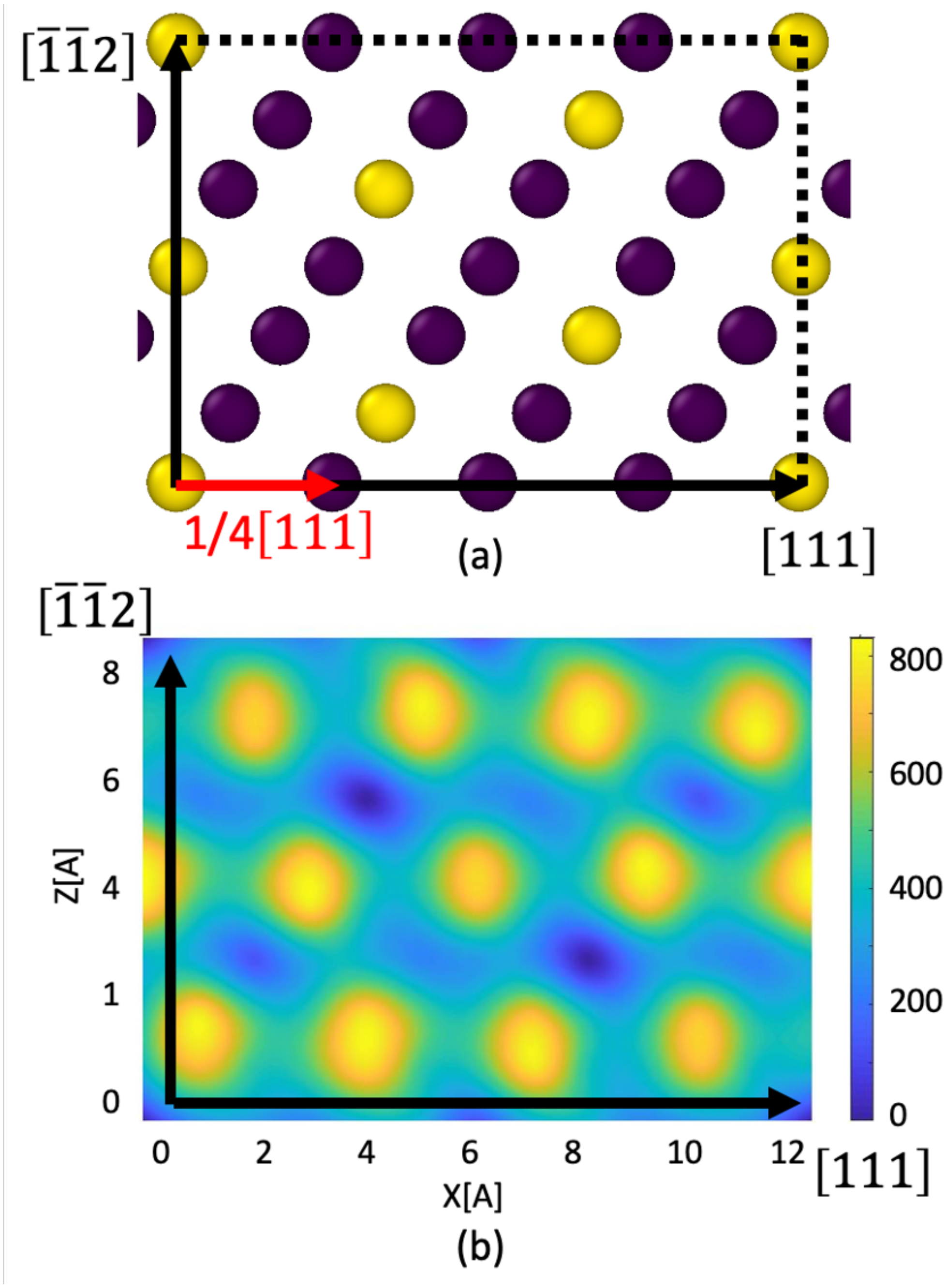

Figure 6.9: (a) A 2D periodic unit cell of $(\bar{1}10)_{\beta 1}$ plane defined by the dashed rectangle, where yellow atoms are Nd or Y. (b) the color contour of the GSF energy landscape on $(\bar{1}10)_{\beta 1}$ plane of D0$_3$ Mg$_3$Y, calculated from MEAM potential [7].

of 1/4$[111]_{\beta 1}$, 1/2$[111]_{\beta 1}$ and 3/4$[111]_{\beta 1}$ generates a local minimum-energy state that corresponds to an anti-phase boundary (APB) on the $(\bar{1}10)_{\beta 1}$ plane, respectively.

In addition, the APB energies corresponding to a 1/4$[111]_{\beta 1}$ and a 3/4$[111]_{\beta 1}$ displace-

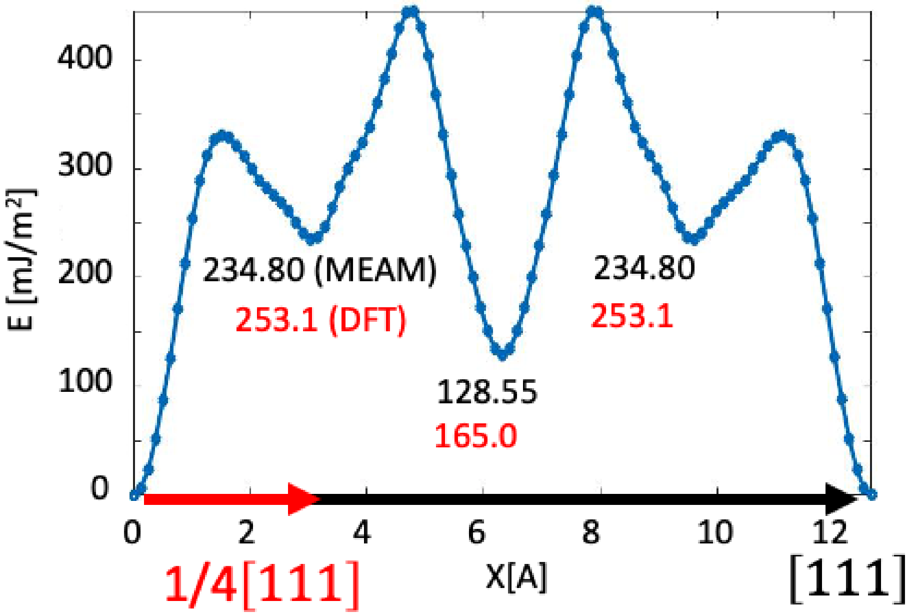

Figure 6.10: The corresponding GSF energy curve for the displacement along $[111]_{\beta 1}$ on $(\bar{1}10)_{\beta 1}$ plane. Numbers in red color are GSF energy values calculated from DFT for Mg3Nd [27], and values in black color are calculated from MEAM potential for Mg_3Y [31].

ments are equivalent (234.80 mJ/m^2) due to the crystal symmetry. The USF energy, which is the maxima occurring along $[111]_{\beta 1}$ GSF curve in Figure 6.10, is approximately 330 mJ/m^2 and 420 mJ/m^2 before the APB generated by 1/4$[111]_{\beta 1}$ and 1/2$[111]_{\beta 1}$ displacement, respectively. These USF and APB energies are much higher than their counterparts for USF and stable SF energies ($<$ 100 mJ/m^2) of partial dislocations on the basal plane in Mg matrix. In addition, the GSF energy landscape in Figure 6.9 (b) does not indicate another minimum energy path with lower energy barriers other than the displacement along $[111]_{\beta 1}$ shown in Figure 6.10. Thus, the main resistance for dislocation cutting the β_1 precipitate is the lattice friction due to high USF and APB energies. We also compared APB energies for the displacement along $[111]_{\beta 1}$ on $(\bar{1}10)_{\beta 1}$ plane generated by the Mg_3Y MEAM potential in the $D0_3$ structure to their counterparts generated by DFT calculations, as shown in Figure 6.7, for Mg_3Nd in the same structure. As shown in Figure 2(d), the APB values for 1/4$[111]_{\beta 1}$, 1/2$[111]_{\beta 1}$ and 3/4$[111]_{\beta 1}$ displacements from DFT calculations are close to MEAM results, and this suggests that the Mg-Y MEAM potential is suitable for a qualitative study of dislocation-precipitate interactions in Mg-Nd alloys.

6.3.3 β_1 precipitate-dislocation interaction

Due to lack of suitable Mg-Nd interatomic potential, we performed MD simulations using the Mg-Y MEAM potential [7]. As shown in Figure 6.7 (b) and Figure 6.10, we identify similar APB energies for the displacements of 1/4$[111]_{\beta 1}$, 1/2$[111]_{\beta 1}$ and 3/4$[111]_{\beta 1}$ on $(\bar{1}10)_{\beta 1}$ plane of D0$_3$ Mg$_3$Y by MS calculations and Mg-Nd by DFT calculations, which indicate the Mg-Y potential is suitable to demonstrate the dislocation interaction mechanism with D0$_3$ Mg$_3$Nd β_1 precipitates. For clarity, we use "Nd" rather than "Y" in the following text. Results in Figure 6.11 to Figure 6.14 were snapshots of MD simulations for edge and screw dislocation interacting with β_1 precipitates at 200 MPa flow stress.

Figure 6.11 shows the MD simulation snapshots that record atomic structures of the single basal $\langle a \rangle$ edge dislocation that interacts with the β_1 precipitate. We employ Ovito [227] to visualize configurations, and color atoms by CNA. Green stands for FCC, blue stands for BCC, and grey indicates unclassified structures. A zoom-out image at the right-bottom corner of each frame shows only Nd atoms (highlighted by yellow color) in Mg$_3$Nd precipitate to demonstrate the details of atomic displacement inside the precipitates. The basal $\langle a \rangle$ edge dislocation dissociated into two 1/3 $\langle 1\bar{1}00 \rangle$ partial dislocations and a stacking fault region (indicated by green color in Figure 6.11). Due to the applied shear stress of 200 MPa, the dislocation glides toward the precipitate and first contacts the precipitate at 38.8 ps of the simulation time, as shown in Figure 6.11 (a). Cutting the β_1 precipitate by the $\langle a \rangle$ dislocation can generate APB inside the precipitate, so the energy barrier to form the APB exerts a resisting force against dislocation cutting the precipitate. Due to the APB force, the dislocation starts bowing around the precipitate and forms interface dislocation on the precipitate-matrix interface. As indicated in the snapshot at 45.2 ps in Figure 6.11 (b), a part of the dislocation glides forward, while the other dislocation segments remain

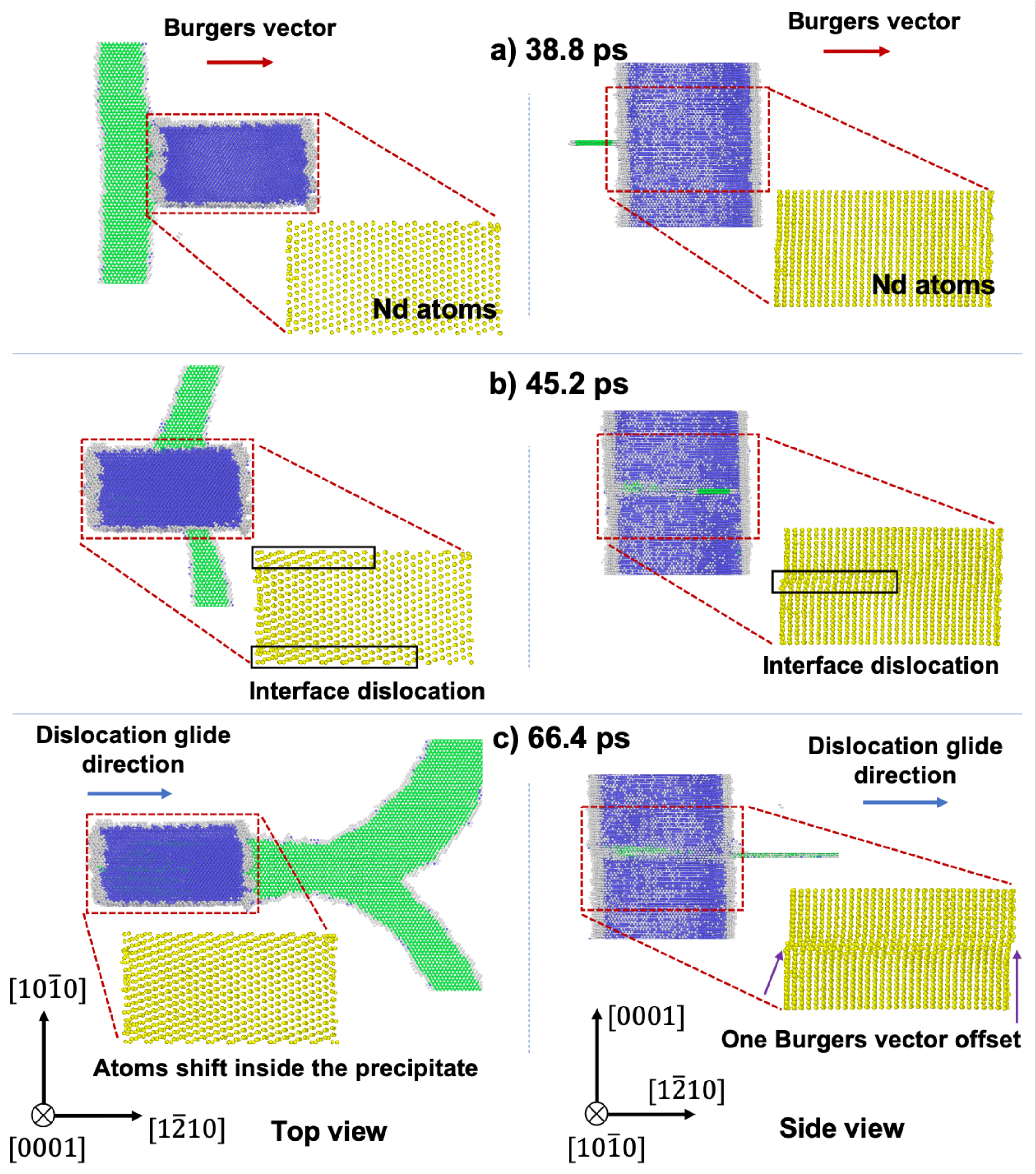

Figure 6.11: Snapshots of the process of the single basal edge ⟨a⟩ dislocation shearing the β_1 precipitate. a) The dislocation starts to meet the precipitate. b) The dislocation bows out and forms the interface dislocation on the precipitate-matrix interface. c) The dislocation almost cut through the precipitate. Each snapshot includes a top view in the top subfigure and a side view in the bottom subfigure.

blocked by the precipitate.

As a result, the dislocation forms two interface dislocations on the two sides of matrix-

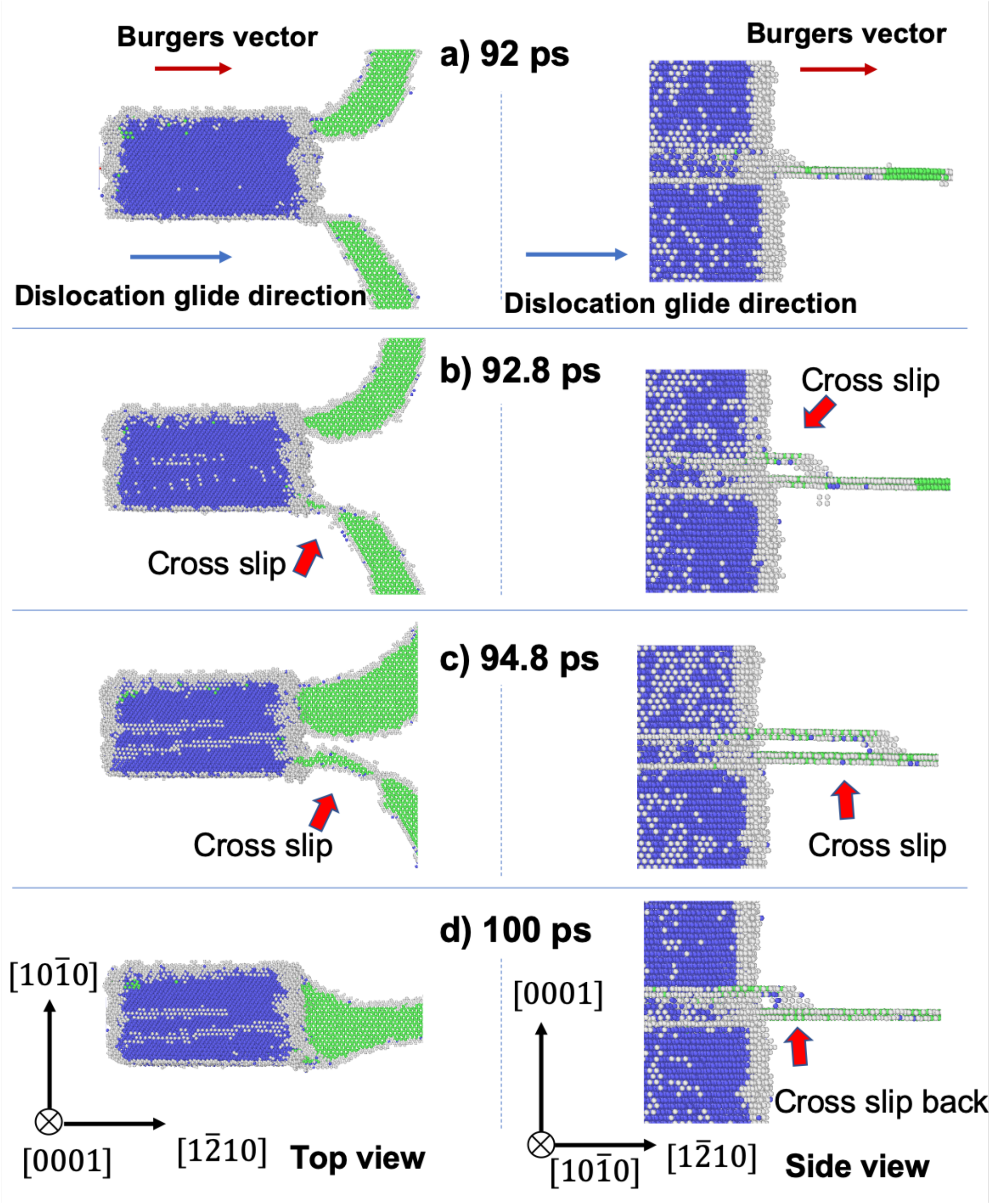

Figure 6.12: Snapshots of a single basal edge ⟨a⟩ dislocation shearing the β_1 precipitate for the second time. a) The dislocation forms a screw component on the precipitate-matrix interfaces perpendicular to [10$\bar{1}$0] due to the dislocation bow-out and interface glide. b) A part of screw component cross slips on the prismatic plane. c) The cross slipped dislocation segment glides on another basal plane. d) The dislocation cross slips back to the original basal plane.

precipitate interfaces. The Nd atomic structure in the precipitate shows that one Burgers vector displacement exists between Nd atoms above and below the slip plane on the two sides of the precipitate-matrix interfaces perpendicular to $[10\bar{1}0]$, highlighted by the black rectangles in Figure 6.11 (b). However, the inner part of the precipitate remains its original ordered $D0_3$ structure. When the unblocked portion of the dislocation moves forward, the dislocation line tension increases and drives the blocked portion of the dislocation line to cut through the precipitate. This change is confirmed by the snapshot shown at 66.4 ps, as shown in Figure 6.11 (c), that the unblocked part of the dislocation line glides forward (out of the screen of the snapshot), and the blocked part of the dislocation line is stretched to cut through the precipitate. Inside the precipitate, Nd atoms above the slip plane shift by a Burgers vector, as shown in Figure 6.11 (c), and there are clear offsets between Nd atoms above/below the slip plane on two sides of the precipitate-matrix interfaces perpendicular to $[1\bar{2}10]$ indicated by the arrows in the bottom of Figure 6.11 (c). Further calculations confirm that the average position of all Nd atoms above the $(\bar{1}10)_{\beta 1}$ slip plane shift by a distance equivalent to $\langle a \rangle$ along the Burgers vector direction relative to the average position of all Nd atoms below the slip. In summary, Figure 6.11 (a)-(c) show that the basal $\langle a \rangle$ edge dislocation completely cuts through the precipitate when it interacts with the precipitate.

Figure 6.12 shows the interaction of a second (successive) basal $\langle a \rangle$ edge dislocation at the sheared location after the first shearing event. Because the second $\langle a \rangle$ dislocation corresponds to the transform of $1/4[111]_{\beta 1}$ displacement to the $1/2[111]_{\beta 1}$ displacement in the β_1 precipitate, as shown in Figure 6.10, it can have different dislocation-precipitate interaction behavior compared with the first $\langle a \rangle$ dislocation. Initially, similar to the first shearing interaction, the dislocation bows out and forms two interface dislocations along its trajectory on the matrix-precipitate interface, as indicated by the frame at 92 ps in Figure 6.12 (a). When the dislocation moves forward, the bowed dislocation portion has a screw component extrapolated out from the precipitate-matrix interfaces perpendicular to $[10\bar{1}0]$ (the prismatic plane), as shown by the frame 92.8 ps in Figure 6.12 (b). Due to the resisting force induced by the precipitate, the screw dislocation portion starts cross-slip on the prismatic plane. Experiment captures similar phenomenon, as shown in Figure 6.4, the dislocation-1 and -2 glide on two parallel basal planes before they first contact with the β_1 precipitate. We use red dashed lines to label glide plane of dislocation-1, and green and blue dots to track the motion of the pinning points of the two dislocations on the precipitate interface. The purple box represents one prismatic plane close to the interacted precipitate. Both dislocation-1 and -2 get pinned on the precipitate, as shown Figure 6.4 (b), and they start to straighten and elongate the screw segment. The dislocation-1 becomes zigzag shape at dislocation segments close to the pinning point, as shown in Figure 6.4 (c). The screw component increases and cross slips on prismatic plane, as shown in Figure 6.4 (d).

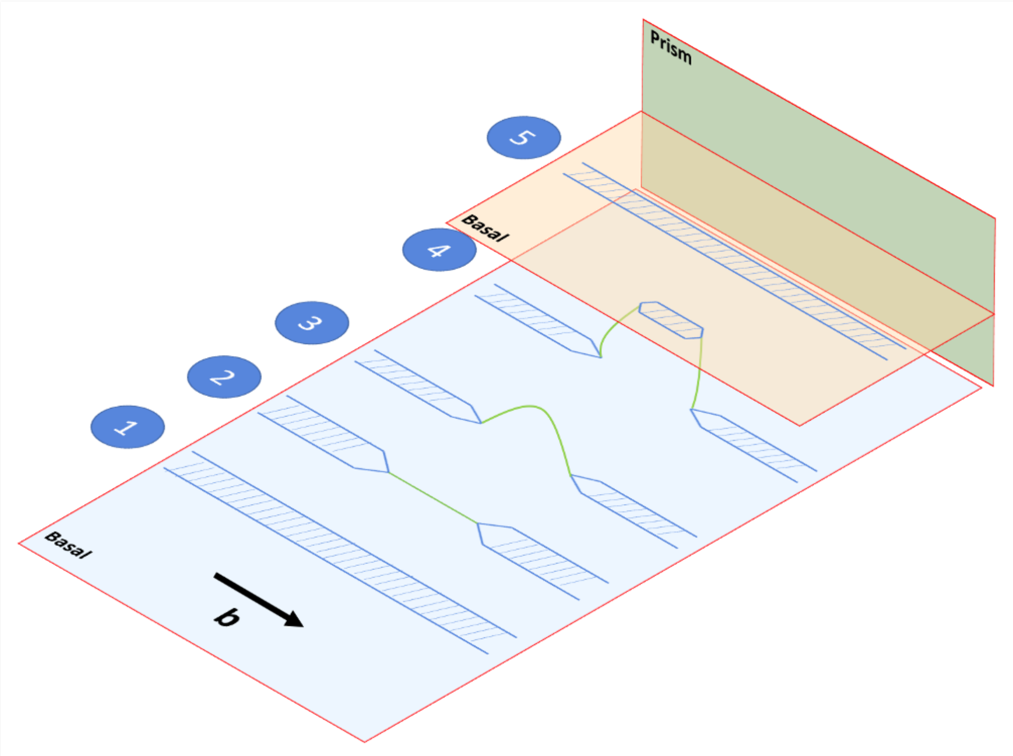

Figure 6.13: Schematic of the FE cross-slip mechanism. A cross-slipped basal dislocation dissociates into two partial dislocations. The shadow areas represent stacking faults on the basal plane (blue) and green lines represent the perfect screw dislocation segment that cross slips on the prismatic plane (green) before dissociation to partials on an adjacent basal plane (orange).

Figure 6.12 (c) shows that the cross-slipped dislocation portion dissociated on another basal plane and starts to glide forward. Accordingly, the cross-slipped screw dislocation forms a prolonged dislocation kink connecting two basal dislocations on different basal planes. This cross-slip behavior resembles the FE cross-slip mechanism [61], as shown in Figure 6.13. However, as indicated at the frame of 100 ps in Figure 6.12 (d), the kink of the screw shrinks and the cross-slipped dislocation portion cross slips back to its original glide plane, possibly because it is easy for the dislocation to cut the precipitate and move forward if it stays on a single basal plane. Eventually, the dislocation returns to its original basal plane and cut through the precipitate for the second time.

Interactions between a screw basal $\langle a \rangle$ dislocation and β_1 precipitates are shown in Figure 6.14. The screw dislocation dissociates into two 1/3 $\left\langle 1\bar{1}00 \right\rangle$ partial dislocations bounded by a stacking fault, and its dissociation distance is smaller than edge dislocation, which is consistent with DFT calculations [262]. Due to periodic boundary conditions along the x-axis, the dislocation cuts the precipitate multiple times during the MD simulations. The snapshot at 102.6 ps in Figure 6.14 (a) shows the dislocation contacts the precipitate for the second time. The snapshot at 103.8 ps in Figure 6.14 (b) shows that the two 1/3 $\left\langle 1\bar{1}00 \right\rangle$ partial dislocations merge to a single complete $\langle a \rangle$ dislocation at the precipitate-matrix interface perpendicular to $[10\bar{1}0]$ (the prismatic plane). A full $\langle a \rangle$ screw dislocation is non-planar and easy to cross slip. Hence a portion of the screw dislocation starts cross-slip on the prismatic plane along the precipitate-matrix interface, and the cross slip continues, as shown by Figure 6.14 (c) and (d). Figure 6.14 (d) shows the dislocation has cross slipped 7-8 nm along $\langle c \rangle$ direction. The other portion of the screw dislocation bows out rather than cross slip along the prismatic plane. The cross slipped dislocation is a dislocation kink that spans 7-8 nm, but it stops propagating due to the limitation of the simulation box size. Unlike the case of edge, the cross-slipped portion of dislocation does not re-dissociate on another basal plane. The cross-slipped part stays on the prismatic plane for a longer time compared with the cross-slipped part for the edge dislocation in Figure 6.12. Finally, the cross-slipped part is pulled back to the original basal plane as the

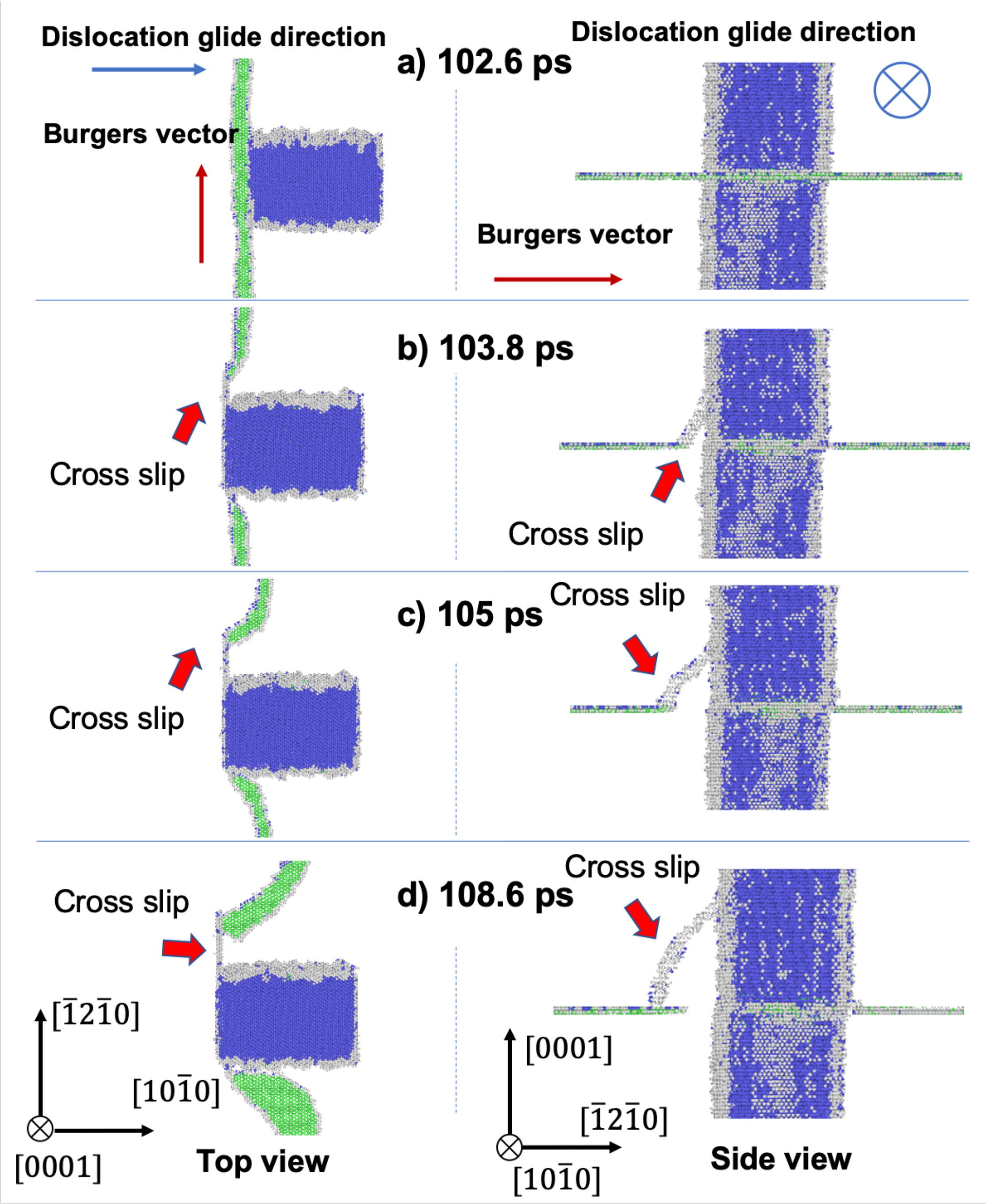

Figure 6.14: Snapshots of the basal screw ⟨a⟩ dislocation interacting with the β_1 precipitate for the second time due to the periodic condition of the supercell. a) The screw dislocation contacts with the precipitate. b) The dislocation starts to cross-slip on the prismatic plane toward ⟨c⟩ direction. c-d) The cross-slip process continues and spans over 7 nm along ⟨c⟩ direction, and the cross-slip portion and bow-out portion of the screw dislocation are pinning each other.

simulation continues (not shown in Figure 6.14).

6.4 Conclusion

We applied DFT calculations and theoretical model to estimate CRSS for dislocation cutting through the β_1 precipitates and simulated dislocation precipitate interactions with MD in Mg-Nd alloys. The β_1 precipitates have a special ordered lattice structure, and the glide of basal dislocations from Mg matrix into the precipitate can generate different types of antiphase boundary (APB) depending the number of dislocations that have cut through the precipitate. Our theoretical CRSS based on the multiple-dislocation-cutting mechanism and DFT calculated APB energies reflects the strong strengthening effects of β_1 precipitates, which explains the dislocation pile-up at β_1 precipitates observed in experiments.

In atomistic simulations of dislocations interacting with β_1 precipitates, we reveal that both edge and screw dislocations can cross slip during their interactions with β_1 precipitates. When interacting with non-screw $\langle$a$\rangle$ dislocations, β_1 precipitates can pin the propagating dislocations, causing unrelieved stress to activate dislocation cross-slip along the c-axis. The cross-slip, similar to Friedel-Escaig (F-E) mechanism, requires the formation of a large portion of screw components and nucleation of kinks. Screw dislocations, when interacting with β_1 precipitate, are easy to cross-slip since their cross-slip occurs on both the front and rear end of the sheared precipitates. In real materials systems, the possibility and magnitude of dislocation cross slip depend on many factors such as the local shear stress, interactions between dislocations, inter-spacing of precipitates, and sizes/shapes of precipitates. The cross-slip generates non-basal (prismatic) dislocation segments that can glide at the broad facet of β_1 precipitates. Besides, dislocations can even double cross slip to overcome the blocking β_1 precipitate. Understanding these glide dislocation-precipitate interaction mechanisms will be helpful in designing the precipitate microstructures that can enhance the strength and ductility of Mg alloys simultaneously.

CHAPTER VII

Summary and Future Work

7.1 Summary

The first work, illustrated in Chapter III, focuses on the intrinsic mechanical properties of refractory metals and alloys studied by first-principles calculations. We applied three different criteria, elastic instability of perfect crystals under ideal tensile deformation, phonon instability of the same perfect crystals, and LEFM analyses of crack tips under Mode I loading to evaluate the intrinsic ductility of W alloys. The intrinsic ductility can be achieved if shear deformation and dislocation nucleation are more favorable than tensile deformation and cleavage fracture propagation under extreme stress conditions.

Our work shows that Ta solutes induce either intrinsically brittle or ductile behaviors of W-Ta alloys depending on the alloy concentrations. For W-Re alloys, despite Re solutes inhibit the elastic shear instability (ESI), transverse phonon modes of imaginary frequencies emerge before the elastic instability at a critical concentration of Re. The phonon instability indicates dislocation nucleation that makes W-Re alloys intrinsically ductile. LEFM analyses provide consistent results of the competition among deformation defects (dislocation nucleation vs. crack propagation). In realistic conditions, plastic deformation and ductility in BCC metals and alloys depend both the dislocation nucleation and the screw dislocation mobility [238, 154, 155, 208, 140, 139, 83, 263, 233]. Therefore, systematic researches on ductility and deformation mechanisms demand larger-scale atomistic simulations on defects evolution in various chemical and thermodynamic conditions.

Accurate atomistic simulations require representative interatomic potentials to reflect the relevant bonding characteristics and defect properties of material systems. The second work, discussed in Chapter IV, tackles the challenge of creating such accurate interatomic potentials for larger-scale atomistic simulations on the defect evolution in BCC refractory metals, which have nearly half-filled d-band electrons to form strong interatomic bonds with directional characteristics. Upon DFT calculations, we applied the evolutionary algorithm (EA) to build a Nb modified embedded-atom method (MEAM) potential that reproduces intrinsic lattice and defect properties. The MEAM potential provides atomistic simulations of Nb with essential characteristics of deformation behavior, such as vacancy migration barrier, ideal tensile and shear strength related to intrinsic ductility, GSF energies, twin boundary energies, phonon spectrum, etc. All these results are consistent with DFT calculations.

Besides, the MEAM potential generates similar-to-DFT dislocation properties, including the core structures, core energies, migration energy barriers, and glide trajectories of 1/2 $\langle 111 \rangle$ screw dislocations. Therefore, our work on the development of the MEAM potentials facilitates the study of defects evolution and plastic deformation of refractory metals with atomistic simulations. We also performed large-scale benchmark MD simulations based on this MEAM Nb potential and another MEAM potential of Mo [179]. The MD results show different types of dislocation activities near crack tips (more dislocation activities near the crack tip of Nb than those in Mo), consistent with their macroscopic ductility characteristics (Nb is generally more ductile than Mo).

The creation of initial configurations of complex defects is another challenge in larger-scale atomistic simulations on defects evolution of crystalline materials. Especially for GBs, despite geometrically described simply by 5 macroscopic degrees of freedom, GBs at the atomistic level exhibit a large amount of microscopic degrees of freedom, especially for general GBs without a high degree of symmetry and GBs in crystals with multiple atoms in one primitive cell (like 2 atoms for one primitive cell of HCP structures). In the third work covered in Chapter V, we invented a new mutation operator of abrupt internal structure changes to boost the EA based exploration of GB structures at grand canonical ensembles. We developed an EA based GB structure search package to generate GB structures for animistic simulations on metallic systems. The package offers qualified GB structure search in FCC, BCC and HCP metals, and has discovered novel GB structures in advanced metallic systems such as BCC W and HCP Mg. Based on large scale atomistic simulations on the GB structures discovered by our GB structure exploration package, we reveal that GB of different misorientation and microstructures can induce different plastic deformation mechanisms such as the nucleation and emissions of dislocations and deformation twinning from GBs. These results also suggest the critical stress for the nucleation of these deformation defects from Mg GBs may depend on many factors of the detailed GB structures. So far it is difficult to correlate the critical stress with one parameter of GB properties, such as GB energies [212]. Additionally, our GB structure search and simulation techniques are ready to be coupled with experimental techniques to study GB structures and deformation properties systematically. For example, high-resolution TEM can characterize atomistic GB structures in experiments, and recent researches demonstrated consistent results of GB structures between atomistic simulations and scanning transmission electron microscopy (STEM) characterization in pure metals [157] and alloys [187]. So far the application of our GB structure search package in binary alloys suggest that we can duplicate the GB structures from STEM characterization of Mg-Zn and Mg-Gd alloys STEM characterization of Mg-Zn and Mg-Gd alloys [171].

The last work, illustrated in Chapter VI, is to apply large scale atomistic simulations to study dislocation-precipitate interactions in Mg-RE alloys. We applied theoretical models and DFT calculations to estimate the CRSS for dislocation cutting through β_1 precipitates in MgNd alloys, which illustrate the dislocation pile-up phenomenon observed by our *In situ* indentation experiment. Besides, we implemented large scale MD simulations of dislocation shearing β_1 precipitates under constant flow stress loading. Our simulations reveal that both edge and screw can cross slip on the prismatic plane when interacting with the β_1 precipitates due to residual stress from precipitates pinning dislocations, which confirms the TEM observation of dislocation cross-slip in MgNd alloys under tensile tests. The dislocation cross-slip in β_1 precipitate dominant microstructure adds two possible slip systems and potentially reduces the basal and prismatic slip anisotropy. Our atomistic simulations and experimental work provide insights into dislocation motion when interacting with β_1 precipitates, which require future experiments and analysis to verify whether cross-slip can increase of tensile ductility in the aged Mg-Nd alloys with β_1 precipitates.

7.2 Suggested future work

In general, from the first-principles calculations to atomistic simulations coupled with experiments, my research works form an integrated framework on the study of defects evolution during plastic deformation in advanced metallic systems. Based on our progress and unresolved problems, I propose several topics for future studies.

First, the analysis of ideal strength and ESI based on DFT calculations showed that Nb is intrinsically ductile for perfect lattice in extreme tensile stress conditions. In experiments, Nb has a low work-hardening rate [116, 52], and Nb can exhibit a double-cross-slip mechanism and bands of secondary slip similar to the dislocation activities observed in typical FCC metals [52], which are usually more ductile compared with BCC metals. Since we have created a Nb MEAM potential that reproduces the ESI revealed by DFT calculations, it is worthwhile in future work to systematically analyze how the intrinsic ESI affects ductility by applying the Nb MEAM potential, together with a Mo MEAM potential [179], to simulate defect nucleation and evolution during plastic deformations. Moreover, considering we developed an EA based force-fitting framework that successfully created the MEAM potential with DFT data, the future work can apply the framework to create Nb-Mo binary MEAM potential, and apply it to explore the effects of Nb solutes on the ductility of Mo-Nb binary alloys by atomistic simulations.

Second, our DFT calculations discovered that Re solutes induce phonon instability in extreme stress conditions in W-Re alloys, and phonon instability indicates the nucleation of dislocations. Ductility also depends on the screw dislocation mobility, which is related to electronic band structures [238, 154, 155, 208, 140, 139]. Based on our EA based empirical potential fitting framework, future researches can construct W-Re binary empirical potential that reproduces the dynamic phonon instability. Atomistic simulations can apply the W-Re potential to study dislocation mobility change with Re concentration, as well as dislocation nucleation at crack tips or grain boundaries, to systematically understand Re contribution to the ductility in W based alloys. On the other hand, compared with pure W, the VCA W-Re system is based on tuning d valence electrons without changing other ionic characteristics; therefore, the phonon instability in W-Re is mainly related to d band filling. Accordingly, we propose at least two criteria for solute elements that may generate similar phonon instability effects in brittle refractory metals such as W and Mo. First, the number of d valence electrons per atom should be increase compared with pure W/Mo. Second, it is thermodynamic stable or metastable to generate such random solid-solution alloys without precipitates. Based on these two criteria, it is worth to generalize our findings to search other alloying elements by applying the same ideal strength and phonon analyses to different types of solid-solution alloys based on W and Mo.

Third, our MD simulations showed that the GB structures affect the nucleation and emission mechanisms of dislocation and deformation twinning in pure HCP Mg. Mg has poor cold formability due to strong basal textures, and experiments showed that rare-earth elements, such as Y and Gd, can segregate at GBs to facilitate texture change and increase the formability of Mg-alloys [84, 206, 207]. Experiments also showed that zinc (Zn) and calcium (Ca) solutes segregate to GB in Mg alloys [271], which enhances the GB cohesion and reduce the nucleation of intergranular cracks at GBs [270]. The future work can apply our EA based GB structure search package on Mg alloys to explore GB structures segregated by solid solutes, and use the structures in MD simulations to study the effects on solute segregation on deformation mechanism at GBs. Furthermore, machine learning techniques based on appropriate local atomistic structure descriptors can be applied to identify the representative GB features to describe the GB-defect interactions and the macroscopic GB strengthening effects [50, 220].

Fourth, studies showed that shear-coupled GB migration, the motion of GB driven by applied shear forces, is based on the model of nucleation and motion of disconnection, which is linear defects of step and dislocation character constrained in GBs. We found stable symmetric tilt grain boundaries (STGB) structures of zigzag grain boundary dislocation (GBD) and nano-step in HCP Mg based on our EA-based GB structure search package [198, 100, 101, 88]. It is worthwhile to apply atomistic simulations on both the novel GB structures and GB structures found by the γ surface method to explore the influence of zigzag GBDs and nano-steps on the formation and migration of disconnection in GBs. Moreover, since there could be many metastable GBs with different types of disconnections that affect the GB kinetics [89, 90, 88], future work can be performed to estimate the GB mobility with bicrystal setup effectively with the spectrum of stable and metastable GBs discovered by our package.

Fifth, our MD simulations have revealed the phenomenon of dislocation cross-slip from the basal plane to the prismatic plane when interacting with β_1 precipitates, which also confirmed by the TEM characterization. The dislocation cross-slip creates a degree of freedom along the normal of the basal plane to facilitate the dislocation overcome β_1 precipitates, which have high CRSS in our theoretical estimation. Limited by the length and time scale, our atomistic simulations only provide an intuitive explanation of the possible increase of ductility measured by our tensile test. Therefore, possible future work can be dislocation dynamics simulations with proper implementation on dislocation cross-slip mechanisms to directly link dislocation evolution to mesoscale plastic deformation and ductility at the influence of β_1 precipitates.

BIBLIOGRAPHY

BIBLIOGRAPHY

[1] Hub I Aaronson, T Furuhara, MG Hall, John P Hirth, Jian Feng Nie, GR Purdy, and WT Reynolds Jr. On the mechanism of formation of diffusional plate-shaped transformation products. *Acta materialia*, 54(5):1227–1232, 2006.

[2] GJ Ackland and MW Finnis. Semi-empirical calculation of solid surface tensions in body-centred cubic transition metals. *Philosophical Magazine A*, 54(2):301–315, 1986.

[3] GJ Ackland and R Thetford. An improved n-body semi-empirical model for body-centred cubic transition metals. *Philosophical Magazine A*, 56(1):15–30, 1987.

[4] GJ Ackland, G Tichy, V Vitek, and MW Finnis. Simple n-body potentials for the noble metals and nickel. *Philosophical Magazine A*, 56(6):735–756, 1987.

[5] MA Adams, AC Roberts, and RE Smallman. Yield and fracture in polycrystalline niobium. *Acta Metallurgica*, 8(5):328–337, 1960.

[6] Sean R Agnew and Özgür Duygulu. Plastic anisotropy and the role of non-basal slip in magnesium alloy az31b. *International Journal of plasticity*, 21(6):1161–1193, 2005.

[7] Rasool Ahmad, Sébastien Groh, Maryam Ghazisaeidi, and William A Curtin. Modified embedded-atom method interatomic potential for mg–y alloys. *Modelling and Simulation in Materials Science and Engineering*, 26(6):065010, 2018.

[8] Michael P Allen and Dominic J Tildesley. *Computer simulation of liquids*. Oxford university press, 2017.

[9] Predrag Andric and WA Curtin. New theory for mode i crack-tip dislocation emission. *Journal of the Mechanics and Physics of Solids*, 106:315–337, 2017.

[10] AJ Ardell. Precipitation hardening. *Metallurgical Transactions A*, 16(12):2131–2165, 1985.

[11] Ali Argon. *Strengthening mechanisms in crystal plasticity*. Oxford University Press on Demand, 2008.

[12] Ali S Argon. Brittle to ductile transition in cleavage fracture. *Acta Metallurgica*, 35(1):185–196, 1987.

[13] Michael M Avedesian, Hugh Baker, et al. *ASM specialty handbook: magnesium and magnesium alloys*. ASM international, 1999.

[14] RA Ayres, GW Shannette, and DF Stein. Elastic constants of tungsten- rhenium alloys from 77 to 298 k. *Journal of Applied Physics*, 46(4):1526–1530, 1975.

[15] DJ Bacon, DM Barnett, and Ronald Otto Scattergood. Anisotropic continuum theory of lattice defects. *Progress in Materials Science*, 23:51–262, 1980.

[16] DJ Bacon, YuN Osetsky, and D Rodney. Dislocation–obstacle interactions at the atomic level. *Dislocations in solids*, 15:1–90, 2009.

[17] Arash Dehghan Banadaki, Mark A Tschopp, and Srikanth Patala. An efficient monte carlo algorithm for determining the minimum energy structures of metallic grain boundaries. *Computational Materials Science*, 155:466–475, 2018.

[18] Zhang Bangwei, Ouyang Yifang, Liao Shuzhi, and Jin Zhanpeng. An analytic meam model for all bcc transition metals. *Physica B: Condensed Matter*, 262(3):218–225, 1999.

[19] DM Barnett and LA Swasger. The elastic energy of a straight dislocation in an infinite anisotropic elastic medium. *Physica status solidi (b)*, 48(1):419–428, 1971.

[20] Stefano Baroni, Stefano De Gironcoli, Andrea Dal Corso, and Paolo Giannozzi. Phonons and related crystal properties from density-functional perturbation theory. *Reviews of Modern Physics*, 73(2):515, 2001.

[21] MI Baskes. Modified embedded-atom potentials for cubic materials and impurities. *Physical Review B*, 46(5):2727, 1992.

[22] Oren M Becker and Martin Karplus. The topology of multidimensional potential energy surfaces: Theory and application to peptide structure and kinetics. *The Journal of chemical physics*, 106(4):1495–1517, 1997.

[23] JJ Bhattacharyya, T Nakata, S Kamado, and SR Agnew. Origins of high strength and ductility combination in a guinier-preston zone containing mg-al-ca-mn alloy. *Scripta Materialia*, 163:121–124, 2019.

[24] Erik Bitzek, Pekka Koskinen, Franz Gähler, Michael Moseler, and Peter Gumbsch. Structural relaxation made simple. *Physical review letters*, 97(17):170201, 2006.

[25] DI Bolef. Elastic constants of single crystals of the bcc transition elements v, nb, and ta. *Journal of Applied Physics*, 32(1):100–105, 1961.

[26] Max Born and Robert Oppenheimer. Zur quantentheorie der molekeln. *Annalen der physik*, 389(20):457–484, 1927.

[27] Stephen Boyd and Lieven Vandenberghe. *Convex optimization*. Cambridge university press, 2004.

[28] Stephan Büchner and Andreas Heuer. Potential energy landscape of a model glass former: Thermodynamics, anharmonicities, and finite size effects. *Physical Review E*, 60(6):6507, 1999.

[29] Kenneth P Burnham and David R Anderson. *Model selection and multimodel inference: a practical information-theoretic approach*. Springer Science & Business Media, 2003.

[30] John W Cahn, Yuri Mishin, and Akira Suzuki. Coupling grain boundary motion to shear deformation. *Acta materialia*, 54(19):4953–4975, 2006.

[31] Wei Cai, Vasily V Bulatov, Jinpeng Chang, Ju Li, and Sidney Yip. Anisotropic elastic interactions of a periodic dislocation array. *Physical Review Letters*, 86(25):5727, 2001.

[32] Patrick R Cantwell, Ming Tang, Shen J Dillon, Jian Luo, Gregory S Rohrer, and Martin P Harmer. Grain boundary complexions. *Acta Materialia*, 62:1–48, 2014.

[33] Keith J Carroll. Elastic constants of niobium from 4.2 to 300 k. *Journal of Applied Physics*, 36(11):3689–3690, 1965.

[34] YT Chou and JD Eshelby. The energy and line tension of a dislocation in a hexagonal crystal. *Journal of the Mechanics and Physics of Solids*, 10(1):27–34, 1962.

[35] John Wyrill Christian and Subhash Mahajan. Deformation twinning. *Progress in materials science*, 39(1-2):1–157, 1995.

[36] Alvin L-S Chua, Nicole A Benedek, Lin Chen, Mike W Finnis, and Adrian P Sutton. A genetic algorithm for predicting the structures of interfaces in multicomponent systems. *Nature materials*, 9(5):418, 2010.

[37] JB Clark. Age hardening in a mg-9 wt.% al alloy. *Acta Metallurgica*, 16(2):141–152, 1968.

[38] DM Clatterbuck, CR Krenn, Marvin L Cohen, and JW Morris Jr. Phonon instabilities and the ideal strength of aluminum. *Physical review letters*, 91(13):135501, 2003.

[39] Thomas H Cormen, Charles E Leiserson, Ronald L Rivest, and Clifford Stein. *Introduction to algorithms*. MIT press, 2009.

[40] AH Cottrell and BA Bilby. Lx. a mechanism for the growth of deformation twins in crystals. *The London, Edinburgh, and Dublin Philosophical Magazine and Journal of Science*, 42(329):573–581, 1951.

[41] A Couret and D Caillard. An in situ study of prismatic glide in magnesium—i. the rate controlling mechanism. *Acta metallurgica*, 33(8):1447–1454, 1985.

[42] XD Dai, JH Li, and Y Kong. Long-range empirical potential for the bcc structured transition metals. *Physical Review B*, 75(5):052102, 2007.

[43] Murray S Daw and Michael I Baskes. Embedded-atom method: Derivation and application to impurities, surfaces, and other defects in metals. *Physical Review B*, 29(12):6443, 1984.

[44] Maarten de Jong, J Kacher, MHF Sluiter, L Qi, DL Olmsted, A Van de Walle, JW Morris Jr, AM Minor, and M Asta. Electronic origins of anomalous twin boundary energies in hexagonal close packed transition metals. *Physical review letters*, 115(6):065501, 2015.

[45] Maarten de Jong, Liang Qi, David L. Olmsted, Axel van de Walle, and Mark Asta. Calculations of planar defect energies in substitutional alloys using the special-quasirandom-structure approach. *Phys. Rev. B*, 93:094101, Mar 2016.

[46] L Dezerald, L Proville, Lisa Ventelon, F Willaime, and D Rodney. First-principles prediction of kink-pair activation enthalpy on screw dislocations in bcc transition metals: V, nb, ta, mo, w, and fe. *Physical Review B*, 91(9):094105, 2015.

[47] Lucile Dezerald, David Rodney, Emmanuel Clouet, Lisa Ventelon, and François Willaime. Plastic anisotropy and dislocation trajectory in bcc metals. *Nature communications*, 7:11695, 2016.

[48] Doyl E Dickel, Michael I Baskes, Imran Aslam, and Christopher D Barrett. New interatomic potential for mg–al–zn alloys with specific application to dilute mg-based alloys. *Modelling and Simulation in Materials Science and Engineering*, 26(4):045010, 2018.

[49] Shen J Dillon, Ming Tang, W Craig Carter, and Martin P Harmer. Complexion: a new concept for kinetic engineering in materials science. *Acta Materialia*, 55(18):6208–6218, 2007.

[50] Jun Ding, Sylvain Patinet, Michael L. Falk, Yongqiang Cheng, and Evan Ma. Soft spots and their structural signature in a metallic glass. *Proceedings of the National Academy of Sciences of the United States of America*, 111:14052–14056, 2014.

[51] M and-S Duesbery and V Vitek. Plastic anisotropy in bcc transition metals. *Acta Materialia*, 46(5):1481–1492, 1998.

[52] MS Duesbery, RA Foxall, and PB Hirsch. The plasticity of pure niobium single crystals. *Le Journal de Physique Colloques*, 27(C3):C3–193, 1966.

[53] DM Duffy. Grain boundaries in ionic crystals. *Journal of Physics C: Solid State Physics*, 19(23):4393, 1986.

[54] Robert C. Ehemann and John W. Wilkins. Force-matched empirical potential for martensitic transitions and plastic deformation in ti-nb alloys. *PHYSICAL REVIEW B*, 96(18), NOV 10 2017.

[55] K Einarsdotter, B Sadigh, G Grimvall, and V Ozoliņš. Phonon instabilities in fcc and bcc tungsten. *Physical review letters*, 79(11):2073, 1997.

[56] Robert Eisberg and Robert Resnick. Quantum physics of atoms, molecules, solids, nuclei, and particles. *Quantum Physics of Atoms, Molecules, Solids, Nuclei, and Particles, 2nd Edition, by Robert Eisberg, Robert Resnick, pp. 864. ISBN 0-471-87373-X. Wiley-VCH, January 1985.*, page 864, 1985.

[57] Mathias Ekman, Babak Sadigh, Kristin Einarsdotter, and Peter Blaha. Ab initio study of the martensitic bcc-hcp transformation in iron. *Physical Review B*, 58(9):5296, 1998.

[58] Mohamed S El-Genk and Jean-Michel Tournier. A review of refractory metal alloys and mechanically alloyed-oxide dispersion strengthened steels for space nuclear power systems. *Journal of Nuclear materials*, 340(1):93–112, 2005.

[59] Haitham El Kadiri, Christopher D Barrett, Jian Wang, and Carlos N Tomé. Why are {101¯ 2} twins profuse in magnesium? *Acta Materialia*, 85:354–361, 2015.

[60] Furio Ercolessi and James B Adams. Interatomic potentials from first-principles calculations: the force-matching method. *EPL (Europhysics Letters)*, 26(8):583, 1994.

[61] B Escaig. L'activation thermique des déviations sous faibles contraintes dans les structures hc et cc par. *physica status solidi (b)*, 28(2):463–474, 1968.

[62] JD Eshelby, WT Read, and W Shockley. Anisotropic elasticity with applications to dislocation theory. *Acta metallurgica*, 1(3):251–259, 1953.

[63] Michael R Fellinger, Hyoungki Park, and John W Wilkins. Force-matched embedded-atom method potential for niobium. *Physical Review B*, 81(14):144119, 2010.

[64] MW Finnis and JE Sinclair. A simple empirical n-body potential for transition metals. *Philosophical Magazine A*, 50(1):45–55, 1984.

[65] Søren L Frederiksen and Karsten W Jacobsen. Density functional theory studies of screw dislocation core structures in bcc metals. *Philosophical Magazine*, 83(3):365–375, 2003.

[66] Daan Frenkel and Berend Smit. *Understanding molecular simulation: from algorithms to applications*, volume 1. Elsevier, 2001.

[67] Timofey Frolov, David L Olmsted, Mark Asta, and Yuri Mishin. Structural phase transformations in metallic grain boundaries. *Nature communications*, 4:1899, 2013.

[68] Timofey Frolov, Wahyu Setyawan, RJ Kurtz, Jaime Marian, Artem R Oganov, Robert E Rudd, and Qiang Zhu. Grain boundary phases in bcc metals. *Nanoscale*, 10(17):8253–8268, 2018.

[69] Timofey Frolov, Qiang Zhu, Tomas Oppelstrup, Jaime Marian, and Robert E Rudd. Structures and transitions in bcc tungsten grain boundaries and their role in the absorption of point defects. *Acta Materialia*, 159:123–134, 2018.

[70] Martin Fuchs and Matthias Scheffler. Ab initio pseudopotentials for electronic structure calculations of poly-atomic systems using density-functional theory. *Computer Physics Communications*, 119(1):67–98, 1999.

[71] Xiang Gao, Shang Ming He, XQ Zeng, LM Peng, Wen Jian Ding, and Jian Feng Nie. Microstructure evolution in a mg–15gd–0.5 zr (wt.%) alloy during isothermal aging at 250 c. *Materials Science and Engineering: A*, 431(1-2):322–327, 2006.

[72] Robert Gehrmann, Matthias M Frommert, and Günter Gottstein. Texture effects on plastic deformation of magnesium. *Materials Science and Engineering: A*, 395(1-2):338–349, 2005.

[73] Paolo Giannozzi, Stefano Baroni, Nicola Bonini, Matteo Calandra, Roberto Car, Carlo Cavazzoni, Davide Ceresoli, Guido L Chiarotti, Matteo Cococcioni, Ismaila Dabo, et al. Quantum espresso: a modular and open-source software project for quantum simulations of materials. *Journal of physics: Condensed matter*, 21(39):395502, 2009.

[74] Josiah Willard Gibbs. *Elementary principles in statistical mechanics: developed with especial reference to the rational foundation of thermodynamics*. C. Scribner's sons, 1902.

[75] Simone Giusepponi and Massimo Celino. The ideal tensile strength of tungsten and tungsten alloys by first-principles calculations. *Journal of nuclear materials*, 435(1-3):52–55, 2013.

[76] David E Goldberg and Kalyanmoy Deb. A comparative analysis of selection schemes used in genetic algorithms. In *Foundations of genetic algorithms*, volume 1, pages 69–93. Elsevier, 1991.

[77] Alan A Griffith. The phenomena of rupture and flow in solids. *Philosophical transactions of the royal society of london. Series A, containing papers of a mathematical or physical character*, 221:163–198, 1921.

[78] David J Griffiths and Darrell F Schroeter. *Introduction to quantum mechanics*. Cambridge University Press, 2018.

[79] Göran Grimvall, Blanka Magyari-Köpe, Vidvuds Ozoliņš, and Kristin A Persson. Lattice instabilities in metallic elements. *Reviews of Modern Physics*, 84(2):945, 2012.

[80] R Gröger, AG Bailey, and V Vitek. Multiscale modeling of plastic deformation of molybdenum and tungsten: I. atomistic studies of the core structure and glide of 1/2<111> screw dislocations at 0 k. *Acta Materialia*, 56(19):5401–5411, 2008.

[81] AM Guellil and JB Adams. The application of the analytic embedded atom method to bcc metals and alloys. *Journal of materials research*, 7(3):639–652, 1992.

[82] P Gumbsch, J Riedle, A Hartmaier, and HF Fischmeister. Controlling factors for the brittle-to-ductile transition in tungsten single crystals. *Science*, 282(5392):1293–1295, NOV 13 1998.

[83] Peter Gumbsch. Brittle fracture and the brittle-to-ductile transition of tungsten. *Journal of Nuclear Materials*, 323(2):304–312, 2003.

[84] JP Hadorn, TT Sasaki, T Nakata, T Ohkubo, S Kamado, and K Hono. Solute clustering and grain boundary segregation in extruded dilute mg–gd alloys. *Scripta Materialia*, 93:28–31, 2014.

[85] JÜRGEN HAFNER. Hafner2010. *Journal of computational chemistry*, 31(16):2967–2970, 2010.

[86] Theo Hahn, Uri Shmueli, and JC Wilson Arthur. *International tables for crystallography*, volume 1. Reidel Dordrecht, 1983.

[87] EO Hall. The deformation and ageing of mild steel: Iii discussion of results. *Proceedings of the Physical Society. Section B*, 64(9):747, 1951.

[88] Jian Han, Spencer L Thomas, and David J Srolovitz. Grain-boundary kinetics: A unified approach. *Progress in Materials Science*, 98:386–476, 2018.

[89] Jian Han, Vaclav Vitek, and David J Srolovitz. Grain-boundary metastability and its statistical properties. *Acta Materialia*, 104:259–273, 2016.

[90] Jian Han, Vaclav Vitek, and David J Srolovitz. The grain-boundary structural unit model redux. *Acta Materialia*, 133:186–199, 2017.

[91] Nikolaus Hansen. The cma evolution strategy: A tutorial. *arXiv preprint arXiv:1604.00772*, 2016.

[92] Nikolaus Hansen, Sibylle D Müller, and Petros Koumoutsakos. Reducing the time complexity of the derandomized evolution strategy with covariance matrix adaptation (cma-es). *Evolutionary computation*, 11(1):1–18, 2003.

[93] JM Harder and DJ Bacon. Point-defect and stacking-fault properties in body-centred-cubic metals with n-body interatomic potentials. *Philosophical Magazine A*, 54(5):651–661, 1986.

[94] G Henkelman, G Jóhannesson, and H Jónsson. Progress on theoretical chemistry and physics. *Kluwer Academic Publishers*, pages 269–300, 2000.

[95] Andreas Heuer. Properties of a glass-forming system as derived from its potential energy landscape. *Physical review letters*, 78(21):4051, 1997.

[96] P Hidalgo-Manrique, JD Robson, and MT Pérez-Prado. Precipitation strengthening and reversed yield stress asymmetry in mg alloys containing rare-earth elements: A quantitative study. *Acta Materialia*, 124:456–467, 2017.

[97] John P Hirth. The influence of grain boundaries on mechanical properties. *Metallurgical Transactions*, 3(12):3047–3067, 1972.

[98] John Price Hirth, Jens Lothe, and T Mura. Theory of dislocations. *Journal of Applied Mechanics*, 50:476, 1983.

[99] JP Hirth and RC Pond. Steps, dislocations and disconnections as interface defects relating to structure and phase transformations. *Acta Materialia*, 44(12):4749–4763, 1996.

[100] JP Hirth, RC Pond, and J Lothe. Disconnections in tilt walls. *Acta Materialia*, 54(16):4237–4245, 2006.

[101] JP Hirth, RC Pond, and J Lothe. Spacing defects and disconnections in grain boundaries. *Acta Materialia*, 55(16):5428–5437, 2007.

[102] Pierre Hohenberg and Walter Kohn. Inhomogeneous electron gas. *Physical review*, 136(3B):B864, 1964.

[103] J Dana Honeycutt and Hans C Andersen. Molecular dynamics study of melting and freezing of small lennard-jones clusters. *Journal of Physical Chemistry*, 91(19):4950–4963, 1987.

[104] Wangyu Hu, Xiaolin Shu, and Bangwei Zhang. Point-defect properties in body-centered cubic transition metals with analytic eam interatomic potentials. *Computational Materials Science*, 23(1):175–189, 2002.

[105] Zhihua Huang, Chaoming Yang, Liang Qi, John E Allison, and Amit Misra. Dislocation pile-ups at $\beta 1$ precipitate interfaces in mg-rare earth (re) alloys. *Materials Science and Engineering: A*, 742:278–286, 2019.

[106] Zhihua Huang, Qi Liang Yang, Chaoming, and Misra Amit Allison, E. John. Dislocation cross-slip in precipitation hardened mg-nd alloys. *Acta Materialia*, under review, 2020.

[107] Liam Huber, Jörg Rottler, and Matthias Militzer. Atomistic simulations of the interaction of alloying elements with grain boundaries in mg. *Acta Materialia*, 80:194–204, 2014.

[108] D Hull, P Beardmore, and AP Valintine. Crack propagation in single crystals of tungsten. *Philosophical Magazine*, 12(119):1021–1041, 1965.

[109] Derek Hull and David J Bacon. *Introduction to dislocations*, volume 37. Elsevier, 2011.

[110] JW Hutchinson. Creep and plasticity of hexagonal polycrystals as related to single crystal slip. *Metallurgical Transactions A*, 8(9):1465–1469, 1977.

[111] Mitsuhiro Itakura, Hideo Kaburaki, and Masatake Yamaguchi. First-principles study on the mobility of screw dislocations in bcc iron. *Acta Materialia*, 60(9):3698–3710, 2012.

[112] Hermann Arthur Jahn and Edward Teller. Stability of polyatomic molecules in degenerate electronic states-i—orbital degeneracy. *Proceedings of the Royal Society of London. Series A-Mathematical and Physical Sciences*, 161(905):220–235, 1937.

[113] LP Jahnke, RG Frank, and TK Redden. Columbium alloys today. *Metal Progr.*, 77, 1960.

[114] Koenraad GF Janssens, David Olmsted, Elizabeth A Holm, Stephen M Foiles, Steven J Plimpton, and Peter M Derlet. Computing the mobility of grain boundaries. *Nature materials*, 5(2):124, 2006.

[115] BJ Jesson, M Foley, and PA Madden. Thermal properties of the self-interstitial in aluminum: An ab initio molecular-dynamics study. *Physical Review B*, 55(8):4941, 1997.

[116] AA Johnson. The ductile—brittle transition in body-centred cubic transition metals. *Philosophical Magazine*, 7(74):177–196, 1962.

[117] RA Johnson. Interstitials and vacancies in α iron. *Physical Review*, 134(5A):A1329, 1964.

[118] Hannes Jónsson, Greg Mills, and Karsten W Jacobsen. Nudged elastic band method for finding minimum energy paths of transitions. In *Classical and quantum dynamics in condensed phase simulations*, pages 385–404. World Scientific, 1998.

[119] A. Kelly and N. H. MacMillan. *Strong solids.* Clarendon Press, Oxford, 1986.

[120] S. Kibey, J. B. Liu, D. D. Johnson, and H. Sehitoglu. A first-principles measure for the twinnability of fcc metals. *Acta Materialia*, 55:6843–6851, 2007.

[121] Ki-Hyun Kim and Byeong-Joo Lee. Modified embedded-atom method interatomic potentials for mg-nd and mg-pb binary systems. *Calphad*, 57:55–61, 2017.

[122] Charles Kittel, Paul McEuen, and Paul McEuen. *Introduction to solid state physics*, volume 8. Wiley New York, 1996.

[123] J Knap and K Sieradzki. Crack tip dislocation nucleation in fcc solids. *Physical review letters*, 82(8):1700, 1999.

[124] S Kohlhoff, P Gumbsch, and HF Fischmeister. Crack propagation in bcc crystals studied with a combined finite-element and atomistic model. *Philosophical Magazine A*, 64(4):851–878, 1991.

[125] Walter Kohn and Lu Jeu Sham. Self-consistent equations including exchange and correlation effects. *Physical review*, 140(4A):A1133, 1965.

[126] J Koike, T Kobayashi, T Mukai, H Watanabe, M Suzuki, K Maruyama, and K Higashi. The activity of non-basal slip systems and dynamic recovery at room temperature in fine-grained az31b magnesium alloys. *Acta materialia*, 51(7):2055–2065, 2003.

[127] J Koike and R Ohyama. Geometrical criterion for the activation of prismatic slip in az61 mg alloy sheets deformed at room temperature. *Acta Materialia*, 53(7):1963–1972, 2005.

[128] CR Krenn, D Roundy, JW Morris Jr, and Marvin L Cohen. Ideal strengths of bcc metals. *Materials Science and Engineering: A*, 319:111–114, 2001.

[129] Georg Kresse and Jürgen Furthmüller. Efficient iterative schemes for ab initio total-energy calculations using a plane-wave basis set. *Physical review B*, 54(16):11169, 1996.

[130] Georg Kresse and Daniel Joubert. From ultrasoft pseudopotentials to the projector augmented-wave method. *Physical review b*, 59(3):1758, 1999.

[131] Anil Kumar, Jian Wang, and Carlos N Tomé. First-principles study of energy and atomic solubility of twinning-associated boundaries in hexagonal metals. *Acta Materialia*, 85:144–154, 2015.

[132] Andrew R Leach and Andrew R Leach. *Molecular modelling: principles and applications*. Pearson education, 2001.

[133] Byeong-Joo Lee, MI Baskes, Hanchul Kim, and Yang Koo Cho. Second nearest-neighbor modified embedded atom method potentials for bcc transition metals. *Physical Review B*, 64(18):184102, 2001.

[134] Stephen Lee and Roald Hoffmann. Bcc and fcc transition metals and alloys: A central role for the jahn- teller effect in explaining their ideal and distorted structures. *Journal of the American Chemical Society*, 124(17):4811–4823, 2002.

[135] EM Lehockey, G Palumbo, and P Lin. Improving the weldability and service performance of nickel-and iron-based superalloys by grain boundary engineering. *Metallurgical and Materials Transactions A*, 29(12):3069–3079, 1998.

[136] Pavel Lejcek. *Grain boundary segregation in metals*, volume 136. Springer Science & Business Media, 2010.

[137] Pavel Lejček, Mojmír Šob, and Vaclav Paidar. Interfacial segregation and grain boundary embrittlement: An overview and critical assessment of experimental data and calculated results. *Progress in Materials Science*, 87:83–139, 2017.

[138] Thomas J Lenosky, Babak Sadigh, Eduardo Alonso, Vasily V Bulatov, Tomas Diaz de la Rubia, Jeongnim Kim, Arthur F Voter, and Joel D Kress. Highly optimized empirical potential model of silicon. *Modelling and Simulation in Materials Science and Engineering*, 8(6):825, 2000.

[139] Hong Li, Claudia Draxl, Stefan Wurster, Reinhard Pippan, and Lorenz Romaner. Impact of d-band filling on the dislocation properties of bcc transition metals: The case of tantalum-tungsten alloys investigated by density-functional theory. *Physical Review B*, 95(9):094114, 2017.

[140] Hong Li, Stefan Wurster, Christian Motz, Lorenz Romaner, Claudia Ambrosch-Draxl, and Reinhard Pippan. Dislocation-core symmetry and slip planes in tungsten alloys: Ab initio calculations and microcantilever bending experiments. *Acta Materialia*, 60(2):748–758, 2012.

[141] Ju Li, Alfonso HW Ngan, and Peter Gumbsch. Atomistic modeling of mechanical behavior. *Acta Materialia*, 51(19):5711–5742, 2003.

[142] Ju Li, Cai-Zhuang Wang, Jin-Peng Chang, Wei Cai, Vasily V Bulatov, Kai-Ming Ho, and Sidney Yip. Core energy and peierls stress of a screw dislocation in bcc molybdenum: A periodic-cell tight-binding study. *Physical Review B*, 70(10):104113, 2004.

[143] Min Liao, B Li, and MF Horstemeyer. Interaction between basal slip and a mg 17 al 12 precipitate in magnesium. *Metallurgical and Materials Transactions A*, 45(8):3661–3669, 2014.

[144] Hong Liu, Yipeng Gao, Liang Qi, Yunzhi Wang, and Jian-Feng Nie. Phase-field simulation of orowan strengthening by coherent precipitate plates in an aluminum alloy. *Metallurgical and Materials Transactions A*, 46(7):3287–3301, 2015.

[145] Hong Liu, Yipeng Gao, YM Zhu, Yunzhi Wang, and Jian Feng Nie. A simulation study of $\beta1$ precipitation on dislocations in an mg–rare earth alloy. *Acta materialia*, 77:133–150, 2014.

[146] Xiang-Yang Liu, James B Adams, Furio Ercolessi, and John A Moriarty. Eam potential for magnesium from quantum mechanical forces. *Modelling and Simulation in Materials Science and Engineering*, 4(3):293, 1996.

[147] Jian Luo, Huikai Cheng, Kaveh Meshinchi Asl, Christopher J Kiely, and Martin P Harmer. The role of a bilayer interfacial phase on liquid metal embrittlement. *Science*, 333(6050):1730–1733, 2011.

[148] Weidong Luo, David Roundy, Marvin L Cohen, and JW Morris Jr. Ideal strength of bcc molybdenum and niobium. *Physical Review B*, 66(9):094110, 2002.

[149] Andriy O Lyakhov, Artem R Oganov, Harold T Stokes, and Qiang Zhu. New developments in evolutionary structure prediction algorithm uspex. *Computer Physics Communications*, 184(4):1172–1182, 2013.

[150] Andriy O Lyakhov, Artem R Oganov, and Mario Valle. How to predict very large and complex crystal structures. *Computer Physics Communications*, 181(9):1623–1632, 2010.

[151] Mihai-Cosmin Marinica, Lisa Ventelon, MR Gilbert, L Proville, SL Dudarev, J Marian, G Bencteux, and F Willaime. Interatomic potentials for modelling radiation defects and dislocations in tungsten. *Journal of Physics: Condensed Matter*, 25(39):395502, 2013.

[152] Richard M Martin and Richard Milton Martin. *Electronic structure: basic theory and practical methods*. Cambridge university press, 2004.

[153] Suveen N Mathaudhu, Wim H Sillekens, Neale R Neelameggham, and Norbert Hort. *Magnesium Technology 2012*. John Wiley & Sons, 2012.

[154] NI Medvedeva, Yu N Gornostyrev, and AJ Freeman. Solid solution softening in bcc mo alloys: Effect of transition-metal additions on dislocation structure and mobility. *Physical Review B*, 72(13):134107, 2005.

[155] NI Medvedeva, Yu N Gornostyrev, and AJ Freeman. Solid solution softening and hardening in the group-v and group-vi bcc transition metals alloys: First principles calculations and atomistic modeling. *Physical Review B*, 76(21):212104, 2007.

[156] Michael J. Mehl, Dimitrios A. Papaconstantopoulos, Nicholas Kioussis, and M. Herbranson. Tight-binding study of stacking fault energies and the rice criterion of ductility in the fcc metals. *Phys. Rev. B*, 61:4894–4897, Feb 2000.

[157] Thorsten Meiners, Timofey Frolov, Robert E Rudd, Gerhard Dehm, and Christian H Liebscher. Observations of grain-boundary phase transformations in an elemental metal. *Nature*, 579(7799):375–378, 2020.

[158] KL Merkle and David J Smith. Atomic structure of symmetric tilt grain boundaries in nio. *Physical Review Letters*, 59(25):2887, 1987.

[159] MPAT Methfessel and AT Paxton. High-precision sampling for brillouin-zone integration in metals. *Physical Review B*, 40(6):3616, 1989.

[160] Walter Mickel, Sebastian C Kapfer, Gerd E Schröder-Turk, and Klaus Mecke. Shortcomings of the bond orientational order parameters for the analysis of disordered particulate matter. *The Journal of chemical physics*, 138(4):044501, 2013.

[161] F Milstein and S Chantasiriwan. Theoretical study of the response of 12 cubic metals to uniaxial loading. *Physical Review B*, 58(10):6006–6018, SEP 1 1998.

[162] Yu Mishin, MJ Mehl, DA Papaconstantopoulos, AF Voter, and JD Kress. Structural stability and lattice defects in copper: Ab initio, tight-binding, and embedded-atom calculations. *Physical Review B*, 63(22):224106, 2001.

[163] Hendrik J Monkhorst and James D Pack. Special points for brillouin-zone integrations. *Physical review B*, 13(12):5188, 1976.

[164] James R Morris, Yiying Ye, and Man H Yoo. First-principles examination of the twin boundary in hcp metals. *Philosophical Magazine*, 85(2-3):233–238, 2005.

[165] Naoyuki Nagasako, Michal Jahnatek, Ryoji Asahi, and Juergen Hafner. Anomalies in the response of v, nb, and ta to tensile and shear loading: Ab initio density functional theory calculations. *Physical Review B*, 81(9):094108, MAR 1 2010.

[166] Anirudh Raju Natarajan, Ellen LS Solomon, Brian Puchala, Emmanuelle A Marquis, and Anton Van der Ven. On the early stages of precipitation in dilute mg–nd alloys. *Acta Materialia*, 108:367–379, 2016.

[167] Chang Ni, Hong Ding, Mark Asta, and Xuejun Jin. Computational study of¡ 11¯ 00¿ symmetric tilt grain boundaries in mg and ti. *Scripta Materialia*, 109:94–99, 2015.

[168] Jian F Nie and Barry C Muddle. Characterisation of strengthening precipitate phases in a mg–y–nd alloy. *Acta materialia*, 48(8):1691–1703, 2000.

[169] Jian Feng Nie. Effects of precipitate shape and orientation on dispersion strengthening in magnesium alloys. *Scripta Materialia*, 48(8):1009–1015, 2003.

[170] Jian Feng Nie, Xiang Gao, and Su-Ming Zhu. Enhanced age hardening response and creep resistance of mg–gd alloys containing zn. *Scripta Materialia*, 53(9):1049–1053, 2005.

[171] Jian Feng Nie, YM Zhu, JZ Liu, and Xi-Ya Fang. Periodic segregation of solute atoms in fully coherent twin boundaries. *Science*, 340(6135):957–960, 2013.

[172] AV Nikulina. Zirconium-niobium alloys for core elements of pressurized water reactors. *Metal science and heat treatment*, 45(7-8):287–292, 2003.

[173] Artem R Oganov and Colin W Glass. Crystal structure prediction using ab initio evolutionary techniques: Principles and applications. *The Journal of chemical physics*, 124(24):244704, 2006.

[174] Artem R Oganov, Andriy O Lyakhov, and Mario Valle. How evolutionary crystal structure prediction works and why. *Accounts of chemical research*, 44(3):227–237, 2011.

[175] Artem R Oganov and Mario Valle. How to quantify energy landscapes of solids. *The Journal of chemical physics*, 130(10):104504, 2009.

[176] Shigenobu Ogata, Ju Li, and Sidney Yip. Energy landscape of deformation twinning in bcc and fcc metals. *Physical Review B*, 71(22):224102, 2005.

[177] David L Olmsted, Stephen M Foiles, and Elizabeth A Holm. Survey of computed grain boundary properties in face-centered cubic metals: I. grain boundary energy. *Acta Materialia*, 57(13):3694–3703, 2009.

[178] A Ostapovets and AD Sheikh-Ali. Misorientation dependence of atomic structure and energy of symmetric tilt boundaries in magnesium. *Philosophical Magazine*, 98(36):3235–3246, 2018.

[179] Hyoungki Park, Michael R Fellinger, Thomas J Lenosky, William W Tipton, Dallas R Trinkle, Sven P Rudin, Christopher Woodward, John W Wilkins, and Richard G Hennig. Ab initio based empirical potential used to study the mechanical properties of molybdenum. *Physical Review B*, 85(21):214121, 2012.

[180] Robert G Parr. Density functional theory of atoms and molecules. In *Horizons of Quantum Chemistry*, pages 5–15. Springer, 1980.

[181] HW Paxton. Experimental verification of the twin system in alpha-iron. *Acta Metallurgica*, 1(2):141–143, 1953.

[182] John P Perdew, Kieron Burke, and Matthias Ernzerhof. Generalized gradient approximation made simple. *Physical review letters*, 77(18):3865, 1996.

[183] John P Perdew, John A Chevary, Sy H Vosko, Koblar A Jackson, Mark R Pederson, Dig J Singh, and Carlos Fiolhais. Atoms, molecules, solids, and surfaces: Applications of the generalized gradient approximation for exchange and correlation. *Physical review B*, 46(11):6671, 1992.

[184] Kristin Persson, Mathias Ekman, and Göran Grimvall. Dynamical and thermodynamical instabilities in the disordered re x w 1- x system. *Physical Review B*, 60(14):9999, 1999.

[185] Kristin Persson, Mathias Ekman, and Vidvuds Ozoliņš. Phonon instabilities in bcc sc, ti, la, and hf. *Physical Review B*, 61(17):11221, 2000.

[186] NJ Petch. The cleavage strength of polycrystals. *Journal of the Iron and Steel Institute*, 174:25–28, 1953.

[187] Nicolas J Peter, Timofey Frolov, Maria J Duarte, Raheleh Hadian, Colin Ophus, Christoph Kirchlechner, Christian H Liebscher, and Gerhard Dehm. Segregation-induced nanofaceting transition at an asymmetric tilt grain boundary in copper. *Physical review letters*, 121(25):255502, 2018.

[188] SR Phillpot and JM Rickman. Simulated quenching to the zero-temperature limit of the grand-canonical ensemble. *The Journal of chemical physics*, 97(4):2651–2658, 1992.

[189] Chris J Pickard and RJ Needs. Ab initio random structure searching. *Journal of Physics: Condensed Matter*, 23(5):053201, 2011.

[190] TJ Pike and B Noble. The formation and structure of precipitates in a dilute magnesium-neodymium alloy. *Journal of the Less Common Metals*, 30(1):63–74, 1973.

[191] Steve Plimpton. Fast parallel algorithms for short-range molecular dynamics. *Journal of computational physics*, 117(1):1–19, 1995.

[192] Tresa M Pollock. Weight loss with magnesium alloys. *Science*, 328(5981):986–987, 2010.

[193] RC Pond, S Celotto, and JP Hirth. A comparison of the phenomenological theory of martensitic transformations with a model based on interfacial defects. *Acta materialia*, 51(18):5385–5398, 2003.

[194] RC Pond and JP Hirth. Defects at surfaces and interfaces. In *Solid State Physics*, volume 47, pages 287–365. Elsevier, 1994.

[195] BM Powell, P Martel, and ADB Woods. Lattice dynamics of niobium-molybdenum alloys. *Physical Review*, 171(3):727, 1968.

[196] William H Press. *Numerical recipes 3rd edition: The art of scientific computing*. Cambridge university press, 2007.

[197] Liang Qi and DC Chrzan. Tuning ideal tensile strengths and intrinsic ductility of bcc refractory alloys. *Physical review letters*, 112(11):115503, 2014.

[198] A Rajabzadeh, M Legros, N Combe, F Mompiou, and DA Molodov. Evidence of grain boundary dislocation step motion associated to shear-coupled grain boundary migration. *Philosophical Magazine*, 93(10-12):1299–1316, 2013.

[199] Sutatch Ratanaphan, David L Olmsted, Vasily V Bulatov, Elizabeth A Holm, Anthony D Rollett, and Gregory S Rohrer. Grain boundary energies in body-centered cubic metals. *Acta Materialia*, 88:346–354, 2015.

[200] R Rebonato, DO Welch, RD Hatcher, and JC Bilello. A modification of the finnis-sinclair potentials for highly deformed and defective transition metals. *Philosophical Magazine A*, 55(5):655–667, 1987.

[201] James R Rice. Dislocation nucleation from a crack tip: an analysis based on the peierls concept. *Journal of the Mechanics and Physics of Solids*, 40(2):239–271, 1992.

[202] Joachim Riedle, Peter Gumbsch, and Hellmut F Fischmeister. Cleavage anisotropy in tungsten single crystals. *Physical review letters*, 76(19):3594, 1996.

[203] JD Rittner and David N Seidman. ¡ 110¿ symmetric tilt grain-boundary structures in fcc metals with low stacking-fault energies. *Physical Review B*, 54(10):6999, 1996.

[204] JD Rittner, David N Seidman, and KL Merkle. Grain-boundary dissociation by the emission of stacking faults. *Physical Review B*, 53(8):R4241, 1996.

[205] R Roberge. Lattice parameter of niobium between 4.2 and 300 k. *Journal of the Less Common Metals*, 40(1):161–164, 1975.

[206] Joseph D Robson. Effect of rare-earth additions on the texture of wrought magnesium alloys: the role of grain boundary segregation. *Metallurgical and Materials Transactions A*, 45(8):3205–3212, 2014.

[207] Joseph D Robson, Sarah J Haigh, Bruce Davis, and David Griffiths. Grain boundary segregation of rare-earth elements in magnesium alloys. *Metallurgical and Materials Transactions A*, 47(1):522–530, 2016.

[208] Lorenz Romaner, Claudia Ambrosch-Draxl, and Reinhard Pippan. Effect of rhenium on the dislocation core structure in tungsten. *Physical review letters*, 104(19):195503, 2010.

[209] D Roundy, CR Krenn, Marvin L Cohen, and JW Morris Jr. Ideal shear strengths of fcc aluminum and copper. *Physical Review Letters*, 82(13):2713, 1999.

[210] D Roundy, CR Krenn, Marvin L Cohen, and JW Morris Jr. The ideal strength of tungsten. *Philosophical magazine A*, 81(7):1725–1747, 2001.

[211] Kaichi Saito and Kenji Hiraga. The structures of precipitates in an mg-0.5 at% nd age-hardened alloy studied by haadf-stem technique. *Materials Transactions*, pages 1109051461–1109051461, 2011.

[212] Michael D Sangid, Tawhid Ezaz, Huseyin Sehitoglu, and Ian M Robertson. Energy of slip transmission and nucleation at grain boundaries. *Acta materialia*, 59(1):283–296, 2011.

[213] Daniel Scheiber, Reinhard Pippan, Peter Puschnig, and Lorenz Romaner. Ab initio calculations of grain boundaries in bcc metals. *Modelling and Simulation in Materials Science and Engineering*, 24(3):035013, 2016.

[214] Jennifer D Schuler and Timothy J Rupert. Materials selection rules for amorphous complexion formation in binary metallic alloys. *Acta Materialia*, 140:196–205, 2017.

[215] A Serra, DJ Bacon, and RC Pond. The crystallography and core structure of twinning dislocations in hcp metals. *Acta Metallurgica*, 36(12):3183–3203, 1988.

[216] A Serra, RC Pond, and DJ Bacon. Computer simulation of the structure and mobility of twinning disclocations in hcp metals. *Acta metallurgica et materialia*, 39(7):1469–1480, 1991.

[217] Wahyu Setyawan and Richard J Kurtz. Effects of transition metals on the grain boundary cohesion in tungsten. *Scripta Materialia*, 66(8):558–561, 2012.

[218] Wahyu Setyawan and Richard J Kurtz. Ab initio study of h, he, li and be impurity effect in tungsten $\sigma 3$ $\{1\ 1\ 2\}$ and $\sigma 27$ $\{5\ 5\ 2\}$ grain boundaries. *Journal of Physics: Condensed Matter*, 26(13):135004, 2014.

[219] Pooja Shah and Charusita Chakravarty. Potential-energy landscapes of simple liquids. *Physical review letters*, 88(25):255501, 2002.

[220] Tristan A. Sharp, Spencer L. Thomas, Ekin D. Cubuk, Samuel S. Schoenholz, David J. Srolovitz, and Andrea J. Liu. Machine learning determination of atomic dynamics at grain boundaries. *Proceedings of the National Academy of Sciences of the United States of America*, 115:10943–10947, 2018.

[221] Z Shen, RH Wagoner, and WAT Clark. Dislocation and grain boundary interactions in metals. *Acta metallurgica*, 36(12):3231–3242, 1988.

[222] Xiaomeng Shi and Jian Luo. Grain boundary wetting and prewetting in ni-doped mo. *Applied Physics Letters*, 94(25):251908, 2009.

[223] Leon J Slutsky and CW Garland. Elastic constants of magnesium from 4.2 k to 300 k. *Physical Review*, 107(4):972, 1957.

[224] M Šob, LG Wang, and V Vitek. Theoretical tensile stress in tungsten single crystals by full-potential first-principles calculations. *Materials Science and Engineering: A*, 234:1075–1078, 1997.

[225] Paul J Steinhardt, David R Nelson, and Marco Ronchetti. Bond-orientational order in liquids and glasses. *Physical Review B*, 28(2):784, 1983.

[226] AN Stroh. Dislocations and cracks in anisotropic elasticity. *Philosophical magazine*, 3(30):625–646, 1958.

[227] Alexander Stukowski. Visualization and analysis of atomistic simulation data with ovito–the open visualization tool. *Modelling and Simulation in Materials Science and Engineering*, 18(1):015012, 2009.

[228] Yuemin Sun and Glenn E Beltz. Dislocation nucleation from a crack tip: a formulation based on anisotropic elasticity. *Journal of the Mechanics and Physics of Solids*, 42(12):1905–1932, 1994.

[229] Adrian P Sutton, Robert W Balluffi, and AP Sutton. *Interfaces in crystalline materials*. Clarendon Press Oxford, 1995.

[230] William C Swope, Hans C Andersen, Peter H Berens, and Kent R Wilson. A computer simulation method for the calculation of equilibrium constants for the formation of physical clusters of molecules: Application to small water clusters. *The Journal of Chemical Physics*, 76(1):637–649, 1982.

[231] E. B. Tadmor and N. Bernstein. A first-principles measure for the twinnability of fcc metals. *Journal of Mechanics Physics of Solids*, 52:2507–2519, 2004.

[232] Geoffrey Ingram Taylor. Plastic strain in metals. *J. Inst. Metals*, 62:307–324, 1938.

[233] E. Tejado, P. A. Carvalho, A. Munoz, M. Dias, J. B. Correia, U. V. Mardolcar, and J. Y. Pastor. The effects of tantalum addition on the microtexture and mechanical behavior of tungsten for iter applications. *Journal of Nuclear Materials*, 467:949–955, 2015.

[234] Aidan P Thompson, Steven J Plimpton, and William Mattson. General formulation of pressure and stress tensor for arbitrary many-body interaction potentials under periodic boundary conditions. *The Journal of chemical physics*, 131(15):154107, 2009.

[235] A Togo and I Tanaka. First principles phonon calculations in materials science. *Scr. Mater.*, 108:1–5, Nov 2015.

[236] Atsushi Togo and Isao Tanaka. First principles phonon calculations in materials science. *Scripta Materialia*, 108:1–5, 2015.

[237] Yeram Sarkis Touloukian and CY Ho. Thermal expansion. metallic elements and alloys. *Thermophysical properties of matter-The TPRC Data Series, New York: IFI/Plenum, 1970-, edited by Touloukian, YS— e (series ed.); Ho, CY— e (series tech. ed.)*, 1970.

[238] Dallas R Trinkle and Christopher Woodward. The chemistry of deformation: How solutes soften pure metals. *Science*, 310(5754):1665–1667, 2005.

[239] Norman Troullier and José Luís Martins. Efficient pseudopotentials for plane-wave calculations. *Physical review B*, 43(3):1993, 1991.

[240] MA Tschopp and DL McDowell. Structures and energies of σ 3 asymmetric tilt grain boundaries in copper and aluminium. *Philosophical Magazine*, 87(22):3147–3173, 2007.

[241] Mark A Tschopp and DL McDowell. Dislocation nucleation in σ 3 asymmetric tilt grain boundaries. *International Journal of Plasticity*, 24(2):191–217, 2008.

[242] Maxime Van den Bossche, Henrik Grönbeck, and Bjørk Hammer. Tight-binding approximation-enhanced global optimization. *Journal of chemical theory and computation*, 14(5):2797–2807, 2018.

[243] H Van Swygenhoven, PM Derlet, and A Hasnaoui. Atomic mechanism for dislocation emission from nanosized grain boundaries. *Physical Review B*, 66(2):024101, 2002.

[244] Lisa Ventelon, F Willaime, E Clouet, and D Rodney. Ab initio investigation of the peierls potential of screw dislocations in bcc fe and w. *Acta Materialia*, 61(11):3973–3985, 2013.

[245] Loup Verlet. Computer" experiments" on classical fluids. i. thermodynamical properties of lennard-jones molecules. *Physical review*, 159(1):98, 1967.

[246] V Vitek. Intrinsic stacking faults in body-centred cubic crystals. *Philosophical Magazine*, 18(154):773–786, 1968.

[247] V Vitek, RC Perrin, and DK Bowen. The core structure of 1/2 (111) screw dislocations in bcc crystals. *Philosophical Magazine*, 21(173):1049–1073, 1970.

[248] S Von Alfthan, PD Haynes, K Kaski, and AP Sutton. Are the structures of twist grain boundaries in silicon ordered at 0 k? *Physical review letters*, 96(5):055505, 2006.

[249] S Von Alfthan, K Kaski, and AP Sutton. Molecular dynamics simulations of temperature-induced structural transitions at twist boundaries in silicon. *Physical Review B*, 76(24):245317, 2007.

[250] Malik Wagih and Christopher A Schuh. Spectrum of grain boundary segregation energies in a polycrystal. *Acta Materialia*, 181:228–237, 2019.

[251] J Wang, IJ Beyerlein, and CN Tomé. Reactions of lattice dislocations with grain boundaries in mg: implications on the micro scale from atomic-scale calculations. *International Journal of Plasticity*, 56:156–172, 2014.

[252] Jian Wang and Irene J Beyerlein. Atomic structures of symmetric tilt grain boundaries in hexagonal close packed (hcp) crystals. *Modelling and Simulation in Materials Science and Engineering*, 20(2):024002, 2012.

[253] Yanchao Wang, Jian Lv, Li Zhu, and Yanming Ma. Crystal structure prediction via particle-swarm optimization. *Physical Review B*, 82(9):094116, 2010.

[254] Yi Wang and Hahn Choo. Influence of texture on hall–petch relationships in an mg alloy. *Acta Materialia*, 81:83–97, 2014.

[255] C. R. Weinberger, B. L. Boyce, and C. C. Battaile. Slip planes in bcc transition metals. *International Materials Reviews*, 58(5):296–314, JUN 2013.

[256] Christopher R Weinberger, Garritt J Tucker, and Stephen M Foiles. Peierls potential of screw dislocations in bcc transition metals: Predictions from density functional theory. *Physical Review B*, 87(5):054114, 2013.

[257] Yan-Ni Wen and Jian-Min Zhang. Surface energy calculation of the bcc metals by using the maeam. *Computational Materials Science*, 42(2):281–285, 2008.

[258] EL Willighagen, R Wehrens, P Verwer, R De Gelder, and LMC Buydens. Method for the computational comparison of crystal structures. *Acta Crystallographica Section B: Structural Science*, 61(1):29–36, 2005.

[259] Dieter Wolf and Sidney Yip. *Materials interfaces: atomic-level structure and properties*. Springer Science & Business Media, 1992.

[260] Matthew D Wolf and Uzi Landman. Genetic algorithms for structural cluster optimization. *The Journal of Physical Chemistry A*, 102(30):6129–6137, 1998.

[261] Z Wu and WA Curtin. Brittle and ductile crack-tip behavior in magnesium. *Acta Materialia*, 88:1–12, 2015.

[262] Z Wu, MF Francis, and WA Curtin. Magnesium interatomic potential for simulating plasticity and fracture phenomena. *Modelling and Simulation in Materials Science and Engineering*, 23(1):015004, 2015.

[263] S. Wurster, B. Gludovatz, A. Hoffmann, and R. Pippan. Fracture behaviour of tungsten?vanadium and tungsten?tantalum alloys and composites. *Journal of Nuclear Materials*, 413:166–176, 2011.

[264] Kelvin Y Xie, Zafir Alam, Alexander Caffee, and Kevin J Hemker. Pyramidal i slip in c-axis compressed mg single crystals. *Scripta Materialia*, 112:75–78, 2016.

[265] Chaoming Yang and Liang Qi. Ab initio calculations of ideal strength and lattice instability in w-ta and w-re alloys. *Physical Review B*, 97(1):014107, 2018.

[266] Chaoming Yang and Liang Qi. Modified embedded-atom method potential of niobium for studies on mechanical properties. *Computational Materials Science*, 161:351–363, 2019.

[267] Chaoming Yang, Mingfei Zhang, and Liang Qi. Grain boundary structure search by using an evolutionary algorithm with effective mutation methods. *Computational Materials Science*, under review, 2020.

[268] Joseph A Yasi, Louis G Hector Jr, and Dallas R Trinkle. Prediction of thermal cross-slip stress in magnesium alloys from direct first-principles data. *Acta materialia*, 59(14):5652–5660, 2011.

[269] Joseph A Yasi, Louis G Hector Jr, and Dallas R Trinkle. Prediction of thermal cross-slip stress in magnesium alloys from a geometric interaction model. *Acta materialia*, 60(5):2350–2358, 2012.

[270] ZR Zeng, MZ Bian, SW Xu, CHJ Davies, N Birbilis, and JF Nie. Effects of dilute additions of zn and ca on ductility of magnesium alloy sheet. *Materials Science and Engineering: A*, 674:459–471, 2016.

[271] ZR Zeng, YM Zhu, SW Xu, MZ Bian, CHJ Davies, N Birbilis, and JF Nie. Texture evolution during static recrystallization of cold-rolled magnesium alloys. *Acta Materialia*, 105:479–494, 2016.

[272] Jian Zhang, Cai-Zhuang Wang, and Kai-Ming Ho. Finding the low-energy structures of si [001] symmetric tilted grain boundaries with a genetic algorithm. *Physical Review B*, 80(17):174102, 2009.

[273] Pinchao Zhang and Dallas R Trinkle. A modified embedded atom method potential for interstitial oxygen in titanium. *Computational Materials Science*, 124:204–210, 2016.

[274] KY Zheng, Jie Dong, XQ Zeng, and WJ Ding. Precipitation and its effect on the mechanical properties of a cast mg–gd–nd–zr alloy. *materials Science and Engineering: A*, 489(1-2):44–54, 2008.

[275] Bijin Zhou, Leyun Wang, Gaoming Zhu, Jie Wang, Wen Wen, and Xiaoqin Zeng. Understanding the strengthening effect of β 1 precipitates in mg-nd using in situ synchrotron x-ray diffraction. *JOM*, 70(10):2315–2320, 2018.

[276] SJ Zhou, AE Carlsson, and Robb Thomson. Crack blunting effects on dislocation emission from cracks. *Physical review letters*, 72(6):852, 1994.

[277] XW Zhou, HNG Wadley, R A_ Johnson, DJ Larson, N Tabat, A Cerezo, AK Petford-Long, GDW Smith, PH Clifton, RL Martens, et al. Atomic scale structure of sputtered metal multilayers. *Acta materialia*, 49(19):4005–4015, 2001.

[278] Qiang Zhu, Amit Samanta, Bingxi Li, Robert E Rudd, and Timofey Frolov. Predicting phase behavior of grain boundaries with evolutionary search and machine learning. *Nature communications*, 9(1):467, 2018.

[279] YM Zhu, MZ Bian, and JF Nie. Tilt boundaries and associated solute segregation in a mg–gd alloy. *Acta Materialia*, 127:505–518, 2017.

[280] YM Zhu, H Liu, Z Xu, Y Wang, and JF Nie. Linear-chain configuration of precipitates in mg–nd alloys. *Acta Materialia*, 83:239–247, 2015.

[281] SJ Zinkle and NM Ghoniem. Operating temperature windows for fusion reactor structural materials. *Fusion Engineering and Design*, 51-52:55–71, NOV 2000.